Turbulence and direct dark matter detection in the X-ray halo of galaxy clusters - implications for eROSITA

Florian Hofmann

München 2016

Turbulence and direct dark matter detection in the X-ray halo of galaxy clusters - implications for eROSITA

Florian Hofmann

Dissertation
an der Fakultät Physik
der Ludwig–Maximilians–Universität
München

vorgelegt von
Florian Hofmann
aus Landshut

München, den 28. September 2016

Erstgutachter: Prof. Dr. Kirpal Nandra
Zweitgutachter: Prof. Dr. Joseph Mohr
Tag der mündlichen Prüfung: 10. November 2016

Contents

List of Figures

List of Tables

Zusammenfassung

Diese Dissertation gliedert sich in drei Teile die sich jeweils mit aktuell wichtigen Fragestellungen in der Forschung an Galaxienhaufen auseinandersetzen.

Ich habe zuerst eine detaillierte Studie zu 33 Galaxienhaufen durchgeführt. Ziel dieser Studie war es Turbulenzen im heißen Plasma zu messen. Ich zeige darüber hinaus wie diese Turbulenzen die Messungen der Massen in den Galaxienhaufen beeinflussen. Die genaue Kenntnis der Masse ist dabei ausschlaggebend für kosmologische Studien an Galaxienhaufen. Ich analysiere tiefe Beobachtungen von 33 Galaxienhaufen, die mit dem *Chandra* Röntgenteleskop für mindestens 100 ks beobachtet wurden. Diese liegen bei Entfernungen zwischen Rotverschiebung 0.025 und 0.45. Die gesamte Belichtungszeit beträgt etwa 8 Ms. Ich messe thermodynamische Fluktuationen in den Röntgenbildern des heißen Gases und vergleiche diese mit hochauflösenden 3D hydrodynamischen Simulationen. Dies ermöglicht mir die Mach Zahl und somit Turbulenz im Medium einzugrenzen. Zusätzlich fand Ich eine negative Korrelation zwischen der Temperatur des Plasmas und dessen Metallizität.

Im zweiten Teil beschäftige Ich mich mit der Suche nach Spektrallinien die vom Zerfall steriler Neutrinos stammen könnten. Diese sterilen Neutrinos wären Kandidaten für die dunkle Materie deren Natur eine der wichtigsten offenen Fragen der Physik darstellt. Die hier studierten Galaxienhaufen sind ideal für solche Untersuchungen da Sie einen sehr großen Anteil dunkle Materie beinhalten. Vor kurzem wurde eine bisher unbekannte Röntgenlinie bei 3.55 keV gefunden und als mögliche Signatur des Zerfalls eines sterilen Neutrino mit einer Masse von 7.1 keV diskutiert. Ich nutzte die vorhandenen Röntgenspektren der 33 Galaxienhaufen meiner Studie um die Signifikanz der Linie einzuschätzen. Ich fand keinen starken Hinweis auf die Linie, konnte aber obere Grenzen ableiten die bisherige Ergebnisse in Frage stellen.

Im dritten Teil simuliere Ich welche Messungen mit dem zukünftigen eROSITA Röntgenteleskop für die von mir studierten Galaxienhaufen möglich sein werden. eROSITA wird annähernd alle massereichen Galaxienhaufen im sichtbaren Universum detektieren (ca. hunderttausend, weit mehr als je zuvor entdeckt) allerdings mit niedrigerer räumlicher Auflösung und kürzerer Belichtungszeit als *Chandra*. Deshalb eignen sich meine Simulationen um wichtige Vorhersagen zu systematischen Unsicherheiten in eROSITA Messungen beispielsweise der Temperatur zu machen. Diese Unsicherheiten haben direkten Einfluss auf die kosmologischen Studien welche das Hauptziel der eROSITA Mission darstellen.

Abstract

This thesis consists of three main parts each of which deals with currently important problems in the research of clusters of galaxies.

First I conducted a detailed study of 33 clusters with the aim of constraining turbulence in the hot phase of the intracluster medium (ICM). I demonstrate how the measured turbulence influences the mass measurements of clusters which is crucial for obtaining accurate cosmological constraints from cluster observations. In high-resolution X-ray observations of the hot plasma in clusters significant structures caused by AGN feedback, mergers, and turbulence can be detected. Many clusters have been observed with *Chandra* to great depths and at high resolution. Using archival data taken with the *Chandra* ACIS instrument I studied the thermodynamic perturbations of the X-ray emitting plasma and applied this to better understand the thermodynamic and dynamic state of the ICM. I analysed deep observations of a sample of 33 clusters with more than 100 ks of *Chandra* exposure each at distances between redshift 0.025 and 0.45. The combined exposure of the sample is 8 Ms. Fitting emission models to different regions of the extended X-ray emission I searched for perturbations in density, temperature, pressure, and entropy of the hot plasma. For individual clusters I mapped the thermodynamic properties of the ICM and measured their spread in circular concentric annuli. Comparing the spread of different gas quantities to high-resolution 3D hydrodynamic simulations, I constrain the average Mach number regime of the sample to $\mathrm{Mach}_{\mathrm{1D}} \approx 0.16 \pm 0.07$. In addition I found a tight correlation between metallicity, temperature and redshift with an average metallicity of $\mathrm{Z} \approx 0.3 \pm 0.1\ \mathrm{Z}_{\odot}$. This study provides detailed perturbation measurements for a large sample of clusters which can be used to study turbulence and make predictions for future X-ray observatories like *eROSITA*, *Hitomi (Astro-H)*, and *Athena*.

Secondly using the deep spectra from the clusters studied in the first part I obtained constraints on X-ray emission from a possible dark matter decay signal in the cluster halos. Recently an unidentified emission line at 3.55 keV has been detected in X-ray spectra of clusters of galaxies. The line has been discussed as a possible decay signature of 7.1 keV sterile neutrinos, which have been proposed as a dark matter candidate. For a sample of 33 high-mass clusters of galaxies I merged all observations from the *Chandra* data archive. The resulting high signal-to-noise spectra are used to constrain the flux of an unknown line emission at 3.55 keV in the individual spectra and a merged spectrum of all clusters. I do not find evidence for an unidentified emission line at 3.55 keV. The sample extends the list of objects searched for an emission line at 3.55 keV and will help to identify the

best targets for future studies of the potential dark matter decay line with upcoming X-ray observatories like *Hitomi (Astro-H)*, *eROSITA*, and *Athena*.

The third and last part of my work is to make predictions on how the upcoming eROSITA observatory will observe the clusters I studied. eROSITA will detect the largest sample of clusters to date (one hundred thousand expected) but at lower spatial resolution and shorter exposure time than the clusters I studied with *Chandra*. This makes it very important to simulate observations of well known clusters and identify possible bias in measured parameters. I simulated a large number of galaxy clusters with known temperature substructures and compared the results from analysing eROSITA simulated observations to results I obtained from *Chandra*. I was able to constrain the expected measurement bias in temperature and flux which is caused by substructures of the cluster emission. To get reliable cosmological parameter constraints from the eROSITA cluster sample it will be important to take into account the systematic bias found in this analysis.

Chapter 1

Introduction

1.1 Preface

Clusters of galaxies are among the largest gravitationally bound structures in the universe. They are excellent probes of cosmological models since they show structure formation on large scales. The best way to directly observe the hot phase of the plasma in clusters is through observation of X-rays emitted by the collisionally ionised plasma with temperatures around ten million Kelvin. There has been a large variety of X-ray telescopes in space over the last decade to observe these highly energetic and hot regions of the universe and there are many more with ever better capabilities planned for the near and far future (e.g. HITOMI (Astro-H), eROSITA, and Athena).

In this study I am using state of the art telescopes to observe the structure of the hot gas in clusters and I try to put constraints on the thermodynamic state and elemental abundances (including the search for dark matter). Due to the large archive of deep observations of galaxy clusters I am able to go into unprecedented detail for a large sample of clusters.

Using the information gained from this study I make predictions for the future eROSITA observatory (Merloni et al. 2012) by simulating observations of galaxy clusters. This allows bias measurements of cluster properties to support the mission's ambitious goals of obtaining the best constraint on dark energy and to detect all massive clusters in the observable universe.

After an introduction to the current state of research on galaxy clusters and an overview of some state of the art instruments in the field and their data reduction I show how I used the available data to obtain new insights to advance the current knowledge on the X-ray halo of galaxy clusters.

This work is structured as follows:

In chapter 1 I introduce the main scientific concepts behind my work and the background of some important previous publications in the field of galaxy clusters. In chapter

2 I describe the instruments and data products that I used for my study. I also describe the sample of clusters I used and how I obtained simulated eROSITA observations. In chapter 3 I describe how I used deep archival *Chandra* observations to obtain turbulence limits in the ICM for a sample of 33 clusters. In chapter 4 I describe how I used the deep X-ray spectra of the 33 clusters to constrain the possibility of a 7.1 keV sterile neutrino as dark matter. In chapter 5 I discuss how I simulated eROSITA survey observations of the 33 clusters to constrain bias in measured temperature and impact on cosmology. Chapter 6 is a summary of my results and gives an outlook on the future direction of the studies.

This work includes sections of the following peer reviewed publications:

Chapter 3 is based on:

F. Hofmann, J. S. Sanders, K. Nandra, N. Clerc, M. Gaspari. 2016a. Thermodynamic perturbations in the X-ray halo of 33 clusters of galaxies observed with *Chandra* ACIS. Astronomy & Astrophysics. Volume 585. A130

Chapter 4 is based on:

F. Hofmann, J. S. Sanders, K. Nandra, N. Clerc, M. Gaspari. 2016b. 7.1 keV sterile neutrino constraints from X-ray observations of 33 clusters of galaxies with *Chandra* ACIS. Astronomy & Astrophysics. Volume 592. A112 (Research highlight in Astronomy & Astrophysics and Nature Magazine)

For all my analysis I used a standard ΛCDM cosmology with $H_0 = 71$ km s^{-1} Mpc^{-1}, $\Omega_M = 0.27$ and $\Omega_\Lambda = 0.73$ and relative solar abundances as given by Anders & Grevesse (1989). See cosmology introduction (section below) for an explanation of the assumed cosmological parameters. In the following $h \equiv 100$ km s^{-1} Mpc^{-1} is sometimes used to express distance measures to easily allow conversion to a cosmology with different Hubble constant H.

The spectral fitting in Chapter 3 and 4 is affected by a recently uncovered bug in the `XSPEC` software which caused the normalisation and metallicity of the `apec` model fits to be depending on redshift z (versions 12.8.1, 12.8.2, and 12.9.0)[1]. The values for normalisation and metallicity in these Chapters have to be multiplied by a factor of 1+z to obtain the correct values. Because most of our results are based on ratios between these values (Chapter 3) or normalisation of the `zgauss` model which was not affected by the bug (Chapter 4) our results will remain unchanged. However the metallicity gradient with redshift in Chapter 3 is affected by this bug and will be properly updated in an erratum to the linked publication (see Hofmann et al., in preparation). The slope of the function of metallicity with redshift is expected to become much shallower. The bug was discovered too close to the end of the project to allow me to include updated results in this thesis.

[1] `https://heasarc.gsfc.nasa.gov/xanadu/xspec/issues/issues.html`

1.2 The ΛCDM cosmological model

In the past decades the most commonly accepted cosmological model has been the ΛCDM model (e.g. Riess et al. 1998; Springel et al. 2005). In this model the universe expands freely after an initial acceleration caused by the big bang with an added cosmological constant Λ which is also known as dark energy (see e.g. Peebles & Ratra 2003; Copeland et al. 2006; Weinberg et al. 2013). The energy content of the universe is mostly ($\sim$ 73 per cent assumed in this study) in the form of this dark energy which causes recent re-acceleration of the expansion of the universe (e.g. Perlmutter et al. 1999). The rest of the energy ($\sim$ 27 per cent assumed in this study) mostly in the form of cold dark matter (CDM) and a smaller fraction baryonic matter (with a mass-ratio of about 5/1 between the two). Cold DM refers to relatively low velocities of the dark matter particles after the big bang (Navarro et al. 1996). Initial density fluctuations in the matter distribution after the big bang are enhanced by gravity over time (Mukhanov et al. 1992). The DM starts forming clumps which create gravitational wells in which baryonic matter is accreted. Fig. 1.1 shows a simulation of how small fluctuations are enhanced over time and form large structures and clumps (for details on structure formation see e.g. Peebles 1993). This is both shown for DM and galaxies which are simulated as point masses in this case (Springel et al. 2005). The largest clusters of galaxies visible in the simulations are eventually observed in X-rays once their halo reaches high enough mass to heat the intergalactic medium to high enough temperatures. The main parameters influencing the expansion and formation of structure are the relative matter density $\Omega_{\rm M} = 0.27$ and the relative dark energy density $\Omega_\Lambda = 0.73$.. These parameters are ever better constrained with new missions (e.g. observations of the cosmic microwave background, CMB Planck Collaboration et al. 2014a; Spergel et al. 2003). The CMB fluctuations are extremely well fit by the ΛCDM model and constrain parameters very well. The parameters $\Omega_{\rm M}$, Ω_Λ, σ_8 (see theoretical framework) can be constrained best with observations of number counts and mass distribution of galaxy clusters (Reiprich & Böhringer 2002; Allen et al. 2008; Vikhlinin et al. 2009a; Mantz et al. 2010). There is currently some tension between the cosmological parameters obtained from CMB and cluster observations which could be caused by yet unknown effect in cluster formation. Non-thermal pressure support in clusters of galaxies would change the mass estimates which are typically obtained from a pure hydrostatic equilibrium assumption (Ponman et al. 1999; Zhang et al. 2010; Navarro et al. 1995). Also massive galaxy clusters are expected to have a ratio of baryonic mass to total mass that is similar to the average value of the local universe (see e.g. White et al. 1993).

The density distributions of galaxies predicted by the ΛCDM model agree very well with the observations of a large number of galaxy surveys. Fig. 1.2 shows an comparison of the structures in the Millenium simulation and some large area galaxy surveys. Distances at cosmological scales are generally given as redshift which assuming a cosmological model can be translated into a physical distance.

The emission of astronomical objects is redshifted depending on their distance from the observer as the photons of any distant source beyond the Local Group of galaxies are shifted to lower energies because of the expansion of the universe during the light travel

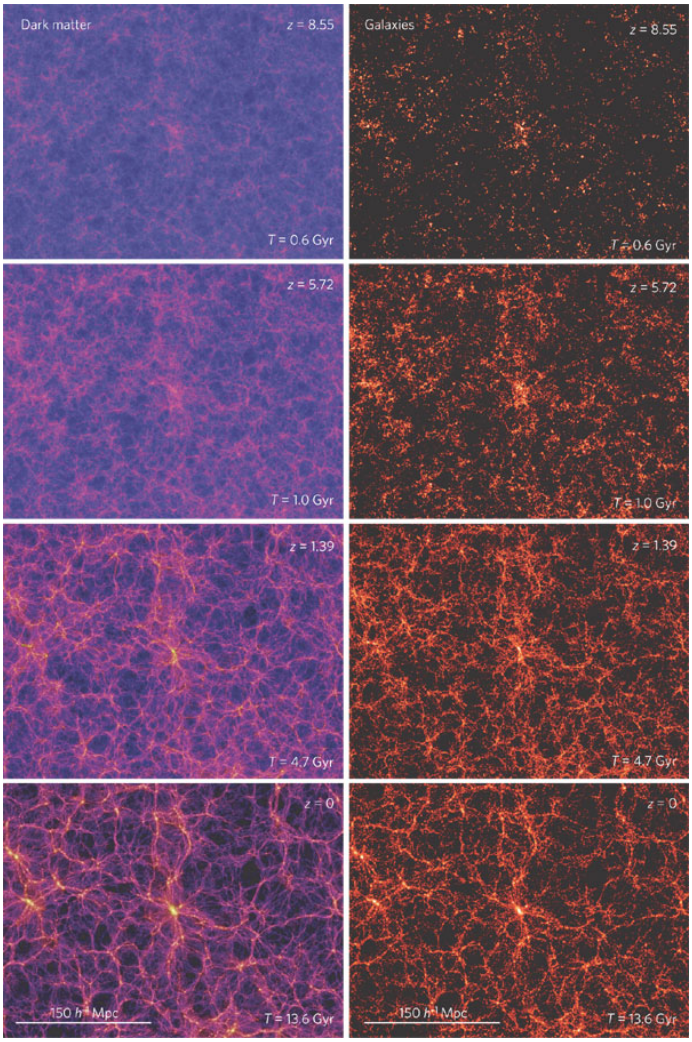

Figure 1.1: The panels on the left show the projected dark matter distribution in slices of thickness 15 h-1 Mpc, extracted at redshifts z = 8.55, z = 5.72, z = 1.39 and z = 0 from the Millennium N-body simulation of structure formation. These epochs correspond to times of 600 million, 1 billion, 4.7 billion and 13.6 billion years after the Big Bang, respectively. The colour hue from blue to red encodes the local velocity dispersion in the dark matter, and the brightness of each pixel is a logarithmic measure of the projected density. The panels on the right show the predicted distribution of galaxies in the same region at the corresponding times obtained by applying semi-analytic techniques to simulate galaxy formation in the Millennium simulation. Each galaxy is weighted by its stellar mass, and the colour scale of the images is proportional to the logarithm of the projected total stellar mass. The dark matter evolves from a smooth, nearly uniform distribution into a highly clustered state, quite unlike the galaxies, which are strongly clustered from the start. Figure and caption from Springel et al. (2006).

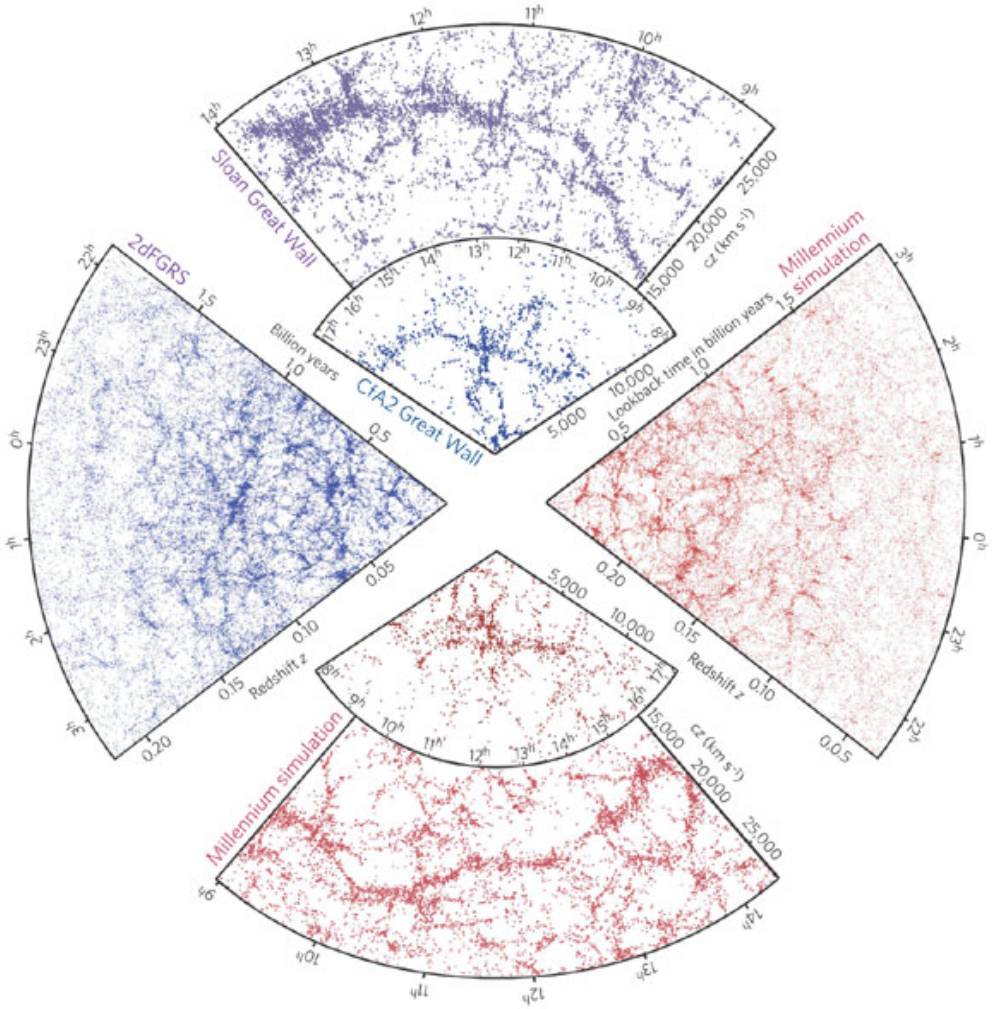

Figure 1.2: The small slice at the top shows the CfA2 "Great Wall" (Freedman et al. 2001), with the Coma cluster at the centre. Drawn to the same scale is a small section of the SDSS (York et al. 2000), in which an even larger "Sloan Great Wall" has been identified. This is one of the largest observed structures in the Universe, containing over 10,000 galaxies and stretching over more than 1.37 billion light years. The cone on the left shows one-half of the 2dFGRS survey (Colless et al. 2001), which determined distances to more than 220,000 galaxies in the southern sky out to a depth of 2 billion light years. The SDSS has a similar depth but a larger solid angle and included over 650,000 observed redshifts in the northern sky in 2006. At the bottom and on the right, mock galaxy surveys constructed using semi-analytic techniques to simulate the formation and evolution of galaxies within the evolving dark matter distribution of the "Millennium" simulation (Springel et al. 2005) are shown, selected with matching survey geometries and magnitude limits. Figure and caption from Springel et al. (2006).

time. This effect occurs only at very large distances for object not gravitationally bound to the same structure as the observer. The redshift of the galaxy clusters can be measured directly from high quality X-ray spectra (see below) or from the redshift of its member galaxies, which is often more accurate and easier to measure in the optical wavelength (see e.g. Zhang et al. 2011a; Rines et al. 2013; Clerc et al. 2014, and Ridl et al., in prep.). The redshift z can be determined by measuring the energy (or wavelength λ) shift of emission lines in high signal-to-noise spectra as,

$$z = \frac{\lambda_{\mathrm{observed}} - \lambda_{\mathrm{emitted}}}{\lambda_{\mathrm{emitted}}} \tag{1.1}$$

The actual distance to the source then depends on the assumed cosmology and the related expansion history of the universe. Throughout this work I used a standard ΛCDM cosmology with $H_0 = 71$ km s^{-1} Mpc^{-1}, $\Omega_M = 0.27$ and $\Omega_\Lambda = 0.73$.

While the N-body ΛCDM simulations are very successful in matching predictions for the observable universe there are still some discrepancies. For example the effects of the gas in massive clusters on the formation has to be better understood. This influences the accuracy of cluster mass estimates and thus also cosmological constraints from cluster surveys (see below). Also it has to be studied if there are better DM candidates than CDM since it creates too many subhalos compared to simulations (see below).

There are a number of recent simulations trying to tackle these problems of pure N-body simulations by including effects of the ICM and feedback from star formation on structure formation (e.g. the Magneticum, EAGLE, and ILLUSTRIS simulations Dolag 2015; Schaye et al. 2015; Vogelsberger et al. 2014). They can be used to study in detail systematic effects in the formation not included in DM only studies (e.g Bocquet et al. 2016).

1.2.1 Theoretical framework

In the ΛCDM cosmology model (which includes dark energy) the Friedmann equation describing the expansion of the universe is given as (see Merloni et al. 2012),

$$H(a) = \frac{\dot{a}}{a} = H_0 \sqrt{\frac{\Omega_M}{a^3} + \frac{\Omega_{\mathrm{rad}}}{a^4} + \frac{\Omega_k}{a^2} + \frac{\Omega_\Lambda}{a^{3(1+\omega)}}} \tag{1.2}$$

where a is the scale factor, H_0 the Hubble constant, Ω_M the matter density and Ω_Λ the dark energy density. Assuming that the curvature density Ω_k is zero (in a flat universe), the equation of state of dark energy $\omega = -1$ (expected from latest Planck results Planck Collaboration et al. 2014a), and neglecting Ω_{rad} which is measured to be orders of magnitudes smaller than Ω_M the Friedmann equation simplifies to,

$$H(a) \approx H_0 \sqrt{\frac{\Omega_M}{a^3} + \Omega_\Lambda} \tag{1.3}$$

The clustering within the expanding universe caused by the gravitational attenuation of primordial density fluctuations is described by the density contrast (in Fourier representation, see e.g. Borgani 2008),

$$\tilde{\delta}(\mathrm{k}) = \frac{1}{(2\pi)^{3/2}} \int \mathrm{d}\mathbf{x}\ \delta(\mathbf{x}) \mathrm{e}^{\mathrm{i}\mathbf{k}\cdot\mathbf{x}} \tag{1.4}$$

where $\mathbf{x}$ is the position vector. With the 2-point correlation function for the density contrast,

$$\xi(\mathrm{r}) = \langle \delta(\mathbf{x_1}) \delta(\mathbf{x_2}) \rangle \tag{1.5}$$

depending only on the modulus of the separation vector $\mathrm{r} = |\mathbf{x_1} - \mathbf{x_2}|$, assuming statistical isotropy of the density field. The power spectrum of the density fluctuations can be written as,

$$\mathrm{P}(\mathrm{k}) = \langle |\delta(\tilde{\mathbf{k}})|^2 \rangle = \frac{1}{2\pi^2} \int \mathrm{dr}\ \mathrm{r}^2 \xi(\mathrm{r}) \frac{\sin(\mathrm{kr})}{\mathrm{kr}} \tag{1.6}$$

then the variance of the fluctuation field on scales R is,

$$\sigma_{\mathrm{R}}^2 = \frac{1}{2\pi^2} \int \mathrm{dk}\ \mathrm{k}^2 \mathrm{P}(\mathrm{k}) \tilde{\mathrm{W}}_{\mathrm{R}}^2(\mathrm{k}) \tag{1.7}$$

where $\tilde{\mathrm{W}}_{\mathrm{R}}$ is the Fourier transform of the window function. The normalization of P(k) is the cosmological parameter σ_8 which is computed with a top-hat window function and scale $\mathrm{R} = 8\ \mathrm{h}^{-1}$ Mpc from Eq.1.7.

With perfectly Gaussian primordial fluctuations (no non-Gaussianity) the cosmological model is described by Ω_{M}, Ω_Λ, σ_8, and the spectral index of perturbations $\mathrm{n_s}$ (see Pillepich et al. 2012, and references therein).

1.3 Cluster formation

According to the current model of structure formation, after the big bang the universe cooled down and small primordial density fluctuations were enhanced over time by gravity. The dark matter which is thought to makes up the largest part of all matter in the universe started hierarchically forming the deepest potential wells. The interaction cross section of dark matter seems to be negligible and thus the clumping can be modeled very well by a purely gravitational collapse (for a more extensive review see Sarazin 1986). The dark matter forms virialised halos with velocity dispersions of typically ~ 1000 km s^{-1} (Navarro et al. 1996). Smaller DM subhalos like individual galaxies fall into the potential wells almost collisionless and become virialised. In the hierarchic formation scenario small halos are formed first and then clump together to form larger DM halos. The larges bound halos are then observed as massive clusters of galaxies (see e.g. Millenium simulation Springel et al. 2005). Virialisation means that the gained potential energy goes into kinetic energy following,

$$\langle \mathrm{T} \rangle = -\frac{1}{2} \sum_{\mathrm{k}=1}^{\mathrm{N}} \langle \mathrm{F_k} \cdot \mathrm{r_k} \rangle \tag{1.8}$$

where T is the kinetic energy, $\mathrm{F_k}$, and $\mathrm{r_k}$ are the force on and position of the k-th particle in the potential, respectively (virial theorem, originally introduced by Clausius 1870).

As the galaxy density of the cluster grows some galaxies start interacting and merge to central elliptical galaxies (brightest cluster galaxies, BCG). These BCGs are made of an old stellar population with very little star formation (De Lucia et al. 2006; De Lucia & Blaizot 2007) but are the largest galaxies in the cluster. They keep growing through mergers but the lack of gas in the central galaxies of a cluster keeps star formation very low (Lin et al. 2013; Kormendy et al. 2009). Galaxies and the thin gas around them make up the Baryonic matter content of the clusters. The largest fraction of this Baryonic matter is in the thin gas between the clumping galaxies called intra cluster medium (ICM, for a detailed review see e.g. Kaastra et al. 2008). The behavior of this gas during accretion into the potential well is far more complex than the accretion DM or galaxies because the interaction cross section can not be neglected in this case.

Massive clusters of galaxies ($\mathrm{M_{total}} \sim 10^{14} - 10^{15}$ $\mathrm{M_\odot}$) consist mostly of dark matter (DM) (~ 80 per cent) which clumped into a virialized DM halo. Baryonic matter was subsequently accreted into the DM potential wells in the form of galaxies and low density gas in between them ($\rho \sim 10^{-2} - 10^{-3}$ $\mathrm{cm^{-3}}$). Most of the baryonic matter (~ 15 per cent of total mass) in those clusters is in the form of this thin gas (intracluster medium, ICM). The rest (~ 5 per cent) is made up of individual galaxies (e.g. Ettori & Fabian 1999; Ettori et al. 2009; Andreon 2010; Zhang et al. 2011b). The accretion into the cluster potential is heating the ICM to temperatures where it emits brightest in X-rays ($10^7 - 10^8$ K).

1.3.1 X-ray emission from clusters of galaxies

Clusters of galaxies can be observed at many different wavelength (see e.g. reviews by Plionis et al. 2008; Kaastra et al. 2008). The individual galaxies in a cluster can be best observed at optical wavelength (1000-100 nm, $\sim 1 - 10$ eV photon energies) allowing to estimate galaxy properties and their mass contribution to the cluster (e.g. Popesso et al. 2004, 2005, 2007). The ultra violet (UV) can be used to observe galaxies and their gas content at higher temperatures (100-10 nm, $\sim 10 - 100$ eV photon energies) tracing star formation regions (e.g. Donahue et al. 2015; Hicks & Mushotzky 2005). In the infrared (IR) colder gas regions can be observed ($1 - 100$ μm, ~ 1 eV $- 10$ meV photon energies) showing potential future star formation regions (e.g. Lin et al. 2003). The large scale diffuse emission of clusters can be observed in radio frequencies between (100 MHz -1000 Ghz, 1 m - 100 μm, ~ 1 μeV $- 10$ meV photon energies). At frequencies around 160 GHz (peak of the cosmic microwave background black-body spectrum, Fixsen 2009) the thin, hot plasma filling the potential well of the cluster can be observed as a shadow against the cosmic microwave background since its photons scatter with the hot gas (SZ-effect,

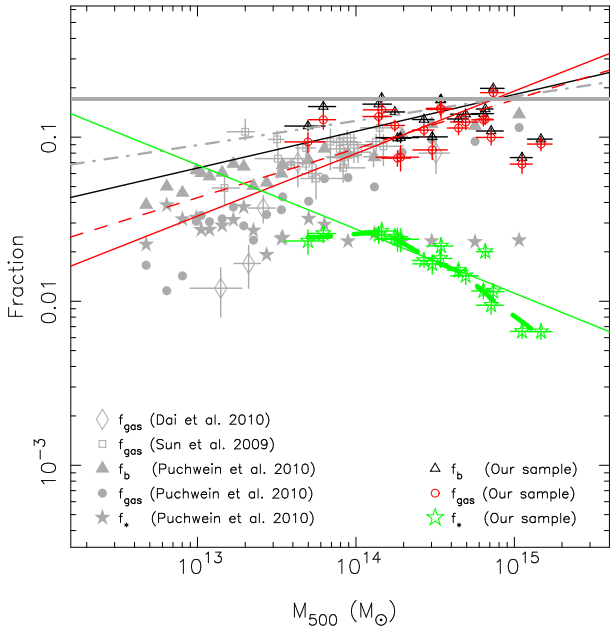

Figure 1.3: Gas-mass fraction (red, open circles), stellar mass fraction (green, open stars), and baryon-mass fraction (black, open triangles) as a function of the total mass and the best fits excluding A2065 and A2029 in the same colors with solid line. Plot from Zhang et al. (2011b). The stellar mass fraction in their observational sample decreases with increasing cluster mass with (20 ± 4) per cent intrinsic scatter for the 19 clusters. For comparison, they also show the gas-mass fraction (gray, solid circles), stellar mass fraction in galaxies (gray, solid stars), and the sum of these two fractions (gray, solid triangles) for the simulated sample of 21 clusters with AGN feedback in Puchwein et al. (2010), as well as the gas mass fractions of the X-ray selected groups in Sun et al. (2009) (gray, open boxes) and near-infrared selected groups in Dai et al. (2010) (gray, open diamonds). The best fit of the baryon-mass fraction as a function of the total mass of the observational sample in Lin et al. (2003) is shown in gray with dot-dashed line. The gray band shows the 1σ measurement from the WMAP 5-year result Dunkley et al. (2009). A2142 displays a baryon-mass fraction of 0.198 ± 0.008, which exceeds the WMAP result with a 3σ significance. The best fit of the gas-mass fractions combining their clusters and the clusters in Sun et al. (2009) is shown in red with dashed line with (26 ± 8) per cent intrinsic scatter. Figure and caption from Zhang et al. (2011b).

see Sunyaev & Zeldovich 1980a,b). Other radio frequencies can be used to observe non thermal emission from galaxy cluster mainly synchrotron radiation in relativistic plasmas with magnetic fields.

While the gas is falling into the potential well the potential energy gained is transformed into thermal energy (kinetic energy of the individual particles in kinetic gas theory). The thin gas heats up to several million kelvin, becomes an ionised plasma and starts emitting X-rays through relaxation of the different elements excited state atoms and Bremsstrahlung caused by scattering of the charged particles.

The collisionally ionised plasma emission from clusters of galaxies can be modeled by a Bremsstrahlung continuum with a range of discrete line emissions on top (e.g. O, Fe, Ne, Mg, see Fig. 1.4). The spectra observed by X-ray telescopes are always folded by a energy dependent efficiency of each instrument.

As reviewed by Sarazin (1986) the total emissivity ϵ of a thin plasma with temperatures of $T_g \sim 10^8$ K and atomic densities of $n \sim 10^{-3}$ is,

$$\epsilon^{ff} \simeq 3.0\text{x}10^{-27}\ T_g^{1/2}\ n_p^2\ \text{erg cm}^{-3}\ \text{s}^{-1} \tag{1.9}$$

The strength of the line emissions on top of the continuum depends on the metallicity of the emitting medium (Böhringer & Werner 2010). In the plasma emission models I to fit the cluster spectra metallicity is the abundance ratio of heavier elements to hydrogen and helium. The metallicity I measure is in units of fraction of solar metallicity. Clusters generally have a metallicity of around 0.3 of solar. This low metallicity as compared to the sun can be explained by the formation history of the clusters.

1.3.2 Metal enrichment

The metallicity in astronomical objects describes the ratio of elements heavier than hydrogen and helium to the abundance of hydrogen and helium. For clusters it is common to give the metallicity as a fraction of the solar metal content (Anders & Grevesse 1989).

After the big bang nucleosynthesis (BBN) gas consisted mainly of hydrogen and helium (Iocco et al. 2009). Over time stars formed and produced heavier elements through fusion. At the end of their lifetime massive stars explode as supernovae and transport the materials to the interstellar medium (ISM). After galaxies cluster the interstellar medium is mixed by various processes with the ICM and enriches the gas with heavier elements (de Plaa et al. 2007; De Lucia et al. 2004).

This mixing dilutes the metals in the ICM (Werner et al. 2008; Simionescu et al. 2009; Zhang et al. 2011b) and thus the metallicity of this gas is generally lower than solar values (typically $\sim 0.1 - 0.5$ of solar metallicity with some outliers, see chapter 3).

Various studies found that the enrichment of the ICM is strongest around the BCG causing a peak in metallicity at the centers of most clusters (see e.g. Böhringer & Werner 2010; de Plaa et al. 2007; Sanders & Fabian 2006a). At larger radii the metallicity quickly drops to the average of around 0.3 solar and remains constant due to more efficient enrichment in the outskirts (see e.g. Werner et al. 2013).

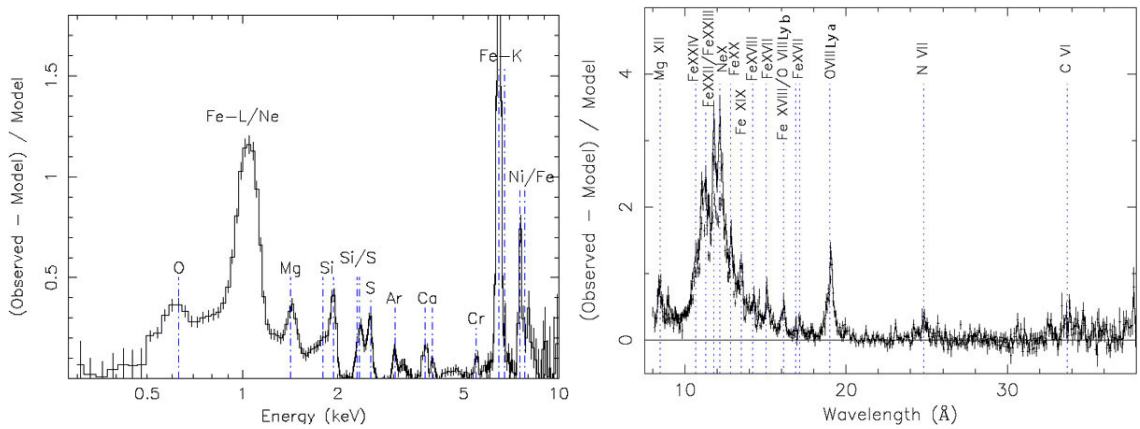

Figure 1.4: Left: XMM-Newton EPIC X-ray spectral lines of the galaxy cluster 2A 0335+096 showing the typical energy resolution of X-ray CCD detectors. The plot shows the residuals of a thermal Bremsstrahlung spectrum without discrete lines (Werner et al. 2006b). Right: XMM-Newton RGS high resolution grating spectrum showing residuals of a model without line emission for M 87. The detected lines are identified by vertical lines in the plot (Werner et al. 2006a).

1.3.3 Cooling and heating

The X-ray emission efficiently radiates energy from the plasma and thus cools down the ICM. The cooling gas can then further settle into the center of the cluster, becoming more dense during this process. As the gas becomes denser, the mean free path of the particles shortens and thus the radiation of X-rays increases, speeding up the cooling even further. It has been proposed that the cooling process will create a so called cooling flow (Fabian et al. 1984; Fabian 1994) that eventually leads to the gas cooling out of the X-ray emitting phase and finally being accreted onto the BCG where it should provide material for renewed star formation. In reality however the expected large amounts of increased star formation or further cooling of the gas have not been observed (also referred to as the cooling flow problem, see e.g. Peterson & Fabian 2006).

This caused an ongoing search for heating mechanisms in clusters of galaxies that would stop the gas from cooling down too much. A very prominent picture is the feedback from strong central active galactic nuclei (AGN feedback, see e.g. Ciotti & Ostriker 2007) or mergers of subclusters that heats the gas by turbulent dissipation of the energy in the medium. AGN feedback is mostly caused by relativistic jets launched from the central supermassive black hole at the center of a BCG. The relativistic particles of the jet heat the ICM at impact to extreme temperatures up to billions of Kelvin. At these temperatures the now relativistic plasma (relativistic effect become important due to high average particle velocity, see kinetic gas theory) mainly emits radio from synchrotron emission of the relativistic particles moving around magnetic field lines (e.g. observed by Sanders et al. 2005a). The high temperature causes the gas to expand and pushes away the colder X-

ray emitting gas. This produces a lower density cavity which rises due to buoyancy from the denser central ICM regions to the lower density outskirts of the cluster (e.g. Dunn et al. 2005). In the wake of these bubbles lower temperature gas can be dragged from the central galaxy and become visible as filaments in optical observation (e.g. Fabian et al. 2003b). Feedback or subhalo merger processes cause sound waves (subsonic) and shocks (supersonic) in the ICM which transport the input energy through the cluster and dissipate the energy to heat the ICM (e.g. Forman et al. 2007). A very prominent example for shocks induced by mergers of clusters is the Bullet cluster which shows a strong edge-on shock travelling through the ICM and heating the cluster (Markevitch et al. 2002). These structures became visible with the highest resolution X-ray instrument (*Chandra* observatory) and there have been numerous studies describing the various effects in different clusters (e.g. Fabian et al. 2003a; McNamara et al. 2000, 2005; Blanton et al. 2010; Sanders & Fabian 2007; Sanders et al. 2005a; Sanders & Fabian 2008; Zhuravleva et al. 2014a,b, 2015).

One possibility for heating the ICM are the larger scale supersonic motions (feedback or mergers) input energy into the ICM and the turbulence cascades down to smaller scales, heating the plasma (see Kolmogorov cascade Kolmogorov 1962). Also other processes like subsonic sound waves can contribute to the heating (e.g. Sanders & Fabian 2008).

1.4 Clusters as cosmological probes

Observations of clusters of galaxies allow for very detailed tests of different cosmological models and in the past decade they have been used for many precision cosmology studies (e.g. Allen et al. 2004; Nagai et al. 2007; Allen et al. 2008; Vikhlinin et al. 2009b,a). For a review on cluster cosmology see e.g. Borgani (2008); Lahav & Liddle (2014). Cosmological studies using clusters constrain best the cosmological parameters σ_8 measuring the amplitude of the power spectrum on scales of 8 Mpc/h and $\Omega_{\rm M}$ (see e.g. Fig.1.5) measuring the average matter density of the universe (e.g. Primack 2005). Along with other observational probes like supernova luminosity distances (Perlmutter et al. 1999; Riess et al. 1998) or the cosmic microwave background radiation (CMB, e.g. Komatsu et al. 2009), clusters of galaxies helped to form the current picture of the evolution of the universe.

One of the most sensitive probes for cosmology uses the redshift dependent number density of massive clusters (see Fig.1.5). In these studies clusters are counted as a function of mass and redshift accounting for survey specific selection effects (see studies listed above and e.g. Reiprich & Böhringer 2002; Böhringer et al. 2004; Vikhlinin et al. 2009a; Clerc et al. 2012). The redshift of massive systems is very well constrained from optical spectra of member galaxies, but the overall masses of the clusters are still uncertain to more than 10 per cent which is the main limitation of cluster cosmology today (e.g. Vikhlinin et al. 2009a).

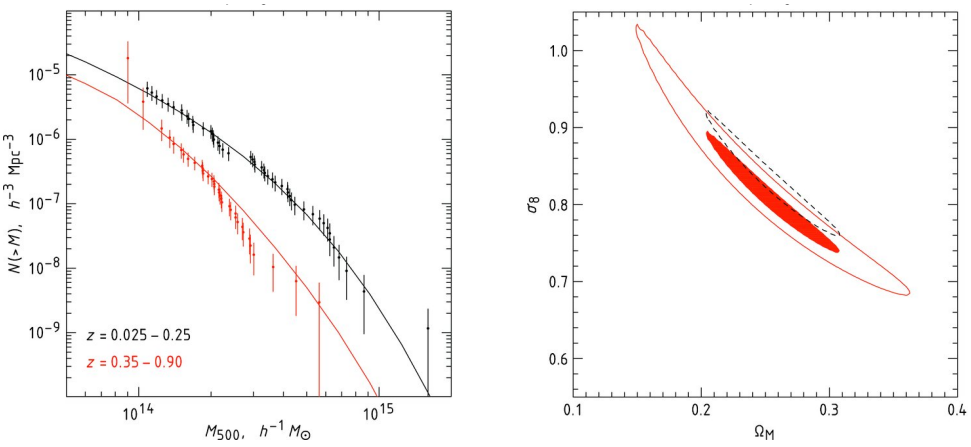

Figure 1.5: Left: Galaxy cluster mass-functions of Vikhlinin et al. (2009b) showing the abundance of clusters of different mass ranges. Assumed cosmology: $\Omega_M = 0.25$, $\Omega_\Lambda = 0.75$, $h = 0.72$. Solid lines show the mass function models (weighted with the survey volume as a function of M and z). Right: Constraints on σ_8, Ω_M parameters in a flat ΛCDM cosmology from the total (both low- and high-redshift) Vikhlinin et al. (2009b) cluster sample. The inner solid region indicates the 68 per cent confidence interval. The solid contour shows the 95 per cent confidence region. The dashed contour shows how the inner solid confidence region is modified if the normalization of the absolute cluster mass vs. observable relations is changed by +9 per cent (their estimate of the systematic errors). Plots from Vikhlinin et al. (2009b).

1.4.1 Hydrostatic equilibrium masses

To first order the ICM can be described as a single temperature (isothermal) gas in hydrostatic equilibrium in the potential well of the galaxy clusters which are dominated by the DM halo. It is often assumed that the cluster density follows a Navarro-Frenk-White (NFW) profile (Navarro et al. 1997) depending on the radius r from the centre,

$$\rho(\mathrm{r}) = \frac{\delta_\mathrm{c}\rho_\mathrm{c}}{\mathrm{r}/\mathrm{r_s}\ (1+\mathrm{r}/\mathrm{r_s})^2} \tag{1.10}$$

$$\delta_\mathrm{c} = \frac{500}{3} \times \frac{\mathrm{C}^3}{\ln(1+\mathrm{C}) - \mathrm{C}/(1+\mathrm{C})} \tag{1.11}$$

where concentration C and radius $\mathrm{r_s}$ are empirical cluster specific values. C describes how strongly peaked the density profile is in the centre and $\mathrm{r_s}$ is a specific radius depending on the extent of the cluster (here I define $\mathrm{r_s} = \mathrm{r_{500}}/\mathrm{C}$). ρ_c is the critical density of the universe at the cluster redshift. In the standard ΛCDM cosmology assumed in this study (see Sect. 4.1) the critical density is given as

$$\rho_c = \frac{3H^2(z)}{8\pi G} \tag{1.12}$$

$$H^2(z) = H_0^2\ (0.27\ (1+z)^3 + 0.73) \tag{1.13}$$

with gravitational constant $G \approx 4.3 \times 10^{-3}$ pc $M_\odot^{-1}$ $(km/s)^2$.

If the gas distribution is assumed to be hydrostatic in a spherically symmetric potential it can be described analytically by the equation (this section follows a review by Sarazin 1986),

$$\frac{1}{\rho_g}\frac{dP}{dr} = -\frac{d\phi}{dr} = -\frac{G\ M(r)}{r^2} \tag{1.14}$$

where r is the radius from the center, M(r) is the mass included by that radius, ρ_g is the gas density, $\phi(r)$ is the spherical gravitational potential, and P is the gas pressure which is related to temperature and density as,

$$P = \rho_g k T_g / \mu m_p \tag{1.15}$$

The gas density has empirically been found to follow the so called beta-model (see e.g. recent studies by Navarro et al. 1995; Vikhlinin et al. 2006; Evrard et al. 1996; Mohr et al. 1995),

$$\rho_g(r) = \rho_{go}[1 + (r/r_c)^2]^{-3\beta/2} \tag{1.16}$$

with cluster specific constants ρ_{go}, r_c, and β. In recent years there have been many improvements to this model by deriving more complex density profiles for the mass calculation (e.g Sanders et al. 2014). X-ray observations allow to directly observe the density profile of the cluster which is proportional to the square root of the X-ray emission. Observations however only give a 2D view of the cluster projected along the line of sight. After deprojecting the density emission profile assuming spherical symmetry one can use this profile instead of a simple beta model for the mass estimate. Assuming a simple beta profile the mass profile can be calculated as (Navarro et al. 1995),

$$M_T(r) = \frac{k}{G\mu m_p}[\frac{3\beta(r/r_c)^2}{1+(r/r_c)^2} + \frac{d\ \ln T}{d\ \ln r}]\ T(r)\ r \tag{1.17}$$

where k is the Boltzmann constant and μm_p is the average particle mass times proton mass. This equation shows that cluster-mass depends strongest on the temperature of the ICM.

1.4.2 Empirical scaling relations

Because of the strong relationship between cluster-mass and temperature of the ICM and the fact that most clusters are only observed long enough to derive one average temperature

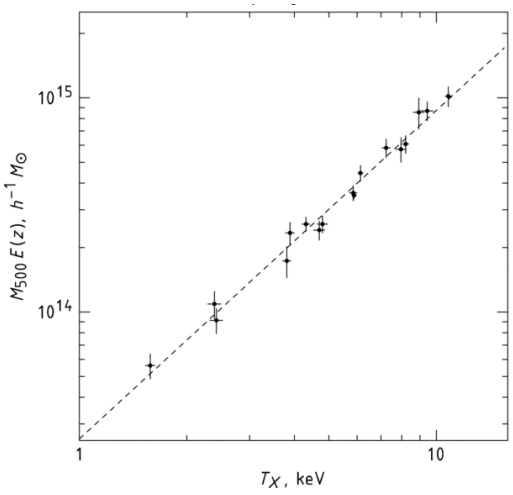

Figure 1.6: T-M scaling relation showing X-ray hydrostatic mass measurements against temperature profile measurements (extending to r_{500}). The mass measurements from Vikhlinin et al. (2006) the temperatures are T_X from Vikhlinin et al. (2009a). Best fit power law as dashed line.

instead of a detailed T profile, empirical relations have become a very important tool for cluster sample studies. Those scaling relations are calibrated by comparing cluster masses in simulations to simulated X-ray properties (e.g. Finoguenov et al. 2001; Vikhlinin et al. 2009a) or by calibrating real X-ray measurements against mass measurements from other techniques like weak-lensing of galaxies by the cluster potential or velocity dispersions of galaxies (e.g. Kettula et al. 2015; Bocquet et al. 2015; Smith et al. 2016). These scaling relations aim at relating an easily observable quantity to the total mass of a galaxy cluster with as little systematic uncertainties as possible (e.g. Zhang et al. 2008). Vikhlinin et al. (2009a) derived one of the most accurate T-M scaling relations from their observations of a large sample of clusters (see Fig.1.6). I used this relation for estimating the mass range of the cluster sample I used in this study. Kravtsov et al. (2006) introduced a more complicated cluster quantity Y_X which is defined as,

$$Y_X = M_{g,\Delta_c}\ T_X \tag{1.18}$$

where M_{g,Δ_c} is the gas mass derived from X-ray imaging data within the radius enclosing an overdensity Ω_c, and T_X is the mean X-ray spectral temperature excluding the innermost region around the cool core (e.g. Mazzotta et al. 2004; Vikhlinin et al. 2006). It has generally been found that removing the core regions of clusters tightens scaling relations (Kravtsov et al. 2006) because the central AGN feedback effects do not affect the overall mass of the system significantly. Y_X is a measure of the overall energy in the cluster and produces tighter scaling relations with total mass than using only temperature.

The best fit T-M scaling relation of Vikhlinin et al. (2009a) is given by,

$$M_{500} = 3.02 \pm 0.11\ 10^{14} h^{-1} M_{\odot}\ (T/5keV)^{1.53\pm0.08}\ E(z)^{-1} \tag{1.19}$$

where E(z) is $H(z)/H_0$. Fig.1.6 shows the best fit correlation and the scatter of different clusters including their measurement uncertainties.

After great progress on the scaling relation slopes and their scatter in recent years, and improved estimates on the mass bias caused by non-thermal pressure support the average Mach number estimate allowed me to put observational constraints on the non-thermal pressure support from turbulent motions in clusters for the first time. This is an important bias to correct for in the eROSITA study of cluster masses. Secondly simulations of cluster observations with eROSITA allowed me to estimate the expected scatter in scaling relations for eROSTIA.

1.5 Gas dynamics

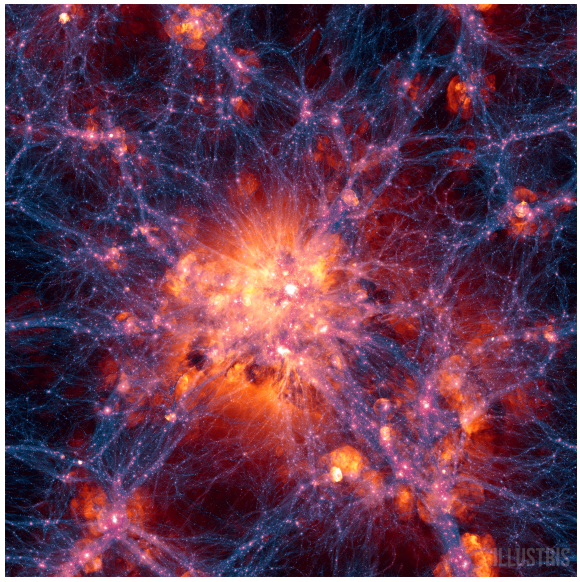

Figure 1.7: Image of the Illustris cosmological simulation showing the dark matter structure (magenta) overlaid with the gas velocity field (yellow) of the simulation. The most massive cluster is located at the center and the image covers about 15 Mpc/h. The image illustrates the wealth of velocity structures in the ICM during accretion processes and there are several shock fronts visible.Credit: Illustris Collaboration.

The dynamics of the ICM plays an important role in the heating processes of galaxy clusters and for cosmological constraints because turbulent motions can provide non-thermal pressure support which would bias cluster mass estimates commonly made assuming hydrostatic equilibrium (hydrostatic masses could be up to 20 per cent biased low Norman &

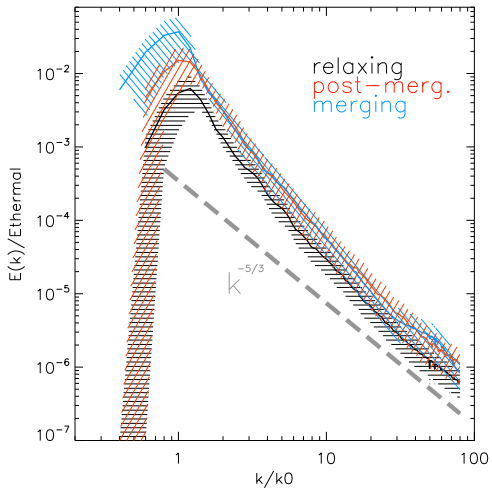

Figure 1.8: Average power spectra of the 3D velocity field for the different classes of galaxy clusters in the Vazza et al. (2011) sample, at z = 0. The dotted line shows the expected Kolmogorov cascade with a slope of -5/3. k is the spatial frequency of the perturbations and k0 the spatial frequency at the virial radius (higher k at smaller physical scales). The energy per scale E(k) is normalised to the total thermal energy within the virial radius. The maximum energy is reached at 1-2 times the virial radius. From Vazza et al. (2011).

Bryan 1999). In cluster cosmology the mass and redshift dependent distribution of clusters is the essential observable allowing for cosmological parameter constraints.

1.5.1 Turbulence expected from simulations

Simulations of cluster formation have long suggested that the formation of clusters of galaxies induces significant gas motions in the ICM. Major cluster mergers, infalling subhalos, or AGN feedback can cause subsonic and supersonic motions in the ICM and thus cause turbulence in the medium (Norman & Bryan 1999; Sunyaev et al. 2003).

The sound speed c_s in the ICM is proportional to the temperature of the plasma as (see e.g. Zhuravleva et al. 2014a),

$$c_s = \sqrt{\frac{5}{3}\frac{k_B\ T}{\mu\ m_p}} \sim 0.15\ \sqrt{T[K]}[km/s] \tag{1.20}$$

with the Boltzmann constant k_B, $\mu = 0.61$ the mean particle weight, and m_p is the proton mass. For a temperature of $T = 10^8$ K ≈ 8.6 keV the sound speed is about 1500 km/s.

Perturbations of the ICM on large scales (~ 100 kpc $- 1$ Mpc) cascade down to smaller dissipative scales where they contribute to the heating of the ICM. The slope (-5/3, see Fig. 1.8) of the energy cascade is ideally (incompressible, viscous fluid at high Reynolds number) described by a Kolmogorov cascade (Kolmogorov 1941).

In recent years there have been many hydrodynamical simulations simulating the ICM dynamics to obtain velocities in the gas (e.g. Dolag et al. 2005; Cassano & Brunetti 2005; Norman & Bryan 1999; Iapichino et al. 2011; Vazza et al. 2011; Nagai et al. 2013). More recently also large scale structure simulations include simulations of the gas physics during structure formation and provide gas velocities on large scales (e.g. the Magneticum, EAGLE, and ILLUSTRIS simulations Dolag 2015; Schaye et al. 2015; Vogelsberger et al. 2014). Fig. 1.7 shows a slice through the ILLUSTRIS simulation with gas velocities illustrated with different colours. The image shows shocks during infall of subhalos, feedback shocks at the centres of clusters and overall higher velocities around the virial radius of massive clusters where new gas is still accreted. Fig.1.7 shows the dark matter structure of the cosmological simulation centered on the most massive cluster in the simulation. The dark matter shows the typical clumping and filamentary known from previous cosmological simulations like the Millenium simulation (Springel et al. 2005). In addition the Illustris simulation (Vogelsberger et al. 2014) also contains Baryonic matter which is mostly in the hot gas between galaxies. Fig.1.7 also shows the gas velocities (brighter yellow regions are at higher velocity) in the simulated accretion of Baryons into the DM potential wells. This simulation like many others indicates that there is significant turbulence in the ICM caused by merging gas halos and ongoing accretion of gas in the outskirts of massive galaxy clusters.

Gas velocities in these simulations range from $100 - 1000$ km/s depending on the rate of mergers with larger subhalos and feedback caused by the central AGN. These velocities are challenging to measure directly with current instruments. Therefore some indirect methods to constrain gas velocities have been proposed.

Most cosmological studies assume hydrodynamic equilibrium when calculating/scaling cluster masses. The mass dependent number density of clusters in the observable universe is the most important input to cluster cosmology studies (see section on clusters as cosmological probes). It is very important to understand how much influence the turbulent motions have on the hydrostatic mass estimates. It is expected that turbulence will provide additional pressure support which means that masses calculated assuming the gas is in hydrostatic equilibrium in the DM potential will be underestimated (Nagai et al. 2007; Zhang et al. 2010; Battaglia et al. 2012; Jeltema et al. 2008; Nelson et al. 2012; von der Linden et al. 2014; Applegate et al. 2016). Rasia et al. (2012) simulated the measurement of X-ray masses for perfectly known cluster masses in a cosmological simulation and found them biased low by 25-35 per cent due to additional non-thermal pressure support. A systematic underestimate of cluster masses will lead to bias in the cosmological parameters derived from studies of clusters of galaxies. In a recent study Smith et al. (2016) found an underestimate of X-ray masses as compared to weak-lensing masses by about 5 per cent. Weak-lensing is a technique for reconstructing the potential well which is slightly distorting the images of background galaxies. This effect is caused by the light bending through mass (effect described by general relativity, see Einstein 1936). The small distortions to galaxies can be measured only statistically on a sample. This technique measures the total mass of the DM halo potential well. Uncertainties and scatter of this technique are higher than for X-ray masses when comparing to simulations but systematic offsets (e.g. like hydrostatic

equilibrium assumptions can cause in mass measurements from X-rays) are expected to be smaller (e.g. Hoekstra et al. 2004; Rasia et al. 2012).

I apply a new way of estimating the non-thermal pressure support to contribute to the solution of the ongoing debate on how much bias there is in hydrostatic mass estimates of clusters of galaxies.

1.5.2 Measuring turbulence in the intracluster medium

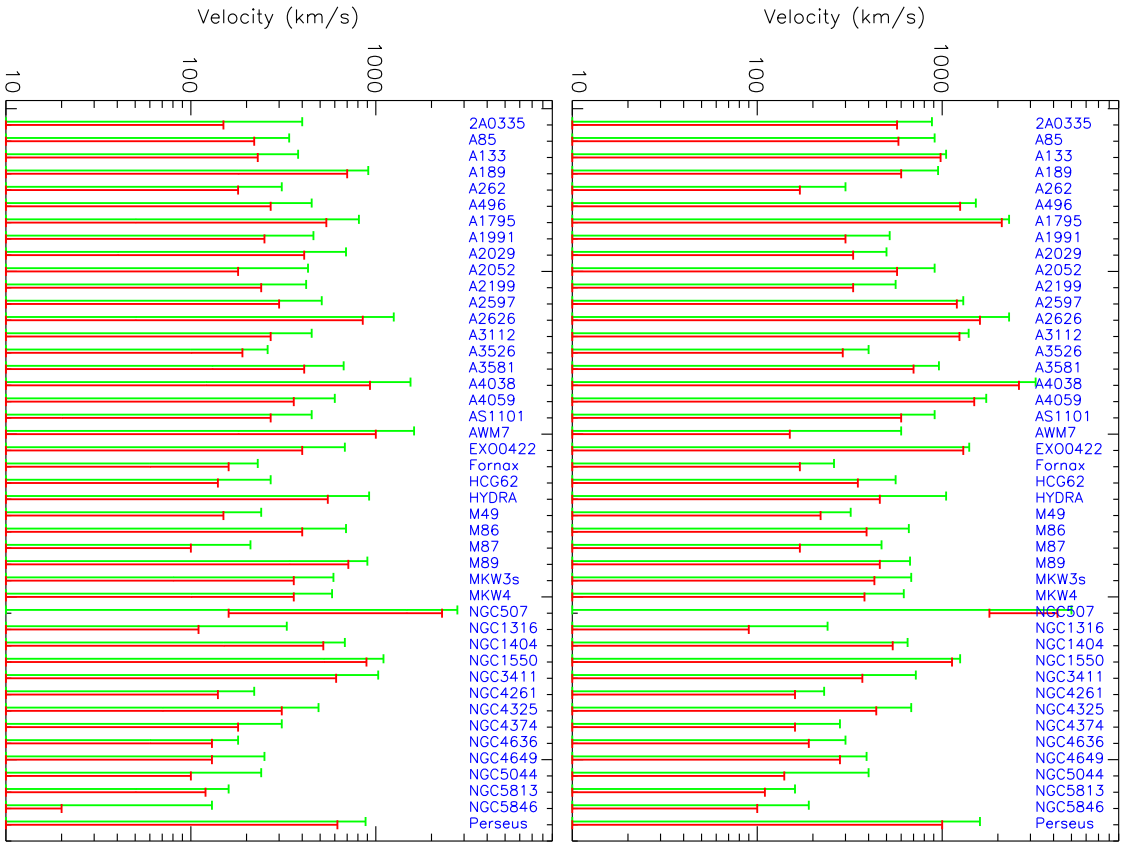

Figure 1.9: Velocity limits of Pinto et al. (2015) for a large sample of clusters from X-ray grating (RGS) observations with XMM-Newton. Confidence levels: 68 per cent (red) and 90 per cent (green). The left and right panel show two different techniques of accounting for the systematics in line broadening measurements with X-ray instruments.

With current X-ray instruments it is not possible to significantly detect line broadening in the range of 100 km/s due to limited spectral resolution (Sanders et al. 2011; Sanders & Fabian 2013; Pinto et al. 2015). Fig.1.9 shows two different methods of accounting for systematics in a recent study. One of the main systematic uncertainties in high resolution X-ray grating spectrometers is that for extended sources it is hard to disentangle line width

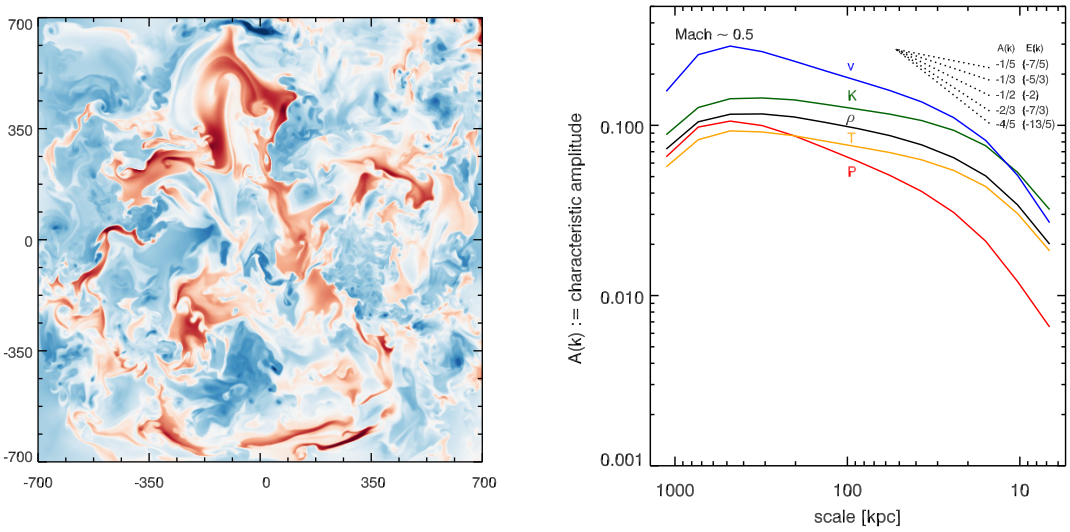

Figure 1.10: Left: Mid-plane cross-section of $\delta\rho/\rho$ in per cent for models with a Mach number of ~ 0.5 and no conduction. Right: Characteristic amplitude of thermodynamic fluctuations for Mach ~ 0.5. Entropy perturbations dominate throughout followed by density perturbations. Figures from Gaspari et al. (2014).

due to actual gas velocity or the extent of the emission region (similar to slit spectroscopy in optical astronomy).

One indirect way of detecting turbulence is the effect of resonant scattering of the brightest X-ray emission lines. While the ICM is mostly optically thin, the resonant scattering of some lines can cause small distortions in spectral shape and surface brightness of a cluster (Churazov et al. 2010). Current instruments are not sensitive enough to detect the resonant scattering effects significantly (e.g. Zhuravleva et al. 2013; Werner et al. 2009).

A very promising indirect detection method are density fluctuations in the X-ray emitting gas which can be related to turbulence of the ICM (see application by Zhuravleva et al. 2014a). I applied a similar technique to a sample of 33 clusters in this study using more thermodynamic properties in addition to density.

In 2014 Gaspari et al. (2014) published a study which directly relates the gas turbulence found in their high-resolution hydrodynamic simulations of the ICM to properties observable in X-rays. They related the normalization of the power spectrum of the leading thermodynamic perturbation to the Mach number of the system (see snapshot of a simulation cross section and an example for related power spectra of thermodynamic perturbations and gas velocities in Fig.1.10). The leading perturbation refers to the property with the highest amplitude in the power-spectrum (pressure or entropy depending on the Mach number regime).

The theoretical basis and the simulation are explained as described by Gaspari & Chu-

razov (2013):

Their simulations were carried out with a 3D hydrodynamics code (Fryxell et al. 2000). The code is used to solve 3D equations of hydrodynamics for a two temperature electron-ion plasma. The turbulence is injected into the Navier-Stokes equation as an additional acceleration term a_{stir},

$$\frac{\partial}{\partial t}\rho\mathbf{v} + \nabla\cdot(\rho\mathbf{v}\otimes\mathbf{v}) + \nabla\mathbf{P} = \rho\mathbf{g} + \rho\mathbf{a}_{\rm stir} \tag{1.21}$$

where ρ is the gas density, $\mathbf{v}$ the velocity, $\mathbf{g}$ the particle acceleration, and P the pressure. To study density perturbations they used the characteristic amplitude defined as,

$$A(k) \equiv \sqrt{P(k)\,4\pi k^3} = \sqrt{E(k)\,k} \tag{1.22}$$

with $k = \sqrt{k_x^2 + k_y^2 + k_z^2}$ ($l = 1/k$ in kpc). The units of the characteristic amplitude are the same as in real space. For the fractional density fluctuations $\delta \equiv \delta\rho/\rho$, the characteristic amplitude $A(k)_\delta$ is equivalent to the typical level of fluctuations at scales k. The peak of $A(k)_\delta$ provides an estimate of the total amount of perturbations. The exact total variance can be computed integrating $P(k)\,4\pi k^2 dk$ over the whole range of scales (the difference may reach a factor of 1.4, depending on the slope of the power-spectrum). This description and a more detailed theoretical framework are given by Gaspari & Churazov (2013).

Their main conclusion relevant for my study was that the peak amplitude is linearly related to the average 3D Mach number as $A(k)_{\delta,\rm max} = c\,M$, where $c \simeq 0.25$ for injection scales $L_{\rm inj} \simeq 500$ kpc. Furthermore the slope of $A(k)_\delta$ is sensitive to the strength of conduction and thus the mixing of different phases of the medium. In a medium without conduction, subsonic stirring motions decay almost according to a Kolmogorov cascade from injection on small scales k to larger scales. The relation for energy deposition in a Kolmogorov cascade is,

$$E(k)_\delta \propto k^{-5/3} \tag{1.23}$$

where E is the scale dependent energy deposition (Gaspari & Churazov 2013). Fig. 1.8 shows this ideal cascade slope in comparison to slopes obtained in simulations of different cluster types. Following the above study, Gaspari et al. (2014) find the average fractional perturbations observed in the ICM of a cluster directly relate to the 1D Mach number of the system. This direct conversion is a good approximation because the peak of $A(k)_{\rm max}$ dominates the integral value over the whole range (see Fig.1.10).

I used these newly proposed observables of perturbation strength to estimate the average Mach-number, turbulence and thus non-thermal pressure support in a sample of 33 clusters. This is the first time this approach has been used on real observations. The derived thermodynamic maps and intermediate products of the analysis are a valuable source for future studies and are publicly available from the CDS online archive. I will introduce a new method for measuring the intrinsic spread of the measured cluster quantities. This spread is equivalent to the integral over the power spectrum of the fluctuations and thus to the 1D Mach number with some limitations.

1.6 Direct dark matter search

To date, dark matter (DM) has only been observed indirectly, as in flat rotation curves of galaxies at large radii (e.g. Navarro et al. 1996) or in major merging clusters where the bulk of the gravitational potential is offset from the hot collisional plasma emission (e.g. the Bullet cluster, 1E 0657-558 Clowe et al. 2006). There are a number of different theoretical particles that have been proposed as candidates for DM. They must have very weak to no self-interaction and have very high mass density. There is an ongoing effort for the direct detection of such theoretically proposed DM candidates in laboratory experiments. As a complimentary approach it is possible to use high energy astronomical observatories to search for emission caused by these DM particles. For example it is possible to use soft X-ray observatories and probe emissions in the 1 to 10 keV range.

One candidate for DM that can be constrained using X-ray observations are sterile neutrinos with masses in the keV range. Their decay signature would be photons in the keV range which would produce a previously unidentified excess emission on top of plasma emission or other models used to describe the observed X-ray spectra. A recent white paper describes all aspects from theory to detection strategies of such keV mass sterile neutrinos in Adhikari et al. (2016).

Sterile neutrinos are hypothetical particles that have long been discussed as dark matter candidates. They are postulated as an extension of the standard model (SM) of particle physics by mechanisms explaining neutrino masses. In the SM, neutrinos have zero mass, but the observation of neutrino oscillations shows that they must have non-zero masses (m_υ see e.g. Kajita & Totsuka 2001). One solution to this problem is the Higgs-independent Majorana mass which implies that the active neutrinos have massive counterparts (m_N) and are their own antiparticles $\upsilon = \overline{\upsilon}$. The masses are divided according to the See-Saw Relation,

$$m_\upsilon \, m_N = m_D^2 \tag{1.24}$$

where m_D is the mass of the Dirac (or active) neutrinos. Sterile neutrinos in this scenario would be right-handed fermions with zero hypercharge and no color. This means the particles only interact through gravity and with their active counterparts through the Majorana mechanism. They would have a right handed chirality. All known neutrinos have only left handed chirality. For all other Fermions right and left handed particles have been observed. If the right handed sterile neutrinos existed this would solve many of the issues with neutrinos in the SM.

In cosmology, sterile neutrinos at keV masses would solve some of the tension between observations and simulations. For example they would lie in between cold and warm dark matter. "Warmer" DM would reduce the number of small DM halos produced in simulation to a number which is closer to the number of typically observed subhalos (see Adhikari et al. 2016). The term "warm" in this context describes the freeze-out velocity (after production during the big bang) of the DM particles compared to the speed of light. Cold dark matter has comparatively low velocities and hot dark matter has velocities close to the speed of

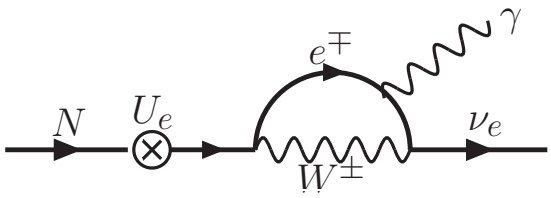

Figure 1.11: Decay channel of the sterile neutrino N with the mass below twice the electron mass. The radiative decay channel allows to look for the signal of sterile neutrino DM in the spectra of DM dominated objects (from Adhikari et al. 2016). The sterile neutrino decays into an intermediate electron/positron ($e^{\pm}$) and a W boson and then into a photon γ and an active neutrino (e.g. an electron neutrino υ_e). For a keV mass sterile neutrino the photons of the radiative channel can be observed with soft X-ray telescopes.

light. Warm dark matter lies in between. The velocity of the particles has a strong influence on the structure formation in the universe as seen in cosmological simulations (e.g. Springel et al. 2005). The higher the initial average velocity of the particles the longer it takes for them to settle into virialised dark matter halos through gravitational collapse. Also the number of small to intermediate size halos is reduced at higher particle velocity.

Fig. 1.11 illustrates the decay channel of sterile neutrinos that would be observable with X-ray observatories from massive DM halos. The width Γ of this decay channel is expected to be

$$\Gamma_{N\rightarrow\gamma\upsilon} = 5.5 \times 10^{-22}\ \Theta^2\ [\frac{m_N}{1\ keV}]^5\ s^{-1} \tag{1.25}$$

with the mixing angle Θ (interaction strength) between the active and sterile neutrino and the sterile neutrino mass of m_N. The smaller this width the fainter is the potentially observable signal.

Two recent papers by Bulbul et al. (2014) and Boyarsky et al. (2014) claimed significant detections of an excess emission around 3.55 keV found in many celestial objects like individual galaxies and clusters of galaxies as well as the Galactic center. These papers sparked a wealth of observational papers, some confirming, some excluding the dark matter interpretation of the line (see e.g. Urban et al. 2015; Anderson et al. 2015; Malyshev et al. 2014; Jeltema & Profumo 2016; Iakubovskyi 2014; Iakubovskyi et al. 2015; Iakubovskyi 2015; Jeltema & Profumo 2015; Tamura et al. 2015; Hofmann et al. 2016a). Fig.1.12 shows several exclusion regions (observational and theoretical) prior to the 2014 detection and shows the detected particle properties as a red data point. The detected unidentified line emission was proposed as the emission from the decay of 7.1 keV sterile neutrinos. In this scenario the sterile neutrinos decay into an active neutrino and an X-ray photon splitting their rest mass between the decay products so that the emitted photon has an energy of 3.55 keV.

The DM interpretation is very intriguing since it would be the first direct detection and possible solution in the hunt for the DM particles, as well as an extension to the standard

model of particle physics. But there have been many other scenarios proposed where the line could instead be explained by unusually strong thermal plasma line emissions in the 3.5 keV region, possibly also due to charge exchange processes with clumps of colder gas moving through the hot plasma of the main cluster (see Bulbul et al. 2014; Gu et al. 2015). Fig.1.13 shows a simulated spectrum of the expected difference between the turbulent line broadening and the broadening from the DM velocity dispersion with the Hitomi (Astro-H) satellite.

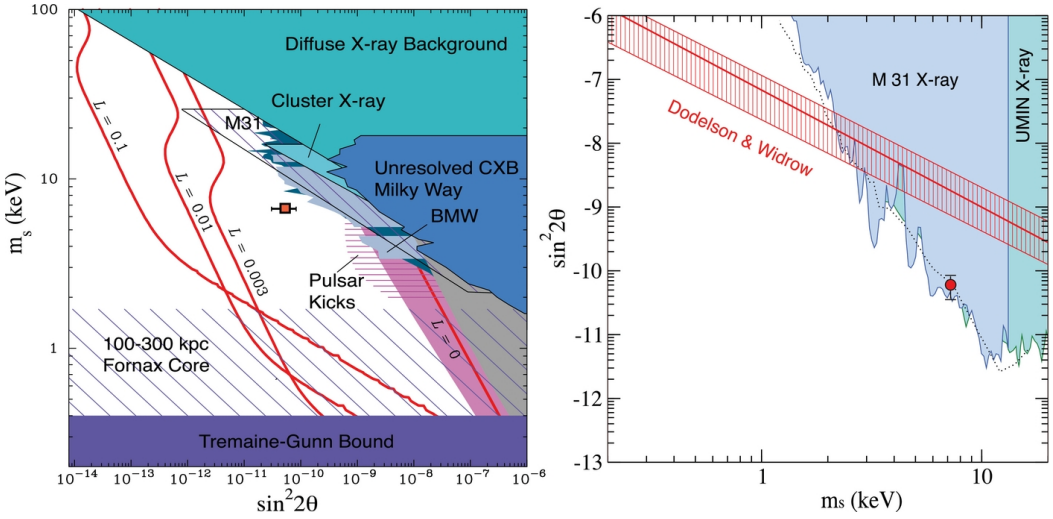

Figure 1.12: Bulbul et al. (2014) full-sample MOS line detection (assuming that the line is from sterile neutrino and that all dark matter is in the form of sterile neutrinos) is shown by red symbols in both panels; error bar is statistical 90 per cent. Left: historic constraints from Abazajian (2009). Red curves show theoretical predictions for the Dodelson–Widrow mechanism assuming that sterile neutrinos constitute the dark matter with lepton numbers L = 0, 0.003, 0.01, and 0.1. See Abazajian (2009) for explanation of the various observational constraints that come from Tremaine & Gunn (1979); Bode et al. (2001); Boyarsky et al. (2006); Strigari et al. (2006); Abazajian et al. (2007). Right: most recent X-ray constraints (reproduced from Horiuchi et al. 2014), based on deep Chandra and XMM-Newton Watson et al. (2012) observations of M31 and Suzaku observations of Ursa Minor (Loewenstein et al. 2009). The red band marked Dodelson & Widrow is the same as the L = 0 curve in the left panel.

1.7 eROSITA cluster cosmology predictions

The main science goal of the eROSITA mission is the observation of clusters of galaxies and to derive tight constraints on cosmological parameters. This will be achieved by observing

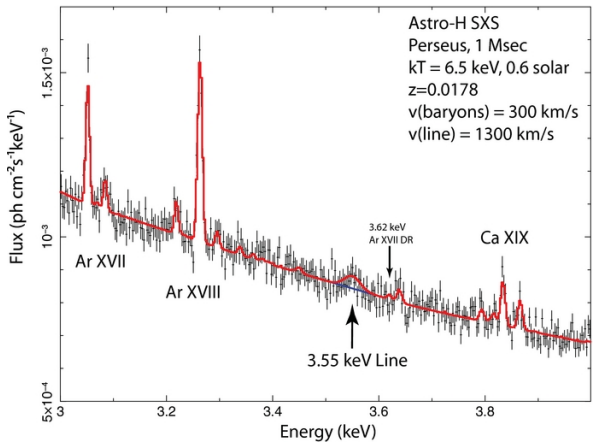

Figure 1.13: 1 Ms Hitomi (Astro-H) SXS simulation of the Perseus Cluster by Bulbul et al. (2014). The line width corresponds to line-of-sight velocity dispersion of 1300 km s^{-1}. The figure shows that the decaying dark matter line broadened by the virial velocities of dark matter particles will easily be distinguished from the plasma emission lines, which are broadened by turbulence on the order of a few 100 km s^{-1} in sufficiently deep observations of the Perseus Cluster.

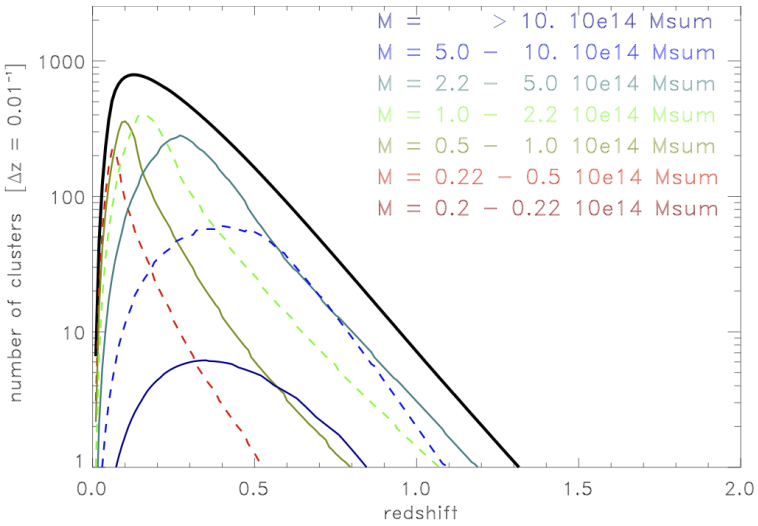

Figure 1.14: Mass - redshift distribution of the detected clusters in the full 4-year eROSITA all-sky survey, assuming 100 photons to secure a detection. Black solid line is for the total, with lines of different colors corresponding to different mass bins, as in the inset. The cluster numbers are given for redshift bins of $\Delta z = 0.01$. Credit: eROSITA science book.

an expected 10^5 clusters, detecting all massive clusters in the observable universe (outside an exclusion region around the Galactic plane, because of too high foreground absorption). As in previous cosmological studies (see above) the abundance of clusters in different mass and redshift bins will be used to constrain cosmological parameters. With perfectly Gaussian primordial fluctuations (no non-Gaussianity) the cosmological model is described by Ω_M, Ω_Λ, σ_8, and the spectral index of perturbations n_s (see Pillepich et al. 2012, and references therein).

A white paper on the mission goals and characteristics was published by Merloni et al. (2012). There have only been minor changes to the mission strategy since, so the science goals are unchanged. Fig.1.14 shows the expected mass-redshift distribution of clusters in the eROSITA survey. The curves show the trade-off between number of observable clusters (with increasing volume) and sensitivity of the survey leading to a peak around redshift 0.2 where most clusters are expected to be observed.

Pillepich et al. (2012) carried out a detailed study (assuming an estimated observed cluster sample) on the cosmological constraints possible with eROSITA observed clusters (see Fig.1.15). They used simulated galaxy-cluster abundance and clustering and compared them to predictions from cosmological models with varied parameters. Simultaneously, they constrained the parameter uncertainties. The predictions come from a set of equations outputting the expected number of observed clusters in the observed area of the sky. This method is less sensitive to uncertainties in cluster scaling relations but a well calculated cluster mass function from precision scaling relations would tighten constraints on cosmological parameters (see Fig. 1.15 for a comparison of different studies).

According to the classification of the DETF report (Dark Energy Task Force Albrecht et al. 2006) eROSITA will be the first "Stage IV" dark energy experiment. The nature of dark energy is currently unknown and new experiments like eROSITA will help distinguish between different dark energy models like new particles or fields in the Standard Model or modifications to General Relativity. The best constraints will be obtained by combining datasets of eROSITA with other observatories and cluster detections like Sunyaev-Zeldovich (SZ) detections of clusters with the Planck satellite (see e.g. Planck Collaboration et al. 2014b) or the WMAP mission (see Komatsu et al. 2011; Hinshaw et al. 2013, for cosmological results). The SZ effect allows to detect the hot ICM of galaxy clusters as depressions in the cosmic microwave background (CMB) because the hot plasma acts as an absorber of the microwave radiation. Fig.1.15 shows how the combined samples of eROSITA and Planck are expected to give the best results of all currently planned missions. Fig. 1.15 does not yet show the final Planck results but they are close to the assumed values for the combined eROSITA+Planck constraints by Pillepich et al. (2012).

The constraints on cosmological parameters will be derived by comparing cluster mass functions of different models with varying parameters and observations. The observed mass function is created by converting the luminosity or temperature distribution of clusters into a mass function using well calibrated scaling relations (e.g. $L_X - M$, $T_X - M$, or $Y_X - M$ conversion functions, correlations functions with some intrinsic scatter).

To obtain a complete mass function one has to account for the selection function of the survey, correcting for different sensitivity to different types of clusters detection limits. The

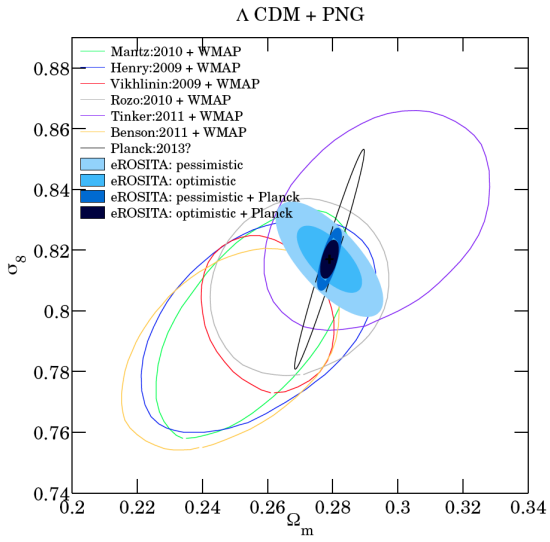

Figure 1.15: Examples for expected cosmological constraints from eROSITA. The pessimistic cases assume current knowledge of the $L_X - M$ relation and photometric redshifts while the optimistic ones assume that uncertainties in the $L_X - M$ relation parameters improve by a factor of two in the coming years and spectroscopic redshifts can be obtained from planned dedicated follow-up surveys, e.g. SPIDERS (SPectroscopic IDentification of ERosita Sources, P.I.: A. Merloni, K. Nandra) and 4MOST, see de Jong et al. (2012). Several existing cluster+WMAP constraints are also shown for comparison. Credit: Pillepich et al. (2012), eROSITA science book.

scaling relations have to be calculated accounting for biases (e.g. Malmquist bias caused by preferred detection of bright objects, see e.g. Clerc et al. 2014). Scatter in the scaling relations will cause some smoothing of the mass function and thus will affect constraints on cosmological parameters.

An important correlation to understand in the survey will be the $T_X - L_X$ relation which compares two important observables for mass scaling relations.

The eROSITA sample will be so large that statistical errors become negligible and the systematic uncertainties in scaling relations etc. will dominate the uncertainties of constraints. There are many studies underway to bring down systematics in cluster cosmology. Part of this work is to better understand individual clusters and the dynamical state. eROSITA will be an excellent tool to study some of the systematics, especially in the full survey.

In preparation for the eROSITA mission I contribute simulations of galaxy cluster observations and study the impact of parameter bias caused by cluster substructures on the derived cosmological constraints that will be possible with the eROSITA observatory within the German eROSITA consortium's Cluster Working Group. I put constraints on the accuracy of measuring average cluster temperatures and investigate what will be the

method of calculating average temperatures in the eROSITA survey that will yield the lowest intrinsic scatter in the $T_X - M$ scaling relations (compare T_X, core excised average temperatures used by Vikhlinin et al. 2009a). In addition I measure the flux F_X observed in simulated clusters and given the known redshift for the clusters in my simulations I retrieve the total luminosity L_X from cosmological distance of the source.

Assuming the redshift is perfectly known the percentage of bias in F_X is the same as in L_X. In the real survey there might also be some bias due to different techniques for measuring the cluster redshift but it is expected to be lower than the bias from X-ray measurements (see e.g. Ridl et al., in preparation and Clerc et al., in preparation).

T_X and L_X are the most commonly used mass-indicators for calculating masses using scaling relations between X-ray properties of a cluster and its physical total mass. These relations are usually calibrated by comparing to cosmological simulations of clusters or by cross-calibrating with masses from SZ or weak-lensing observations. By investigating $T_X - L_X$ depending on the amount of substructure in a cluster will help to understand scatter and possible bias in the scaling relations used in the final eROSITA sample and thus improve the accuracy of the retrieved cosmological parameters and their uncertainties. In addition I simulated the same clusters at different redshifts so redshift dependent systematics can be better understood in the future survey.

I made simulations both for the cluster images to for example investigate detection efficiency in the eROSITA survey depending on substructure and redshift of a cluster (see Clerc et al., in preparation and Ramos Ceja et al., in preparation) and for cluster spectra to constrain bias in fitted cluster properties in the eROSITA cluster survey spectra (see this work and Hofmann et al., in preparation).

A recent review by Reiprich et al. (2013) shows how multi-temperature plasma can cause biased average temperatures when fitting the X-ray spectra with a one temperature model of collisionally ionised plasma (see also Rasia et al. 2006). Fig.1.16 shows how the X-ray emission line complex in a plasma emission model changes with plasma temperature. Due to the different line-strength ratios at different temperatures the complex blend of lines shifts its peak. The lines are typically blended together like this because of the limited energy resolution of currently available X-ray CCD detectors of $\gtrsim 100$ eV. This form of the line complex is the main indicator for plasma (gas, depending on temperature and degree of ionisation) temperature at lower photon energies around 1 keV. eROSITA will be especially sensitive to lower energy photons in this range and so model fits will mostly depend on the line complex. Fig.1.16 however shows that the line intensity strongly decreased with temperature. This is caused by higher ionisation fraction and thus lowered recombination probability (which would cause the discrete emission lines). As a consequence it is harder to measure higher temperature gas since it hardly changes the line complex in a lower energy (softer) X-ray spectrum.

Fig.1.17 shows how this effect biases eROSITA temperature measurements by comparing the best fit plasma model average temperature in a two temperature plasma emission model. It is particularly interesting that at a balance of emission from colder and hotter gas eROSITA is strongly biased to measuring a lower average temperature. The cluster spectra in eROSITA will not have high enough signal to noise to fit multi temperature

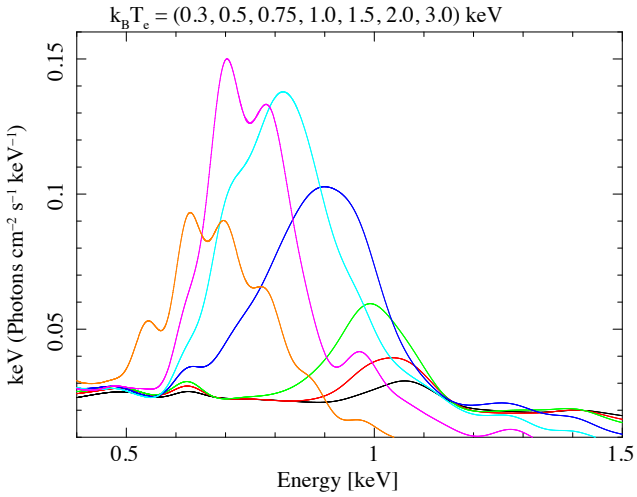

Figure 1.16: Typical appearance of the low energy line complex in X-ray CCD spectra. The main emission lines are caused by Fe and O. The assumed metal abundance is 0.3 of solar metallicity the neutral hydrogen column density is $n_H = 3 \times 10^{20}$ cm^{-2} and the redshift is $z = 0.05$. The different colors indicate temperatures from 0.3 keV (orange) to 3 keV (black). The line-complex peak continually shifts to higher energies with higher plasma temperature (from Reiprich et al. 2013).

components to the spectrum and so for the vast majority of clusters one has to rely on average temperatures measured from the X-ray spectra.

It has been found in many studies over the past decade that there is significant temperature structure in the ICM (e.g. Reiprich et al. 2004; Sanders & Fabian 2007; Million & Allen 2009; Lovisari et al. 2011). The structures depend to some extent on the type of cluster. It can be more pronounced on larger scales in merging systems. Recent studies like (Chon et al. 2012; Weißmann et al. 2013; Parekh et al. 2015; Zhang et al. 2016) have tried to find substructure estimators which would also work on low S/N images of galaxy clusters. However the relatively shallow eROSITA all-sky survey with relatively large average PSF will make it very challenging to constrain different structure types. I tested some morphology estimators on eROSITA images and as it became clear that this will only give reliable results for a small subset of clusters I focused on getting bias estimates for an average sample instead of getting a substructure differentiated picture. Chapter 5 shows the results and only a weak trend of bias with substructure type.

This shows how important it is to understand exactly how T_X and F_X measurements will be biased in the eROSITA survey and this became my works prime focus. Chapter 2 introduces the simulation and data reduction approach to this end, and Chapter 5 explains my results in detail and puts them in context to previous findings.

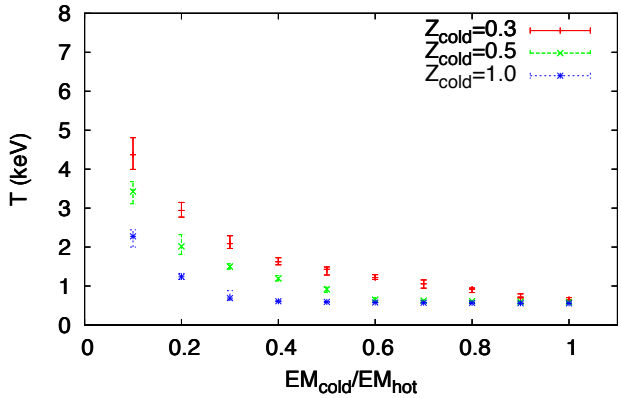

Figure 1.17: Temperature bias as simulated for the eROSITA instrument for a two-temperature plasma fitted with a one-temperature model. The plots shows the measured average temperature over the fraction of cold gas in the plasma emission (from 10 to 100 per cent). The different colors indicate how this bias depends on the metallicity of the colder gas component (from Reiprich et al. 2013).

Chapter 2

Instruments and data reduction

This chapter introduces the main instruments used in this work and describes the primary data formats of observations which were used in later chapters for further reduction and analysis. I also introduce the simulation software SIXTE and its input file format SIMPUT which were used to obtain realistic simulated observation expected from the eROSITA survey.

2.1 X-ray observatories

X-rays are strongly absorbed in the atmosphere of the earth and thus all modern observatories for X-ray astronomy are based on satellites mostly in highly eccentric orbits around earth to avoid contaminations. Todays state of the art dedicated soft X-ray instruments (from around 0.1 to 10 keV) are the Chandra (lead by NASA, USA), XMM-Newton (lead by ESA, Europe), and Suzaku (lead by JAXA, Japan) observatories. Planned instruments for the near and intermediate future are Hitomi (Astro-H Kitayama et al. 2014), eROSITA (Merloni et al. 2012), and the Athena (Nandra et al. 2013) observatories aiming for higher spectral resolution, larger sky coverage, and larger grasp (effective collecting area times field of view).

In this study I mainly used archival observations of the *Chandra* telescope and simulated eROSITA observations based on the deep *Chandra* observations.

2.1.1 *Chandra*

The *Chandra* X-ray observatory was launched in late 1999. For the past 15 years it has carried out many deep observations of celestial X-ray sources. It delivers the highest spatial resolution obtained in X-ray astronomy so far and one of the best spectral resolution CCDs with the ACIS instrument.

The Chandra Project is managed by NASA's Marshall Space Flight Center. The Project Scientist is Martin C. Weisskopf. Day-to-day responsibility for Chandra science operations lies with the Chandra X-ray Center (CXC) , Belinda Wilkes, Director. The

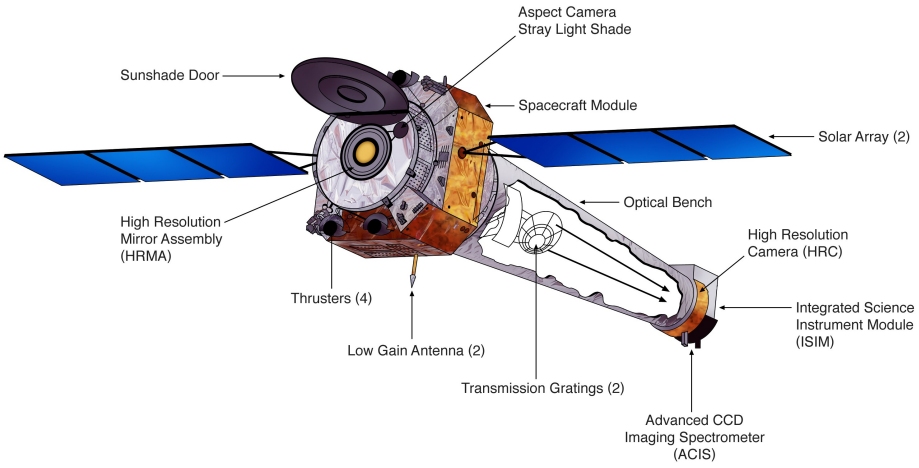

Figure 2.1: Technical overview of the *Chandra* X-ray observatory spacecraft. Image courtesy of National Aeronautics and Space Administration (NASA) (obtained from Brissenden 2001).

CXC is located at the Cambridge Massachusetts facilities of the Smithsonian Astrophysical Observatory (SAO) and the Massachusetts Institute of Technology (MIT). The Chandra Operations Control Center (OCC) is also located in Cambridge. The CXC uses the OCC to operate the Observatory for NASA. See the *Chandra* proposer's observatory guide[1] for details on this section.

Fig.2.1 shows the complete *Chandra* spacecraft. It consists of a spacecraft module with the necessary pointing reaction wheels and thrusters, a communication antenna, and power supply from the solar panels. The scientific instrument consists of a high-resolution mirror array (HRMA) which focuses X-rays onto the CCD detectors. It is also possible to use a transmission grating for high resolution X-ray spectroscopy. The HRMA is the highest resolution X-ray telescope to date with a point spread function (PSF) with a full-width half-maximum (FWHM) of ~ 0.5 arc seconds and a maximum effective collecting area of ~ 800 cm^2 at 0.25 keV. The mirror consists of four pairs of concentric grazing-incidence Wolter Type-I mirrors (for a review see Aschenbach 1985), each with a pair of paraboloid

[1] `http://cxc.harvard.edu/proposer/POG/html/index.html`

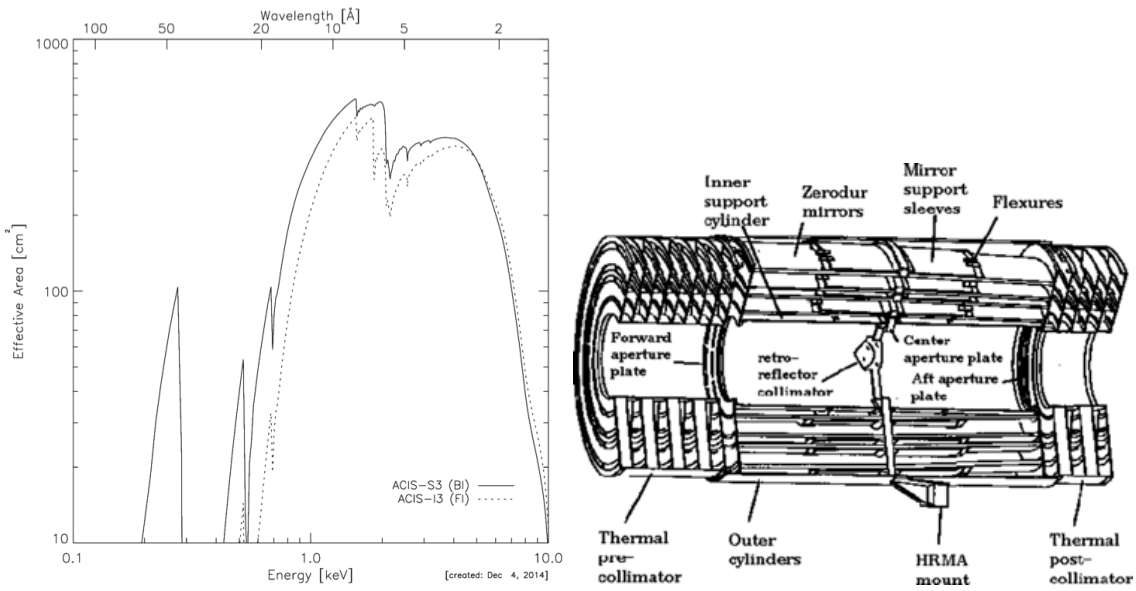

Figure 2.2: Left: effective collecting area of the *Chandra* HRMA combined with the quantum efficiency of the CCD detectors (separately for front- and back-illuminated chips). Right: Overview of the HRMA showing the mounting of the four mirror shells and the front and back collimators. Credit: CXO Proposer observatory guide v17.0

and hyperboloid mirrors made of polished Zerodur glass, coated with iridium. Fig.2.2 shows the energy dependent effective area of the whole instrument and the technical structure of the HRMA.

This study is based on observations with the Advanced CCD Imaging Spectrometer (ACIS, Garmire et al. 2003) which offers simultaneous high-resolution imagines and moderate resolution spectra[2]. ACIS contains ten 1024x1024 pixel CCD chips (layout see Fig.2.3). Four are arranged to form the ACIS-I 2x2 array used only for imaging and a row of six CCDs form the ACIS-S array which can be used for imaging or higher resolution spectra in combination with the grating spectrometer. Two of the CCDs are back-illuminated (BI) as shown in Fig.2.3, which means they are reversed with respect to the rest. The advantage of the BI chips is that the response is better at low energies and the average energy resolution is better than for front-illuminated (FI) chips (due to damage from protons early in the mission for FI chips). However the background noise of the BI chips is higher. ACIS-I is generally used for more extended lower redshift clusters and ACIS-S for higher redshift and less extended sources as the FOV is smaller (see Fig.2.3).

The pixel size in celestial coordinates is about 0.49 arc seconds. The energy resolution of the CCDs at 1.5 keV varies from $\sim 100 - 150$ eV FWHM line width depending on the chip type and the position within the chip. The BI chips (S1 and S3 in Fig.2.3) have the best energy resolution of the array.

[2] `http://cxc.harvard.edu/proposer/POG/html/index.html`

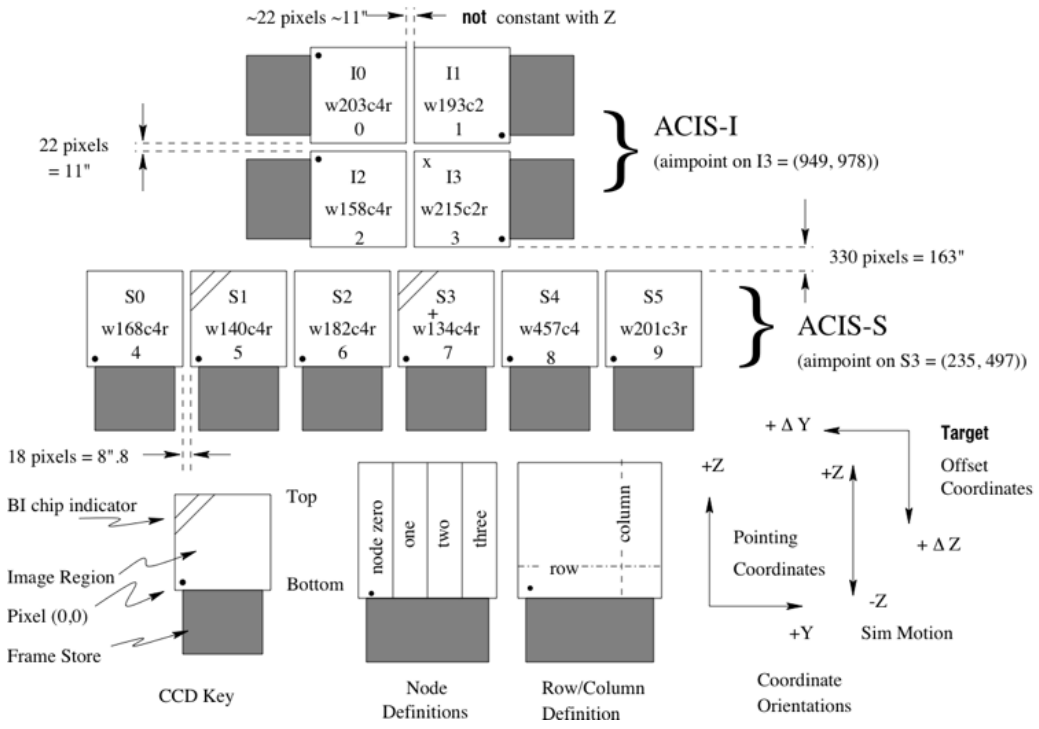

Figure 2.3: Technical overview of the ACIS focal plane showing the alignment of all instrument CCDs and the detector coordinate directions. The two back-illuminated (BI) CCDs 1 and 3 are marked. The lower right side of the figure indicates the coordinate systems used in the *Chandra* standard event files. Depending on the science goals the observer can choose the chips to use in the observation (telemetry constraints only allow to use four CCDs in parallel). Credit: CXO Proposer observatory guide v17.0

The observatory operation center provides analysis tools and standard file packages allowing the user to account for all the above mentioned characteristics of the instrument and retrieve the real properties of observed sources. After the data reduction the products can be used for a scientific analysis (see below).

2.1.2 eROSITA

The extended Roentgen Survey with an Imaging Telescope Array (eROSITA observatory Predehl et al. 2007, 2010) is currently scheduled to launch in 2017 on board of the Russian/German Spectrum Roentgen Gamma mission (SRG) together with a second science instrument the Astronomical Roentgen Telescope - X-ray Concentrator (ART-XC, see e.g. Pavlinsky et al. 2011) which observes high energy X-rays (6-30 keV energy range). eROSITA is a soft X-ray (0.3-10 keV energy range) observatory consisting of seven identi-

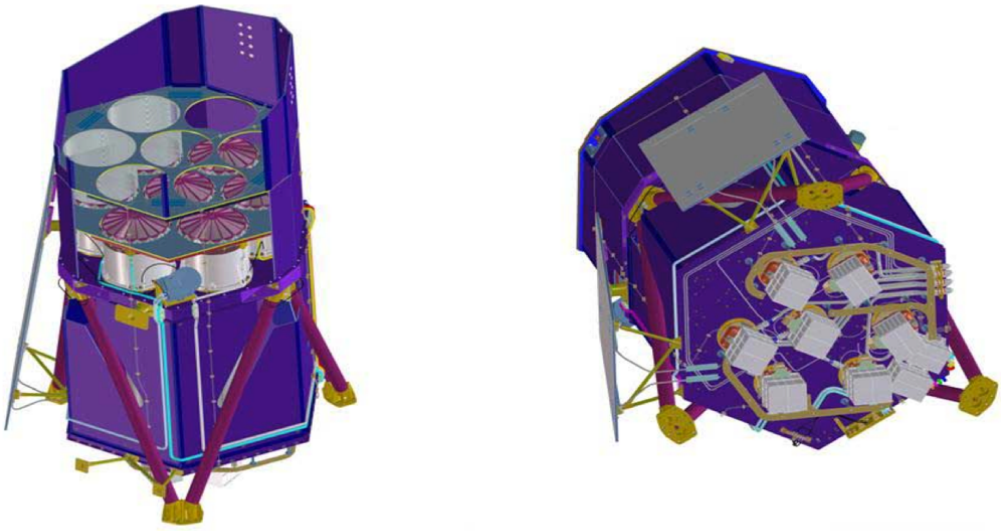

Figure 2.4: Technical drawings of the eROSITA telescope structure that will be mounted as one of two science instruments on board the spacecraft of the SRG mission. The image shows the seven separate mirror modules (left side) and the detectors in their focal plane (right side showing the bottom of the structure). Collimators on top of the mirrors reduce the amount of stray light on the detectors. The overall structure is made of carbon fibre and on the sides the heat regulation plates are visible which are connected to the detector boxes with special heat-pipes. Credit: eROSITA science book.

cal mirror modules with seven individual CCD detectors in their focal plane.

Fig. 2.4 shows a technical drawing of the full telescope structure with an opening on the side to show the mirror array.

A detailed observatory description and its science goals are given in the eROSTIA science book by Merloni et al. (2012). Several predictions for the scientific capabilities have been made by Pillepich et al. (2012); Borm et al. (2014); Salvato et al. (2011); Kolodzig et al. (2013); Zandanel et al. (2015). The main goals of eROSITA include obtaining the largest X-ray selected galaxy cluster sample ($\sim 10^5$) and to detect more AGN in X-rays than ever before. Capability tests (e.g. by Pillepich et al. 2012) showed the eROSITA 4yr survey will allow the tightest constraints on dark energy to date. However this requires very good knowledge of the selection function of galaxy clusters in the survey as well as the bias and scatter in mass scaling relations (see introduction on cosmology). The simulations I made in this study will both help to characterise the selection function (see Clerc et al., in preparation) and estimate the scatter or possible bias in the mass scaling relations (Hofmann et al., in preparation).

eROSITA will be the second X-ray all-sky survey after the ROSAT mission. The new survey will extend to higher energies and will be ~ 15 times deeper than ROSAT at softer energies (in the 0.3-2.4 keV energy band). eROSITA will not cover softest ROSAT energies between 0.1-0.3 keV. In survey mode eROSITA will constantly rotate around an axis toward the sun. Each X-ray photon is detected individually and with the pointing and timing information the exact sky position will be reconstructed.

The SRG spacecraft will be in orbit around the second Lagrangian point (L2) of the Earth-Sun system where it is supposed to be shielded from the sun's particle winds by the earths magnetic field and far away from the earth to minimize pointing constraints. The second Lagrangian point lies on the far side of earth with respect to the sun and is stable in two directions (saddle point in the effective potential of the rotating earth-sun system). With this survey strategy the typical exposure of the sky will be about 2 ks with much deeper exposure at the survey poles where multiple scans overlap. A significant fraction of the sky will have more than 20 ks of exposure. Fig. 2.5 shows a detailed view of the sky in Galactic coordinates. For better orientation the contours of the eROSITA exposure map (simulations of the four years of survey by J. Robrade, Merloni et al. 2012) are plotted on top of a 408 MHz continuum emission all-sky image (Haslam et al. 1982) which shows regions of charged particle accelerations and is a good indicator for Galactic foreground material. Regions of the cluster sample used in this study are shown as blue circles (size linearly related to the redshift of the source).

There will be several background components measured in the detectors which have to be very well understood in order to obtain clean source spectra and images. One component will be the detector background which was measured in the laboratory and estimated in simulations. The particle background which has been recorded by previous missions in L2 will also cause some background detections in the CCD arrays. Last there is the X-ray sky background which is unresolved emission from sources like the diffuse emission in the Galaxy and resolved and unresolved extragalactic AGN population. This background has to be modeled well depending on the science objective. In case of cluster observations it has to be removed. It is very important to model the background correctly for observations of low surface brightness clusters and outskirts of clusters. eROSITA's high-energy particle background, modeled by Tenzer et al. (2010) has a normalization of 1151 counts $\mathrm{keV}^{-1}\mathrm{s}^{-1}\mathrm{sr}^{-1}$ and a flat spectral energy distribution (see Fig.2.6 for expected particle and sky background).

The effective area of eROSITA is relatively high at photon energies below 2 keV and drops off steeply at higher energies, comparable to current instruments (see Fig.2.6). The half energy width (HEW) of the telescope PSF is ~ 28 arcsec (survey average) at 1 keV and the energy resolution of the CCD detectors is about 138 eV at 6 keV.

The data from the satellite will be delivered to the user as event lists in standard `FITS` format with one entry per detected X-ray photon. There will be an extended Science Analysis Software package (eSASS) based on previously developed software for ROSAT and XMM-Newton which is currently under development by the German eROSITA consortium. In preparation for the real observations I used a simulation package (SIXTE, see below) which creates realistic eROSITA event files and used first versions of the eSASS tools to

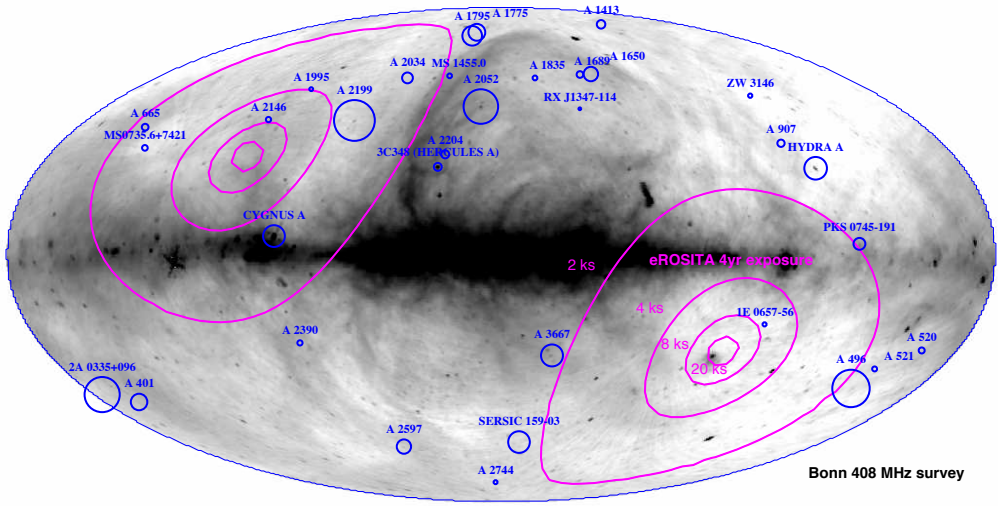

Figure 2.5: eROSITA 4yr survey exposure contours (magenta, 2, 4, 8, 20 ks) plotted on a 408 MHz continuum emission all-sky image showing charged particle accelerations in the Galactic foreground (roughly traces where X-ray emission is absorbed by the Galactic material). The image is projected in Galactic coordinates (Hammer-Aitov). The survey exposure is deepest at the survey poles because of the increasing overlap of individual scans. The blue regions show the 33 clusters of the sample. The circle size marking the position scales linearly with the redshift (larger circles at lower redshift between 0.025 and 0.45). Image credit: NASA *SkyView*.

analyse the simulated observations.

2.2 eROSITA simulations with SIXTE and SIMPUT

The Simulator for X-ray telescopes (SIXTE[3], Schmid et al. 2010) can produce X-ray event lists for various X-ray telescopes, given an input source list in the SIMPUT (SIMulation inPUT) format[4] and a set of telescope specific parameters. This section gives a summary of the descriptions of the simulator and input source list formats. I used a setup of the simulation software emulating the properties of the eROSITA Telescope for the eROSITA simulated observations.

[3]http://www.sternwarte.uni-erlangen.de/∼schmid/simulation.php
[4]http://hea-www.harvard.edu/heasarc/fitsformats-heasarc.html

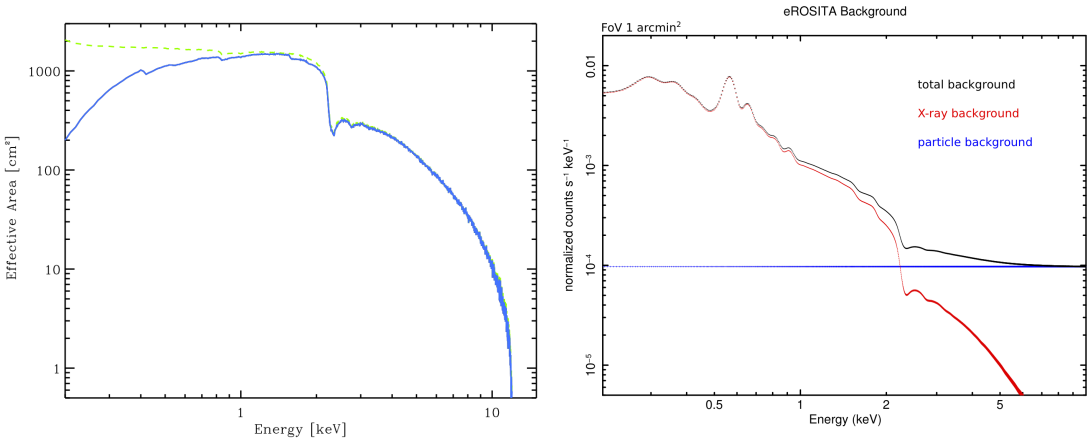

Figure 2.6: Left: FOV averaged effective area for the eROSITA 7-telescopes systems (blue curve), including vignetting, the effects of filters and CCD quantum efficiency; the dashed green line show the effective area for the mirror systems only. Right: Simulated (XSPEC) eROSITA background (black) and spectral components: in red the photon X-ray background (galactic and extragalactic), in blue the particle background and in black the total. Courtesy of K. Borm. Credit: eROSITA science book

SIXTE is a generic X-ray instrument simulator created to obtain simulated observations of future missions (see Schmid et al. 2010, for a detailed description). The software uses a Monte Carlo based technique to generate photon event lists. The output has standard formatting to allow analysis with the standard data processing pipelines. Simulations are used for testing existing instruments or making predictions for future missions and their science goals. The simulator can be adjusted to different missions by providing an XML file with general telescope information. It contains the FOV of the instrument, dimensions of the CCDs, energy range, and readout time. Most importantly it also contains the information on the calibration files of the instrument. An X-ray telescope is characterised by a file describing the vignetting of the telescope, a file giving the position-dependent PSF size and form, and the energy dependent effective area. The CCD detectors are characterised by the energy- and position-dependent quantum efficiency, and by the input-energy output-channel mapping. The effective are and quantum efficiency of the CCDs are usually combined into an Auxiliary Response File (ARF) and the energy-to-channel mapping is described by a 2d matrix, the Response Matrix File (RMF). With this information the simulator can create accurate simulations of the X-ray photons the telescope would observe for a given source. The source characteristics are input via a SIMPUT file.

The SIMPUT format is a standardised source list format for X-ray observatories based on the `FITS` format. The files are tables with multiple extensions and can be linked to external files. Each entry in the table provides all information needed about an astrophysical source in X-rays. It contains source position on the sky, energy flux in a given range, spectrum (normalised by the energy flux value), an image showing extent of the source (if

applies) on the sky, and timing information in case of variable sources.

Based on these input informations it is possible to study variability, images and spectra of sources as they would be observed with different X-ray observatories.

2.3 Cluster sample and datasets

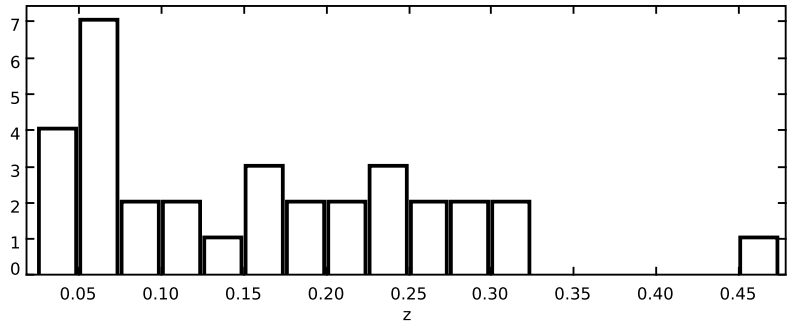

Figure 2.7: Histogram of the redshift (z) distribution of the final sample of 33 clusters.

I used archival observations with the *Chandra* Advanced CCD Imaging Spectrometer (ACIS, Garmire et al. 2003) using the imaging (-I) or spectral (-S) CCD array (about 0.1 to 10 keV energy range). This instrument provides high spatial ($\sim$ 1 arcsec) and spectral resolution ($\sim$ 100 eV full width half maximum, FWHM). The field of view (FOV) is limited, so that only the inner $5 - 10$ arcmin of any cluster are homogeneously covered. See Sect. A.2 for a list of all analysed clusters and their individual exposure times.

This study is based on a sample of the massive clusters with the deepest *Chandra* observations available from the *Chandra* archive. The final sample consists of 33 clusters of galaxies and covers a wide range of different morphologies. Due to the selection of the clusters by observation time this sample is not complete and the found properties cannot directly be extrapolated to the whole cluster population of the universe.

All studies in this work are based on the sample of 33 clusters. Extensive data on the sample including general properties and maps of several physical cluster properties are published at CDS at `http://cdsarc.u-strasbg.fr/viz-bin/qcat?J/A+A/585/A130`. The sample is described in detail in Hofmann et al. (2016b) which chapter 3 of this work is based on. Fig. 2.5 shows the sky positions of the 33 clusters.

The clusters were selected in the following way (see also Chapter 3):

I based the sample selection on the NORAS (378 sources, see Böhringer et al. 2000), REFLEX (447 sources, see Böhringer et al. 2004), and CIZA (73 sources, see Ebeling et al. 2002) catalogues. They all have been derived from *ROSAT* observations, which deliver the only true imaging all-sky X-ray survey to date. NORAS and REFLEX cover the regions

Table 2.1: Sample properties.

Cluster[a]	Abbrev.[a]	n_H [10^{22} cm^{-2}]	< Tmap > [keV]	r_{FOV}[b] [Mpc]	r_{500}[c] [Mpc]	M_{500}[c] [10^{14} $M_\odot$]	r_{FOV}/r_{500}
RX J1347-114	rxj1347	0.046	14.7±0.125	0.48	1.57±0.05	17.7±1.8	0.31
1E 0657-56	1e0657	0.049	12.6±0.112	0.98	1.58±0.06	15.3±1.9	0.62
A 2390	a2390	0.062	10.8±0.104	0.55	1.51±0.07	12.4±1.8	0.36
A 1689	a1689	0.018	10.4±0.115	0.41	1.52±0.07	12.1±1.8	0.27
A 401	a401	0.099	8.6±0.071	0.36	1.45±0.09	9.5±1.7	0.25
A 2204	a2204	0.057	8.5±0.035	0.42	1.39±0.08	9.0±1.6	0.30
A 2034	a2034	0.015	8.3±0.107	0.31	1.40±0.09	8.8±1.6	0.22
A 1413	a1413	0.018	8.3±0.107	0.36	1.38±0.08	8.7±1.6	0.26
A 2744	a2744	0.014	8.7±0.229	1.09	1.30±0.08	8.6±1.5	0.84
A 1835	a1835	0.020	8.5±0.040	0.42	1.32±0.08	8.5±1.5	0.32
PKS 0745-191	pks0745	0.373	7.9±0.031	0.40	1.37±0.09	8.2±1.6	0.29
A 665	a665	0.043	7.3±0.137	0.48	1.26±0.09	6.9±1.5	0.38
CYGNUS A	cygnusa	0.272	6.9±0.022	0.29	1.30±0.10	6.8±1.5	0.22
ZW 3146	zw3146	0.025	7.0±0.064	0.39	1.18±0.09	6.3±1.4	0.33
A 520	a520	0.057	6.7±0.073	0.79	1.20±0.09	6.1±1.4	0.66
A 1795	a1795	0.012	6.2±0.008	0.30	1.23±0.10	5.8±1.4	0.24
A 1650	a1650	0.013	6.0±0.036	0.28	1.20±0.10	5.5±1.4	0.23
A 3667	a3667	0.044	5.8±0.025	0.37	1.20±0.10	5.3±1.4	0.31
A 907	a907	0.054	5.8±0.061	0.28	1.14±0.10	5.0±1.3	0.24
A 521	a521	0.049	5.9±0.177	0.54	1.10±0.10	4.8±1.3	0.49
A 1995	a1995	0.012	5.9±0.173	0.31	1.06±0.09	4.7±1.2	0.29
A 2146	a2146	0.030	5.7±0.031	0.50	1.08±0.10	4.6±1.2	0.46
MS0735.6+7421	ms0735	0.033	5.5±0.030	0.30	1.08±0.10	4.5±1.2	0.28
MS 1455.0+2232	ms1455	0.032	5.1±0.055	0.31	1.01±0.10	3.9±1.2	0.30
A 2199	a2199	0.009	4.4±0.010	0.19	1.05±0.12	3.5±1.2	0.18
A 496	a496	0.038	4.3±0.012	0.20	1.04±0.12	3.4±1.2	0.19
A 2597	a2597	0.025	4.0±0.014	0.21	0.98±0.12	2.9±1.1	0.21
3C348 (HERCULES A)	3c348	0.062	3.9±0.032	0.23	0.94±0.12	2.7±1.1	0.25
A 1775	a1775	0.010	3.7±0.047	0.22	0.94±0.13	2.6±1.1	0.23
HYDRA A	hydraa	0.047	3.5±0.009	0.22	0.93±0.13	2.4±1.1	0.23
2A 0335+096	2a0335	0.175	2.9±0.005	0.18	0.84±0.15	1.8±1.0	0.21
SERSIC 159-03	sersic159	0.011	2.8±0.012	0.17	0.82±0.15	1.7±0.9	0.20
A 2052	a2052	0.027	2.3±0.002	0.15	0.76±0.17	1.3±0.9	0.19

[a] Most commonly used cluster name and abbreviated catalogue names of clusters (compare to tables A.1,A.2, and A.3). Sorted on descending mass (M_{500}).
[b] Maximum radius (from X-ray peak) covered in this analysis.
[c] Overdensity radii r_{500} and M_{500} were calculated using the mass-temperature scaling relation from Vikhlinin et al. (2009a) for an estimate on the r_{500} fraction covered in each object. < T map > was used as input for the scaling relation and errors were estimated assuming a 0.5 keV systematic uncertainty (see scatter in Fig. 3.2).

north and south of the galactic plane (±20°), excluding the Magellanic Clouds. The CIZA sample covers the Galactic plane and thus adds some interesting clusters to the sample. However in the Galactic plane I have to deal with higher foreground absorption of X-rays (due to the column density n_H of the Galaxy).

Not all of these clusters have been observed with *Chandra*, but predominantly X-ray bright clusters have, where the structure of the ICM could be well studied. I matched all *Chandra* ACIS observations available from the *Chandra* Data Archive (CDA[5] on 2013-10-09) with cluster positions in the *ROSAT* catalogues mentioned above.

I set a luminosity cut on the ~ 300 clusters correlated with *Chandra* observations, and only added clusters to the sample which had a luminosity of more than 2.0x10^{44} erg/s in the 0.1-2.4 keV *ROSAT* energy band. I only accepted clusters and groups of galaxies with a redshift of $z \gtrsim 0.025$ to ensure all clusters fit reasonably well into the *Chandra* ACIS FOV. This excludes some nearby extended systems where larger radii are not homogeneously covered (e.g. the Coma cluster, see Vikhlinin et al. 2009b). After these selections I used all clusters with $\gtrsim 100$ ks raw *Chandra* exposure time. The final sample consists of 33 X-ray bright, massive, nearby clusters of galaxies. The velocity dispersion of galaxies in the clusters is around 1000 km/s for most systems. The cluster halo masses within the overdensity radius r_{500} range from 1×10^{14} $M_\odot$ to 2×10^{15} $M_\odot$ (Tab. 2.1). At r_{500} the average density of the cluster is 500 times the critical density of the universe at the cluster redshift. The luminosity range is $(2-63)$x10^{44} erg/s (0.1-2.4 keV X-ray luminosity, see Tabs. A.1, A.2, and A.3), the redshift ranges from 0.025 to 0.45 (see Fig. 2.7) and the total exposure analysed in this work is ~ 8 Ms (corresponding to more than 90 days of observations). For a list of observations used in this study see Tab. A.4.

2.4 Data reduction pipelines

Astronomical data is usually provided in the `FITS` standard file system with images projected to the world coordinate system (WCS, see Hanisch et al. 2001; Greisen & Calabretta 2002; Pence et al. 2010) which is a standardized table system with header informations. In case of X-ray event files the header contains general information on the observation like instrument, exposure time, start date of observation, and reference points and dimensions for mapping between detector and sky coordinates (WCS).

2.4.1 *Chandra* CIAO data reduction

For the analysis of the *Chandra* observations the CIAO[6] package of science analysis tools was created by the *Chandra* collaboration (Fruscione et al. 2006). The archival *Chandra* data at the first level contains lists of X-ray photons with detector coordinates of detection and pulse height. The lists are reprocessed with the latest calibration files to obtain lists with sky coordinates, energies and exact timing of each event. The sky coordinates are

[5] http://cxc.harvard.edu/cda/

[6] `cxc.harvard.edu/ciao/`

calculated from a file giving the exact pointing of the telescope in fine time bins. At this stage higher level processing can be performed by the user. CIAO includes tools to remove bad pixels from the images or to estimate the background and spectrum of the background in each observation. Times of high background due to flares of charged particles hitting the detectors (e.g. solar wind) can be removed. Sky coordinates can be checked by cross-correlating with existing catalogues to correct for residual pointing uncertainties of the telescope.

I used a pipeline downloading all relevant datasets for a given cluster from the *Chandra* data archive (CDA) and reprocesses them using the *Chandra* standard data processing (SDP) with the *Chandra* Interactive Analysis of Observations software package (CIAO, Fruscione et al. 2006) version 4.5 and the *Chandra* Calibration Database (CalDB, Graessle et al. 2007) version 4.5.9.

Based on the properly calibrated files I extracted source spectra in spatial bins to map the X-ray emission of the clusters as projected along the line of sight.

2.4.2 The XSPEC fitting package

The XSPEC fitting package was developed for fitting different emission models to X-ray spectra and finding the best fit parameters of a model. For example this allows to constrain the temperature of a collisionally-ionised plasma as in the ICM of galaxy clusters. The XSPEC manual[7] describes the fitting method as follows:

From the X-ray observatories we obtain photon counts (C) within specific instrument channels, (I). This observed spectrum is related to the actual spectrum of a source (f(E)) by

$$\mathrm{C(I)} = \int_0^\infty \mathrm{f(E)\ R(I,E)\ dE} \tag{2.1}$$

where R(I,E) is the instrumental response and is proportional to the probability that an incoming photon of energy E will be detected in channel I. Ideally, then, we would like to determine the actual spectrum of a source, f(E), by inverting this equation, thus deriving f(E) for a given set of C(I). This is not possible in general, as such inversions tend to be non-unique and unstable to small changes in C(I).

The usual alternative is to choose a model spectrum, f(E), that can be described in terms of a few parameters (i.e., $\mathrm{f(E, p_1, p_2, ...)}$), and match, or "fit" it to the data obtained by the spectrometer. For each f(E), a predicted count spectrum ($\mathrm{C_p(I)}$) is calculated and compared to the observed data (C(I)).

The model parameters are varied to find the parameter values that give the most desirable fit statistic. These values are referred to as the best-fit parameters. The model spectrum, $\mathrm{f_b(E)}$, made up of the best-fit parameters is considered to be the best-fit model.

Most commonly χ^2 statistics are used to determine the best fitting model to the data.

[7] `https://heasarc.gsfc.nasa.gov/xanadu/xspec/manual/XspecSpectralFitting.html`

For quicker calculations these models are usually saved within XSPEC on a discrete parameter grid and not calculated each time.

$$\chi^2 = \sum \frac{(\mathrm{C(I)} - \mathrm{C_p(I)})^2}{\sigma(\mathrm{I})} \tag{2.2}$$

where σ(I) is the uncertainty for channel I. By minimising this quantity the best fit model is obtained. From the change in χ^2 for a range of model parameters the uncertainty range for each parameter is calculated for a given confidence level. Using this fitting method I could convert the observed X-ray spectra in different regions of a cluster into physical properties of the hot plasma.

2.4.3 Mapping cluster ICM properties

For the *Chandra* data reduction I used a pipeline of various *Python* and *C++* scripts to accurately map the structure of the ICM. The pipeline downloads all relevant datasets from the *Chandra* data archive (CDA) and reprocesses them using the *Chandra* standard data processing (SDP) with the *Chandra* Interactive Analysis of Observations software package (CIAO, Fruscione et al. 2006) version 4.5 and the *Chandra* Calibration Database (CalDB, Graessle et al. 2007) version 4.5.9. Cosmological calculations were done using `cosmocalc` by Wright (2006).

A background light-curve for each observation is created and times of high background are removed from the event files, by iteratively removing times where the count rate is more than 3σ from the median of the light-curve. Using the CIAO tool `acis_bkgrnd_lookup`, I find a suitable blank-sky background file, which is provided by the *Chandra* X-ray centre (see e.g. Markevitch et al. 2003) and derive the background in each of the cluster observations. I correct residual spatial offsets between the individual observations if necessary by detecting point sources in each image with `wavdetect` and correlating the individual detection lists. Using the deepest observation as a reference, offsets in other event files are corrected by updating their aspect solution. With this procedure I ensure the best resolution of small-scale ICM variations. The following steps were applied to obtain spatially resolved spectra of the cluster emission:

1. I created images from the event file of each dataset using an energy range of 0.5 keV to 7.0 keV and binning the image by a factor of two (1pix $\sim$ 0.98 arcsec). The energy range was chosen to contain the most of the emission from the cluster. By cutting the lowest and highest energies mostly background is removed and thus the contrast of the cluster image is improved. The images were binned to save computing time and because the PSF of the instrument is higher than the pixel resolution so there is almost no information lost doing this binning.

2. For each image an exposure-map was created for an energy of 1.5 keV. This energy was chosen because it is at the peak of the cluster emission. I assumed the effective exposure to be independent of photon energy in the energy range of chosen for the images. This is a common approach which is known to provide a good approximation.

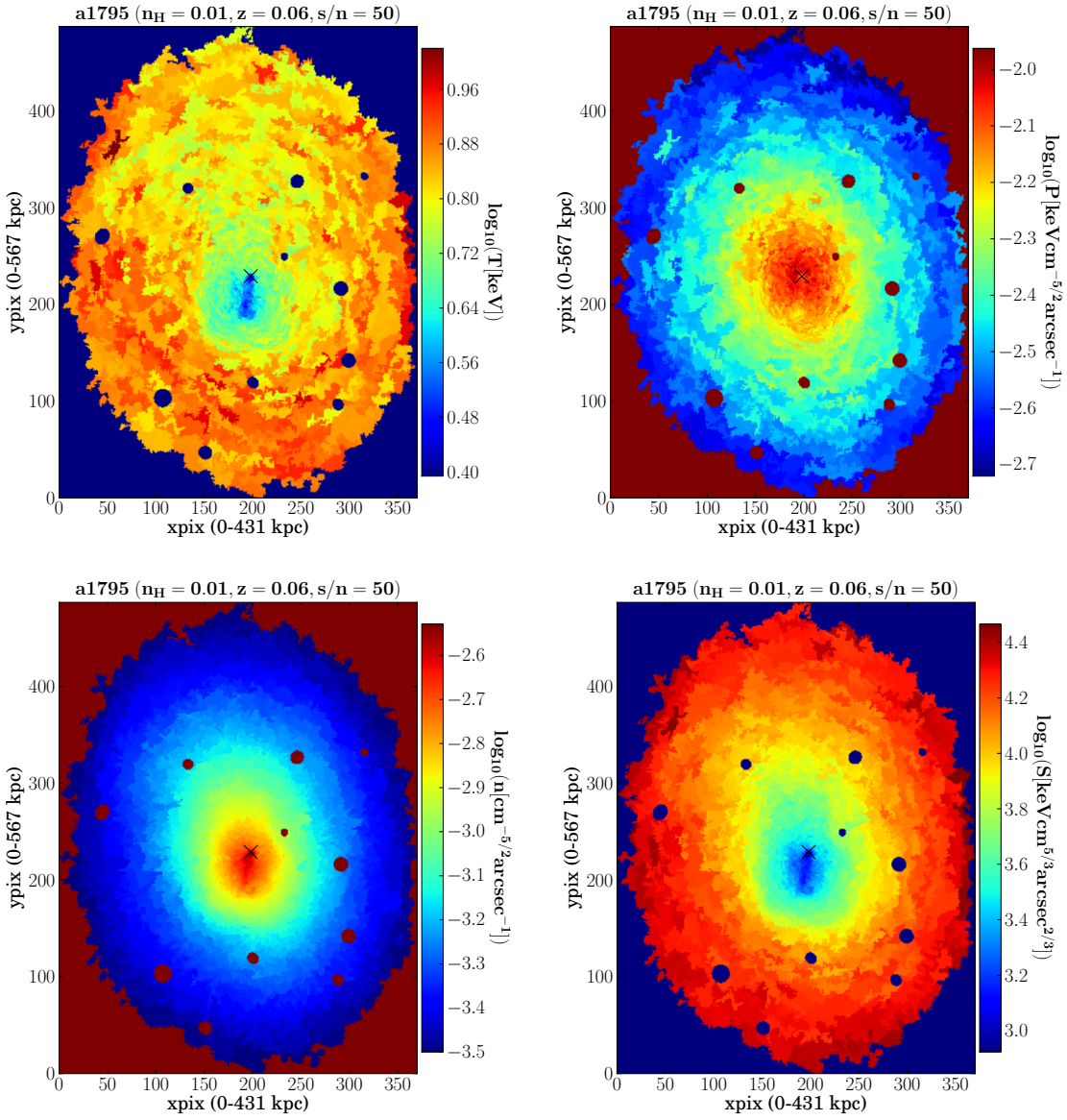

Figure 2.8: From top left to bottom right: 2D maps of projected temperature, pressure, density and entropy of A 1795. The cross marks the X-ray peak and centre for profile analysis. Point sources and regions below the surface brightness cut are set to zero. xpix and ypix are pixels along RA and DEC direction and the overall range in kpc is given. Scale: 1pix $\sim$ 1 arcsec. The plot titles indicate the abbreviated cluster name, the average foreground column density n_H [cm^{-2}], and the redshift.

3. After the analysis of the individual observations, all images, background-, and

exposure-maps were merged. A second point source detection with `wavdetect` is run on the merged images and after carefully screening the detection list, the point sources are masked from the image.

4. In the following steps the image is adaptively smoothed with *snsmooth* = 15 and then binned into regions of equal S/N ratio of 50 (>2500 counts per bin) using the contour binning technique `contbin` (see Sanders 2006). I generated maps with S/N = 25 (>625 counts per bin) for clusters where I obtained less than 50 independent spatial-spectral bins from the S/N = 50 analysis. For each of the bins a detector response is calculated and the count spectrum extracted.

Spectra of the same detectors are added together (ACIS-I and ACIS-S separately) and fitted using C-Statistics in `XSPEC version 12.8.2` (Cash 1979; Arnaud 1996a) with the `apec` model for collisionally-ionised diffuse gas, which is based on the ATOMDB code v2.0.2 (Foster et al. 2012). The fit was done using a fixed foreground column density (n_H [cm^{-2}], see Tab. 2.1), which is determined from the Leiden/Argentine/Bonn (LAB) survey of Galactic HI (based on Kalberla et al. 2005), and a fixed redshift from the *ROSAT* catalogues.

Only in the special case of PKS 0745-191 was the fit done with n_H as a free parameter due to its location behind the Galactic plane and strong n_H variation within the FOV.

The free parameters of the fit to the count spectrum are temperature T [keV], the metal abundance Z as a fraction of solar abundances (reference solar abundance $Z_\odot$ from Anders & Grevesse 1989) and the normalisation η [cm^{-5} $arcsec^{-2}$] of the fit, which is defined as,

$$\eta = \frac{10^{-14}}{4\pi\ {D_A}^2\ (1+z)^2} \int n_e\ n_p\ dV \tag{2.3}$$

with D_A the angular diameter distance to the source, n_e and n_p the electron and hydrogen densities being integrated over the volume V. Assuming a spherical source, uniform density, and full ionisation with 10 per cent helium, 90 per cent hydrogen abundance (i.e. $n_e \sim 1.2\ n_p$) the hydrogen density can be calculated as

$$n_p = \sqrt{\frac{(1+z)^2\ 10^{14}\ \eta}{1.2\Theta^3\ D_A}} \equiv \xi \cdot \sqrt{\eta} \tag{2.4}$$

where Θ is the angular size of the source (see the ATOMDB webpage[8] for these equations). The factor ξ changes for different clusters and assumed geometries. I assumed $n_p \sim \sqrt{\eta}$ within any given cluster.

The fit parameters of each bin are translated into images to obtain maps of the temperature, metal abundance and normalisation of the ICM per unit area.

From the 2D maps of the spectral fitting, I calculated a projected pseudo density, pressure, and entropy in each spatial bin of the ICM emission. I assumed a constant line-of-sight depth for all spectral regions calculating pseudo density n as square root of the fit normalisation, normalised by region size,

[8] http://atomdb.org/faq.php

$$\mathrm{n} \equiv \sqrt{\eta}\ [\mathrm{cm}^{-5/2}\ \mathrm{arcsec}^{-1}] \tag{2.5}$$

pseudo pressure as,

$$\mathrm{P} \equiv \mathrm{n} \times \mathrm{temperature}\ [\mathrm{keV}\ \mathrm{cm}^{-5/2}\ \mathrm{arcsec}^{-1}] \tag{2.6}$$

and pseudo entropy as,

$$\mathrm{S} \equiv \mathrm{n}^{-2/3} \times \mathrm{temperature}\ [\mathrm{keV}\ \mathrm{cm}^{5/3}\ \mathrm{arcsec}^{2/3}] \tag{2.7}$$

I adopted a common definition of entropy for galaxy cluster studies, which is related to the standard definition of thermodynamic entropy s per particle through

$$\mathrm{s} \equiv \mathrm{k_B}\ \ln(\mathrm{S}^{3/2}\ (\mu\ \mathrm{m_p})^{5/2}) + \mathrm{s_0} \tag{2.8}$$

with mean particle mass μ, proton mass $\mathrm{m_p}$, and a constant $\mathrm{s_0}$ (see e.g. Voit 2005). Relative cooling times of the ICM are proportional to

$\mathrm{n}^{-1} \times \mathrm{temperature}^{1/2}$ [$\mathrm{keV}^{1/2}$ $\mathrm{cm}^{5/2}$ arcsec] where Bremsstrahlung emission dominates (see e.g. Sarazin 1986, and references therein).

All distances were calculated using the redshift given in the *ROSAT* cluster catalogues. All uncertainties are 1σ confidence intervals unless stated otherwise. All further analysis only includes regions where the area-normalised normalisation of the fit was above 10^{-7} cm^{-5} arcsec^{-2}. This corresponds roughly to a surface brightness cut below which there were insufficient counts for detailed spectral analysis. For an example refer to the maps of Abell 1795 in Fig. 2.8.

2.4.4 eROSITA simulated cluster observations

Cluster models were derived from the deep *Chandra* observations and then used to simulate clusters in the eROSITA survey. The clusters were simulated both at their real position and at different redshifts to investigate not only the impact of the blending of different temperature regions in the eROSITA survey due to larger PSF compared to *Chandra* but also how this effect depends on redshift.

SIXTE eROSITA event files

For the simulation of eROSITA observations I used the SIXTE (SImulator of X-ray TElescopes) simulator (see e.g. Schmid et al. 2010) to produce X-ray event lists for eROSITA observations of clusters.

The simulation software calculates the photon energy distribution and flux at the telescope position given the plasma emission model and distance of a model cluster. The arriving photons are then folded through a energy dependent detection efficiency of the telescope. The software then calculates the impact position on the detector given the energy dependent vignetting and PSF of the X-ray telescope. On the detector the photon

creates a electron cloud upon impact and is registered by 1-4 neighbouring detector pixels depending on photon position and energy. The registered pulse height amplitude (PHA registered by the electronic readout) of a photon in several pixels can then be calculated back to an original energy by using a calibrated energy-PHA conversion. This conversion is different for photons registered by one (singles), two (doubles), three (triplets), and four (quadrupole) pixels. If one event is detected by more than one pixel it is called a split-event.

The cluster models are input to the simulation software via SIMPUT[9] files which contain all source information. The simulator provides calibration files for different X-ray observatories which describe the different steps from original photon to detected energy of an event (see description above). I used the eROSITA calibration as given by the simulator and provided a attitude file describing the pointing of the telescope during the eROSITA all-sky survey. For more details on the calibration files see Chapter 5.

I used the *Chandra* maps described above to simulate realistic clusters in the eROSITA survey. This was done by converting the maps into the SIMPUT format. Every spatial-spectral region was treated as a separate source with a reference position and a mask giving the extent of the region. The best fit spectrum from the *Chandra* data analysis pipeline is given as source spectrum in the SIMPUT table and normalised to the total flux.

As descended in more detail in Chapter 5 I simulated the clusters at different redshifts by modifying the SIMPUT files. To redshift the SIMPUT models of the clusters I re-calculated the expected extent on the sky by modifying the mask images for each region, shifted the spectrum of the source using XSPEC, and recalculated the total flux normalisation.

The re-normalisation of flux and source extent is calculated with the factor of difference in the plate scale and luminosity distance of the source. All cosmological calculations were done with the tool `cosmocalc` (see Wright 2006). The Python implemented version of this tool was written by James Schombert.

This was done for every cluster in five redshift bins. Every individual model was then simulated 100 times using SIXTE for better statistics on average cluster properties. This required separate simulations of $33 \times 100 \times 5 = 16500$ cluster models. By doing this I obtained errors on average cluster properties which are small enough to constrain systematics of the survey and in this way I could study expected bias in the eROSITA survey. These simulated data were analysed with an early version of the the eSASS tools which will be the science analysis software for the eROSITA Instrument.

XSPEC eROSITA spectra

The above method creates highly accurate images of the clusters in different bands including the estimated total X-ray background of in the survey (see Chapter 5 for more details). However the latest calibration information for the eROSITA survey (as of July 18, 2016) from the latest calibration measurements in the labs of the Max-Planck-Institute for extraterrestrial Physics (MPE). For spectral analysis and model fitting I found in my

[9] http://hea-www.harvard.edu/heasarc/fitsformats-heasarc.html

analysis that SIXTE event file spectra are not sufficiently accurate and caused some spurious offsets in fit temperatures. There was a significantly too low count rate for lower energies for split events which caused systematically much too high temperatures.

To isolate the bias caused by the temperature substructure of ICM emission I made secondary simulations using the XSPEC spectral fitting package to simulate cluster spectra in the eROSITA survey. I set up the simulations using `XSPEC fakeit` which creates fake spectra of a source emission model folded by the response of a X-ray telescope.

I used the same cluster sample as with SIXTE (the same 33 throughout this thesis, see Hofmann et al. 2016b). I made 100 simulations of every cluster model at five different redshifts (0.1, 0.2, 0.4, 0.8, and 1.6). Every model consists of on average ~ 200 isothermal ICM regions. The spectrum of each isothermal region in each cluster was simulated separately and then merged to one blended cluster spectrum.

The exact same procedure was done twice the first run with the real measured temperature substructure of the cluster and one where the cluster of each cluster map bin was set to the median temperature of the cluster.

2.4.5 eROSITA eSASS analysis pipeline

The eSASS (eROSITA Science Analysis Software System) software package is under development for the upcoming eROSITA mission. The programming efforts are lead by H. Brunner. I could access beta versions of the software provided for running tests on simulated eROSITA observations. The main tool is called `SRCTOOL` (by T. Dwelly) and can be used to extract spectra including response files and background estimates from the simulated event files of the eROSITA survey. The output spectra are then ready for fitting XSPEC models to the simulated data.

`SRCTOOL` is used to derive source properties from the the calibrated eROSITA event files and their ancillary data. For my application I used the tool to derive background-subtracted spectra of the extended galaxy cluster sources in the simulated observations. `SRCTOOL` can produce spectra, light-curves, as well as ARF and RMF files specific to the observation. The input to the tool includes: the simulated event file (SIXTE simulation tool output), the source coordinates (position assumed to be known, no detection), the number of sub-telescopes used for the analysis, ARF/RMF/vignetting calibration files, a file containing bad-pixel coordinates on the detector (only necessary for real instrument), a extraction region for the source and the estimated background.

For my analysis I assumed the source coordinates to be known since I tested systematics of the instrument without detection efficiency. Future work by Ramos-Ceja et al., in preparation and Clerc et al., in preparation will study detection efficiency separately. I assumed a fixed extraction radius based on the input model extent and a concentric annulus around it to estimate the typical background in the observation. The extraction radius was identified by eye in the simulated images to include all cluster emission. By fitting `XSPEC apec` models to the extracted spectra from the simulated observations I was able to constrain the cluster ICM properties the same way as in the *Chandra* data.

If the emission spectra of two regions of different temperature gas are blended together

(depends on PSF) depending on the effective at different energies, the contribution of one phase can be higher than another in different instruments (Reiprich et al. 2013).

Chapter 3

Thermodynamic perturbations

In this chapter I present the analysis of the 33 clusters in the deepest massive compact cluster sample observed with the *Chandra* satellite. This chapter is based on Hofmann et al. (2016b).

3.1 Introduction

In the current picture of the evolution of the universe, clusters of galaxies have formed in the deep potential wells created by clumping of dark matter (DM) around remnant density fluctuations after the big bang. The majority of the mass in clusters is made of DM, which is only observed indirectly through its gravitational effects. The second component of clusters is baryonic matter consisting mainly of very thin hot plasma (the intra cluster medium, ICM), heated by the gravitational accretion into the potential wells, and emitting strongest in X-ray wavelength due to its high temperatures. The smallest fraction of the mass is in the stellar content of the clustered galaxies, which is observable in visible light. The behaviour of DM in the cluster potential is believed to be well understood from cosmological simulations (e.g. Springel et al. 2005) and observations of gravitational lensing effects on visible light (Broadhurst et al. 1995; Kaiser et al. 1995; Allen et al. 2002; Bradač et al. 2006; Zhang et al. 2008; Mahdavi et al. 2013). The member galaxies of a cluster are well described as collisionless particles moving in the cluster potential by measuring the line of sight velocity dispersion in the optical (see e.g. Zhang et al. 2011a; Rines et al. 2013). The complex dynamic and thermodynamic processes in the hot ICM can be studied with X-ray observations. Other phases of the ICM have been studied at different wavelength with UV and Hα (e.g. McDonald et al. 2011) or radio observations (e.g. Dolag et al. 2001; Govoni et al. 2004).

Schuecker et al. (2004) first related fluctuations in the projected pressure maps of the hot, X-ray emitting, ICM of the Coma cluster to turbulence. Turbulence has been discussed as a significant heating mechanism (see Dennis & Chandran 2005; Ruszkowski & Oh 2010; Gaspari et al. 2012a), which is important to understand the heating and cooling balance (see cooling flow problem, Fabian 1994) in clusters and estimate the amount of

non-thermal pressure support (see e.g. simulations by Nelson et al. 2014). Zhuravleva et al. (2014a) recently studied turbulence in the Perseus and Virgo cluster by analysing fluctuations in the surface brightness of the cluster emission. Asymmetries and fluctuations within thermodynamic properties of the hot plasma can be used to estimate the amount of turbulence (e.g. Gaspari & Churazov 2013; Gaspari et al. 2014). This has been studied in the PKS 0745-191 galaxy cluster by Sanders et al. (2014). I applied a similar technique to the current sample of 33 clusters and compared the results to the findings of cluster simulations (e.g. Vazza et al. 2009; Lau et al. 2009).

The amount of turbulence in the hot ICM is hard to directly measure. Simulations of galaxy clusters predict turbulent motions of several hundreds of km/s (e.g. Dolag et al. 2005; Nelson et al. 2014; Gaspari et al. 2014). Sanders et al. (2011), Sanders & Fabian (2013), and Pinto et al. (2015) were able to obtain upper limits on the velocity broadening of spectra for a large sample of clusters. However current X-ray instruments do not provide the spectral resolution needed to detect significant broadening due to turbulence in all but a few possible cases.

The basis for this study was the X-ray all-sky survey of the *ROSAT* mission (1990 to 1999, see Truemper 1982). The clusters identified in this survey (e.g. Böhringer et al. 2000, 2004) were followed up with the current generation X-ray telescopes *Chandra*, *XMM-Newton*, and *Suzaku*. For the substructure study I used observations of *ROSAT*-clusters with the X-ray observatory on board the *Chandra* satellite which delivers the best spatial and very good spectral resolution. Since its launch in 1999 *Chandra* has frequently been used to study clusters of galaxies as individual systems and as cosmological probes (e.g. Allen et al. 2004, 2008; Vikhlinin et al. 2009b,a). Its high resolution showed an unexpected complexity of the ICM structure in many cases (e.g. Fabian et al. 2000; McNamara et al. 2000; Markevitch et al. 2000, 2002; Sanders et al. 2005b; Fabian et al. 2006; Forman et al. 2007). Based on the large archive of deep cluster observations I analysed a sample of clusters and mapped their thermodynamic properties. I specifically investigated perturbations in the thermodynamic parameters of the ICM, which according to recent high-resolution simulations can be used to trace turbulence in the ICM via the normalisation of the ICM power spectrum (e.g. in density, Gaspari et al. 2014). By measuring the slope of the power spectrum I can constrain the main transport processes in the hot ICM, such as thermal conductivity (Gaspari & Churazov 2013).

The paper is structured as follows: Sect. 2 describes the analysis of perturbations, in Sect. 3 the main results are presented, Sect. 4 contains results for individual systems, in Sect. 5 the findings are discussed, and Sect. 6 contains the conclusions.

The cluster sample selection and data reduction for obtaining the thermodynamic cluster maps which the asymmetry study is based on is described in Chapter 2.

For all the analysis I used a standard ΛCDM cosmology with $H_0 = 71$ km s^{-1} Mpc^{-1}, $\Omega_M = 0.27$ and $\Omega_\Lambda = 0.73$ and relative solar abundances as given by Anders & Grevesse (1989).

3.2 Analysis of perturbations

Based on the very detailed spatial-spectral analysis of this sample of clusters with deep *Chandra* observations I were able to study the ICM in great detail for a large sample of clusters.

3.2.1 Asymmetry measurement

One of the main goals of this study was to better characterise the thermodynamic state of the ICM in individual clusters and identify general trends in the whole sample. Important indicators of the state of the hot gas are fluctuations in thermodynamic properties. Gaspari & Churazov (2013) and Gaspari et al. (2014), in recent high-resolution simulations, have shown a connection between such fluctuations and the Mach number of gas motion in the ICM.

I examined the asymmetry (i.e. the spread) of thermodynamic properties in concentric, circular annuli of radius r around the peak X-ray emission. As input I used the S/N 50 ICM-maps (see Sect. 2.4.3). For nine clusters (a907, ms1455, a521, a665, a2744, a1775, a1995, 3c348, zw3146) I used S/N 25 instead to obtain at least five radial spread-bins with a minimum of five data points per bin for all clusters. Assuming the data points are scattered statistically due to their uncertainties $\sigma_{\rm stat}$ I tested for intrinsic spread $\sigma_{\rm spread}$ in the radial profiles (see e.g. Fig. 3.1).

To avoid contamination of the spread-measurement by the slope, I modelled the radial profile by interpolating between several nodes. This modelled average profile can be described by a function $\mu(\mathrm{r}, \mu_1, ..., \mu_{\rm N})$ with N=7. The nodes divide the cluster profile into bins with equal number of data points. I used a minimum of five data points per model-node and if this criterion was not met I reduced the number of nodes. The intrinsic fractional spread is given by a function of the form $\sigma_{\rm spread}(\mathrm{r}, \sigma_{\rm spread,1}, ..., \sigma_{\rm spread,M})$. I performed three independent spread measurements, splitting the profiles into one, two, and five radial bins (M=1,2,5) to measure the spread in the clusters with different radial resolutions.

For every data point I obtained the mean value $\mu(\mathrm{r_i})$ of the thermodynamic profile at its radius $\mathrm{r_i}$ by interpolating between the model-nodes (see grey lines in Fig. 3.1). The individual spread values of each data point $\sigma_{\rm spread}(\mathrm{r_i})$ are constant within a given radial bin (see spread profile in Fig. 3.1).

The intrinsic spread of cluster properties was estimated using a Markov Chain Monte Carlo (MCMC) method implemented using `emcee` (see Foreman-Mackey et al. 2013) with 100 walkers, 1000 iterations, and a burn-in length of 1000. The total scatter of data values (i) was assumed to follow a Gaussian distribution with standard deviation of $\sigma_{\rm tot}$ calculated as,

$$\sigma_{\rm tot,i} = \sqrt{\sigma^2_{\rm stat,i} + \sigma^2_{\rm spread}(\mathrm{r_i})} \tag{3.1}$$

For each iteration of the MCMC χ^2 was calculated as,

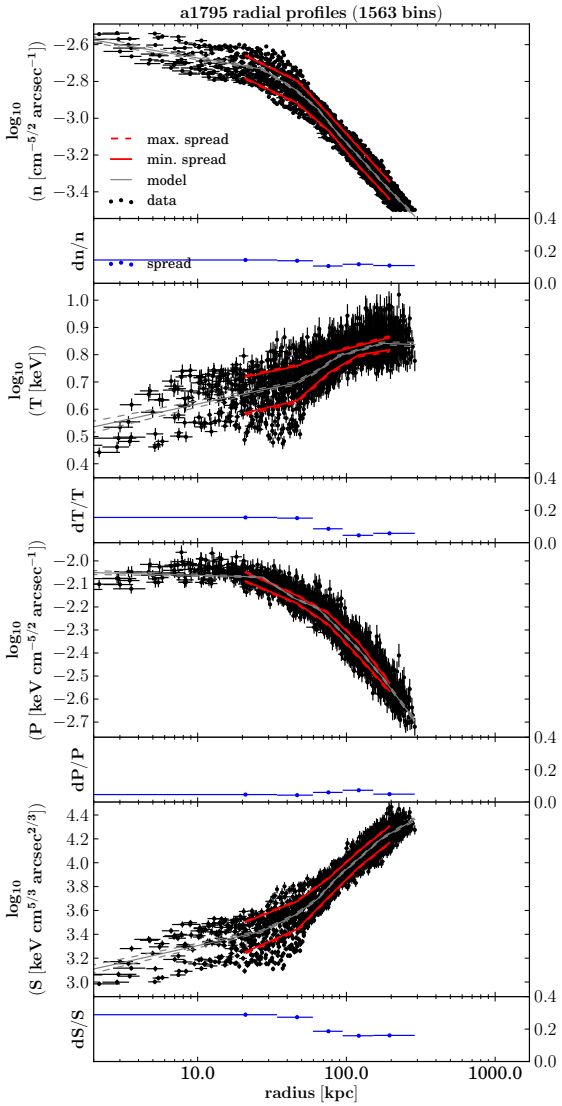

Figure 3.1: Radial profiles of projected density, temperature, pressure, and entropy of A 1795. The centre is marked by a cross in Fig. 2.8. Error bars are the fit-errors and the standard deviation of the radial distribution of the respective spatial-spectral bin. The Plotted lines show limits on intrinsic scatter around an average seven-node model (grey lines) within the given radial range (see Sect. 3.2.1). The small panels show the measured fractional scatter (M=5) with confidence- and radial-range.

$$\chi^2 = \sum_{\mathrm{i}=1}^{\mathrm{n}} \frac{(\mathrm{D_i} - \mu(\mathrm{r_i}))^2}{\sigma^2_{\mathrm{tot,i}}} \tag{3.2}$$

where $\mathrm{D_i}$ are the individually measured values of the n data points (see Fig. 3.1). The mean-model and spread-values have $\mathrm{N} + \mathrm{M}$ free parameters. Using the MCMC method these parameters were varied, giving as probability value for each iteration, the logarithm of the likelihood (see e.g. Hogg et al. (2010)),

$$\log \mathrm{L} = -\frac{1}{2}\,\chi^2 - \frac{1}{2}\,\sum_{\mathrm{i}=1}^{\mathrm{n}} \log(2\pi\ \sigma^2_{\mathrm{tot,i}}) \tag{3.3}$$

From this procedure I obtained a distribution of mean and spread values. I selected the best fit value for each parameter as the maximum of the distribution and estimated the uncertainty by giving the range containing 34 per cent of the obtained values on each side of the maximum. If the distribution was consistent with zero, I give the 68 per cent range as an upper limit.

The spread measurements performed with just one radial spread-bin (M=1) were used to compare the overall fractional spread dn, dT, dP, and dS among clusters (see e.g. Figs. 3.4, 3.5, 3.8, and Tab. A.5) and constrain the general ICM properties. For additional comparison of larger and smaller physical radii I measured the spread inside and outside of 100 kpc from the X-ray peak (M=2, see e.g. $\mathrm{dP_{cen}}$ and $\mathrm{dP_{out}}$ Sect. 3.3.2). From the spread analysis with five radial spread-bins (M=5) I obtained profiles of the intrinsic fractional standard deviation of thermodynamic properties dn/n, dT/T, dP/P, and dS/S (see Fig. A.3) in individual systems. The spread measurements are consistent with the results of a second Monte Carlo simulation based technique, which was not based on Markov Chains (similar to Sanders et al. 2014).

3.2.2 Surface brightness substructures

The emissivity of the ICM and thus its surface brightness in X-rays is proportional to the plasma density squared (for a review, see e.g. Sarazin 1986). From the data reduction pipeline I obtained merged count and exposure images of the clusters. To remove any structure due to inhomogeneous exposure I divide the count image by the exposure image and obtain an image of the count rate. To identify small surface brightness fluctuations I enhanced the contrast of those images by unsharp-masking, a method commonly used in image analysis. This method is implemented by subtracting two versions of an image, smoothed by two different Gaussian filters, from each other. I subtracted an image smoothed with a Gaussian function of $\sigma = 2$pixel width from an image smoothed with a Gaussian function of $\sigma = 5$pixel width (see Fig. A.2). The obtained unsharp-masked images enhance surface brightness features, complementing the analysis of substructure in thermodynamic properties, and highlighting disturbed systems.

3.2.3 Average cluster temperatures

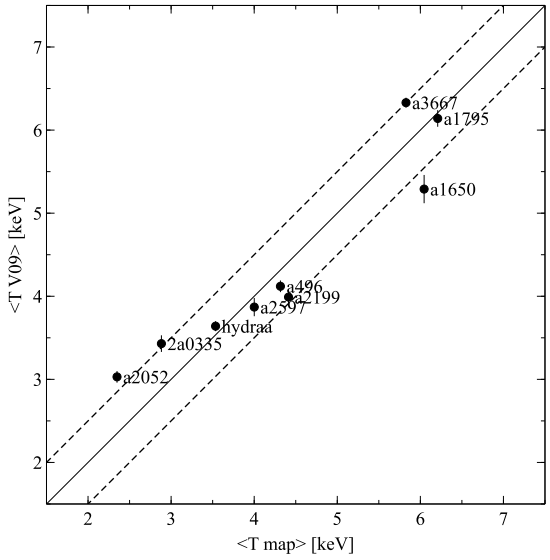

Figure 3.2: Comparison of area- and error-weighted average 2D map temperatures $< \mathrm{T\ map} >$ with overlapping low-z sample temperatures of V09 (Vikhlinin et al. 2009a) showing a scatter of about 0.5 keV around the one-to-one relation.

I calculated average cluster temperatures $< \mathrm{T\ map} >$ as the area- and error-weighted mean value of all measurements. I computed the average of the bin temperature ($< \mathrm{T\ prof} >$, see data points in Fig. 3.1) which is usually lower than $< \mathrm{T\ map} >$, because $< \mathrm{T\ prof} >$ is weighted more on emission than area. Hotter regions in the outskirts are generally larger with lower emission and the relatively colder, X-ray bright, central regions cover a smaller area.

I compared the approach for estimating overall cluster temperatures with previous studies like V09 (using *Chandra*) or HiFLUGS (using *ROSAT*) (Vikhlinin et al. 2009a; Reiprich & Böhringer 2002) as shown in Fig. 3.2 and Fig. 3.3. Fig. 3.2 shows significant scatter of up to 0.5 keV between V09 and this study. This is expected since I use a different approach by averaging many independently fitted bins weighting by area and error-bars rather than by counts. The averaging of many different bins results in small error bars on the average temperature. Fig. 3.3 shows similar scatter when accounting for the larger error bars on the *ROSAT* measurements. Note that I also use different extraction radii than the studies I compared to which influences the measured temperature.

To estimate the mass range of the cluster sample (see Tab. 2.1) I used the mass-temperature scaling relation from Vikhlinin et al. (2009a) with the $< \mathrm{T\ map} >$ temperatures as input to calculate the overdensity radius r_{500} and the total mass M_{500} included by this radius. I accounted for uncertainties in the scaling by assuming a systematic temperature uncertainty of 0.5 keV (see scatter in Fig. 3.2). The average map temperature (area

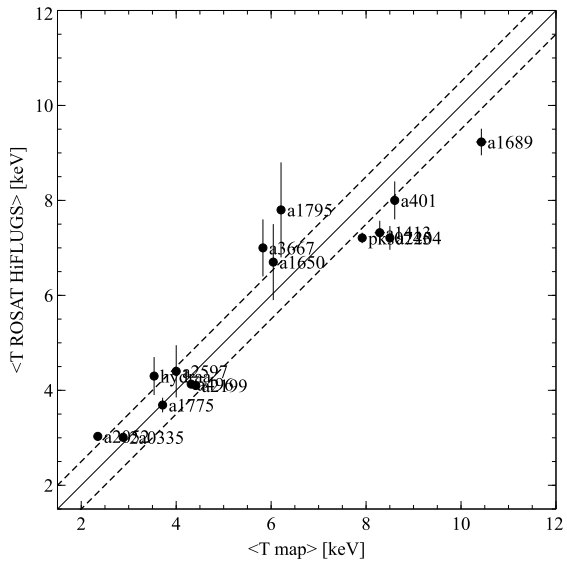

Figure 3.3: Comparison of area- and error-weighted average 2D map temperatures $< \mathrm{T\ map} >$ with HiFLUGS temperatures (Reiprich & Böhringer 2002) from *ROSAT* observations for the clusters overlapping with the sample. The dashed lines show a one-to-one relation with a scatter of 0.5 keV.

weighted) is comparable to the core-excised average temperature used for the scaling by Vikhlinin et al. (2009a).

3.2.4 Table description

The main results of the analysis of this study are summarized in separate tables for each cluster. I created 2D maps from the merged observations of every cluster and measured the asymmetries in thermodynamic parameters in circular concentric annuli around the centre.

Map tables

The primary data products of this analysis are 2D maps of the thermodynamic properties of the ICM based on the merged observations of ACIS-S and ACIS-I for every cluster in the sample (see Sect. 2.4.3). Tables and images are available in electronic form at `http://cdsarc.u-strasbg.fr/viz-bin/qcat?J/A+A/585/A130`. This astronomical data archive is operated by the Centre de Données astronomiques de Strasbourg (CDS).

Tables 2-34 contain the 2D map information (one table per cluster). Each table lists the properties for every pixel in the cluster maps (1pix $\sim$ 0.98arcsec). The map tables contain X (east-west direction) and Y (south-north direction) position (x, y, Cols. 1, 2) of the pixel, the index of the independently-fitted spatial-spectral bin it belongs to (binnum,

Col. 3), the photon counts (cts, Col. 4), the background counts (bgcts, Col. 5), the effective exposure time (exp, Col. 6), the temperature and its upper and lower limits (T, Tup, Tlo, Cols. 7, 8, 9), the relative metallicity and limits (Z, Zup, Zlo, Cols. 10, 11, 12), the fit normalisation and limits (norm, normup, normlo, Cols. 13, 14, 15), the redshift (redshift, Col. 16), the foreground column density n_H (NH, Col 17), distance from the centre in pixels, arc seconds, and kpc (cen_dist, rad_arcsec, rad_kpc, Cols. 18, 19, 20), the angle with respect to the west direction (cen_angl, Col. 21), the calculated projected pressure and symmetric uncertainty (P, P_err, Cols. 22, 23), projected entropy and uncertainty (S, S_err, Cols. 24, 25), and density and uncertainty (n, n_err, Cols. 26, 27). All uncertainties are on 1σ confidence level.

Asymmetry tables

The secondary data products are based on the 2D maps and contain the measured spread (i.e. asymmetry, deviation from radial symmetry of the thermodynamic parameters, see M=5 in Sect. 3.2.1).

Tables 35-67 provide the measured properties in the concentric annuli for one cluster each. They contain the average radius of the annulus (rr, Col. 1), average bin-temperature $< T >$ and uncertainty (T, Te, Cols. 2, 3), and average bin-metallicity and uncertainty (Z, Ze, Cols. 4, 5). For the intrinsic fractional spread values in projected properties best fit value and 1σ upper and lower confidence limits are provided. Spread measurements contain the intrinsic spread in pressure with upper and lower limits (dP, dP_eu, dP_el, Cols. 6, 7, 8), entropy with limits (dS, dS_eu, dS_el, Cols. 9, 10 ,11), density with limits (dn, dn_eu, dn_el, Cols. 12, 13, 14), and temperature with limits (dT, dT_eu, dT_el, Cols. 15, 16, 17).

3.3 Results

The detailed analysis of this sample of clusters enabled us to derive information on the thermodynamic state of the ICM in individual clusters and the whole sample in general.

3.3.1 Perturbations in thermodynamic properties

I studied the average fluctuations in thermodynamic properties of all clusters in the sample using the M=1 spread calculations from Sect. 3.2.1. Comparing the average measurements for all systems in the sample enabled us to find general trends.

Fig. 3.4 indicates that, on average, entropy fluctuations (fractional spread, dS) dominate pressure fluctuations (fractional spread, dP). For some clusters I only obtained upper limits (e.g. A 1689). There are some outliers (e.g. A 2146 and A 3667), which are heavily disturbed systems (see Sect. 3.5.1). Overall most clusters lie off a one-to-one correlation with an average of 16 per cent fluctuations in entropy and 9 per cent in pressure (see Tab. 3.67).

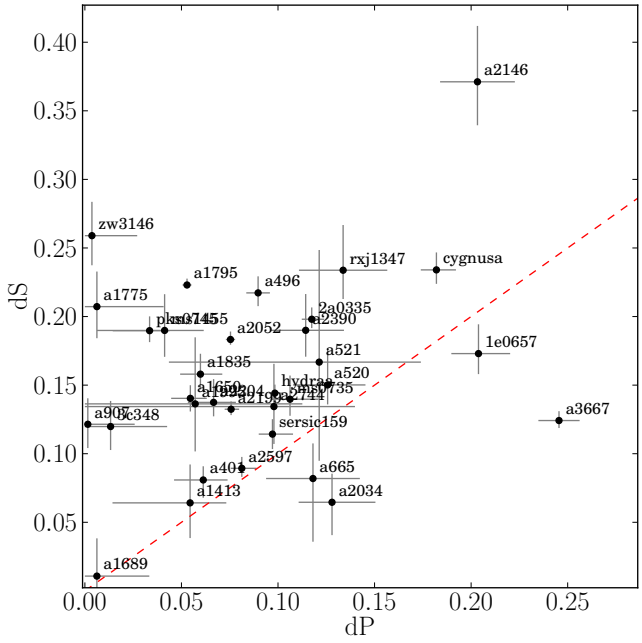

Figure 3.4: Comparison of average projected pressure and projected entropy fluctuations for all clusters in the sample. The dashed line represents a one-to-one relation. The plot suggests that entropy fluctuations dominate in most clusters of the sample. Error bars are the statistical uncertainty from the MCMC measurements.

Fig. 3.5 shows a smaller offset between the average density fluctuations (fractional spread, dn) and temperature fluctuations (fractional spread, dT). I measure significant spread in dn for every cluster in the sample but only obtain upper limits on the dT spread for some. There are some outliers which show very strong density fluctuations (e.g. A 2146, 1E 0657-56, and Cygnus A). Overall most clusters are close to a one-to-one correlation with an average of 11 per cent fluctuations in density and 9 per cent in temperature (see Tab. 3.67).

3.3.2 Perturbations on different scales

I found evidence for larger pressure perturbations dP at larger scales. Fig. 3.6 shows a clear separation of the distribution for central regions $\lesssim$ 100 kpc (cen) from the centre and regions beyond (out). To compare the distribution of spread values on different scales I used the asymmetry measurements from Sect. 3.2.1 where the cluster profile is divided at $\sim$ 100 kpc. The division at 100 kpc was chosen, after visual inspection, as a robust separation radius between central substructure and outer more homogeneous regions. I did not choose the regions relative to r_{500} to ensure I are testing the same physical scale of

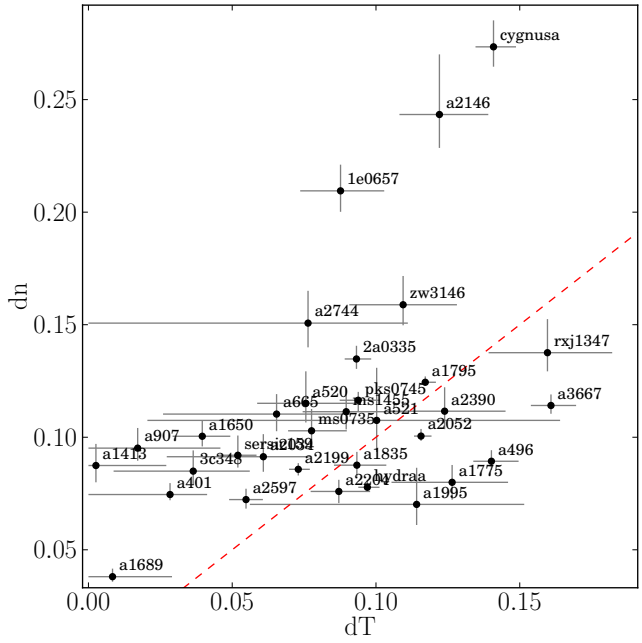

Figure 3.5: Comparison of average temperature and projected density fluctuations for all clusters in the sample. The dashed line represents a one-to-one relation. Error bars are the statistical uncertainty from the MCMC measurements.

the ICM fluctuations.

To estimate the mean of the distributions I used a bootstrapping re-sampling technique, calculating the mean value for 1000 permutations with repetition. The contours are at 15, 50, and 85 per cent of the maximum of the obtained distribution of mean values. In addition Fig. 3.6 contains the output of a Kolmogorov-Smirnov (KS) test to quantify the difference between the cen and out distributions. The D value states the maximum fractional offset between the cumulative distribution graphs and the p value is the probability of the null hypothesis. This means the probability that the dP distributions are different is 96 per cent and thus just above the 2σ level. It should be noted that the offset in dP is dominated by low dP data points and decreases to about 1σ level when only including data points above 0.05 dP. For the thermodynamic properties dS, dn, and dT there is no significant difference between inner and outer radii.

3.3.3 Metallicity correlations

I found an anti-correlation between the average temperatures (< T map >, see Sect. 3.2.3) of the clusters and their average metallicity. The best fit linear correlation is

$$Z/Z_{\odot} = -(1.0 \pm 0.7)\ T/100\mathrm{keV} + (0.34 \pm 0.06).$$

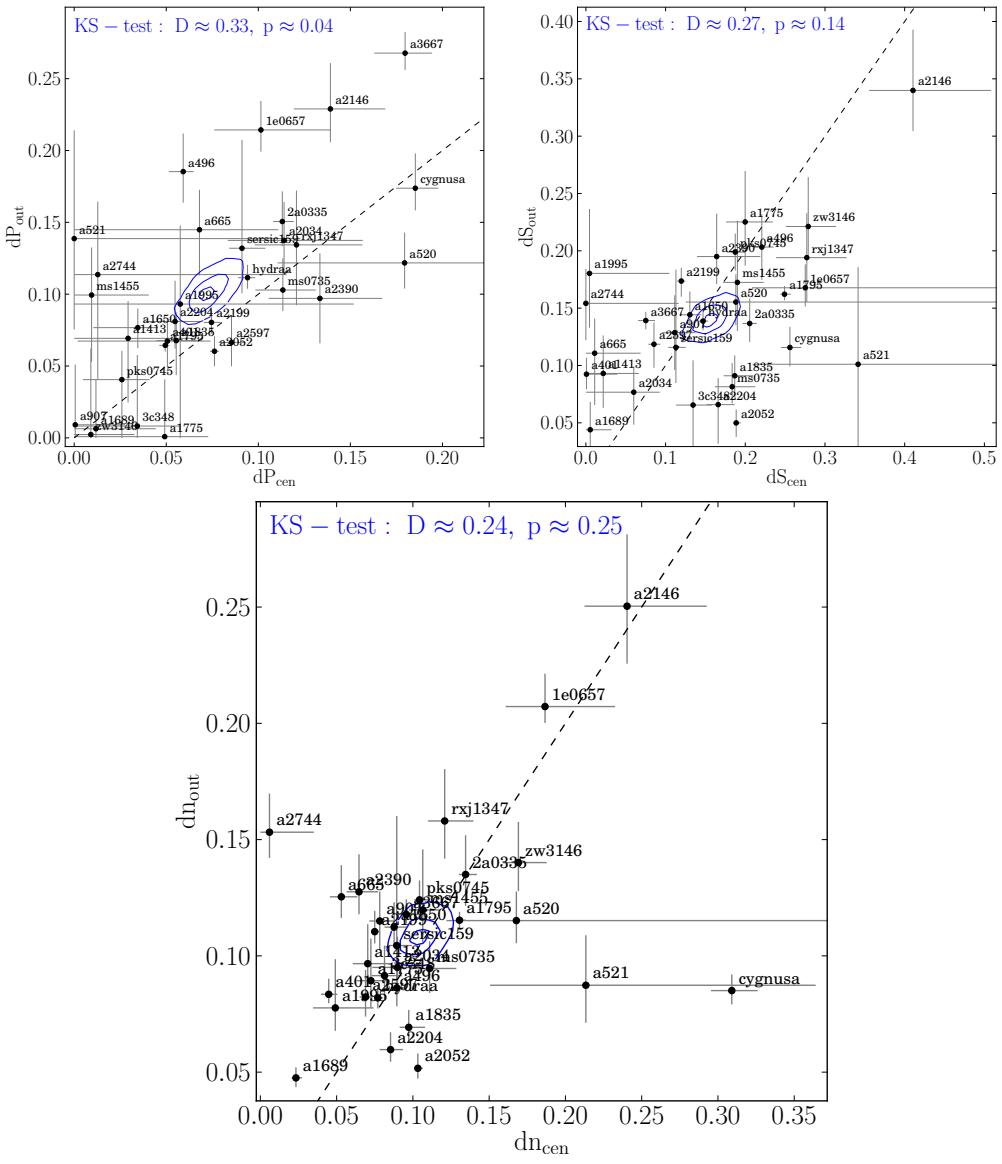

Figure 3.6: Comparison of pressure- (top), entropy- (middle), and density-perturbations (bottom) in the central $\lesssim 100$ kpc and outer $\gtrsim 100$ kpc regions. Confidence regions of the mean value as contours (85, 50, and 15 per cent of peak value). KS-test results on top. One-to-one correlation as dashed line.

Table 3.67: Average perturbations.

$< dP >^a$	$< dS >^a$	$< dn >^a$	$< dT >^a$
0.09 ± 0.06	0.16 ± 0.07	0.11 ± 0.05	0.09 ± 0.04

[a] Average fractional perturbations in thermodynamic properties of the 33 sample clusters. Standard deviation as confidence range.

The average metallicity of the clusters have been weighted by area and error in the same way as the average map temperatures in Sect. 3.2.3. A similar correlation can be found within the individual clusters (see maps in Sect. 3.2.4). By repeating the same slope analysis for the inner ($\lesssim 100$ kpc) and outer ($\gtrsim 100$ kpc) regions of the cluster I found that the average metallicity is higher in the central regions and the slope of the T-Z anti-correlation is steeper. Testing different weighting methods for the average temperature and metallicity I obtained consistent correlations with some scatter. Temperature is also correlated to the redshift of the clusters in this sample (more luminous and massive systems at higher redshift due to selection bias).

I investigated the redshift-metallicity (z-Z) relation and found the correlation with redshift to be tighter than with temperature (see Fig. 3.7). The best fit linear correlation of metallicity and redshift is $Z/Z_\odot = -(0.6 \pm 0.2)\ z + (0.36 \pm 0.04)$ (see Fig. 3.7). There was no evidence that the z-Z anti-correlation is steeper in the central regions. The average metallicity of the sample is $Z \approx 0.3 \pm 0.1\ Z_\odot$. The significance of a correlation was estimated using a re-sampling technique, performing a linear fit on random sub-samples of 17 clusters and using the mean value and 1σ width as best fit and error range of slope and normalisation.

3.4 Individual clusters

In addition to the sample properties the data contain important information on the properties of individual systems. The sample consists of clusters with a wide range of different structures from more relaxed systems like A 496 and A 2199 to disturbed clusters like the 1E 0657-56 and A 2146. I highlight some special cases below. Temperature maps, unsharp-masked images, and radial profiles of thermodynamic properties can be found in Sect. A.5, A.6, and A.7.

Abell 1795 has the deepest exposure in the sample and thus the most detailed spatial-spectral information on the ICM could be derived in this system. Oegerle & Hill (1994) found that its central cD galaxy has a peculiar radial velocity of 150 km s^{-1} within the cluster, while they measured the velocity dispersion of cluster members at $\sigma = 920$ km s^{-1}. According to Fabian et al. (2001) the simplest explanation for the visible soft X-ray filament would be a cooling-wake behind the cD galaxy (approximate position at the cross in

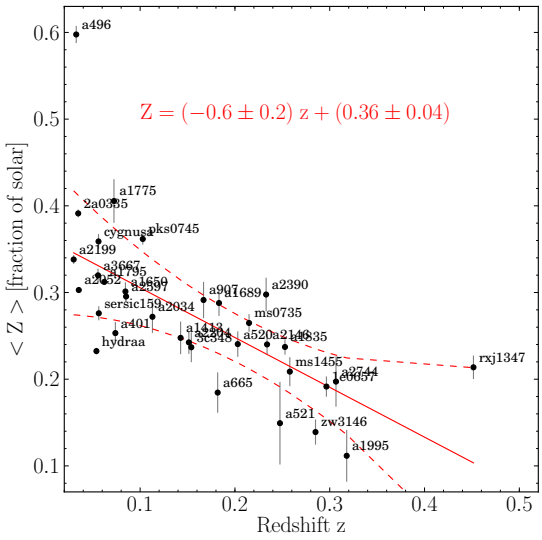

Figure 3.7: Comparison of the cluster redshift z and the area- and error-weighted average 2D map metallicity measured in the ICM (full radial range). The red line and equation show the best fit linear correlation. Dashed lines indicate the 1σ scatter around the best fit. Error bars are the statistical uncertainty of the weighted average.

Fig. 2.8, filament extending to the south), which is oscillating in the DM potential of the galaxy cluster. The centre is surrounded by linear surface-brightness features which might be remnants of past mergers with subhalos or created by the outburst of a strong AGN (see e.g. Markevitch et al. 2001; Ettori et al. 2002; Walker et al. 2014; Ehlert et al. 2015).

The deep unsharp-masked count images in this study show the central surface-brightness features at higher significance than previous studies (see Fig. A.2). The maps (Fig. 2.8) contain 1563 bins with a S/N count ratio of 50. The detailed radial profiles of the projected thermodynamic properties (Fig. 3.1) were the basis for the radial asymmetry measurements. Entropy perturbations seem to dominate throughout the cluster, suggesting that the 1D Mach number is comparable to the variance of entropy (see below, Sect. 3.5.2). The perturbation measurements are influenced by the presence of a cooler X-ray filament (inner ~ 40 kpc) and projection-effects (see Sect. 3.5.1). The central filament seems to increase the spread in density, temperature, and entropy, but pressure seems unaffected (see scatter in Fig. 3.1). The profiles follow the average trend of higher pressure perturbations in the outskirts (see Sect. 3.3.2). The findings confirm and improve the detection of many surface-brightness features at the centre of the cluster. The detailed analysis of thermodynamic perturbations support a model where isobaric processes dominate the central ICM.

1E 0657-56 (the Bullet Cluster) offers an almost edge-on view of two massive merging subclusters (Markevitch et al. 2002). It was possible to find a significant offset between

the total mass profile from weak-lensing and the X-ray emission of the hot ICM and thus make a very convincing case for the existence of DM (Markevitch et al. 2004; Clowe et al. 2004, 2006; Randall et al. 2008).

I found the strongest surface-brightness fluctuations around the prominent Mach cone from the impact of the smaller subcluster (see Fig. A.2). The density fluctuations in the cluster are among the highest in the observed sample (see Fig. 3.5). Pressure fluctuations around the "Bullet" are significantly weaker than at larger radii (see Fig. A.3). It should be noted that major merger shocks and AGN feedback are not modelled in the Gaspari et al. (2014) simulations and thus in those cases the direct connection between Mach number and fluctuations in thermodynamic parameters might change (see Sect. 3.5.1). 1E 0657-56 has the second highest $<$ T map $>$ in the sample (after RX J1347-114) and the lowest average metallicity (see Fig. 3.7). The Bullet Cluster has a particularly flat pressure profile with large scatter when compared to other clusters. In the most disturbed systems the pressure profile is flat and does not drop with radius.

Abell 2052 hosts an extended region of colder ICM at its centre caused by rising colder gas due to strong AGN feedback from the central cD galaxy. The radio source connected to the central AGN and its effect on the surrounding ICM have been studied in detail by Blanton et al. (2001, 2003, 2011). Feedback from the radio source pushes the X-ray emitting gas away from the centre and creates a sphere of enhanced pressure around the central region. Machado & Lima Neto (2015) investigated different merger scenarios in recent simulations of the cluster.

In the measurements the cluster emission shows a large scale ellipticity which could be an indicator of a past merger. The cluster has the lowest average temperature in the sample ($<$ T map $>\sim$ 2.3 keV, see Tab. 2.1) and one of the largest drops in entropy asymmetry from the centre to the outskirts (see Fig. 3.6). At about 20 kpc from the central AGN I detect an enhancement in projected pressure of more than a factor of two compared to the enclosed ICM (see Fig. A.3). On larger scales the cluster shows a spiral structure in surface brightness which is most likely caused by sloshing of gas due to a past merger (see Fig. A.2). In A 2052 all thermodynamic profiles are heavily influenced by the AGN feedback at the center. Only the strongest feedback cases in the sample show a deviation from a radially decreasing pressure profile.

Abell 2146 is a major merger viewed almost edge-on. Russell et al. (2010, 2011, 2012) detected two opposing shock fronts in the cluster and investigated transport processes in the ICM. They find the system to be less massive and thus colder than the Bullet Cluster merger (see also Fig. 3.8). Unlike in the Bullet Cluster, the secondary BCG in A 2146 seems to be slightly lagging behind the shockfront (Canning et al. 2012).

The cluster shows the highest entropy perturbations in the sample (see Fig. 3.4). Asymmetries are especially high around the cluster centre which I choose on the smaller merging subcluster (see the cross in Fig. A.1). Like in 1E 0657-56, pressure fluctuations around the merging subcluster are rather low but increase at larger radii (see Fig. 3.6). The difference in dP/dS between outer and inner radii is among the highest in the sample

(see Fig. 3.6). The extreme entropy perturbations in A 2146 indicate the highest average Mach number in the sample (see Sect. 3.5.2), almost twice as high as in the Bullet Cluster. If the two merging systems have similar impact velocities, the lower temperature of A 2146 could cause the Mach number of the turbulence induced by the merger to be twice as high as in the Bullet Cluster.

Cygnus A and Hydra A are two similar systems with strong AGN feedback. Both sources have strong radio jets emerging from the central AGN causing complex structures in the X-ray emitting ICM around the nucleus (see e.g. McNamara et al. 2000; Smith et al. 2002, for Hydra A and Cygnus A respectively). Nulsen et al. (2002, 2005) found AGN feedback to influence the ICM on large scales in Hydra A.

The unsharp-masked analysis of the surface-brightness images clearly shows the strong feedback structures around the central AGN (Fig. A.2). Average perturbations and temperature in Cygnus A are significantly higher than in Hydra A (see Figs. 3.4, 3.8). Cygnus A shows enhanced density and temperature at larger radii to the north-west (see Fig. A.1). Hydra A has a very asymmetric temperature distribution which is mainly caused by continuous radial structures of colder gas extending from the centre (see Fig. A.1). The average metallicity of Cygnus A is significantly higher than for Hydra A (see Fig. 3.7). The thermodynamic profiles of Cygnus A are more disturbed which would indicate a stronger or more recent AGN outburst.

Abell 2199 is a typical relaxed cluster with a cool core and AGN feedback structures at its centre (Markevitch et al. 1999; Johnstone et al. 2002). Nulsen et al. (2013) found various substructures in deep *Chandra* observations of the cluster, including evidence for a minor merger ~ 400 Myr ago. Sanders & Fabian (2006b) found a weak isothermal shock (~ 100kpc from the centre to the south-east) likely caused by the supersonic inflation of radio lobes by jets from the central AGN (3C 338).

The maps indicate a weak temperature jump in the area where the shock has been detected (see Fig. A.1) and show a large scale asymmetry in the temperature distribution between north and south (also visible in the scatter of the radial profile, see Fig. A.3). The surface brightness unsharp-masked image shows some of the structures at the centre and a weak indication of the surface brightness jump due to the shock to the south-east. The perturbations in entropy, pressure, temperature, and density are in the average regime of the sample as expected for an overall relaxed system (see Figs. 3.4, 3.5). The radial profiles show a prominent discontinuity around 50 kpc from the center, related AGN feedback. Just outside this jump there is a region where the fit uncertainties are larger due to overlapping chip gaps of many observations, which could bias the results (see faint spurious linear structures in Fig. A.1).

Abell 496 is a relaxed cluster with relatively high metallicity around the cool core and non-uniform temperature distribution on large scales (Tamura et al. 2001; Tanaka et al. 2006; Ghizzardi et al. 2014). By comparing dedicated simulations of the cluster to deep *Chandra* observations Roediger et al. (2012) concluded that the cluster was most likely

perturbed by a merging subcluster 0.6-0.8 Gyr ago.

The spiral surface brightness excess structure and the northern cold front is clearly visible in the new images of temperature and unsharp-masked count images (see Fig. A.1, A.2). The radial profiles and asymmetry measurements show relatively large spread in entropy (see Fig. A.3). Figs. 3.4 and 3.5 show that the cluster has a large average temperature spread (due to the large scale asymmetry caused by the sloshing of colder gas from the centre) and thus also larger spread in entropy. A 496 has a flat pressure profile similar to the strongest merging systems in the sample. The average metallicity is the highest I measured.

PKS 0745-191 is a relaxed cluster at large scales out to the virial radius (George et al. 2009). Sanders et al. (2014) found AGN feedback and sloshing structures in deep *Chandra* observations.

The AGN feedback features are most prominent in the unsharp-masked image (Fig. A.2) and indication of weak asymmetry in temperature on large scales can be seen in Fig. A.1. The radial profiles of the cluster follow the expected trend for relaxed systems but show remarkably low intrinsic scatter in pressure and relatively high scatter in entropy (see Fig. A.3). The scatter measurements of Sanders et al. (2014) are consistent with the method for dn, dT, dP, and dS in this study. This is the only cluster in the sample where n_H was set as a free parameter in the spectral fits, because the foreground column density of this system is knows to vary significantly.

3.5 Discussion

The perturbation measurements for this cluster sample constrain the average Mach number of the systems. The sample covers a wide range of dynamic ICM-states providing insight to the influence of different perturbation events.

3.5.1 Caveats of perturbation measurements

It has been shown by Sanders et al. (2014) that in the PKS0745-191 cluster projection effects in the measured parameters caused the calculated projected spread to be only about half of the real spread in the ICM. Therefore I expect projection effects to strongly affect the absolute values of the spread parameters. But since the effect seems to be similar on all parameters in the PKS0745-191 system the comparison of ratios between different spreads should not be affected. All asymmetry measurements are based on circular extraction regions, which means ellipticity of the cluster emission, as in PKS0745-191, will add to the spread values. Thus strong ellipticity could also influence the measured ratios between perturbations. Sanders et al. (2014) showed for PKS0745-191 that different bin sizes within a certain range lead to consistent results in the spread analysis. However if the bins are too large like for some more distant clusters in the sample, I generally obtain larger absolute spread-values (e.g. zw3146 in Fig. 3.4). Overall the comparison of spread measurements on maps with a S/N of 25 and 50 were in good agreement.

In real clusters there are many factors influencing perturbation measurements. The clusters that lie outside the relations expected from simulations seem to be dominated by processes that have not been included in the simulations (like mergers, AGN feedback bubbles, shocks, or uplifted cold gas). Also projection effects in the measurements and the overall geometry of a system could cause deviations. Note that the parameters dS and dP are not independent, since they are derived from the independent fit parameters T and η (see Sect. 2.4.3). Uncertainties in the spectral fits are larger at higher temperatures. The size of the error bars of individual measurements limit the sensitivity for finding additional spread in the MCMC calculations (see Sect. 3.2.1). In the case of Abell 1689 the absolute spread measurements are very low and I only obtain upper limits for this system, which is caused by very low fluctuations and high temperatures, lowering the sensitivity for detecting additional spread.

With the caveats described above the measurements allow for a rough estimate of the average Mach number and thus turbulence trends in the ICM for a large sample of massive clusters of galaxies. Future simulations will help to better quantify the influence of the above described caveats on the Mach number estimates.

3.5.2 Relating perturbations to turbulence

Recent high-resolution 3D hydrodynamic simulations by Gaspari et al. (2014) show that entropy and pressure drive the main perturbations in the ICM depending on the Mach number in the medium. In the low Mach number case ($\mathrm{Mach_{3D}} < 0.5$) perturbations are mainly isobaric, implying:

dP/P is negligible, $\mathrm{dS/S} \sim \mathrm{Mach_{1D}}$, and $\mathrm{dn/n} \sim \mid \mathrm{dT/T} \mid$

For large Mach numbers ($\mathrm{Mach_{3D}} > 0.5$) perturbations shift to the adiabatic regime (because turbulence becomes more violent, overcoming the cluster stratification), implying:

dS/S becomes negligible, $\mathrm{dP/P} \sim \mathrm{Mach_{1D}}$,
and $\mathrm{dn/n} \sim 1/(\gamma - 1)\ \mathrm{dT/T} \sim 1.5\ \mathrm{dT/T}$

The measurements of the average perturbations in the sample suggest a mixture of the two states (see Figs. 3.4 and 3.5). I observed that entropy perturbations are slightly dominating pressure fluctuations (Fig. 3.4) and density fluctuations are comparable to temperature fluctuations with a possible tendency of slightly dominating dn (Fig. 3.5). Enhanced temperature asymmetry can be caused by displaced cold gas from the central region due to strong feedback like e.g. in Cygnus A or strong cold fronts as observed in Abell 3667. Additional conduction in the ICM can weaken temperature perturbations (Gaspari et al. 2014).

Assuming entropy perturbations dominate in the sample would it follows that
$\mathrm{dS/S} \sim \mathrm{Mach_{1D}}$.

The dS/S value is related to the normalisation of the power spectrum, which is related

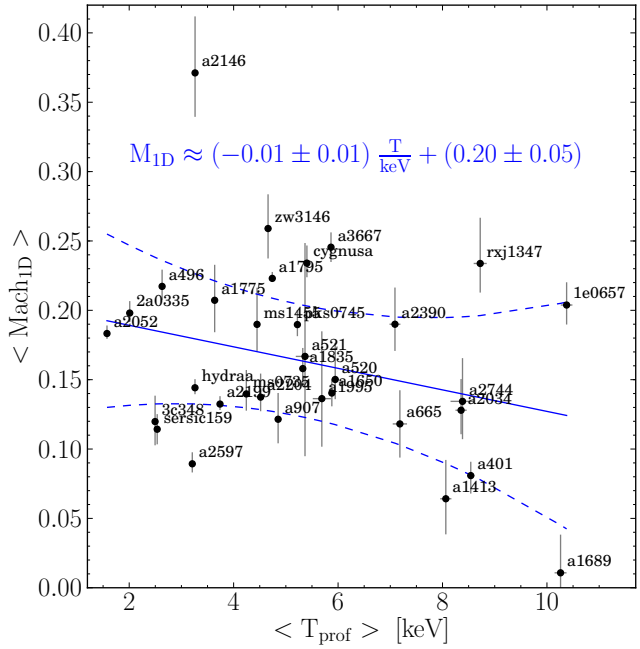

Figure 3.8: Relation between the average cluster temperature < T prof > and the fractional spread value of the dominating perturbation (dS or dP), which is proportional to the 1D Mach number. The solid and dashed lines represent the best linear correlation and its 1σ scatter. Error bars are the statistical uncertainty from the MCMC measurements.

to the peak of the power spectrum, that occurs at large physical radii (low wavenumber k), typically $\gtrsim 100$ kpc or $\gtrsim 0.1\ r_{500}$. As an approximation I used the overall average of perturbations (M=1, see Sect. 3.2.1) as turbulence indicator since the assumption that dS dominates does not hold in the outer regions $\gtrsim 100$ kpc of the clusters (see Sect. 3.3.2). The measurements on average suggest $\mathrm{Mach_{1D}} \approx 0.16 \pm 0.07$ (see Fig. 3.8).
Hydrodynamical simulations of galaxy clusters usually find the ratio between turbulence energy E_{turb} and the thermal energy E_{therm} to be $E_{turb} \approx 3 - 30\%\ E_{therm}$, from relaxed to unrelaxed clusters (Norman & Bryan 1999; Vazza et al. 2009; Lau et al. 2009; Vazza et al. 2011, 2012; Gaspari et al. 2012b; Miniati 2014; Schmidt et al. 2014). Since,

$$E_{turb} = 0.5\ \gamma\ (\gamma - 1)\ \mathrm{Mach_{3D}^2}\ E_{therm} \simeq 0.56\ \mathrm{Mach_{3D}^2}\ E_{therm} \tag{3.4}$$

where the adiabatic index $\gamma = C_P/C_V = 5/3$ (C_P, C_V heat capacity of the medium at constant pressure and volume respectively), it follows that $\mathrm{Mach_{3D}} \simeq 0.23 - 0.73$ and thereby,

$$\mathrm{Mach_{1D}} = \mathrm{Mach_{3D}}/\sqrt{3} \simeq 0.13 - 0.42 \tag{3.5}$$

which is consistent with the measured average of $\mathrm{Mach_{1D}} \approx 0.16 \pm 0.07$. This would

suggest that turbulence energy in this sample of clusters is on average about four per cent of the thermal energy in the systems. $E_{turb}/E_{therm} \approx 0.04$ is at the low end of expectations for relaxed low-redshift clusters in Vazza et al. (2011). Fig. 3.8 indicates a weak anti-correlation with average cluster temperature. In the best fit linear regression

$\mathrm{Mach_{1D}} \approx -(0.01 \pm 0.01) \ < \mathrm{T_{prof}} > /\mathrm{keV} + (0.20 \pm 0.05)$,

the slope is consistent with zero within the errors. The significance of the slope was estimated using the re-sampling technique of Sect. 3.3.3 by investigating the distribution of fit functions in 1000 fits to random sub-samples of half the size of the original. Note that the absolute values used as Mach number indicator are subject to some uncertainty like projection- and feedback-effects that have not been taken into account in the simulations I compare to (see Sect. 3.5.1).

Finoguenov et al. (2007) found that dispersion in pressure is systematically larger in groups than in clusters of galaxies, while entropy dispersion is similar. This would suggest higher Mach number and more turbulence in lower mass systems and would be in agreement with my findings. Extending this study to lower mass systems (to the left in Fig. 3.8) could provide further evidence for the trend that lower mass systems are on average more turbulent.

3.5.3 Difference between core and outskirts

If the enhanced pressure perturbations in the outer regions of the clusters in this sample can be confirmed this could be interpreted as a change in the thermodynamic state of the ICM from the center to the outer regions. With increasing pressure perturbations dP I expect more turbulent, pressure-wave driven, motions in the ICM.

This fits the expectation of less relaxed outer regions in clusters where the ICM is not yet virialised and still being accreted into the cluster potential (e.g. Lau et al. 2009). The change of the dP/dS ratio could also be due to the dependence of the ratio on the probed scales (e.g. Gaspari & Churazov 2013; Gaspari et al. 2014). In annuli at larger radii I probe larger scales of ICM fluctuations. A change in dP/dS with scale would also show a radial dependence in the sample.

3.5.4 ICM metallicity

The metallicity of the ICM and its local distribution are of great interest when studying the processes which are enriching the ICM with heavier nuclei. They are thought to be mainly produced by supernova explosions in the galaxies (mainly in the brightest clusters galaxy, BCG) within the clusters and then transported into the ICM (see e.g. Böhringer & Werner 2010; de Plaa et al. 2007).

The observed anti-correlation between average cluster temperature and metallicity (Fig. 3.7) could have many different causes. Sanders et al. (2004) found a similar relation between metallicity and temperature in the Perseus cluster. After testing for various systematic effects they found the correlation to be real but no definite explanation for the effect has

been found so far. Sloshing structures of colder gas have been found to coincide with higher metallicity (see e.g. Roediger et al. 2011), which could partially explain an anti-correlation.

The temperatures of the clusters in the sample are correlated to their redshift and the metallicity anti-correlates with redshift as well as temperature. Balestra et al. (2007) probed a sample of clusters in the redshift range $0.3 < z < 1.3$ and found significant evolution in metallicity between their higher and lower redshift clusters by more than a factor of two. This trend was confirmed by Maughan et al. (2008). Both studies also found a correlation between cluster temperature and metallicity. In a separate study using a Bayesian approach Andreon (2012) found a similar trend in metallicity evolution for a different cluster sample. However e.g. Baldi et al. (2012) found no significant evolution of abundance with redshift. It is not clear whether to expect any evolution within the narrow redshift range ($0.025 \leq z \leq 0.45$) I probed. This corresponds to a time span of $\Delta t \approx 4$ Gyr in the standard cosmology assumed in this study.

In individual clusters there is a general trend of lower metallicity at larger radii (see also De Grandi & Molendi 2001; Sanders et al. 2004; Leccardi & Molendi 2008) which means the average metallicity will be lower when I cover larger radial ranges for clusters at higher redshift. The metallicity drops from the centres ($Z_{\rm solar} \approx 0.4 - 0.8$) with typically lower temperature gas out to ~ 300 kpc where the profile flattens around 0.2 solar metallicity fraction. Uniform metallicity distribution at larger radii has been observed in great detail in the Perseus cluster (Werner et al. 2013).

The colder gas generally resides in the cluster centres, often in the vicinity of large cD galaxies, that might cause enhanced enrichment. More massive (higher temperature) systems will also have undergone more mergers and generally have stronger AGN feedback, which contributes to the dilution of metals in the X-ray halo (e.g. Gaspari et al. 2011) and affects the average area- and error-weighted metallicity calculated in this study. Also multiphasedness of the hot ICM along the line of sight could influence the correlation as I typically probe larger volumes for higher temperatures. Multiphase gas has been found to bias the ICM metallicity measurements from X-ray spectra in some clusters (e.g. Panagoulia et al. 2013). Unresolved 2D structure of the ICM could bias the measured metallicity to higher values for systems with intermediate temperatures (see Rasia et al. 2008; Simionescu et al. 2009; Gastaldello et al. 2010). This study reduced multiphase effects by resolving the spatial structure and measuring the average metallicity of many spatial-spectral bins.

Another factor of influence could be that star formation efficiency decreases with cluster mass and temperature (e.g. Böhringer & Werner 2010). There have been many studies in the infrared wavelength (e.g. Popesso et al. 2012, 2015) which show quenching of star formation in massive DM halos of galaxy clusters and groups. The sample predominantly consists of relatively massive systems (see Tab. 2.1) at low to intermediate redshifts and in different stages of evolution. Note that all metallicity measurements are based on a fixed solar abundance model (Anders & Grevesse 1989).

3.6 Summary and conclusions

In this chapter I presented a very large sample of detailed cluster maps with application to understand the thermodynamic processes in clusters of galaxies. The deep observations of the individual clusters helped to identify structures in the ICM caused by mergers or AGN feedback. By comparing to recent high-resolution simulations of perturbations in the ICM I constrained the average 1D Mach number regime in the sample to $\mathrm{Mach_{1D}} \approx 0.16 \pm 0.07$ with some caveats (see Sect. 5.5). Comparing to simulations this would suggest $\mathrm{E_{turb}} \approx 0.04\ \mathrm{E_{therm}}$ (see Sect. 3.5.2). By comparing perturbations in the central regions ($\lesssim 100$ kpc) and in the outer regions ($\gtrsim 100$ kpc) I found an indication for a change in the thermodynamic state from mainly isobaric to a more adiabatic regime.

In addition the sample shows a tight correlation between the average cluster metallicity, average temperature and redshift. The best fit linear correlation between metallicity and redshift is $\mathrm{Z/Z_\odot} = -(0.6 \pm 0.2)\ \mathrm{z} + (0.36 \pm 0.04)$ and between metallicity and temperature the best fit is $\mathrm{Z/Z_\odot} = -(1.0 \pm 0.7)\ \mathrm{T/100keV} + (0.34 \pm 0.06)$. The average metallicity of the sample is $\mathrm{Z} \approx 0.3 \pm 0.1\ \mathrm{Z_\odot}$.

Future X-ray missions like Astro-H (Kitayama et al. 2014) and Athena (Nandra et al. 2013) will help to further investigate turbulent velocities and chemical enrichment in the ICM. The eROSITA observatory (Merloni et al. 2012) will detect a large X-ray cluster sample for cosmological studies and the detailed cluster mapping can be used to make predictions on the scatter in scaling relations due to unresolved structures in temperature. To encourage further analysis based on this unique sample of cluster observations all maps and asymmetry measurements used in this study are made publicly available in electronic form.

Chapter 4

7.1 keV sterile neutrino limits

In this chapter I demonstrate how I obtained tight constraints on the scenario that 7.1 keV sterile neutrinos constitute all dark matter in the universe. This scenario has long been discussed as a likely explanation for the dark matter problem. However only recently after large X-ray telescopes had accumulated very deep observations of X-ray halos around clusters of galaxies and nearby dwarf galaxies it became possible to obtain tight constraints. In the general introduction to the thesis I discuss the previously obtained limits and possible first detections claimed in the literature. Constraints are obtained by estimating the limits on unexpected emission lines in the X-ray spectra of the hot gas in massive DM halos in addition to the current plasma emission models. The chapter is based on Hofmann et al. (2016a).

4.1 Introduction

Bulbul et al. (2014) and Boyarsky et al. (2014) recently found indications for a weak unidentified emission line (E $\sim$ 3.55 keV) in X-ray CCD spectra of the Andromeda galaxy and in deep cluster observations using *Chandra* and XMM-Newton data. There is an ongoing discussion on the existence and possible nature of the line with studies using other instruments like the *Suzaku* observatory (Urban et al. 2015) and looking at other objects like individual galaxies (e.g. Anderson et al. 2015). The line has been proposed as a candidate for a dark matter (DM) decay line and could be explained by decay of sterile neutrinos with a mass of $m_s = 7.1$ keV. In this model they decay into an X-ray photon with $E_\gamma = m_s/2$ and an active neutrino ν. Sterile neutrinos with masses in the keV range have long been discussed as a possible component of DM (e.g. Dodelson & Widrow 1994; Abazajian et al. 2001; Boyarsky et al. 2009), but up until recently only upper limits could be derived (e.g. from observations of the Andromeda galaxy or the Bullet Cluster by Boyarsky et al. 2008a,b).

In the case of sterile neutrino decay the measured additional flux at $\sim$ 3.55 keV would be related to two defining properties of the particles: The particle mass m_s and the mixing-angle $\sin^2(2\Theta)$, which describes interaction of the sterile neutrinos with its active neutrino

counter-parts and thus the likelihood of decay in the γ/ν channel. They are related through (as used by Bulbul et al. 2014)

$$\sin^2(2\Theta) = \frac{F_{DM}\ 10^{14}\ M_\odot}{\frac{12.76}{cm^2\ s}\ M_{DM}^{FOV}\ (1+z)} \left(\frac{D_L}{100\ Mpc}\right)^2 \left(\frac{1\ keV}{m_s}\right)^4 \quad (4.1)$$

where F_{DM} is the observed flux of the DM decay line, M_{DM}^{FOV} is the expected DM mass within the field of view (FOV) of the observation, D_L is the luminosity distance of the cluster, and z its redshift.

The paper is structured as follows: Sect. 2 describes the sample of clusters and the data reduction, Sect. 3 describes the fitting of individual cluster spectra, in Sect. 4 the procedure for fitting merged spectra is introduced, Sect. 5 explains how DM masses in the FOV were estimated, in Sect. 6 the upper limits for an additional 3.55 keV line emission are presented, in Sect. 7 the results are discussed comparing to other studies, and in Sect. 8 my findings are summarized.

For all the analysis I used a standard ΛCDM cosmology with $H_0 = 71$ km s^{-1} Mpc^{-1}, $\Omega_M = 0.27$ and $\Omega_\Lambda = 0.73$ and relative solar abundances as given by Anders & Grevesse (1989).

4.2 Observations and data reduction

I studied X-ray spectra of a sample of 33 clusters of galaxies. For a detailed description of the sample selection and data reduction see Hofmann et al. (2016b). They were selected as the most X-ray luminous clusters with more than 100 ks raw exposure with the *Chandra* Advanced CCD Imaging Spectrometer (ACIS, energy range about 0.1 to 10 keV, Garmire et al. 2003). The combined exposures of the sample are ∼ 5.7 Ms for ACIS-I and ∼ 2.3 Ms for the ACIS-S detectors. The redshift range of the sample is $0.025 < z < 0.45$ with a mass range of 1×10^{14} $M_\odot$ to 2×10^{15} $M_\odot$.

The instruments spectral resolution is $\sim 110 - 150$ eV which is broader than the energy difference to some neighbouring emission lines in the 3.55 keV region so their influence has to be carefully modelled (see discussion in Sect. 5.5). I obtained the observational data from the *Chandra* data archive and reprocessed them using the standard data processing. I added all available observations for each cluster to obtain the deepest images of the systems. On the reduced images a spatial-spectral extraction was performed by using the contour binning technique `contbin` (see Sanders 2006), which divides the cluster emission into smaller regions of equal signal-to-noise (here S/N = 50 or 25 depending on data quality). Based on the obtained maps of the cluster I added all spectra above a fixed surface brightness where the cluster emission is homogeneously covered by all observations and obtained deep X-ray spectra for each cluster (separately for ACIS-I/-S). For a detailed description of the data reduction see Hofmann et al. (2016b).

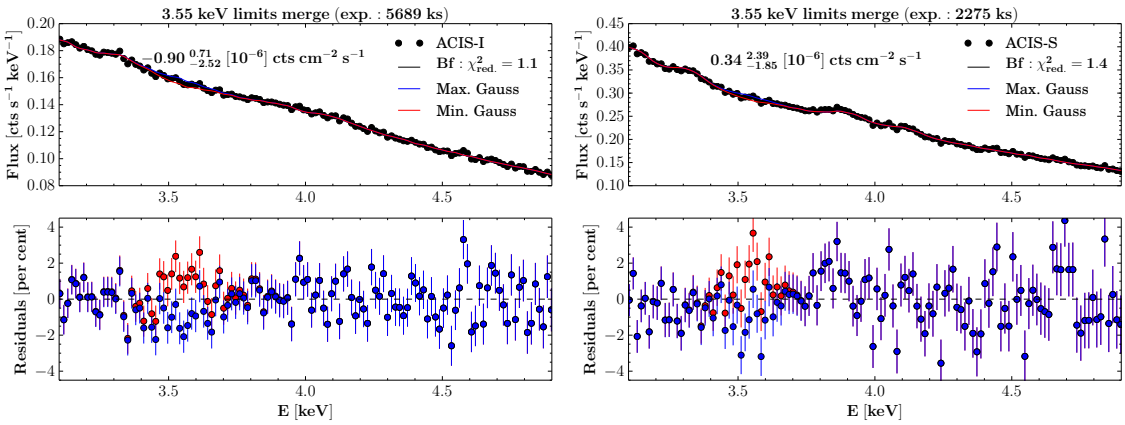

Figure 4.1: Merged X-ray spectra (ACIS-I top and ACIS-S bottom) of the cluster sample with residuals of different fitted models. Fitted XSPEC models: `apec+apec+zgauss` with best-fit (Bf), upper and lower confidence values (99.7 per cent) of the Gaussian flux in counts cm^{-2} s^{-1}. The annotations show the best-fit value and the confidence interval obtained using MCMC. Residuals are shown for the fit with upper (blue) and lower (red) confidence limit of the Gaussian flux.

4.3 Fitting individual spectra

For every cluster I added the source and background spectra of every spatial bin from the maps (see Sect. 4.2, only inner regions with high surface brightness and homogeneous coverage for both ACIS-I/-S). The background was renormalised to match the count rate in the 10.0-12.5 keV energy range. The response files were averaged and weighted by the number of counts in the spectrum (both auxiliary response files, ARF, and redistribution matrix files, RMF). For analysing the spectra I used `XSPEC` version 12.9.0 (Arnaud 1996a) and ATOMDB version 2.0.2 (Foster et al. 2012).

To estimate the upper limit of the flux allowed for an additional emission line, I searched for the best fitting `apec` model (with two temperature components) for collisionally-ionized plasma with absorption and an additional zero-width Gaussian line redshifted corresponding to the cluster distance (see Fig. B.3 for spectra of individual clusters). The normalisation of the Gaussian was allowed to be negative to avoid bias. All spectra were grouped to contain a minimum of 22 raw counts in each bin (using `grppha`) and I used the range from 2-5 keV for fitting the spectral model to the data (using χ^2 statistics). Free parameters of the fit were the normalisation of the spectral components, the temperatures, and the relative abundances of the `apec` models. If the two temperatures were separated by less than 30 per cent or if the normalisation of one component was less than one per cent of the second I discarded the second component and fit only a one-temperature `apec` model (see Tab. B.1). Once the best fit was identified, I calculated the confidence intervals (99.7 per cent) for the additional flux added by the Gaussian using a Monte Carlo Markov Chain (MCMC) method with length of 10000 and burn-in length of 1000.

As a robustness test I used a Bayesian fitting code (BXA; Buchner et al. 2014), implemented in the XSPEC package with flat priors for the same parameter ranges as my standard fitting method and obtained consistent results. A non-negative prior for the additional Gaussian flux did not improve the constraints. This analysis was used as an additional robustness test of the MCMC error estimates calculated using the standard XSPEC fitting code.

4.4 Fitting merged spectra

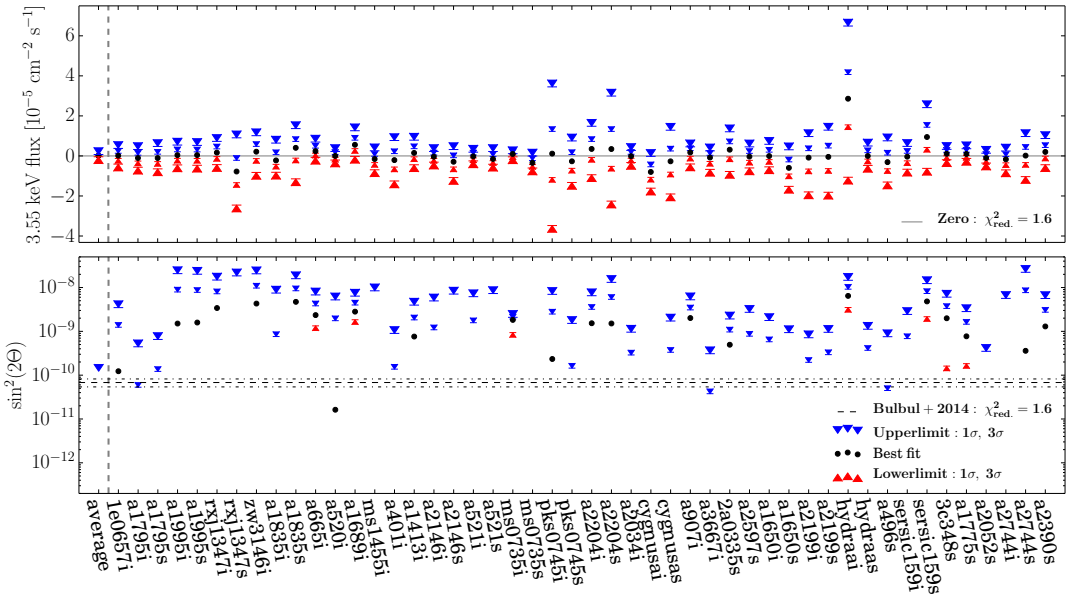

Figure 4.2: Top: limits on an additional Gaussian flux component at 3.55 keV for all clusters in the sample. Bottom: limits on the mixing-angle in case of a 7.1 keV sterile neutrino. The limits are separately calculated for ACIS-S and ACIS-I, which is indicated by -s or -i following the cluster identification on the x-axis. Most lower limits and some best fit values lie outside the plotted range. The dashed line shows the Bulbul et al. (2014) detection in their full XMM-Newton MOS sample. Limits show the 1σ (small symbols) and 3σ (big symbols) confidence range.

To obtain deeper limits on the line I added all cluster spectra in the sample. I de-redshifted all spectra by re-binning the counts to the channel-grid of the new spectra after randomising each count position within the channel width. The ARFs were de-redshifted by calculating the new energy values of the spectral channels and then mapping back to the original channel-grid by interpolating the shifted response. For the RMF I treated the integer value of the response matrix in each pixel (2D detector response matrix for

channel to energy mapping) as a number of counts and applied the same de-redshifting procedure with randomisation as to the spectra. To approximate the new response files better I repeated the process 100 times and calculated the average. Residual noise from the re-mapping (caused by the discrete energy grid) was reduced by smoothing the responses with a Gaussian filter ($\sigma = 1$ pixel). The width of the energy bins is ~ 0.01 keV for both detectors (see response in Fig. B.2). The de-redshifting was based on optical redshifts known from previous catalogues (see Tab.B.2). I added all de-redshifted, unabsorbed spectra and averaged the response files with weights according to the fraction of the total counts of the merged spectrum (in the 2-5 keV range). The average exposure times of each observation were added to obtain an average count rate in the final spectra. The background spectrum was renormalised to match the 10.0-12.5 keV energy range count rate. I used the XSPEC models `apec+apec+zgauss` without absorption and z=0 to fit the spectra and estimate the additional flux allowed for a line at 3.55 keV. The fit of the merged spectra was performed between 3-5 keV because there is no strong variation in the detector response in that region and thus possible systematics in the calculated average response are minimal. Fig. 4.1 shows some residual structures due to the modelling of a complex stack of cluster spectra with a two-temperature `apec` model. I tried fitting the emission features in the spectrum with separate Gaussian lines on top of an `apec` model without lines (compare e.g. Bulbul et al. 2014). This procedure provided a good fit (when allowing slight variation of the line energies) but did not improve the overall fit significantly. I used simulations to verify the line-detection efficiency of the stacking and modelling method (see Appendix B.2).

4.5 Estimating cluster masses

To constrain the expected strength of the DM emission line in the cluster spectra I need to estimate the DM mass in the FOV. With the measured average temperatures of the clusters I used temperature-mass scaling relations from Vikhlinin et al. (2009a) to estimate the overall cluster mass M_{500} and the related overdensity radius r_{500} (see Hofmann et al. 2016b, for details).

I assumed the cluster density follows an NFW profile (Navarro et al. 1997) and used a fixed concentration (C=4), as the expected average value of the sample (compare e.g. Vikhlinin et al. 2006). By integrating $\rho(r)$ along the line of sight I obtained the DM mass surface density profiles (see e.g. Wright & Brainerd 2000; Urban et al. 2015). I estimated the DM mass in the FOV of an observation by adding up the surface densities within the footprint of the extraction region for the spectra. The footprints of each observation and the maximum covered radius have been published by Hofmann et al. (2016b).

For A 1795 I obtained an M_{DM}^{FOV} of 1.6×10^{14} $M_\odot$ (2.75×10^{14} $M_\odot$ for M_{2500} given by Vikhlinin et al. 2006). I estimate the systematic uncertainties of M_{DM}^{FOV} to be 35 per cent on average due to scatter in the scaling relations for the total mass and scatter around the average concentration. The scatter will average out when adding together properties of the whole sample which means that I expect much smaller systematic uncertainties in

the average M_{DM}^{FOV} used for limits on the merged cluster spectra (see Tab. B.2).

4.6 Upper limits on 3.55 keV line

I investigated the possible existence of an unidentified X-ray emission line at ~ 3.55 keV in the cluster spectra. I put limits on the existence of such a line in all the clusters individually and in a merged spectrum of the whole sample. A possible interpretation for this line has been the emission from decaying sterile neutrinos with a mass of ~ 7.1 keV which could be a candidate for DM.

4.6.1 Limits in individual spectra

Fig. 4.2 shows the upper limits on the flux derived from observations of A 1795 (deepest observation in the sample), where I obtained a 3σ upper limit of 3.22×10^{-6} cm^{-2} s^{-1} from merged ACIS-I observations (~ 613 ks) and 4.73×10^{-6} cm^{-2} s^{-1} from ACIS-S (~ 241 ks).

Using equation (4.1) this translates to one of the deepest upper limits on the mixing-angle for individual clusters $\sin^2(2\Theta) \leq 4.4 \times 10^{-10}$ (ACIS-I data). The limits on the additional flux that I could derive in the individual systems depend on the exposure time and on how well the cluster emission is modelled by a two component collisionally-ionised plasma model. For a detailed list of constraints see Tab. B.3.

4.6.2 Limits in merged spectra

The fits to the merged data provide deeper upper limits on the flux by about a factor of three for ACIS-I compared to the individual spectra (see Fig. 4.1 and Tab. 4.1). To turn this flux into a limit on the expected mixing-angle in the 7.1 keV sterile neutrino scenario I estimated the average mass and luminosity distance of the cluster sample. I weighted the contributions to the average with their expected contribution $\omega_{i,DM}$ to the DM line flux with the formula used by Bulbul et al. (2014),

$$\omega_{i,DM} = \frac{M_{i,DM}(1+z_i)}{4\pi\ D_{i,L}^2} \times \frac{exp_i}{exp_{tot}} \tag{4.2}$$

where i denotes the properties of the ith cluster and exp_i/exp_{tot} is the fraction of the total exposure for the ith cluster. This is done for ACIS-I and ACIS-S separately (see weights in Tab. B.2).

The most stringent limit on the mixing-angle from this analysis is $\sin^2(2\Theta) \lesssim 10 \times 10^{-11}$ (99.7 per cent confidence) for the merged ACIS-I spectra of the sample. All 3σ (99.7 per cent) upper limits are compatible with the value of $\sin^2(2\Theta) \sim 7 \times 10^{-11}$ found for the full sample of Bulbul et al. (2014). A simultaneous fit of the merged ACIS-I and ACIS-S spectrum did not improve the limits.

4.7 Multi-temperature residuals in ACIS-S

When we fit the merged spectrum of the cluster sample for the ACIS-S detectors (Fig. 4.1) there were two significant residuals ($> 1\sigma$). In the simulated merged spectra such strong residuals are not found (Fig. B.2). We simulated each cluster with a two-temperature plasma X-ray emission model (`XSPEC apec`) and then modelled the merged spectrum with two temperatures (actually the average of 2×33 temperatures). The reasons for stronger residuals in the real observations of ACIS-S could be that multi-temperature effects are stronger or that there are additional components not modelled by the current plasma emission model. As discussed in the paper there are two significant line-like residuals in ACIS-S at ~ 3.85 keV and ~ 4.7 keV. The ~ 3.85 keV residual could be explained by stronger than expected Ca XIX emission lines (several lines known between $\sim 3.86 - 3.90$ keV). The ~ 4.7 keV line could be due to Ti XXI (see Sect. 5.5).

To test whether the two temperature fit is sufficient to obtain reliable 3.55 keV line limits from the merged observations we modelled the two lines with additional Gaussian lines. The line-width was set to zero and the energy set to the two values estimated above. The goodness of fit improved from $\chi^2_{\text{red.}} = 1.4$ to 1.3 and the residual features seen in the original fit disappear (see Fig.4.3). Both lines are detected at $> 1\sigma$.

The obtained limits on the 3.55 keV flux however are very well consistent with the original fit showing that the additional residuals are negligible for our estimates.

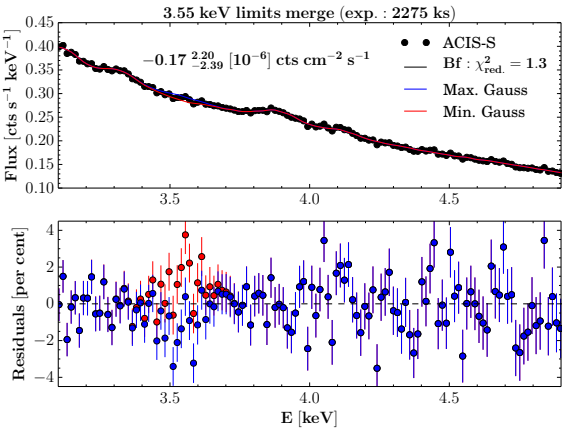

Figure 4.3: Merged X-ray spectrum (ACIS-S) of the cluster sample with residuals of different fitted models. Fitted `XSPEC` models: `apec+apec+zgauss(3.55 keV) +zgauss(3.85 keV) +zgauss(4.7 keV)` with best-fit (Bf), upper and lower confidence values (99.7 per cent) of the Gaussian flux at 3.55 keV in counts cm^{-2} s^{-1}. The annotations show the best-fit value and the confidence interval obtained using MCMC. Residuals are shown for the fit with upper (blue) and lower (red) confidence limit of the 3.55 keV Gaussian flux. For the effective-area curve see Fig. B.2.

4.8 Discussion

Table 4.1: Limits from merged spectra.

Merged Spec.	F_X $[10^{-6}$ cm^{-2} s$^{-1}]^a$	$\sin^2(2\Theta)$ $[10^{-11}]^b$	$< n_H >$ $[10^{22}$ cm$^{-2}]^c$	$< z >$	$< M_{DM}^{FOV} >$ $[10^{14}$ M$_\odot]^c$	$< M_{DM}^{FOV}/D^2 >$ $[10^{10}$ M$_\odot$ Mpc$^{-2}]$
mergei	$-0.9^{+1.6}_{-1.6}$	$-12.7^{+22.8}_{-22.9}$	0.06	0.11	2.08	0.197
merges	$0.3^{+2.1}_{-2.2}$	$5.7^{+34.6}_{-37.0}$	0.10	0.07	1.26	0.172

[a] Best fit and 3σ confidence range of a possible additional flux added by a Gaussian line at 3.55 keV.
[b] Mixing-angle limits (3σ confidence) for the 7.1 keV sterile neutrino decay scenario (negative mixing-angle unphysical, results from allowing negative flux).
[c] Average properties of the cluster sample weighting contributions as described in equation (4.2) in Sect. 4.6.2.

I did not find evidence for an unidentified emission line at 3.55 keV (see Fig. 4.2). The average value of the Gaussian flux measured in the cluster sample is consistent with zero with some scatter ($\chi^2_{\rm red.} = 1.6$), suggesting mild additional systematic uncertainties (~ 25 per cent). This is a conservative estimate because the high $\chi^2_{\rm red.}$ value is mainly driven by outliers like Hydra A. The average of the calculated mixing-angle is much lower than the value of Bulbul et al. (2014), but is consistent within the 3σ upper limit (see Fig. 4.2). The highest 3σ upper limit and best fit is obtained for the spectrum of a ~ 20 ks ACIS-I observation of Hydra A. The width of the fit line in this case is unusually broad and the line is not detected in a ~ 200 ks observation of the same cluster with ACIS-S (see Fig. 4.2 for derived limits on mixing-angle).

A difference to the Bulbul et al. (2014) analysis is that I used only core regions of the clusters where the gas emission causes a higher background for detection of any DM line emission and I might thus be less sensitive. Using *Chandra* ACIS I could not extend the analysis to larger radii due to the limited FOV. Another difference in the analysis is that I did not use a separately weighted response for the Gaussian DM line for modelling the merged data.

Urban et al. (2015) used deep data taken with the *Suzaku* observatory and found some evidence for the predicted emission line in spectra of the Perseus cluster. However their study of the Coma, Virgo, and Ophiuchus clusters disfavour the DM nature of the line. Anderson et al. (2015) excluded the existence of the DM decay line in the merged spectra of nearby galaxy halos, where the ratio of DM to baryonic, X-ray emitting matter, is expected to be higher (see also Malyshev et al. 2014).

The Draco dwarf spheroidal galaxy was targeted by very deep observations with the *XMM-Newton* satellite. Depending on the modelling these observations are in tension with the dark matter interpretation of the line with $\sim 2\sigma$ (see Jeltema & Profumo 2016). In the same dataset Ruchayskiy et al. (2016) found a weak detection of the line which is slightly fainter than expected in the scenario that the sterile neutrinos with 7.1 keV make up all DM in the halo. Jeltema & Profumo (2015) found evidence of a line around 3.5 keV in *XMM-Newton* data of the Galactic centre. Other detections of the additional line include measurements of the Galactic center X-ray emission (Boyarsky et al. 2015). The recent *XMM-Newton* flux measurements for an additional line in the 3.5 keV regime in a sample

of clusters of galaxies by Iakubovskyi et al. (2015) is in weak tension with the limits (e.g. $\sim 2\sigma$ for Abell 2199). Riemer-Sørensen et al. (2015) used deep observations of the Bullet cluster with the NuSTAR satellite to constrain possible decay lines up to higher energies but due to lower sensitivity at 3.5 keV do not exclude previous detections.

Franse et al. (2016) recently put tight constraints on the line in the outskirts (out to r_{200}) of the Perseus cluster using the *Suzaku* observatory.

Berg et al. (2016) recently claimed detection of a absorption line around 3.5 keV in the spectrum of NGC 1275 which is the central AGN of the Perseus cluster. They claimed this could be explained by absorption of photons in the DM halo of Perseus by Axion-like DM particles with an excited state at about 3.5 keV.

The main caveat of the mixing-angle calculations is the uncertainty of the DM masses in the FOV which are derived from scaling relations with the temperature of the hot ICM. The main caveats of the flux constraints are possible uncertainties in the calibration of the effective area and detector response and in the assumed background spectrum (derived from *Chandra* blank sky observations). Alternative explanations for the potential line could be unexpectedly strong plasma emission lines or charge exchange processes around 3.55 keV (see discussion by Bulbul et al. 2014; Gu et al. 2015). Candidate plasma lines are K XVIII (3.476, 3.496 and 3.515 keV), Cl XVII (3.510 and 3.509 keV) as well as Ar XVII (3.617 and 3.618 keV) [1].

The merged spectra in Fig. 4.1 show an additional weak ($\gtrsim 1\sigma$) residual around 4.7 keV (mainly in ACIS-S) which is not visible in the simulations (see Fig. B.2). This could be explained by an unexpectedly high abundance (higher than assumed in `apec` metallicity model) of Titanium (Ti XXI, multiple lines between 4.70-4.76 keV). The residual at 4.7 keV disappears for 1-3 times solar abundance but in this case the line of Ti XXII at about 4.9 keV is not observed at the expected strength.

Fig. 4.4 shows a comparison of this work to previous measurements (see also discussion above). The results show conservative limits from the *Chandra* ACIS-S and ACIS-I analysis and the offset shows possible systematics between instruments. The average value of all individual limits is closer to the ACIS-I measurement since the sample has higher exposure in ACIS-I and more clusters have ACIS-I observations. Most detections are consistent with my 95 per cent confidence regions. Reasons for the more conservative limits can be the smaller FOV of *Chandra*, the lower combined exposure compared to some sample studies, the smaller effective area of *Chandra* compared to *XMM-Newton*, and a more conservative modelling approach.

[1] http://atomdb.org

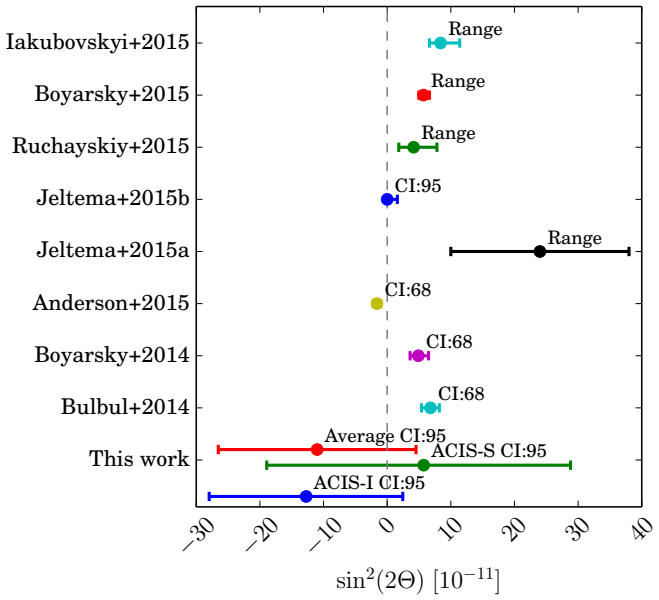

Figure 4.4: Comparison of this works constraints to selected literature values. The best fit line energy varies between $\sim 3.4 - 3.6$ keV. This work: 95% confidence interval (CI) for *Chandra* ACIS-I (bottom) and ACIS-S (middle) stacked spectra and for the error-weighted average of all individual limits (top). Bulbul et al. (2014): 68% CI for the full cluster sample using the *XMM-Newton* MOS detectors. Boyarsky et al. (2014): 68% CI (statistical only) for the M 31 *XMM-Newton* data. Anderson et al. (2015): 68% CI for negative residual in stacked *XMM-Newton* data of galaxy halos. Jeltema+2015a (see Jeltema & Profumo 2015): range of values obtained for different mass models of the Galactic center with *XMM-Newton* observations. Jeltema+2015b (see Jeltema & Profumo 2016): 95% CI upper limit from a deep observation of the Draco dwarf galaxy with *XMM-Newton*. Ruchayskiy+2015 (see Ruchayskiy et al. 2016): range of values obtained for different mass models of the Draco dwarf galaxy with the *XMM-Newton* PN instrument. Boyarsky et al. (2015): best fit range for observations of the Galactic center with the *XMM-Newton* MOS instrument. Iakubovskyi et al. (2015): range of best fit values for a sample of galaxy clusters observed with *XMM-Newton*. Negative mixing-angles are unphysical but result from equation (1) when allowing negative flux. The plot only shows selected constraints from the listed publications.

4.9 Conclusions

This study presents a large sample of deep cluster spectra with limits on the previously detected emission at 3.55 keV assuming the line originated from the decay of sterile neutrino DM ($m_s = 7.1$ keV). I extend the number of objects previously searched for the line and provide further insight to whether the line only occurs in special observations or objects. This is the first study using a large sample of *Chandra*-observed clusters to constrain the 3.55 keV line. The driving cluster property behind the depth of the upper limit on the mixing-angle in the sterile neutrino scenario is the DM mass in the FOV where the spectra have been extracted divided by the luminosity distance squared. To maximize this property, homogeneous, deep coverage out to large radii of a massive nearby system is needed (higher [10^{10} $M_\odot$ Mpc^{-2}] value in Tab. B.2). In this sample the best candidate for such a study with *Chandra* was Abell 1795 because of its very deep exposure (see Tab. B.2).

As demonstrated by Bulbul et al. (2014) a 1 Ms observation of the Perseus cluster with the *Hitomi (Astro-H)* SXS instrument (Kitayama et al. 2014) will allow to distinguish between a plasma emission line of the ICM, broadened by the turbulence in the cluster ($\sim$ 300 km/s) and a DM decay line, broadened by the virial velocity ($\sim$ 1300 km/s) of the DM halo. Hitomi Collaboration et al. (2016b) recently published the results from the only observation of the Hitomi satellite before its critical failure. They obtained a spectrum of the ICM based on a 230 ks observation and excluded the previously detected emission line at 3.5 keV at $\gtrsim 3\sigma$ (in case of a broad emission line from DM with $\sim$ 1300 km/s velocity dispersion).

The large FOV of the *eROSITA* observatory (Merloni et al. 2012) will allow for tight constraints on the line (see also Zandanel et al. 2015), homogeneously covering nearby X-ray bright clusters to large radii, even with lower effective area at 3.55 keV compared to XMM-Newton and *Chandra*. Only deeper observations with current or future instruments will allow to finally decide the nature of the detection as summarised in a recent white paper on keV sterile neutrinos (Adhikari et al. 2016).

eROSITA will have the capability to provide competitive upper limits on possible dark matter lines in the X-ray range and its all-sky survey will cover a large sample of objects and will for the first time provide a complete view of the Galaxy in the X-ray range above 2 keV. This will allow to put tight constraints on a possible 3.55 keV emission from DM in the Galaxy and especially around the Galactic center.

Chapter 5

Simulations and forecast for eROSITA cluster cosmology

This chapter first introduces a process I used to create simulated observations of clusters of galaxies in the eROSITA survey. Those simulations of well studied cluster models were then used to test for possible bias expected in the eROSITA survey. The bias I found for the cluster temperature and flux in this chapter was used by N. Clerc to estimate the impact on cluster mass-functions and cosmological parameters from the eROSITA survey (see end of this chapter). The findings will be published in Hofmann et al., in preparation.

5.1 Introduction

Clusters of galaxies reveal the large-scale structure of the universe and allow the observation of astrophysical processes on large scales. They are the largest gravitationally bound structures observable in the universe and one of the most sensitive methods for detecting them is by the X-ray radiation of their intra-cluster-medium (ICM). The importance of cluster observations for cosmological studies has been proven by the first imaging X-ray all-sky survey with the ROSAT satellite (Truemper 1982). This survey delivered the spatial distribution of a large number of clusters across the sky (e.g. Böhringer et al. 2004, 2000). Before the start of the ROSAT mission, there have been detailed simulations of cluster observations (Cruddace et al. 1991) in order to estimate the total number of expected cluster detections during the survey and to prepare for the data analysis once the real data was available.

Since the end of the ROSAT mission, many of the clusters originally detected with ROSAT have been observed deeper and at higher spectral and spatial resolution with the new large X-ray observatories *Chandra* and *XMM-Newton*. However those telescopes only observe individual clusters and do not provide a large all-sky sample.

The second imaging all-sky X-ray survey mission, the extended Roentgen Survey with an Imaging Telescope Array (eROSITA) on the Spectrum-Röntgen-Gamma (SRG) satellite (Merloni et al. 2012; Predehl et al. 2010) will perform a $\sim$ 15 times deeper survey in

the 0.5-2.0 keV ROSAT X-ray band and the first truly imaging survey for energies from 2-10 keV. The main science goal of the mission is the detection of the largest sample of galaxy clusters ($\sim 10^5$) out to a red-shift of $z \gtrsim 1$. This sample will deliver strong constraints on cosmological models and their parameters, especially dark energy. Therefore it is very important to understand the characteristics of the clusters which will be detected with eROSITA. First simulations of clusters in the eROSITA survey were made to derive estimates on the number of clusters and the general reliability of cluster temperatures (e.g. Pillepich et al. 2012; Borm et al. 2014). These estimates are based on theoretical predictions and isothermal cluster simulations without accounting for temperature substructures in the ICM.

In this study I simulate eROSITA observations of a sample of clusters, which have been well studied with the high resolution instrument *Chandra* ACIS. Hofmann et al. (2016b) analysed deep *Chandra* observations and derived emission models for 33 clusters (see also Chapter 3). I used these cluster models to simulate eROSITA observations and to identify bias due to unresolved substructures in the eROSITA survey caused by the lower spatial resolution of the eROSITA instrument compared to *Chandra* and shorter average exposure.

For all the analysis I used a standard ΛCDM cosmology with $H_0 = 71$ km s^{-1} Mpc^{-1}, $\Omega_M = 0.27$ and $\Omega_\Lambda = 0.73$ and relative solar abundances as given by Anders & Grevesse (1989) (same assumptions as throughout my study).

The calibration files and characteristics of the eROSITA instrument are currently only available within the German eROSITA consortium and can thus not be released along with this thesis. They will be made publicly available together with the first public data release of the mission.

5.2 Simulating eROSITA cluster observations

I made simulations of eROSITA observations for the 33 clusters of galaxies analysed in Chapter 3. This allowed me to study how the eROSITA spectra and images of known clusters will be affected by the characteristics of the eROSITA instrument.

5.2.1 Cluster sample

I created simulated eROSITA observations for a well defined and analysed sample of *Chandra*-observed clusters of galaxies (see sample by Hofmann et al. 2016b). The clusters in the sample have halo masses ranging from 1×10^{14} $M_\odot$ to 2×10^{15} $M_\odot$ (within the overdensity radius r_{500}). At r_{500} the average density of the cluster is 500 times the critical density of the universe at the cluster redshift. The luminosity range is $(2 - 63)$x10^{44} erg/s (0.1-2.4 keV X-ray luminosity), and the redshift ranges from 0.025 to 0.45.

For the simulation of eROSITA observations I used the Simulator for X-ray telescopes (SIXTE[1], Schmid et al. 2010, version of July 1, 2014), which can produce X-ray event lists

[1] http://www.sternwarte.uni-erlangen.de/~schmid/simulation.php

for various X-ray telescopes, given an input source list in the SIMPUT format[2] and a set of telescope specific parameters. I used a setup of the simulation software emulating the properties of the eROSITA Telescope.

eROSITA is a X-ray survey instrument on board the Russian/German Spektrum Roentgen Gamma mission (SRG). The instrument consists of seven X-ray telescopes with separate detector arrays. In the survey the average expected half energy with (HEW) of a point source is ~ 28 arcsec at 1 keV, the energy range is about 0.3-10 keV, and the spectral resolution is 138 eV at 6 keV. The main survey will last four years with an average exposure time of 2 ks and an effective area of about 1400 cm^2 for 1 keV photon energies.

5.2.2 Event file simulations using SIXTE

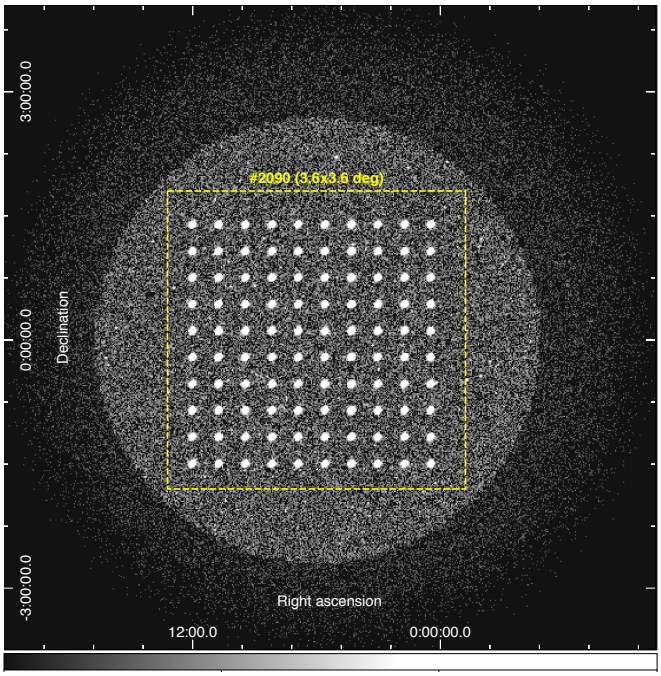

Figure 5.1: Overview of one cluster simulation of field #2090. The image shows the eROSITA CCD1 of the Bullet cluster simulation at redshift 0.2. The yellow region marks the eROSITA field #2090. The event file has been binned by a factor of 1024 for this image. The circular emission beyond the field are different background components.

I used spectral maps, which were derived for a sample of clusters by Hofmann et al. (2016b) as input for the simulated eROSITA observations. These maps contain the best

[2]http://hea-www.harvard.edu/heasarc/fitsformats-heasarc.html

fit collisionally-ionized plasma emission model for many spatial bins of each cluster, and deliver accurate 2D cluster models.

From these 2D models I derived a SIMPUT source list containing images, best-fit spectra and X-ray flux for each region of a given cluster. For the telescope pointing of the simulations I used an attitude file, which was created from simulations of a 4 year survey with rotation axis of the satellite pointing toward the sun (simulations by Jan Robrade, Hamburger Sternwarte). Using the list and the attitude of the satellite as input I ran the `erosim` tool, which is part of the SIXTE software distribution and simulates eROSTIA event lists. From these event lists images can be created using other subroutines of SIXTE, mapping the detector coordinates to sky coordinates by using the telescope pointing information (attitude file). Aside from the model of the ICM, I also had to account for other contributions to the observations in a typical eROSITA field (for a more detailed description of the simulator see Clerc et al., in prep.).

The `erosim` program can create a simulated detector background, which is based on `Geant4` simulations by Tenzer et al. (2010). Those simulations accurately account for the physical structure of the eROSITA instrument and the estimated radiation levels at the second Lagrange point L2 of the earth-sun system (based on the CREME96 model, by Tylka et al. 1997), around which eROSITA will be in orbit. Other background components in the cluster observations are based on simulated observations of eROSITA fields without clusters (*Synthetic Simulations* by Nicolas Clerc, MPE). For the cluster simulations the exact same simulations setup as for the *Synthetic Simulations* was used to allow merging the separately simulated clusters with the expected background (see Clerc et al., in preparation). Another background component is the diffuse X-ray emission of the Galaxy, which consists mainly of unresolved Galactic X-ray sources and diffuse emission of the inter-stellar-medium (ISM) (see e.g. Lumb et al. 2002). I simulated this background component, by assuming a mean spectrum and flux distributed uniformly across the observation (spectral model by Thomas Boller, MPE). I also included emission from active galactic nuclei (AGN) in the simulations, since they contribute a major fraction of the X-ray radiation in the simulated fields (see e.g. Gilli et al. 2007; Hasinger et al. 2005). The AGN contribution is divided into resolved and unresolved sources using the Hasinger et al. (2005) luminosity function. Whether a source is resolved or not depends on the telescope resolution and the exposure time of the observed field. The resolved sources are simulated as point sources with typical flux and spectral distribution, measured for the overall AGN population. The unresolved part is simulated using a summed spectrum and flux uniformly covering the simulated field (same procedure as for Galactic background).

The calibration files and instrument properties assumed for eROSITA in my SIXTE simulations are estimated properties for the eROSITA performance as of December 2014. The response files were based on the calibration of the XMM-Newton EPIC PN detector (created by Frank Haberl, MPE) which is very similar to the newly developed eROSITA detectors. The focal length and other telescope specifications did not change since then. The PSF was estimated from ray-tracing simulations of the instrument setup and are very similar to the finally measured PSF at the *PANTER* facility of MPE.

For the analysis the eROSITA sky will be divided into 3.6×3.6 deg^2 fields (specifica-

tions done by Hermann Brunner and Konrad Dennerl, MPE). For this study I simulated the cluster models in field #2090 which lies in the equatorial region of the all-sky scan and has an average exposure of ~ 2 ks. I chose this field to obtain a representative average depth of the cluster observations. The largest part of the final 4-yr survey will have a similar exposure time. To improve the confidence regions on derived parameters for individual clusters I simulated the identical model 100 times per field in a grid of 10x10 making sure there is no overlap between the emission (see Fig. 5.1).

In addition I simulated each cluster at five different redshifts. To change the redshift of a cluster model I adjusted the spectral shape in XSPEC and changed the normalisation of the spectrum keeping the same Galactic foreground absorption as measured in the original *Chandra* observation. The flux of a spectrum was calculated according to the change in luminosity distance in the standard cosmology. To maintain the original physical size of the object the source images for each bin were scaled in size according to the change in plate scale at the new redshift. In the covered redshift range higher redshift means the clusters appear smaller on the sky. Each cluster was simulated at redshift 0.1, 0.2, 0.4, 0.8, and 1.6 (see e.g. Bullet cluster in Fig. 5.2). Overall I created 16500 (500 for each cluster) simulated observations of the clusters in the sample. Note that due to the limited field-of-view (FOV) of *Chandra* ACIS the cluster models only cover a limited radius (e.g. real redshift of Bullet cluster ~ 0.3, compare Fig. 5.2).

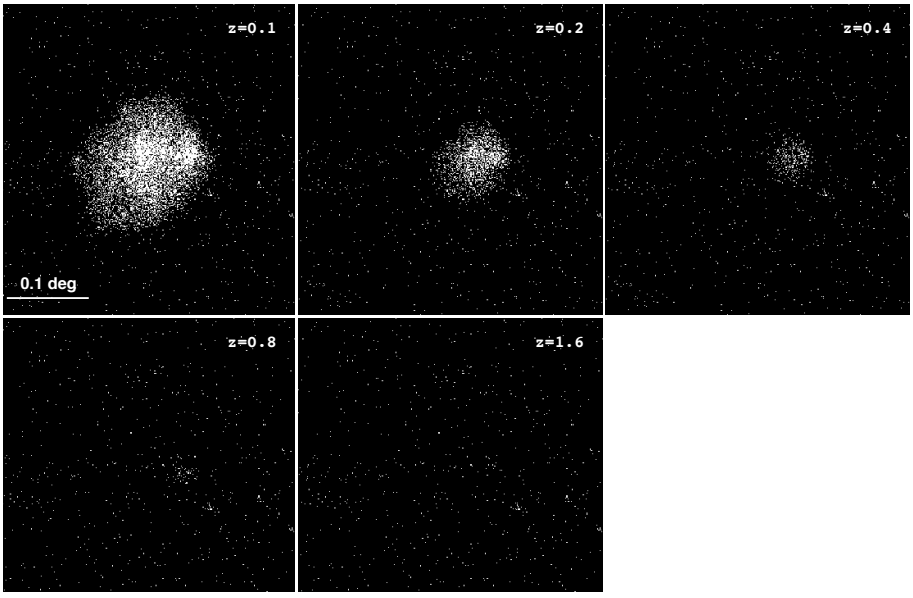

Figure 5.2: Zoom into the Bullet cluster simulation (CCD1) at different redshifts z. The images are binned by a factor of 80 corresponding to a pixel size of about 4x4 arcsec (eROSITA detector pixel size).

These simulations are well suited for detection studies (see Clerc et al., in preparation and Ramos Ceja et al., in preparation) and for hardness ratio studies of clusters. I released the simulated eROSITA observations within the German eROSITA consortium for further eROSITA performance tests.

However after many tests it turned out that due to slightly inconsistent treatment of split events in the SIXTE simulator the detailed cluster spectra of the simulations are not usable for spectral bias studies of X-ray cluster properties. Fig.5.3 shows discrepancies in the simulated cluster spectra to the model which increase from single events to quadruple events. This offset affects the measurements especially for eROSITA because the split event fraction is relatively high compared to other instruments. Only ~ 20 per cent of all events are singles (electron cloud from photon impact only detected in a single pixel). Fig.5.3 shows that there is a significant depression in count rate at low energies for split events. This causes a systematic overestimation of the temperatures when fitting a model to the average pattern data.

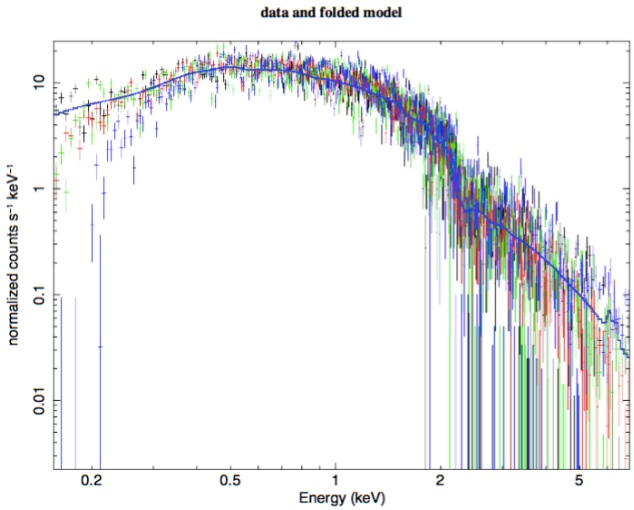

Figure 5.3: Spectrum of an isothermal cluster with ICM temperature of 11 keV extracted from the event file of my SIXTE cluster simulation. The colour code shows the spectrum for single events (black), double events (green), triple events (red), and quadruple events (blue). All spectra are normalised to the same count rate. The input model is shown as the continuous line.

For testing the simulation software I used an isothermal cluster spectrum to see how well the parameters can be retrieved after fitting a model to the simulated spectrum. I used a custom fitting procedure which uses a Bayesian parameter estimation technique developed by Johannes Buchner and described by Buchner et al. (2014). The fitting code uses the code MultiNest by Feroz et al. (2009) and connects it with the `XSPEC` fitting package (see Arnaud 1996b). The code samples the parameter space (given by Bayesian priors) and tries to maximize the probability for a given model describing the spectrum.

By doing this it creates a probability distribution for the free parameter values of the fit. This technique proved most robust in trying to fit low S/N spectra.

Fig.5.4 shows the obtained probability distributions on the model temperature (kT) for different cluster spectra. This test showed that the SIXTE spectrum causes a significant overestimation of the temperature. This effect becomes much smaller when making a spectrum of only single events but is still present. Better results were obtained for the `XSPEC fakeit` spectrum and I decided to make new simulations for the detailed spectral analysis using this method.

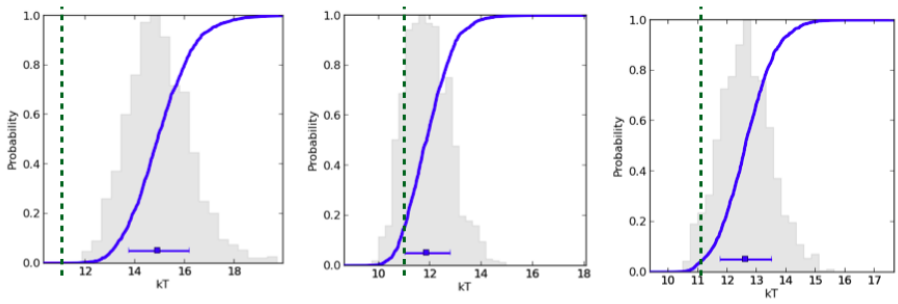

Figure 5.4: BXA probability histogram of best fit temperature (kT) for spectra of a 2 ks X-ray observation of a bright 11 keV plasma emission at redshift of z = 0.1. The input temperature is shown as a dotted vertical line. The cumulative probability is shown by a solid blue line. Left: Standard SIXTE spectrum containing all pattern events. Middle: `XSPEC fakeit` spectrum. Right: SIXTE spectrum containing only single pattern events.

5.2.3 Simulated spectra with XSPEC

I used the latest response files and exposure estimates available to the eROSITA consortium (state of the art on July 14, 2016) for the new simulation run.

To validate the simulation and fitting methods I made two identical simulation runs which were processed with the exact same analysis procedure. The only difference in the two simulations was that one contains the cluster substructure as measured from the deep *Chandra* sample, and the second contains the exact same cluster model with the only difference that the temperature in each substructure element was set to the median temperature of the cluster emission (overall isothermal clusters). This median temperature of the cluster maps corresponds with a scatter of about one per cent to an emission weighted temperature of the cluster (see Fig.5.6).

I simulated the spectra of the clusters from the best fit values of the *Chandra* cluster sample maps in each spectral-spatial region (see Chapter 3). Each of these partial spectra was simulated using `XSPEC` (version 12.9.0o) `fakeit` which creates a measured spectrum of a model emission applying an instrument response and Poisson noise on the counts in each spectral channel of the detector. The eROSITA spectra have 1024 energy channels

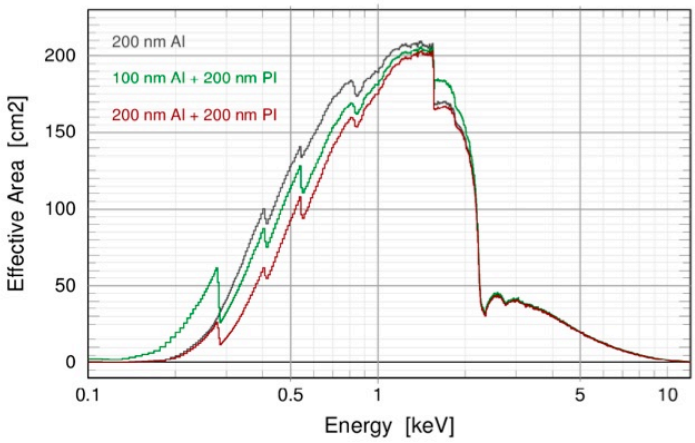

Effective areas of the three filter combinations for one eROSITA camera, composed of the expected effective area of one mirror assembly (averaged over the FoV), the

Figure 5.5: Latest measurements of eROSITA ARF for different filter combinations (preliminary). The plot shows the effective area over energy for one of seven telescopes taking into account the mirror, filter transmission and CCD quantum efficiency. The response is averaged over the FoV of the telescope. (credit: Konrad Dennerl, MPE).

with a width of ~ 50 eV. Each spectrum was created with an absorbed `apec` model which is defined by normalisation, temperature, foreground absorption, redshift, and metallicity. Normalisation, temperature, and foreground absorption (by neutral hydrogen) were taken from the *Chandra* cluster sample maps. The foreground absorption by neutral hydrogen column density between observer and source is modelled by the `phabs` model. The redshift is set according to the simulated redshift bin of the simulation. The metallicity is fixed at the average sample value of $Z/Z_{solar} = 0.3$ (see introduction for solar metallicity reference used in this work). The normalisation of a spectrum is directly proportional to the count flux of the source and can be converted to an energy flux if the source spectrum is known (see Chapter 2). The normalisation of the spectrum was scaled according to the change in luminosity distance between the *Chandra* spectrum and the simulated eROSITA spectrum (assuming same standard cosmology throughout this study). The exposure of the simulated spectra is 2 ks which is the average exposure of the most recent survey strategy for the all-sky survey after four years.

For the response files I assumed seven identical telescopes with a 200 nm on-chip aluminium (Al) filter (see top curve in Fig.5.5). Fig.5.5 shows the effective X-ray collecting area (ARF file) for one telescope so for seven identical telescopes the average effective area between 1-2 keV will be about $200 \times 7 = 1400$ cm^2. The second calibrated response file is the RMF which is a two dimensional matrix describing the calibrated probability with which an incoming photon is measured at a certain energy in the detector. I used an RMF averaged over all split events (accounting for measured split event fractions) for the 200 nm

on-chip Al filter case. All these new response files have been measured with the flight hardware in the MPE labs and at the BESY facility in Berlin (filter transmission curves) and put together into a format readable by the `XSPEC` fitting package by Konrad Dennerl at MPE. These have been provided internally to the German eROSITA consortium in May 2015.

In the SIXTE simulations every one of the 33 clusters was simulated 100 times and at 5 different redshifts. With the additional simulation of the isothermal cases and an average of 200 partial spectra per cluster the simulation includes more than six million individual spectra.

5.3 Measuring substructure X-ray cluster mass-proxy bias

All following analysis investigates the possible bias in measured cluster temperature T and flux F induced by the substructure in temperature and is based on the `XSPEC` simulations (see Sect. 5.2.3). I applied the same Bayesian parameter estimation technique to all simulated spectra to obtain a distribution of median values for the cluster properties T and F.

My fitting script in detail works as follows. The spectra between 0.3-6.0 keV are loaded into `XSPEC`, the background is set to zero, and the a `apec` x `phabs` model is initialized. The priors for the BXA fitting procedure are uniform distributions between fixed limits. The limits for temperature (T) are 1.0-20.0 keV and for normalisation (norm) relatively unconstrained between $0 - 10^{10}$. With these priors BXA is run and gives a distribution of values for both norm and T. For each BXA step the flux in the 0.3-6.0 keV band is calculated and appended to a separate distribution. From these distributions I obtain the median value and upper and lower bound as percentiles of the distributions for T and F (15, 50, and 85 per cent as lower, median, and upper values). This corresponds to best fit and 1σ range for a Gaussian distribution.

I have 100 spectra per cluster and thus 100 median values for each parameter. For the further analysis I plot the percentiles (15, 50, and 85 per cent) of the distribution of the 100 median values. This is a good approximation of what will be measured for a certain type of cluster in the large eROSITA survey. The plotted best-fit values in the following results thus are medians of medians of the 100 simulations per cluster.

5.3.1 Substructure types

There is a large range of different substructure types in the *Chandra* cluster sample. These types are mainly characterised by how strongly disturbed the ICM of a clusters is. There can be strong AGN feedback where jets from the AGN in the central galaxy heat the surrounding ICM and perturb the hydrostatic equilibrium of the system causing large temperature asymmetries. Mergers with subhalos can also cause strong perturbations to the ICM in the DM potential well of the cluster and cause shocks and sloshing motions.

The magnitude of these effects depends on the mass and velocity of the merging subhalo, determining the energy input to the ICM. If a system is unperturbed for a longer time the central gas starts radiative cooling and creates a peak of colder plasma at the cluster center. Hotter gas from higher levels in the atmosphere starts settling down towards the center as it cools (cooling flow). The rest of the plasma atmosphere slowly settles into hydrostatic equilibrium. For more detailed description of these processes see Chapter 1.

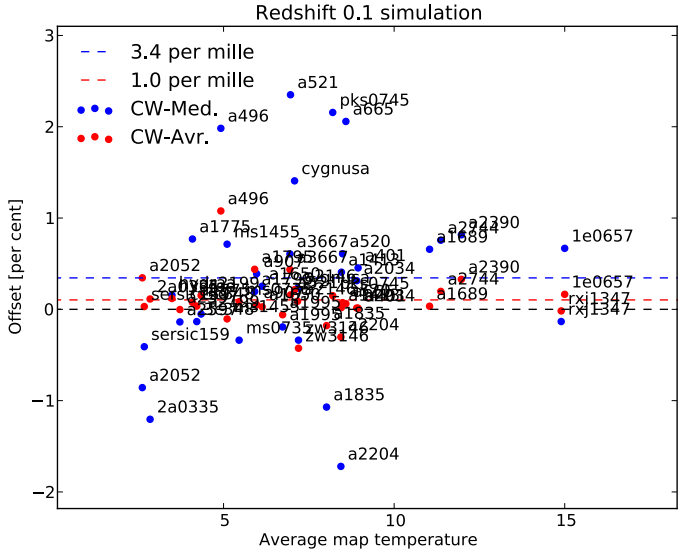

Figure 5.6: Offset between median (Med.), average (Avr.), and emission weighted (CW) map temperatures. The average offsets of the samples are shown as dotted lines. Temperatures are given in keV.

In my high resolution maps of *Chandra* observed clusters it is easy to identify the different types by eye. There have been many studies trying to find quantitative measures for substructure (for some recent studies see e.g. Chon et al. 2012; Weißmann et al. 2013; Parekh et al. 2015; Zhang et al. 2016). Together with Benjamin Kaiser from Elon University, I tested the application of these quantitative measures to the eROSITA images but could not find significant detections of substructure except for very bright low-redshift systems.

For the purpose of this study I divided the clusters into three different substructure types by eye using the high resolution maps I obtained from *Chandra* observations (see Chapter 3). The substructure types are:

1. Cool Core: largely unperturbed systems with at least some hint of cooling flow at the center. Includes 15 clusters: a1795, a1835, ms1455, a1413, ms0735, a2204, cygnusa, a907, 2a0335, a2597, a1650, a2199, hydraa, 3c348, and a2052

2. Disturbed: elevated level of perturbation visible in temperature and density maps like (e.g. by sloshing of colder gas in the potential well due to recent mergers). Includes

11 clusters: a1995, rxj1347, zw3146, a1689, a401, pks0745, a2034, a3667, a496, sersic159, and a2390

3. Two Peak: double peaked systems which are the result of a strong merger. Those are among the most perturbed clusters observed so far. Includes 7 clusters: 1e0657, a665, a520, a2146, a521, a1775, and a2744

These substructure types give a rough estimate of how perturbed the hot ICM halo is but off course there are intermediate systems and the transition between the three types is rather smooth. The classification also shows that more disturbed systems are more rare which is expected from cosmological simulations (e.g. Springel et al. 2005).

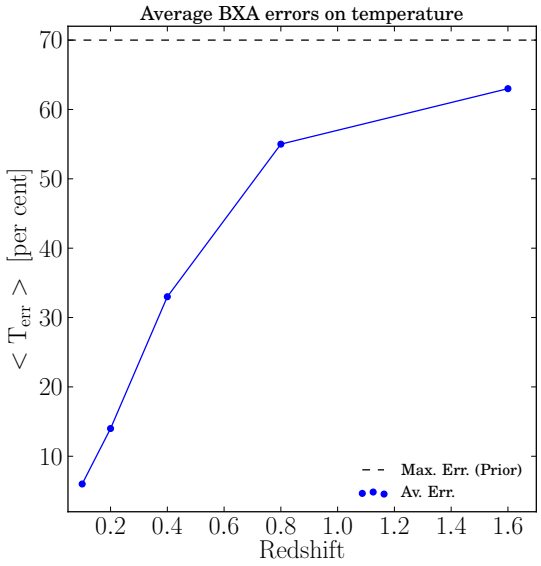

Figure 5.7: Average error on eROSITA temperature measurements in individual clusters in the all-sky survey. The dotted line indicates the maximum error (temperature measurement not possible) using the BXA fitting approach employed in this study.

The detailed temperature maps make defining an average cluster temperature difficult. Fig.5.6 compares the offset between emission weighted temperatures, average map temperature and median map temperature. The emission weighted temperature is obtained by taking the average of the temperatures in the spatial-spectral bins (see Chapter 3), weighted by the flux contribution of the bin. Taking the median temperature of the map bins or the average corresponds to the emission weighted temperature with a scatter of about two per cent. This is because the map bins have the same S/N and thus taking their average value corresponds to an emission weighting. The average offset of the differently weighted parameters is below 0.5 per cent. For the substructure bias analysis I used the median map temperature for the isothermal cluster simulations.

5.3.2 Bias in temperature T

For estimating eROSITA temperature bias due to temperature substructure in the cluster ICM I used the output of the `XSPEC` simulations described above. At five redshifts (0.1, 0.2, 0.4, 0.8, and 1.6) I simulated the sample of 33 clusters both with real substructure (sub) and as isothermal (iso) clusters. Each simulation was done 100 times and I extracted the distribution of the median values in temperature. I calculated the significance of offset between the distribution of the real and isothermal cluster cases as,

$$\mathrm{Bias_T} = \frac{\mathrm{T_{sub}} - \mathrm{T_{iso}}}{\mathrm{T_{average}}} \tag{5.1}$$

,where $\mathrm{T_{sub}}$ is the temperature measured in the simulation with substructure, $\mathrm{T_{iso}}$ is the temperature measured in the isothermal case, and $\mathrm{T_{average}}$ is the average temperature of the two.

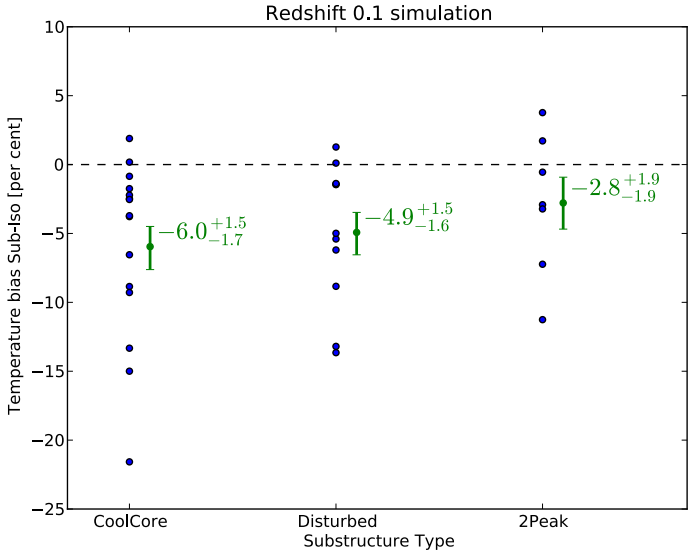

Figure 5.8: Temperature substructure bias for different types of clusters. the annotations show the best fit values with 1σ uncertainties from a bootstrap re-sampling technique.

Figs.C.1 in Appendix C show the results of comparing the input temperature to the temperature measured in the simulated eROSITA survey observation. The sub-iso measurements allowed me to extract the bias due to temperature substructure because there is also bias due to the fitting method (see Figs.C.1) which increases at higher redshift where the X-ray emission detected from the clusters becomes very faint. This bias specific to the data reduction procedure creates the same offset for both iso and sub spectra and thus cancels out in the difference between the two.

Fig.5.7 shows the evolution of the statistical measurement uncertainties increasing with redshift. I assume a prior on temperature and if the temperature cannot be constrained the probability distribution becomes flat. Because best fit and uncertainties are extracted using percentiles of the distribution the best fit value then tends towards the middle of the prior at 10.5 keV. The maximum uncertainty in this case is ~ 70 per cent.

The top panels of Figs.C.1 in Appendix C show the relation between input and fit temperature and a bias correction for the fitting method based on the isothermal cluster simulations. To indicate the bias of the fitting procedure I fit a linear correlation to the isothermal measurements and correct the values (iso and sub) with this function.

My analysis does not show significant difference ($\lesssim 1\sigma$) in the temperature bias between different substructure types of clusters. However Fig.5.8 shows a slight trend of less bias in more disturbed systems. This can be understood because the low temperature components of cool cores are over-weighted in the soft eROSITA spectra and more disturbed systems have generally higher temperatures where the effect is smaller (see e.g. Reiprich et al. 2013).

Because I found no significant difference in the bias for different substructure types it will be possible to correct for an average bias for all clusters. Fig.5.9 shows the average bias for the cluster sample at different redshifts. Because the temperature measurements become more noisy at higher redshift the bias decreases for redshift $z \gtrsim 0.8$. Most clusters will be below redshift 0.8 in the eROSITA survey so it will be the most important range for bias correction. The most reliable bias estimate I could obtain from the simulations is a bias of -5.08 ± 0.27 per cent in the redshift range $0.1 \leq z \leq 0.8$. Due to possible bias by using different average cluster temperatures (see Fig.5.6) I used a conservative value of -5 per cent bias for the mass function and cosmology predictions below.

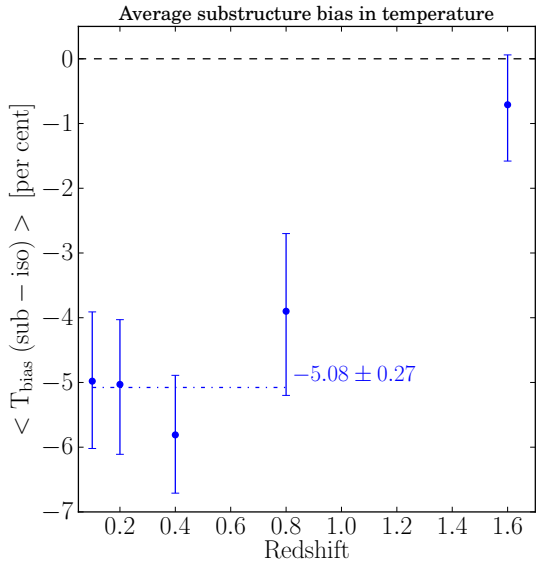

Figure 5.9: Temperature bias due to substructure at different redshifts. The annotation shows the average bias between redshift 0.1 and 0.8. Errorbars are 1σ uncertainties from a bootstrap re-sampling technique.

5.3.3 Bias in flux F

From the analysis of the simulated eROSITA spectra I obtained a distribution of best fit X-ray fluxes (0.3-6.0 keV energy band). The top panels of Figs.C.2 in Appendix C show the input flux versus measured eROSITA flux. The bottom panels show the differential offset between sub and iso measurements in per cent.

At lower fluxes the bias due to the fitting procedure increases because the distribution of best fit normalisations peaks at zero. When extracting percentiles from this distribution I obtain values which are biased high. However this does not affect our substructure bias measurements because the same effect is observed for iso and sub spectra and so it cancels out in their offset.

Fig.5.10 shows that the bias in flux is much lower than in temperature but there is also a significant offset that is solely due to the temperature substructure of the clusters. This can be due to correlation of the temperature and normalisation of a fit in the `apec` model. This correlation is clearly present in the parameter chains created by the BXA fitting procedure. If the measured temperature is lower also the flux will be underestimated by a certain amount. The bias in flux is about 30 per cent of the bias in temperature.

The most reliable estimate of the flux bias is -1.46 ± 0.03 per cent in the redshift range $0.1 \leq z \leq 0.8$. Bias in flux translates directly into bias in X-ray luminosity L_X which is an important mass-proxy for galaxy clusters (L-M scaling relations, see e.g. Pratt et al. 2009; Zhang et al. 2011a; Ettori 2013). However the redshift of the source has to be known to determine intrinsic luminosity from observed flux. The uncertainties and systematics

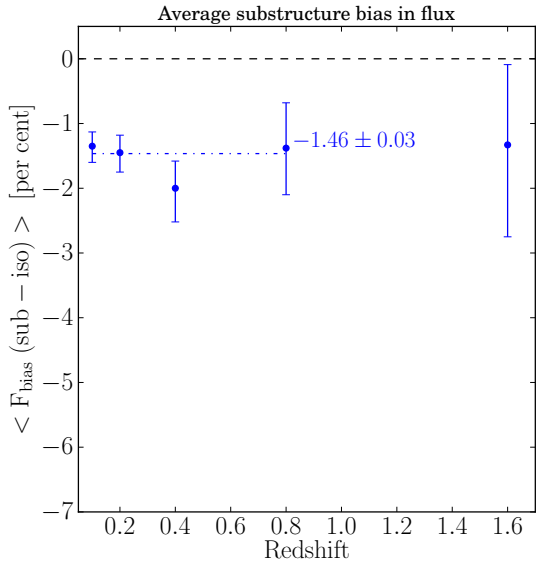

Figure 5.10: Flux bias due to temperature substructure at different redshifts. The annotation shows the average bias between redshift 0.1 and 0.8. Errorbars are 1σ uncertainties from a bootstrap re-sampling technique.

in the redshifts vary between spectroscopic and photometric estimates (see Ridl et al., in preparation). For the cosmological bias estimates I used temperature as mass-proxy because it is independent of systematic effects from the optical follow-up of clusters. Only the X-ray data is needed for clusters cosmology in this way.

5.3.4 Caveats

Additional bias can arise from effects which have not been accounted for in the `XSPEC` simulations. These include background in the observations and contamination of cluster spectra by AGN as well as uncertainty in the redshift of the clusters. Leccardi & Molendi (2007) found the temperature bias to increase when background is added to observations. Missing part of the cluster emission due to detection efficiency can cause additional bias. The measured cluster masses from fitting models to the spectra can also be biased by inaccuracies in the models or assumptions made in the models which do not apply to the investigated system (e.g. non-thermal pressure support see Chapter 3).

The `XSPEC` simulations only provide blended spectra without background and can thus not be used for core-excising tests or other spatially resolved temperature analysis.

The luminosity of a cluster will contain additional bias from the redshift measurements. It will depend on the quality and quantity of the available cluster redshifts whether L_X or T_X will be the better mass-proxy in the eROSITA survey.

In the special case of bias due to temperature substructures it does not seem to be necessary to correct for different bias depending on substructure. From first tests it was not

clear whether there is a reliable measurement for quantifying substructure in the eROSITA survey. This is mainly due to Poisson noise in the relatively shallow observations and a relatively large average survey PSF which will blur any substructure features in the cluster emission.

Because the bias does not have a strong dependence on the cluster type it is not critical how representative of the real cluster population of the universe my cluster sample is. The sample used in this stud covers a fairly large redshift range from 0.05 to 0.45 and a large range of masses and substructure types. Even if the fraction of different types is not perfectly representative I estimate the systematic uncertainty of the bias measurement to be less than one per cent.

The simulations assume that the cluster sample is the same in each redshift bin. This means that evolution in the cluster properties over time can not be probed. For example evolution in mass profiles (e.g Andreon 2008; Biviano & Poggianti 2010) or the ratio of cool core clusters to merging systems in the course of hierarchical halo formation (see e.g. from cosmological simulations Navarro et al. 1997).

5.4 Mass function and cosmology bias

The temperature of the hot ICM measured from X-ray spectra is an important proxy for the mass of the observed cluster (for a recent review on different mass-proxies, see e.g. Kravtsov & Borgani 2012). Temperature can only be measured accurately in high S/N spectra. The X-ray flux from a cluster can be measured accurately also in observations with lower S/N and can be used to estimate the mass (see e.g. L-M relation in Reiprich & Böhringer 2002; Reichert et al. 2011). For the mass function bias estimates I focus on the mass bias from temperature scaling relations because the L-M relation requires accurate redshifts of the clusters while T-M can be obtained from X-ray observations directly. Depending on the quality of the X-ray spectra the redshift can be measured from the X-ray spectrum. In the following study M200c corresponds to M_{200} as introduced in previous chapters.

The measured bias allowed me to put constraints on the expected mass bias from the most important mass-proxy (temperature of the hot ICM phase) for clusters of galaxies in X-ray band observations. I investigated how the bias in the mass-proxy would affect the cluster mass function expected in the eROSITA survey. The mass function calculations and constraints on cosmological parameters were obtained together with Nicolas Clerc (MPE) using his cosmological code. The mass function (histogram of the number of clusters of a given mass, see Bocquet et al. 2016, for a recent study) of an observed cluster sample together with a selection function describing the sensitivity of the instrument for detecting certain cluster types can be converted into the real cluster population of the universe and thus directly influences the derived cosmological parameters from the survey (for a review on cluster cosmology, see e.g. Allen et al. 2011).

Fig.5.11 shows the systematic change in the mass function assuming all masses were calculated from X-ray halo temperatures. The figure shows the cluster number density as it is distributed in the redshift - cluster mass plane.

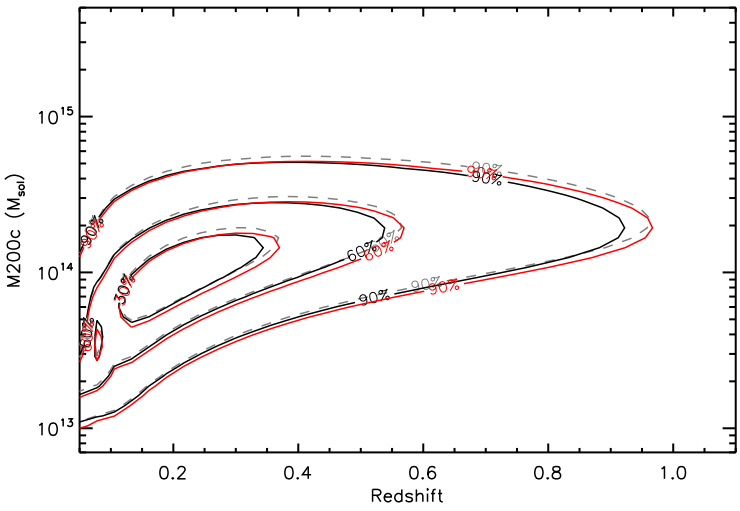

Figure 5.11: Simulation of observed eROSITA cluster density in the redshift - mass (M200c) plane. The total number of clusters is $\sim 10^5$. The contours include the denoted fraction of total observed clusters in the four year all-sky survey. The grey-dotted (higher in mass) contours show the expected observed distribution accounting for the selection function of the eROSITA survey (see PhD thesis of Miriam Ramos-Ceja, AIfA Bonn). The red (lower in mass) contours show the distribution as it will be measured with a five per cent low bias in X-ray halo temperatures. The solid black contours indicate best-fit mass function (see below). Credit: Nicolas Clerc.

The cluster mass M scales with temperature T as (see e.g. Finoguenov et al. 2001; Pierpaoli et al. 2003; Vikhlinin et al. 2009a; Pacaud et al. 2016),

$$\mathrm{M} \sim \mathrm{T}^{1.5} \tag{5.2}$$

The bias of $\frac{\mathrm{T_{real}}-\mathrm{T_{obs}}}{\mathrm{T_{average}}} = 0.05$ over a redshift range of $\mathrm{z} = 0.1 - 0.8$ translates into an average mass bias of $1.5 \times 5 = 7.5$ per cent.

This small systematic shift in the mass function will cause a systematic offset in the derived cosmological parameters and has to be accounted for when comparing the eROSITA cosmology constraints with other measurements like CMB studies.

To quantify the impact of the measured mass bias on the derived cosmological parameters the following technique is used. The overall mass function histograms of number of clusters in up to twelve mass bins was created for 3 different redshift ranges (see Fig.5.12). The offset significance between the fiducial and the biased mass-function is shown in the lower panels of Fig.5.12. This shows how the mass function changed due to the cluster mass bias.

The fiducial mass function was calculated using the Tinker et al. (2008) mass function and the cosmological parameters from WMAP9 (Hinshaw et al. 2013). This means the

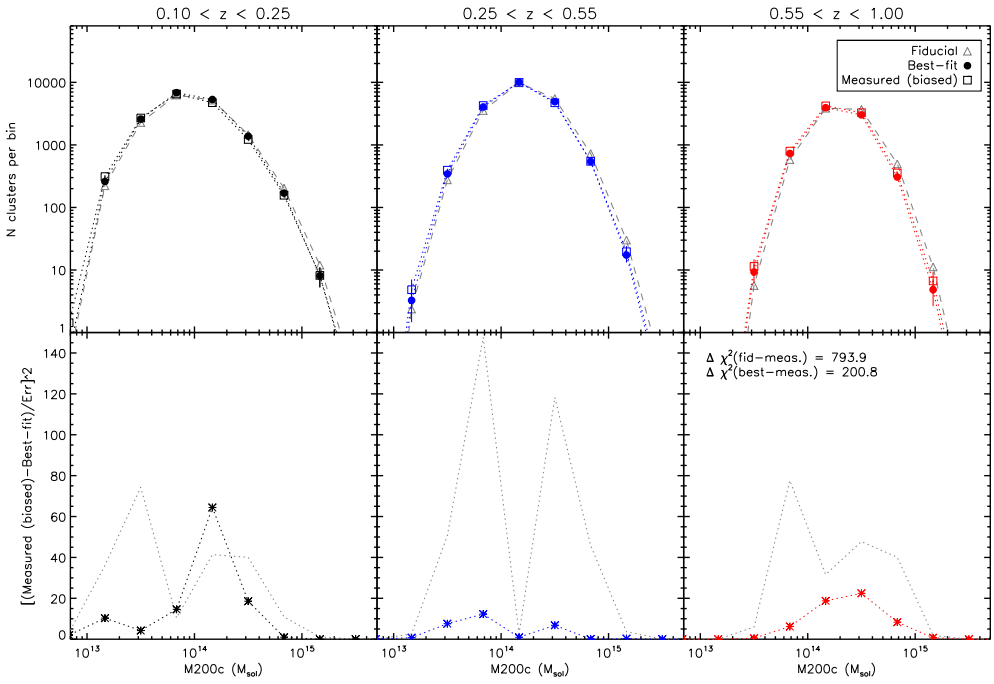

Figure 5.12: eROSITA mass function bias in different redshift bins. The top panels show the mass function (number of clusters in a given mass range M_{200c}) in increasing redshift ranges (left: 0.1 to 0.25, middle: 0.25 to 0.55, right: 0.55 to 1.0). The triangles show the eROSITA mass function as expected in the standard cosmology (fiducial cosmology WMAP9 Hinshaw et al. 2013). The open squares show the same mass function but with the estimated mass bias of about 7.5 per cent. The filled circles show the mass function for the best-fit cosmological parameters to the biased mass function. The errors on data-points are Poisson errors on the number of clusters per bin. The bottom panels show the offset significance between the fiducial model and biased mass function (grey dotted lines) and between the best-fit model and the biased mass function (crosses with coloured dotted line). Credit: Nicolas Clerc.

fiducial cosmology parameters are $\Omega_M \approx 0.28$ and $\sigma_8 \approx 0.82$. Using the scaling relations the cluster masses can be converted to observables like X-ray temperature, flux, and source extent. Here we used relations found in the XMM-Newton XXL-100 survey (Pacaud et al. 2016; Giles et al. 2016; Lieu et al. 2016). An instrument specific selection function putting limits on detectability in flux and source extent can then be used to relate the instrument specific observed mass function to the true mass function of clusters in the observed universe. Here we used the latest eROSITA selection function derived in the PhD thesis of Miriam Ramos-Ceja, AIfA Bonn.

The mass function can also be changed by varying the cosmological parameters Ω_M and σ_8. These parameters constrain the matter fraction of the total energy of the universe and

the clustering amplitude of DM halos (see Chapter 1).

The number density of DM halos of different masses can be calculated for different cosmologies assuming purely gravitational collapse (see early work by Press & Schechter 1974; Bond et al. 1991). Tinker et al. (2008) in recent work provide a universal function $f(\sigma)$ describing the shape of a cosmological halo mass function mostly independent of redshift or cosmological model. The expected number of clusters N in a mass range is described as (see Tinker et al. 2008),

$$N = f(\sigma)\ \frac{\bar{\rho}_m}{M}\ \Delta(\ln(\sigma^{-1})) \tag{5.3}$$

where $\bar{\rho}_m$ is the mean matter density, cluster mass in the bin is M, and $\Delta(\ln(\sigma^{-1}))$ is the logarithmic change in the parameter σ which is obtained by integrating over all wave numbers k of density fluctuations,

$$\sigma^2 = \int P(k)\ \hat{W}(kR)\ k^2\ dk \tag{5.4}$$

the variance of the matter density field P(k) smoothed with the Fourier transform $\hat{W}$ of a top-hat window function with radius R,

$$R = (\frac{3M}{4\pi\ \bar{\rho}_m})^{1/3} \tag{5.5}$$

The Tinker function is given as,

$$f(\sigma) = A\Big[\Big(\frac{\sigma}{b}\Big)^{-a} + 1\Big]\ e^{-c/\sigma^2} \tag{5.6}$$

with specific constants A, b, a, and c which vary for different choices of characteristic radius R. A is the overall normalisation, a and b are the slope and normalisation of the low-mass power law, and c gives the scale of the high-mass exponential drop in cluster numbers (see description by e.g. Tinker et al. 2008; Bocquet et al. 2016).

Here σ_8 influences the normalisation of the function σ and Ω_M changes the mean matter density $\bar{\rho}_m$.

These equations provide a total mass function of halos which then is convolved with the eROSITA detection probability at different masses (selection function of eROSITA). As selection function the latest simulations of cluster detections was used in combination with latest scaling relation measurements from the *XMM-Newton* XXL survey (from PhD thesis of Ramos-Ceja and Clerc et al., in preparation, see above). The function has decreasing detection probability at lower masses because low mass halos have lower X-ray luminosities and lower ICM temperatures.

For a grid of different Ω_M and σ_8 (see grey diamonds in Fig.5.13) an expected true mass function was created (cosmology calculations by Nicolas Clerc, MPE). For each combination of parameters the offset significance between true and biased mass-function was calculated to find the best fitting set of cosmological parameters (for details on this method see

Clerc et al. 2012). Fig.5.13 shows the best fit parameters and confidence contours around them.

The goodness-of-fit between the measured and simulated mass function was calculated as,

$$\chi^2 = \sum \left(\frac{\text{Measured} - \text{Model}}{\text{Error}} \right)^2 \tag{5.7}$$

which is the sum of the offset significance (χ^2 test) between the measured and model data points summed over all mass- and redshift-bins (see Fig.5.12). The annotated χ^2 values show that the improvement of χ^2 between the measured (biased) mass function and the best fit simulated mass function compared to the fiducial mass function improved by $\Delta\chi^2 = 693.1$.

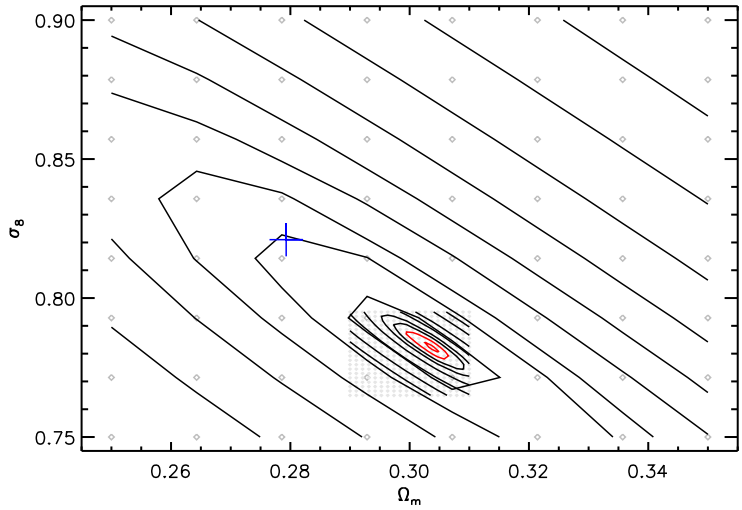

Figure 5.13: eROSITA cosmology contours for biased mass function for $\Omega_{\rm M}$ versus σ_8. The cross shows the input (true) cosmology value, the star shows the best fit value for the biased mass function. The black contours give the sum of the offset significance between the biased and fit mass function. The contours were obtained by interpolating the offset significance values calculated for the grid of cosmological parameters (see grey diamonds). The red contours show the 1 and 3 σ confidence level. The plot shows more coarse and finer contour levels around the best fit values. Credit: Nicolas Clerc.

For an input cosmology with $\Omega_{\rm M} = 0.28$ and $\sigma_8 = 0.82$ we obtained a best fit of $\Omega_{\rm M} \approx 0.31$ and $\sigma_8 \approx 0.78$. This corresponds to a low bias of ~ 5 per cent in σ_8 and a high bias ~ 10 per cent in $\Omega_{\rm M}$.

These trends can be understood because lower normalisation of the clustering σ_8 would produce less massive halos consistent with the measurement bias. If the measured masses are biased low this creates detections where the probability from the selection function

is very low and thus the real expected number density at low masses is disproportionally boosted to increase the average expected matter density $\Omega_{\rm M}$.

Given that the error contours on the input cross in Fig.5.13 will be similar to the ones for the biased value the offset is highly significant.

5.5 Discussion

The most important mass proxy for galaxy cluster mass in X-ray surveys is the electron temperature of the ICM which can directly be measured from the X-ray spectra of a cluster. The ICM is generally assumed to be in thermal equilibrium in the observed regions and thus the electron temperature corresponds to the gas temperature. The temperature is obtained by fitting an emission model of a collisionally ionized plasma to the intrinsic X-ray spectrum of the source. Every X-ray instrument however has a slightly different response (i.e. detection efficiency) depending on incoming photon energy and position on the detector. The intrinsic source spectrum can be obtained by folding the observed spectrum by the instrument response.

As many previous studies of deep X-ray observations of clusters have shown there is significant temperature structure in the ICM (e.g. Reiprich et al. 2004; Sanders & Fabian 2007; Million & Allen 2009; Lovisari et al. 2011). It is possible to disentangle this structure only in the plain of the sky using high resolution observations and mapping the 2D temperature structure (see Chapter 3). There is also multi-temperature gas along the line of sight but disentangling this can only be done approximately using multi-component fitting of single regions in the 2D maps. One can only approximate an average temperature in a certain volume but doing so at ever higher resolution like in Chapter 3 of this study reduces bias in average temperatures.

Many previous works studied the capability to measure the ICM temperature using different X-ray observatories. Reiprich et al. (2013) reviewed the influence of multi-temperature ICM on the obtained average temperature of a cluster especially in the outskirts. They found that eROSITA will significantly underestimate cluster temperatures by simulating a spectrum with two temperature components (0.5 keV and 8.0 keV). In a spectrum where the emission from cold and hot component was split 50/50 per cent the average temperature should be measured as 4.25 keV. It was found however that in a single-temperature fit to the eROSITA spectrum the temperature was ~ 1.5 keV suggesting a bias of lower temperature of about 60 per cent. The bias they measured is also varying with the assumed metallicity of the colder component. The temperature difference assumed in their simulations is more extreme than in the sample of clusters I analysed but demonstrates the expected trends for eROSITA. My results show that in real clusters the bias towards lower temperatures due to substructures will be only about 5 per cent.

The main features determining the model fit to the spectra are the exponential bremsstrahlung cut-off at high energies (maximum energy loss of the electron in the collision), the slope of the bremsstrahlung emission at intermediate energies, and the form and peak of the complex blend of emission lines at lower energies (see e.g. Reiprich et al. 2013)

eROSITA is a rather soft X-ray telescope which means its effective collecting area is highest between $1-2$ keV and drops by a factor of about ten above 2 keV. Because of this eROSITA is more sensitive to spectral features at low energies and thus more effective at detecting lower temperature gas. This biases the estimated average temperature when there is a second hotter gas component present in the spectrum (as explained by Reiprich et al. 2013).

Borm et al. (2014) tested how well temperature can be constrained for clusters in the eROSITA survey. For the brightest clusters with more than 100 counts in the eROSITA survey (with 1.6 ks exposure) they found uncertainties from $\sim 5-40$ percent (up to a redshift of $z \sim 1$). The temperature uncertainty mostly increases with higher redshift and lower cluster mass. They found a trend of increasingly biased-low temperature with higher redshift suggesting cluster temperatures will be biased by 20 per cent low at $z \sim 1$ in an average eROSITA field (if the redshift is a known quantity when fitting the spectrum). All these estimates were based on `XSPEC fakeit` simulations of isothermal clusters with a $\beta-$ model surface brightness profile.

For cluster masses of $\sim 2 \times 10^{14}$ $M_{\odot}$ (almost half of my sample lies in that mass range), an exposure time of 1.6 ks, and assuming the redshift is perfectly known, Borm et al. (2014) found a bias correction function given as,

$$< T_{\rm fit} > / T_{\rm Input} = -0.45 \cdot e^{3.85 \cdot \log_{10}(z)} + 1 \tag{5.8}$$

with redshift z this equation gives the ratio between temperature from the fit to the eROSITA spectra ($< T_{\rm fit} >$) and the input temperature of the isothermal $\beta-$ model ($T_{\rm Input}$). At redshift $z = 1$ this would mean $\sim 2 \times 10^{14}$ $M_{\odot}$ clusters have 45 per cent too low temperatures in the eROSITA survey.

The bias Borm et al. (2014) found does not include the substructure bias I investigated in this study because they used symmetrical beta models instead of real cluster substructures. The bias they found is caused by the fitting method for the cluster X-ray spectra. In my study bias from the fitting method is cancelled out because I used the difference in temperature between two simulations with and without substructure. The bias I found thus has to be added to obtain as unbiased masses as possible for all cosmological cluster studies with eROSITA.

Mathiesen & Evrard (2001) investigated hydrodynamic simulations of a sample of 24 clusters. They created mock X-ray spectra as they would be observed by observatories like *Chandra*. They analysed the influence of the chosen X-ray band in the mock spectra on the fitted average temperature. The simulations showed that the mass-weighted average temperature was $\sim 10-20$ per cent higher than the measured temperature in the 0.5 to 9.5 keV band (similar to *Chandra*). They furthermore found that temperatures determined from a softer energy band (0.5-9.5 keV) are generally lower than if they were determined from a harder band (2.0-9.5 keV). The relation they found is,

$$T_{\rm s,[0.5-9.5]} = (0.81 \pm 0.01)\ T^{1.09 \pm 0.01}_{\rm s,[2.0-9.5]} \tag{5.9}$$

For lower temperature clusters the bias is stronger than for higher temperature.

Mazzotta et al. (2004) found significant differences between mass- and emission-weighted temperatures in their cluster simulations and concluded that mass-weighted temperatures are better suited to compare to temperatures from *Chandra* or *XMM-Newton* X-ray spectra.

Rasia et al. (2005) found a bias of $\sim 20 - 30$ per cent lower temperatures from mock X-ray spectra compared to the emission-weighted average temperature from their simulations. This causes a mass bias in the observed M-T relation of ~ 50 per cent too low masses in their sample and leads to an underestimate of σ_8 by about 10 to 20 per cent.

After the above results Vikhlinin (2006) introduced an algorithm to better compare temperatures from simulations and from real cluster spectra.

The X-ray temperature is particularly important for cosmological studies because it is one of the best observable mass proxies for clusters of galaxies (see e.g. Finoguenov et al. 2001). Pierpaoli et al. (2003) have shown that the normalisation of the T-M scaling relation strongly influences the determination of the σ_8 cosmological parameter. They showed at high significance that a lower normalisation in the mass causes a lower predicted value for σ_8. Lower normalisation of the T-M function is the same as a low mass bias due to temperature measurement bias as found in my study. They found that a ten per cent lower normalisation causes about a five per cent lower value for σ_8 which is consistent with my results. Their results were obtained for fixed $\Omega_{\rm M} = 0.3$.

Bocquet et al. (2016) analysed the influence of baryons (mostly in form of hot gas like in the ICM) on the mass function using data from the Magneticum simulations (Dolag et al., in preparation). Comparing the results of DM-only simulations and simulations including baryons they found that in case of eROSITA the change in the obtained mass-function could lead to an underestimate of about one per cent in $\Omega_{\rm M}$.

Pillepich et al. (2012) made the most detailed predictions for eROSITA cluster cosmology so far. They used the halo-mass function of Tinker et al. (2008) obtained from N-body simulations of a ΛCDM universe. Using L-M and T-M relations they converted the masses into detected photon count in eROSITA using early estimates of instrument properties. This allowed them to estimate uncertainties on cosmological parameters. They estimate that with eROSITA cluster counts, angular clustering measurements, photometric redshifts for all systems and cosmology priors from the *Planck* mission it will be possible to obtain uncertainties of $\Delta\sigma_8 = 0.014 \lesssim 2$ per cent and $\Delta\Omega_{\rm M} = 0.0039 \lesssim 2$ per cent. At such high precision it will be crucial to correct for the bias I estimate to be 5-10 per cent especially when combining eROSITA with priors from other instruments.

In this study I investigated an additional effect which is caused by the substructure in temperature by directly comparing the spectroscopically measured temperatures in isothermal and real clusters.

5.6 Summary and conclusions

In this Chapter I presented eROSITA simulations of count images and spectra for a large sample of galaxy clusters. All simulations were based on real cluster observations and

provide a representative sample of galaxy clusters in the local universe.

The cluster images of the simulated eROSITA observations will be used to constrain the detection efficiency and cluster selection function in the survey. This is very important to avoid additional bias the cosmological studies with the eROSITA cluster sample.

In the redshift range of $0.1 \leq z \leq 0.8$ I estimated a bias in the eROSITA cluster temperatures T_X of -5.08 ± 0.27 per cent and a bias in flux of -1.46 ± 0.03 per cent.

Assuming temperature will be used as the prime eROSITA mass-proxy this causes a bias of about 7.5 per cent lower masses. This will cause an offset of ~ -5 per cent in the cosmological parameter σ_8 and $\sim +10$ per cent in Ω_M which eROSITA will be most sensitive to.

Depending on the fitting method a specific correction function has to be used to correct for first order effects. C.1 shows the correction function necessary when using my custom Bayesian fitting pipeline. Correction functions for other methods have been published by e.g. Borm et al. (2014). In addition to the bias from these fitting methods for isothermal clusters the bias due to substructure described in this chapter has to be corrected for. I found it to be nearly constant over all substructure types and redshifts.

When estimating the cluster masses from scaling relations the hydrostatic mass assumptions commonly used counteract the bias from substructure because they lead to overestimated masses. Chapter 3 shows that this effect is about +4 per cent.

It is crucial to correct for the bias found in this study as eROSITA should obtain confidence limits of ~ 2 per cent on these cosmological parameters.

Chapter 6

Summary and conclusions

6.1 Summary

It is important to understand the physics in individual systems at great detail before using clusters as cosmology probes. In this work I outlined contributions to studying turbulence in clusters and the implications for future high precision cluster cosmology studies with the eROSITA observatory. In addition I investigated in detail how the sample can be used to constrain the existence of 7.1 keV sterile neutrinos constituting the dark matter in the universe.

Chapter 3 is based on the publication:

F. Hofmann, J. S. Sanders, K. Nandra, N. Clerc, M. Gaspari. 2016a. Thermodynamic perturbations in the X-ray halo of 33 clusters of galaxies observed with *Chandra* ACIS. Astronomy & Astrophysics. Volume 585. A130

In this chapter I presented a very large sample of detailed cluster maps with application to understand the thermodynamic processes in clusters of galaxies. The deep observations of the individual clusters helped to identify structures in the ICM caused by mergers or AGN feedback. By comparing to recent high-resolution simulations of perturbations in the ICM I constrained the average 1D Mach number regime in the sample to $\mathrm{Mach_{1D}} \approx 0.16 \pm 0.07$ with some caveats (see Sect. 5.5). Comparing to simulations this would suggest $\mathrm{E_{turb}} \approx 0.04\ \mathrm{E_{therm}}$ (see Sect. 3.5.2). By comparing perturbations in the central regions ($\lesssim 100$ kpc) and in the outer regions ($\gtrsim 100$ kpc) I found an indication for a change in the thermodynamic state from mainly isobaric to a more adiabatic regime.

In addition the sample shows a tight correlation between the average cluster metallicity, average temperature and redshift. The best fit linear correlation between metallicity and redshift is $\mathrm{Z/Z_\odot} = -(0.6 \pm 0.2)\ \mathrm{z} + (0.36 \pm 0.04)$ and between metallicity and temperature the best fit is $\mathrm{Z/Z_\odot} = -(1.0 \pm 0.7)\ \mathrm{T/100keV} + (0.34 \pm 0.06)$. The average metallicity of the sample is $\mathrm{Z} \approx 0.3 \pm 0.1\ \mathrm{Z_\odot}$.

Future X-ray missions like Astro-H (Kitayama et al. 2014) and Athena (Nandra et al.

2013) will help to further investigate turbulent velocities and chemical enrichment in the ICM. The eROSITA observatory (Merloni et al. 2012) will detect a large X-ray cluster sample for cosmological studies and the detailed cluster mapping can be used to make predictions on the scatter in scaling relations due to unresolved structures in temperature. To encourage further analysis based on this unique sample of cluster observations all maps and asymmetry measurements used in this study are made publicly available in electronic form.

Chapter 4 is based on:
F. Hofmann, J. S. Sanders, K. Nandra, N. Clerc, M. Gaspari. 2016b. 7.1 keV sterile neutrino constraints from X-ray observations of 33 clusters of galaxies with *Chandra* ACIS. Astronomy & Astrophysics. Volume 592. A112

In this study I presented a large sample of deep cluster spectra with limits on a previously detected emission at 3.55 keV assuming the line originated from the decay of sterile neutrino DM ($m_s = 7.1$ keV). I extend the number of objects previously searched for the line and provide further insight to whether the line only occurs in special observations or objects. This is the first study using a large sample of *Chandra*-observed clusters to constrain the 3.55 keV line. The driving cluster property behind the depth of the upper limit on the mixing-angle in the sterile neutrino scenario is the DM mass in the FOV where the spectra have been extracted divided by the luminosity distance squared. To maximize this property, homogeneous, deep coverage out to large radii of a massive nearby system is needed (higher [10^{10} $M_\odot$ Mpc^{-2}] value in Tab. B.2). In this sample the best candidate for such a study with *Chandra* was Abell 1795 because of its very deep exposure (see Tab. B.2).

As demonstrated by Bulbul et al. (2014) a 1 Ms observation of the Perseus cluster with the *Hitomi (Astro-H)* SXS instrument (Kitayama et al. 2014) will distinguish between a plasma emission line of the ICM, broadened by the turbulence in the cluster ($\sim$ 300 km/s) and a DM decay line, broadened by the virial velocity ($\sim$ 1300 km/s) of the DM halo. The large FOV of the *eROSITA* observatory (Merloni et al. 2012) will allow for tight constraints on the line (see also Zandanel et al. 2015), homogeneously covering nearby X-ray bright clusters to large radii, even with lower effective area at 3.55 keV compared to XMM-Newton and *Chandra*. Only deeper observations with current or future instruments will allow to finally decide the nature of the detection as summarised in a recent white paper on keV sterile neutrinos (Adhikari et al. 2016).

eROSITA will have the capability to provide competitive upper limits on possible dark matter lines in the X-ray range and its all-sky survey will cover a large sample of objects and will for the first time provide a complete view of the Galaxy in the X-ray range above 2 keV. This will permit tight constraints on a possible 3.55 keV emission from DM in the Galaxy and especially around the Galactic center.

Chapter 5 will be published as:
F. Hofmann, et al., in preparation.

I this chapter I presented eROSITA simulations of count images and spectra for a large sample of galaxy clusters. All simulations were based on real cluster observations and provide a representative sample of galaxy clusters in the local universe. In the redshift range of $0.1 \leq z \leq 0.8$ I measured a bias in the eROSITA cluster temperatures T_X of -5.08 ± 0.27 and a bias in flux F_X of -1.46 ± 0.03.

Assuming temperature will be used as the prime eROSITA mass-proxy this causes a bias of about 7.5 per cent lower masses. This will cause an offset of ~ -5 per cent in the cosmological parameter σ_8 and $\sim +10$ per cent in Ω_M.

6.2 Outlook

Future studies related to this project include investigating bias in the eROSITA cluster survey in more detail, and the possibility to conduct even more realistic simulations of clusters of galaxies before and after launch of eROSITA to better characterize the expectations from the first full-sky coverage.

The *Chandra* maps can be used for further studies like conduction constraints in the ICM. Simulations have shown that the energy deposited in the ICM at different scales E(k) varies with conduction (e.g. Gaspari & Churazov 2013). Investigating perturbations on different scales in the maps of my sample might allow to put constraints on conduction (see Chapter 1). At higher conduction the E(k) function steepens at smaller scales.

The sample of deep high resolution cluster maps I made publicly available will provide valuable input for many future studies including comparison with multiwavelength data from other observatories.

For future observations related to studying major mergers between massive galaxy clusters I proposed new Chandra observations of a very peculiar major merger candidate at redshift greater than 0.3.

The procedures and data published during this study as well as the scientific interpretations found will be of significant value for future studies in the field of cluster research.

6.2.1 eROSITA

From an expected launch at the end of 2017 to early 2018 eROSITA will create the largest sample of X-ray detected galaxy clusters over the following four years. With the final cluster catalog expected in 2022 and after all redshift determination in follow-up optical observations has been completed the mission will provide the best constraints on dark energy to date. It will be crucial to remove all instrument specific and physically related biases in the measurements in order to tighten cosmological constraints by combination with data from other missions which are based on different observables.

6.2.2 Athena

With an expected launch around 2028 Athena will be the most advanced X-ray telescope ever built in many aspects. It will have an especially high effective area, obtaining high resolution spectra of the ICM already in relatively short observations (see white paper for main science goals, Nandra et al. 2013). The capabilities for studying the astrophysics and evolution of galaxy groups and clusters was presented by Ettori et al. (2013) and Pointecouteau et al. (2013). Especially accretion of baryonic matter into the DM potential well in the outskirts of the clusters will be much better studied with Athena's large effective area. One of two science instruments is an X-ray calorimeter which will allow very high energy resolution in spatially resolved X-ray images. This will allow to study gas motions of the hot ICM phase in clusters in unprecedented detail and will help understand the physics of the ICM. Understanding the gas motions better will greatly improve the mass estimates of clusters and thus the cosmological constraints from cluster surveys like eROSITA.

With the WFI instrument it will be possible for the first time to conduct a survey of low mass groups of clusters at high redshift. This will extend the mass function of clusters to lower masses and allow much better constraints on the evolution of structure formation.

After a significant number of massive clusters from the eROSITA survey have been followed up with Athena the cosmological constraints should improve even further. This should allow to fully exploit the eROSITA sample for cosmology and especially dark energy constraints by the end of the 2030ies.

The high spectral resolution and effective area will also allow to put very tight constraints on dark matter emission lines in the 2-10 keV energy range.

6.3 Proposed future observation of SPT-CLJ2031-4037

Co investigators of the proposal: Jeremy Sanders, Elke Roediger, Nicolas Clerc, Jethro Ridl, Massimo Gaspari, and Stephen Walker.

I proposed a 60 ks *Chandra* ACIS-S observation of the hot intracluster medium (ICM) in a massive merging cluster. The observation will add to a sample of very rare major merging clusters. I propose an observation of SPT-CLJ2031-4037 ($z = 0.342$), which in a $\sim$ 10ks *Chandra* ACIS-I X-ray observation showed two peaks in surface brightness and indicates that this system could be a major merger very similar to the Bullet cluster, but at higher redshift. One of its subclusters is a very well studied strong lensing cluster. *Chandra* is the only instrument with high enough spatial resolution in X-rays to study small scale substructure in this system and find the expected shock front in the ICM.

In addition to the X-ray observations I was awarded (co investigator Jethro Ridl, MPE) a 20 min. observation with the MPG 2.2 m telescope in La Silla, Chile. The observation will be carried out with the GROND instrument and will provide a galaxy density map of the cluster to support the X-ray analysis.

The results from combining X-ray and optical data can be used for independent constraints on dark matter self-interaction (for similar approach on a different system see e.g. Markevitch et al. 2004).

6.3.1 Scientific Justification

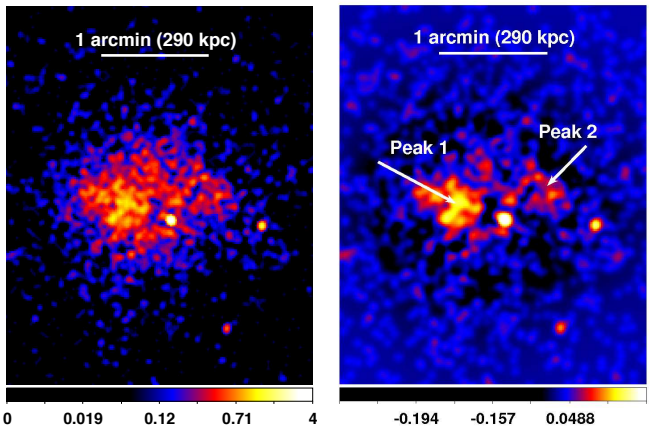

Figure 6.1: Unsharp masked (right), smoothed *Chandra* count image (left) of SPT-CLJ2031-4037, showing two peaks in the X-ray surface brightness. Bright point sources are well resolved in this image. Energy range 0.5 - 7.0 keV.

Studying the merger history of clusters of galaxies is essential for understanding the structure formation of the universe at large scales. The formation history is imprinted in the substructure of the hot, X-ray emitting ICM by shock fronts traveling through the cluster as a result of major mergers. The ICM is also heated to much higher average temperature by the large amount of energy deposited in the hot plasma during the collision.

There are only a dozen major merger clusters found above a redshift of 0.3 like El Gordo or MACS J005.4-1222 (Menanteau et al. 2012; Bradač et al. 2008) and they are predicted to be very rare by ΛCDM cosmological simulations. In this small sample SPT-CLJ2031-4037 is one of the hottest, most massive systems and possibly the first to show a Bullet-like Mach cone (Randall et al. 2008). The cluster is bright enough in X-rays that I expect to clearly resolve a Bullet-like Mach cone if present.

SPT-CLJ2031-4037 (ROSAT name RXCJ2031.8-4037, see Plagge et al. 2010, for a sample of massive SPT clusters) is a clear major merger candidate (see Fig.6.1). Deep *Chandra* observations are the only way to detect shock fronts in this system, which can be used to determine the Mach number, and velocity of the shock, closely related to the relative velocity of the subcluster (Markevitch & Vikhlinin 2007).

One of the main objectives is to obtain spatially resolved spectra of the two peaks which are just visible in the 10 ks X-ray count image (see Fig.6.1 for an unsharp-masked count

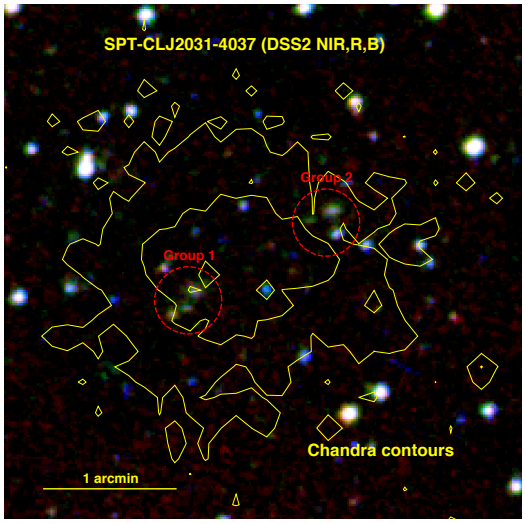

Figure 6.2: *Chandra* X-ray contours plotted on an RGB optical image (red: DSS2 near-infrared, green: DSS2 red, blue: DSS2 blue). The two red circles mark the positions of two subclusters of galaxies.

image, enhancing structures, PI of observation: Garmire), and to detect possible shock fronts. This will allow us to judge whether there is a major merger taking place in this cluster and to put constraints on the mass ratio of the merging systems. In the currently available *Chandra* data on this cluster it is only possible to define four regions with a signal-to-noise ratio (S/N) of 20 for the extraction of spectra, which do not resolve the two surface-brightness peaks (seen in Fig.6.1). The current spectral fits suggest temperatures of ~ 9 keV for the innermost 100 kpc and ~ 12 keV out to 200 kpc. A deprojected radial profile of the cluster shows a temperature just under 10 keV throughout the cluster (see Fig.6.4). McDonald et al. (2013) found an average temperature of about 12 keV.

The REFLEX catalog (Böhringer et al. 2004) provides a luminosity of $12 \times 10^{44}\,\mathrm{erg\,s^{-1}}$ from which I infer a mass of about $5.6 \times 10^{14}\,\mathrm{M_\odot}$ using scaling relations from Stanek et al. (2006). The redshift is given as $z = 0.342$, which corresponds to a plate-scale of 1 arcsec ≈ 4.8 kpc. From the given mass and critical density I infer $r_{200} \approx 1.5$ Mpc (approximate virial radius), where r_{200} is the radius at which the mean enclosed density is $\times 200$ the critical density (see Reichert et al. 2011, and references therein). For these calculations I assumed a standard ΛCDM cosmology with $H_0 = 71$ km s^{-1} Mpc^{-1}, $\Omega_M = 0.27$ and $\Omega_\Lambda = 0.73$. The deprojected profiles in Fig.6.4 suggest a mass of about $M_{500} \approx 10^{15}\,\mathrm{M_\odot}$ which would also be expected from temperature mass scaling relations for a 10 keV cluster (Vikhlinin et al. 2009a). In the MCXC catalog (source MCXCJ2031.8-4037, Piffaretti et al. 2011) collecting X-ray constraints on clusters of galaxies the cluster is listed with a total mass of $M_{500} = 6.6 \times 10^{14}\ \mathrm{M_\odot}$ and a critical radius of $r_{500} \approx 1.2$ Mpc. SZ observations of the cluster with the South Pole Telescope (SPT) were used to estimate a total mass of

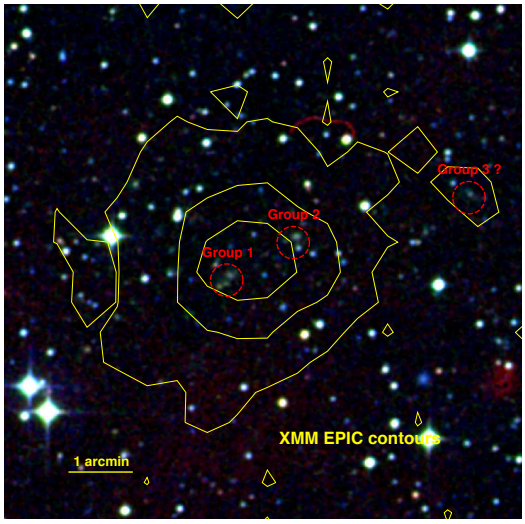

Figure 6.3: *XMM-Newton* EPIC X-ray contours plotted on an RGB optical image (red: DSS2 near-infrared, green: DSS2 red, blue: DSS2 blue). The red circles mark the positions of probable subclusters of galaxies on larger scales. The whole image would be covered by one *Chandra* ACIS-S chip.

$M_{500} = 9.8 \times 10^{14}$ $M_\odot$ (see catalog by Bleem et al. 2015). The SPT catalog flags the cluster without followup data except for the short *Chandra* exposure.

The significant offset between SZ and X-ray scaling relation masses suggests that the cluster is not in hydrostatic equilibrium. In a recent paper McDonald et al. (2016) infer a stellar mass of about 1.3×10^{12} $M_\odot$ which would suggest an extremely low stellar mass fraction (compared to expectations from Andreon 2010).

The high resolution of the *Chandra* telescope will be crucial in resolving the structure at the core of this cluster. In $\sim$ 30 ks archival *XMM-Newton* observations (PI: Chon) the two peaks are not resolved due to point source contamination between the peaks (see Fig.6.1). The point source between the two peaks is clearly resolved in the short *Chandra* exposure and coincides with a relatively strong emission in the DSS2 blue band suggesting an AGN as the source (see Fig.6.2). The EPIC contours in Fig.6.3 show a large scale ellipticity and even a hint of a third galaxy group (Group 3) from optical and possibly extended X-ray emission. Deeper *Chandra* data will prove whether the emission is truly extended or a blur of point sources in that region. Group 3 and the main cluster emission could be covered by one ACIS-S chip.

Group 1 in Fig.6.2 is also known as SMACSJ2031.8-4036 which is a well studied cluster with strong-lensing features in the optical. All available deep high-resolution optical imaging with HST, MUSE (see Richard et al. 2015) and X-SHOOTER only cover Group 1. The colors and extent of Group 2 in the DSS2 image suggest that it is a similar subcluster at about the same redshift range. The redshift given for Group 1 is 0.331 (Richard et al.

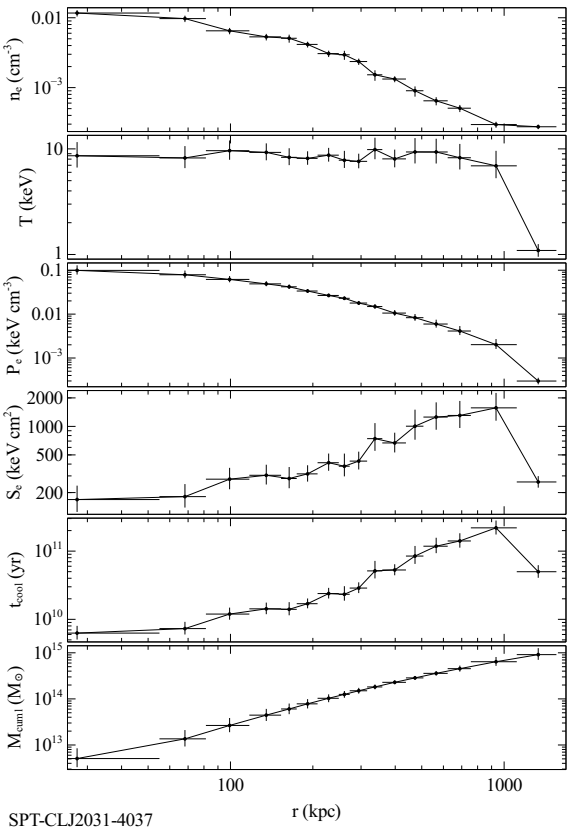

Figure 6.4: The profile was produced assuming hydrostatic equilibrium given an NFW mass model, a density profile in radial bins and an outer pressure. The model was compared to Chandra X-ray surface brightness profiles in ten different energy bands, computing the parameter uncertainties using Markov Chain Monte Carlo. The resulting thermodynamic profiles were calculated from the model parameters in the output chain. The median and 1-sigma percentile values are shown as the points with error bars. From top to bottom: density, temperature, pressure, entropy, cooling time, and cumulative mass. Outermost radial bin might be unreliable.

2015) which differs by 0.011 from the redshift given for the X-ray cluster (0.342, Böhringer et al. 2004).

The deeper *Chandra* exposure would also allow first estimates on overall turbulence in the ICM (see e.g. Hofmann et al. 2016b; Gaspari et al. 2014).

There are three strong indications for the system to be a major merger: 1. The substructure of the X-ray emission in the center (Fig.6.1) and elongation on larger scales (see large scale form in Fig.6.3). 2. The offset of two groups of galaxies in the optical from the X-ray emission (see Fig.6.2). The axis connecting the groups coincides with the axis along which the X-ray emission is elongated. Fig.6.5 even shows how the derived mass model

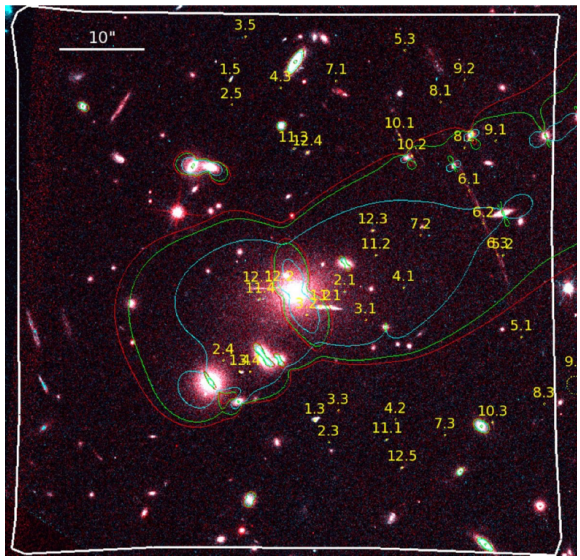

Figure 6.5: Overview from Richard et al. (2015) showing a Hubble color image of SMACSJ2031.8-4036 (F606W and F814W). The white region shows the 1x1 arcmin field-of-view of the MUSE instrument. The cyan, green, and red lines show critical lines from their mass model. The yellow numbers mark MUSE sources used in their analysis. Note the mass model extends towards the galaxies of Group 2 as seen in the wider DSS2 image.

from optical observations (Richard et al. 2015) extends in the direction of the second group. 3. Using a deprojection method introduced by Sanders et al. (2014) I obtained radial profiles of the cluster temperature suggesting an average temperature of almost 10 keV. This high temperature throughout the cluster suggests that it is undergoing strong heating and mixing of the ICM.

One ACIS chip ($\sim$ 5 arcmin radius) could cover 1.45 Mpc ($\sim 0.9\,r_{200}$). Given the brightness profile in the current data I expect to detect the cluster emission to a radius of $\sim$ 400 kpc with the additional 60 ks. The deeper observations will enable us to resolve surface brightness structure down to about 5 kpc in the central region to detect the expected surface brightness discontinuities caused by shocks in the ICM.

6.3.2 Technical Feasibility

The proposed 60 ks observation will significantly improve the spatial-spectral resolution for mapping the thermal structure of the cluster and allow us to detect a possible Mach cone as expected in a Bullet like major merger. As shown above one ACIS chip is sufficient to cover the cluster emission plus possible groups in the outskirts (Group 3, Fig.6.3). Since ACIS-S has better spectral resolution and higher sensitivity than ACIS-I, I propose to observe the cluster using ACIS-S. The higher background count rate of the ACIS-S chips should not affect my main analysis significantly since I focus on resolving the high surface

brightness regions of the cluster. The expected background count rate will be 0.15 cts/s in the 2 arcmin radius where I extracted the net source counts. For spatial-spectral bins with a S/N of 30, the cluster emission is detected with at least 5σ significance.

In the archival *Chandra* ACIS-I observation (ObsID 13517 from 2011-11-25 UT) I extracted $\sim 3.0 \times 10^3$ net counts from an extraction region with a radius of 2 arcmin around the center. Simulating the count rate in a new 60 ks ACIS-S observation of this cluster, I expect to obtain $\sim 2.3 \times 10^4$ additional counts. This would be an increase by a factor of 8.6 and I expect to increase the number of spectral-extraction bins from currently four to more than 30 bins (at S/N of 20 per bin). In the central area with negligible background the average S/N would increase by a factor of three. This will enable us to probe spatially resolved spectra to below 40 kpc, to obtain resolved spectra for the two surface-brightness peaks (see Fig.6.1), and probe possible temperature differences. The expected Galactic column density is $n_H = 3.95 \times 10^{20}\,cm^{-2}$.

To support the analysis of the outskirts there are 30 ks archival *XMM-Newton* observations (ObsID 0690170501 and 0690170701 from 2013-03-31 and 2013-04-22). The main subcluster of the system is a very prominent strong-lensing cluster with a large archive of high quality multiwavelength data to support future studies (so far only for one of the subclusters, SMACSJ2031.8-4036). Because the high resolution X-ray data of the system is comparatively very shallow it is important to obtain deeper *Chandra* data of the system.

6.4 Final conclusions

I presented one of the most detailed high resolution studies of a large sample of galaxy clusters to date with applications to understand the physics of the hot ICM phase and how this influences cluster cosmology studies. Furthermore I investigated the potential for direct dark matter search in X-ray spectra of galaxy clusters triggered by recent progress in the field. Finally I used my findings from cluster observations with current state of the art X-ray observatories to make predictions about the capabilities of the upcoming eROSITA all-sky survey.

The most important conclusions of my work are:

1. In the very deep dataset of *Chandra* X-ray cluster observations there is no significant indication for the presence of an unidentified X-ray emission line at 3.55 keV. This puts tight constraints on the mixing angle in a proposed scenario where hypothetical sterile neutrinos make up all of the DM in the universe. I did find other residual lines in the spectral fits indicating that the models for cluster X-ray emission have to be updated for the very deep observations which have been obtained over the past decade of X-ray astronomy.

2. I found significant evidence that there are turbulent motions in the ICM. This turbulence on average has a Mach number of 0.2 (velocities on the order of 200 km/s) and contains about four percent of the thermal energy of the ICM. These additional four per cent cause a non-thermal pressure support to the cluster gas so cluster masses estimated from hydrostatic equilibrium will be overestimated by four percent on average. This exact

number has recently been confirmed in the center of the Perseus cluster by the only observation of the Hitomi observatory (Hitomi Collaboration et al. 2016a) before its critical failure.

3. I found a significant low bias in the cluster temperatures (due to blended temperature substructure) expected to be obtained by the upcoming eROSITA survey. Simulations of cluster spectra showed that cluster temperatures obtained in the all-sky X-ray survey of eROSITA will be biased low by about five per cent (between redshift 0.1 and 0.8). This means that the cluster masses obtained from hydrostatic equilibrium scaling relations $T_{X,eROSITA} - M_{tot,cluster}$ will be underestimated by about 7.5 per cent. Together with conclusion 2 (see above) this means that assuming hydrostatic equilibrium cluster masses will be $-7.5 + 4 = -3.5$ per cent underestimated in the eROSITA four year all-sky survey.

Appendix A

Thermodynamic perturbations

A.1 Intrinsic spread python code

This section shows the python code developed to derive the intrinsic scatter of data points in radial profiles with error-bars. It constitutes the central calculation for the analysis of thermodynamic perturbations in the cluster maps I derived from *Chandra* observations.

```
#!/usr/bin/env python

##Authors: Jeremy Sanders & Florian Hofmann (MPE, 2015)##

#calculate spread for a set of data points
#main input: x, y, yerr (assumes kpc as x units)
#input sorted on x!


#-----------------------------------------------------
#import needed modules

import numpy as np
import emcee                    #see http://dan.iel.fm/emcee/current/
import matplotlib.pyplot as plt #only needed for test plots
import atpy                     #see https://atpy.readthedocs.org/en/latest/

#setup chain properties
nwalkers = 100
niters = 1000
nburn = 1000


#-----------------------------------------------------
```

```
#define main function

def spread_constraints(rads, data, errs, num, radius):
    """Return 1 sigma constraints on the mean and spread of the data.

    rads: array of radii
    data: array of numbers
    errs: array of errors (1sigma)
    num: number of nodes for spread calculation (radial bins)
    radius: 0 for automatic binning
            radius (in same units as rads) for splitting the profile
            (inside and outside region comparison)
    """

    def makenodes(rads, data):
        #set annuli
        nodesx = []
        nodesy = []
        binl = np.int16(len(rads)/7.)
        if binl < 5.:
            binl = 5
        b = 0
        for i in range(len(rads)/binl):
            nodesx.append(rads[b])
            nodesy.append(data[b])
            b += binl
        nodesx.append(rads[-1])
        nodesy.append(data[-1])
        return nodesx, nodesy

    def calcmodel(y):
        mean = 10**(np.interp(np.log10(rads),np.log10(nx),y))
        return mean

    def lnprob(pars):
        #y1, y2, y..., spread = pars
        y = pars[:len(nx)]
        spread = pars[len(nx):]

        spread = spread[bins]

        mean = calcmodel(y)
```

```
        spread = mean*spread

        if np.max(spread) > 1e10 or np.min(spread) < -1e10:
            return -np.inf

        comberr2 = errs**2 + spread**2
        chi2 = np.sum( (data-mean)**2 / comberr2 )

        loglikelihood = -chi2/2 + \
        np.sum(np.log(1/np.sqrt(2*np.pi*comberr2)))
        if np.isnan(loglikelihood):
            print "!!!", loglikelihood, chi2, comberr2, mean
        return loglikelihood

    # initial parameters
    # sort by radius (comment if already sorted input)
    #sorting = np.argsort(rads)
    #rads = rads[sorting]
    #data = data[sorting]
    #errs = errs[sorting]

    # get number of nodes
    nx, guess_y = makenodes(rads,data)
    if radius == 0:
        binl = np.int16(len(rads)/np.float(num))
        if binl < 5.:
            binl = 5
            num = np.int16(len(rads)/5.)
        guess_spread = [ 0.05 for i in range(num) ]
        # get spread nodes
        bins = []
        for k in range(num):
            binl = np.int16(len(rads)/np.float(num))
            for l in range(binl):
                bins.append(k)
        if len(bins) < len(rads):
            for l in range(len(rads)-len(bins)):
                bins.append(k)
    else:
        #split by given radius in kpc
        num = 2
        guess_spread = [ 0.05 for i in range(num) ]
        # get spread nodes
```

```
        bins = []
        for k in range(len(rads)):
            if rads[k] < radius:
                bins.append(0.)
            else:
                bins.append(1.)
    p0 = []
    for n in range(nwalkers):
        parlst = ()
        for k in range(len(nx)):
            parlst += (np.random.normal(loc=1,scale=0.001)\
            *np.log10(guess_y[k]),)
        for k in range(num):
            parlst += (np.random.normal(loc=1,scale=0.001)\
            *guess_spread[k],)
        p0.append(parlst)


    sampler = emcee.EnsembleSampler(nwalkers, len(p0[0]), lnprob)

    # print "Burning in"
    pos, prob, state = sampler.run_mcmc(p0, nburn)
    sampler.reset()

    # print "Running"
    sampler.run_mcmc(pos, niters)

    y_vals = []
    for k in range(len(nx)):
         y_vals.append(10**(np.ravel(sampler.chain[:,:,k])))
    # note abs here as the spread is symmetric (squared above)
    spread_vals = []
    for k in range(num):
         spread_vals.append\
         (np.abs(np.ravel(sampler.chain[:,:,len(nx)+k])))

    # 1 sigma percentiles
    y_perc = []
    spread_perc = []
    for k in range(len(nx)):
         y_perc.append(np.percentile(y_vals[k], [15.87, 50, 84.13]))
    for l in range(num):
        his = np.histogram(spread_vals[l],bins=100,\
```

```
range=(0.,np.percentile(spread_vals[1], 95.)))
peaky = np.max(his[0])
peakx = his[1][his[0] == peaky][0]
j = 0.
x = np.where(his[0] == peaky)
x = np.mean(x)
x = np.int(x)
rgts = np.float(np.sum(his[0][x:]))/(nwalkers*niters*0.95)
fac = rgts/0.5
while j <= nwalkers*niters*0.95*0.3413*fac:
    if peaky > nwalkers*niters*0.95*0.5:
        k = 2.
        break
    if j == 0.:
        j += his[0][x]/2.
    else:
        j += his[0][x]
    k = his[1][x]
    x += 1
    if k > np.percentile(spread_vals[1], 95.):
        k = np.percentile(spread_vals[1], 95.)
        break
errup = k
j = 0.
x = np.where(his[0] == peaky)
x = np.mean(x)
x = np.int(x)
rgts = np.float(np.sum(his[0][:x]))/(nwalkers*niters*0.95)
fac = rgts/0.5
###account for cut part
if his[0][0] >= 10. and x != 0:
    slo = (peaky-his[0][0])/(peakx)
    deltax = his[0][0]/slo
    fac2 = (((peakx+deltax)*peaky)-deltax*his[0][0])\
           /((peakx+deltax)*peaky)
else:
    fac2 = 1
###
while j <= nwalkers*niters*0.95*0.3413*fac*(1/fac2):
    if peaky > nwalkers*niters*0.95*0.5:
        k = 0.
        break
    if j == 0.:
```

```
            j += his[0][x]/2.
        else:
            j += his[0][x]
        k = his[1][x]
        x -= 1
        if x == 0:
            k = 0.
            break
    errlo = k
    if peakx == 0.:
        errlo = 0.
    spread_perc.append([peakx,errup-peakx,peakx-errlo])

return bins, nx, y_perc, spread_perc


#-----------------------------------------------------
######enable for testing the script:##########

#first radius not at 0!
rads = np.arange(100)+1
data = np.random.rand(100)*100
errs = 2*np.abs(np.random.normal(data,scale=1.0)-data)
num = 2
radius = 0

print '----------------input:----------------\n'
print 'radii:  \n\n', rads, '\n'
print 'data:  \n\n', data, '\n'
print 'errors:  \n\n', errs, '\n'
print 'number of bins:  \n\n', num, ' \
       fixed splitting radius:', radius, '\n'

print ' --- '
print 'running script'
print ' --- ', '\n\n'

bins, nx, y_perc, spread_perc = \
spread_constraints(rads, data, errs, num, radius)

print '----------------results:---------------\n'
print 'radial bin number of radii:  \n\n', bins, '\n'
```

```
print 'radii of model nodes:  \n\n', nx, '\n'
print '[lower, middle, and upper] percentile \
       values for model at each node:  \n\n', y_perc, '\n'
print 'most likely intrinsic spread and upper/\
       lower errors (per radial bin):  \n\n', spread_perc, '\n'
```

A.2 Cluster sample

Table A.1: *Chandra* cluster sample (CIZA clusters).

Cluster[a]	Exp[b] [ks]	RA (J2000) [deg]	DEC (J2000) [deg]	Flux[c] [10^{-15} W/m^2]	z	Obj. ID (CIZA)	L_X[d] [10^{37} W]
CYGNUS A	232	299.877	40.741	52.82	0.0561	J1959.5+4044	7.08
PKS 0745-191	174	116.883	-19.290	45.73	0.1028	J0747.5-1917	20.36

[a] Most commonly used name of cluster or central object.
[b] Combined ACIS-S/-I exposure after excluding times of high background.
[c] ROSAT 0.1-2.4 keV X-ray flux in 10^{-15} W/m^2
[d] ROSAT 0.1-2.4 keV X-ray luminosity in 10^{37} W (CIZA column: LX)

Table A.2: *Chandra* cluster sample (NORAS clusters).

Cluster[a]	Exp[b] [ks]	RA (J2000) [deg]	DEC (J2000) [deg]	Flux[c] [10^{-15} W/m^2]	z	Obj. ID (NORAS)	L_X[d] [10^{37} W]
A 2052	651	229.182	7.013	47.94	0.0353	RXC J1516.7+0701	2.58
A 1775	99	205.448	26.352	12.58	0.0724	RXC J1341.8+2622	2.83
A 2199	156	247.188	39.553	97.92	0.0299	RXC J1628.6+3932	3.77
2A 0335+096	102	54.665	10.007	80.91	0.0347	RXC J0338.6+0958	4.21
3C348 (HERCULES A)	112	252.778	4.985	5.39	0.154	RXC J1651.1+0459	5.49
A 2034	255	227.532	33.515	11.94	0.113	RXC J1510.1+3330	6.49
MS0735.6+7421	520	115.421	74.266	4.06	0.2149	RXC J0741.7+7414	7.94
A 2146	418	239.006	66.352	3.99	0.2339	RXC J1556.1+6621	9.31
A 1795	958	207.221	26.596	59.29	0.0622	RXC J1348.8+2635	9.93
A 1413	136	178.769	23.369	12.61	0.1427	RXC J1155.3+2324	10.91
A 401	163	44.727	13.579	50.29	0.0739	RXC J0258.9+1334	11.76
A 1995	100	223.168	58.049	3.18	0.3179	RXC J1452.9+5802	13.42
MS 1455.0+2232	108	224.253	22.33	4.89	0.2579	RXC J1457.2+2220	13.73
A 520	527	73.546	2.977	8.33	0.203	RXC J0454.1+0255	14.52
A 665	140	127.637	65.89	11.18	0.1818	RXC J0830.9+6551	15.69
A 2204	97	248.186	5.557	24.11	0.1514	RXC J1632.7+0534	23.43
A 2390	110	328.403	17.683	11.01	0.2329	RXC J2153.5+1741	25.15
ZW 3146	84	155.906	4.167	8.77	0.285	RXC J1023.6+0411	29.91
A 1835	223	210.271	2.895	12.12	0.2528	RXC J1401.0+0252	32.56

[a] Most commonly used name of cluster or central object.
[b] Combined ACIS-S/-I exposure after excluding times of high background.
[c] ROSAT 0.1-2.4 keV X-ray flux in 10^{-15} W/m^2
[d] ROSAT 0.1-2.4 keV X-ray luminosity in 10^{37} W (NORAS column: LX)

Table A.3: *Chandra* cluster sample (REFLEX clusters).

Cluster[a]	Exp[b] [ks]	RA (J2000) [deg]	DEC (J2000) [deg]	Flux[c] [10^{-15} W/m^2]	z	Obj. ID (REFLEX)	L_X[d] [10^{37} W]
SERSIC 159-03	106	348.515	-42.713	23.412	0.0564	J2313.9-4244	3.74
A 496	88	68.403	-13.25	72.075	0.0326	J0433.6-1315	3.89
HYDRA A	224	139.527	-12.092	39.461	0.0539	J0918.1-1205	5.61
A 1650	229	194.664	-1.781	20.909	0.0845	J1258.6-0145	6.99
A 2597	146	351.337	-12.136	20.558	0.0852	J2325.3-1207	7.22
A 3667	528	303.211	-56.855	70.892	0.0556	J2012.5-5649	10.02
A 907	103	149.528	-11.086	7.833	0.1669	J0958.3-1103	10.13
A 521	165	73.558	-10.273	4.944	0.2475	J0454.1-1014	12.97
A 2744	124	3.586	-30.352	4.964	0.3066	J0014.3-3023	19.79
A 1689	197	197.808	-1.337	15.332	0.1832	J1311.4-0120	23.59
1E 0657-56	566	104.751	-55.904	9.079	0.2965	J0658.5-5556	35.55
RX J1347-114	232	206.889	-11.734	6.468	0.4516	J1347.5-1144	63.43

[a] Most commonly used name of cluster or central object.
[b] Combined ACIS-S/-I exposure after excluding times of high background.
[c] ROSAT 0.1-2.4 keV X-ray flux in 10^{-15} W/m^2
[d] ROSAT 0.1-2.4 keV X-ray luminosity in 10^{37} W (REFLEX column: LumCor, h=0.5)

A.3 *Chandra* datasets

Table A.4: *Chandra* datasets used in this study.

Cluster[a]	*Chandra* ObsID[b]
1e0657	554,3184,4984,4985,4986,5355,5356,5357,5358,5361
2a0335	919,7939,9792
3c348	1625,5796,6257
a1413	537,1661,5002,5003,7696
a1650	4178,5822,5823,6356,6357,6358,7242,7691
a1689	540,1663,5004,6930,7289,7701
a1775	12891,13510
a1795	493,494,3666,5286,5287,5288,5289,5290,6159,6160,6161,6162,6163, 10432,10433,10898,10899,10900,10901,12026,12027,12028,12029,13106,13107, 13108,13109,13110,13111,13112,13113,13412,13413,13414,13415,13416,13417, 14268,14269,14270,14271,14272,14273,14274,14275,15485,15486,15487,15488,15489, 15490,15491,15492,16432,16433,16434,16435,16436,16437,16438,16439,16465,16466, 16467,16468,16469,16470,16471,16472
a1835	495,496,6880,6881,7370
a1995	906,7021,7713
a2034	2204,7695,12885,12886,13192,13193
a2052	890,5807,10477,10478,10479,10480,10879,10914,10915,10916,10917
a2146	10464,10888,12245,12246,12247,13020,13021,13023,13120,13138
a2199	497,498,10748,10803,10804,10805
a2204	499,6104,7940
a2390	500,501,4193
a2597	922,6934,7329,15144
a2744	2212,7712,7915,8477,8557
a3667	513,889,5751,5752,5753,6292,6295,6296,7686
a401	518,2309,14024
a496	931,3361,4976
a520	528,4215,7703,9424,9425,9426,9430
a521	430,901,12880,13190
a665	531,3586,7700,12286,13201,15148
a907	535,3185,3205
cygnusa	360,5830,5831,6225,6226,6228,6229,6250,6252
hydraa	575,576,4969,4970
ms0735	4197,10468,10469,10470,10471,10822,10918,10922
ms1455	543,4192,7709
pks0745	508,2427,6103,7694,12881
rxj1347	506,507,3592,13516,13999,14407
sersic159	1668,11758
zw3146	909,9371

[a] Abbreviated cluster name.
[b] List of *Chandra* observations used in this study (indicated by their ObsID, observation identification number).

A.4 Perturbation table

Table A.5: Measured fractional perturbations.

Cluster[a]	dP[b] [per cent]	dS[b] [per cent]	dT[b] [per cent]	dn[b] [per cent]
1e0657	$20.4^{+1.6}_{-1.4}$	$17.3^{+2.1}_{-1.5}$	$8.8^{+1.5}_{-1.4}$	$20.9^{+1.2}_{-0.9}$
2a0335	$11.7^{+0.6}_{-0.5}$	$19.8^{+0.9}_{-0.6}$	$9.3^{+0.5}_{-0.4}$	$13.5^{+0.6}_{-0.4}$
3c348	$1.3^{+2.9}_{-1.3}$	$12.0^{+1.9}_{-1.7}$	$3.6^{+2.0}_{-2.8}$	$8.5^{+0.9}_{-0.6}$
a1413	$5.4^{+1.9}_{-4.0}$	$6.4^{+2.8}_{-2.6}$	$0.3^{+2.4}_{-0.3}$	$8.7^{+1.0}_{-0.7}$
a1650	$5.5^{+0.9}_{-1.0}$	$14.0^{+1.0}_{-1.0}$	$4.0^{+1.0}_{-1.0}$	$10.0^{+0.7}_{-0.5}$
a1689	$0.6^{+2.7}_{-0.6}$	$1.1^{+2.8}_{-1.1}$	$0.8^{+2.1}_{-0.8}$	$3.8^{+0.4}_{-0.2}$
a1775	$0.6^{+3.5}_{-0.6}$	$20.7^{+2.6}_{-2.3}$	$12.6^{+1.9}_{-2.1}$	$8.0^{+0.8}_{-0.8}$
a1795	$5.3^{+0.2}_{-0.2}$	$22.3^{+0.5}_{-0.2}$	$11.7^{+0.4}_{-0.1}$	$12.4^{+0.3}_{-0.1}$
a1835	$6.0^{+1.1}_{-1.1}$	$15.8^{+1.5}_{-1.1}$	$9.3^{+1.0}_{-0.8}$	$8.8^{+0.6}_{-0.5}$
a1995	$5.7^{+5.5}_{-5.7}$	$13.6^{+4.9}_{-3.5}$	$11.4^{+3.7}_{-5.8}$	$7.0^{+1.6}_{-0.9}$
a2034	$12.8^{+2.2}_{-1.7}$	$6.5^{+2.1}_{-2.4}$	$6.1^{+1.6}_{-3.4}$	$9.1^{+1.0}_{-0.7}$
a2052	$7.5^{+0.2}_{-0.2}$	$18.3^{+0.6}_{-0.4}$	$11.6^{+0.4}_{-0.2}$	$10.1^{+0.3}_{-0.2}$
a2146	$20.3^{+1.9}_{-1.9}$	$37.1^{+4.1}_{-3.2}$	$12.2^{+1.7}_{-1.4}$	$24.3^{+2.7}_{-1.5}$
a2199	$7.6^{+0.4}_{-0.3}$	$13.2^{+0.6}_{-0.4}$	$7.3^{+0.4}_{-0.3}$	$8.6^{+0.3}_{-0.3}$
a2204	$6.7^{+1.2}_{-1.3}$	$13.7^{+1.7}_{-1.0}$	$8.7^{+1.1}_{-1.0}$	$7.6^{+0.5}_{-0.5}$
a2390	$11.4^{+2.0}_{-1.8}$	$19.0^{+2.6}_{-1.9}$	$12.4^{+2.1}_{-2.0}$	$11.2^{+1.1}_{-0.8}$
a2597	$8.1^{+0.8}_{-0.6}$	$8.9^{+0.8}_{-0.6}$	$5.5^{+0.6}_{-0.6}$	$7.2^{+0.5}_{-0.4}$
a2744	$9.8^{+4.2}_{-9.8}$	$13.4^{+3.1}_{-2.7}$	$7.6^{+3.5}_{-7.6}$	$15.1^{+1.4}_{-1.1}$
a3667	$24.6^{+1.1}_{-1.1}$	$12.4^{+0.7}_{-0.5}$	$16.1^{+0.9}_{-0.7}$	$11.4^{+0.5}_{-0.4}$
a401	$6.1^{+1.3}_{-1.5}$	$8.1^{+1.0}_{-1.3}$	$2.8^{+1.3}_{-2.8}$	$7.5^{+0.5}_{-0.3}$
a496	$9.0^{+0.6}_{-0.6}$	$21.7^{+1.2}_{-1.0}$	$14.0^{+0.9}_{-0.6}$	$8.9^{+0.5}_{-0.4}$
a520	$12.6^{+2.0}_{-1.8}$	$15.0^{+2.6}_{-1.4}$	$7.6^{+1.9}_{-1.7}$	$11.5^{+1.4}_{-0.9}$
a521	$12.1^{+5.3}_{-7.8}$	$16.7^{+8.2}_{-7.2}$	$10.0^{+6.4}_{-8.0}$	$10.7^{+2.3}_{-1.4}$
a665	$11.8^{+2.4}_{-2.4}$	$8.2^{+2.6}_{-4.6}$	$6.5^{+2.6}_{-3.9}$	$11.0^{+0.9}_{-0.8}$
a907	$0.2^{+2.4}_{-0.2}$	$12.1^{+1.9}_{-1.7}$	$1.7^{+2.9}_{-1.7}$	$9.5^{+0.9}_{-0.6}$
cygnusa	$18.2^{+1.0}_{-0.8}$	$23.4^{+1.3}_{-1.0}$	$14.1^{+0.8}_{-0.6}$	$27.3^{+1.2}_{-0.9}$
hydraa	$9.8^{+0.4}_{-0.3}$	$14.4^{+0.6}_{-0.5}$	$9.7^{+0.4}_{-0.3}$	$7.8^{+0.3}_{-0.2}$
ms0735	$10.6^{+1.5}_{-0.9}$	$14.0^{+1.7}_{-1.2}$	$7.8^{+1.2}_{-0.8}$	$10.3^{+1.0}_{-0.7}$
ms1455	$4.1^{+2.0}_{-3.5}$	$19.0^{+2.6}_{-1.9}$	$9.0^{+2.0}_{-1.5}$	$11.1^{+1.0}_{-0.8}$
pks0745	$3.4^{+1.0}_{-1.9}$	$19.0^{+1.0}_{-0.8}$	$9.4^{+0.8}_{-0.6}$	$11.6^{+0.4}_{-0.5}$
rxj1347	$13.4^{+2.3}_{-2.3}$	$23.4^{+3.3}_{-2.1}$	$16.0^{+2.3}_{-2.0}$	$13.8^{+1.5}_{-0.8}$
sersic159	$9.7^{+1.1}_{-0.7}$	$11.4^{+1.1}_{-1.1}$	$5.2^{+0.6}_{-0.6}$	$9.2^{+0.9}_{-0.5}$
zw3146	$0.4^{+2.3}_{-0.4}$	$25.9^{+2.5}_{-2.2}$	$10.9^{+1.9}_{-1.9}$	$15.9^{+1.3}_{-0.9}$

[a] Abbreviated cluster name.
[b] Measured average fractional spread of thermodynamic properties for the whole cluster (see Sect. 3.2.1, M=1) in per cent.

A.5 2D Maps

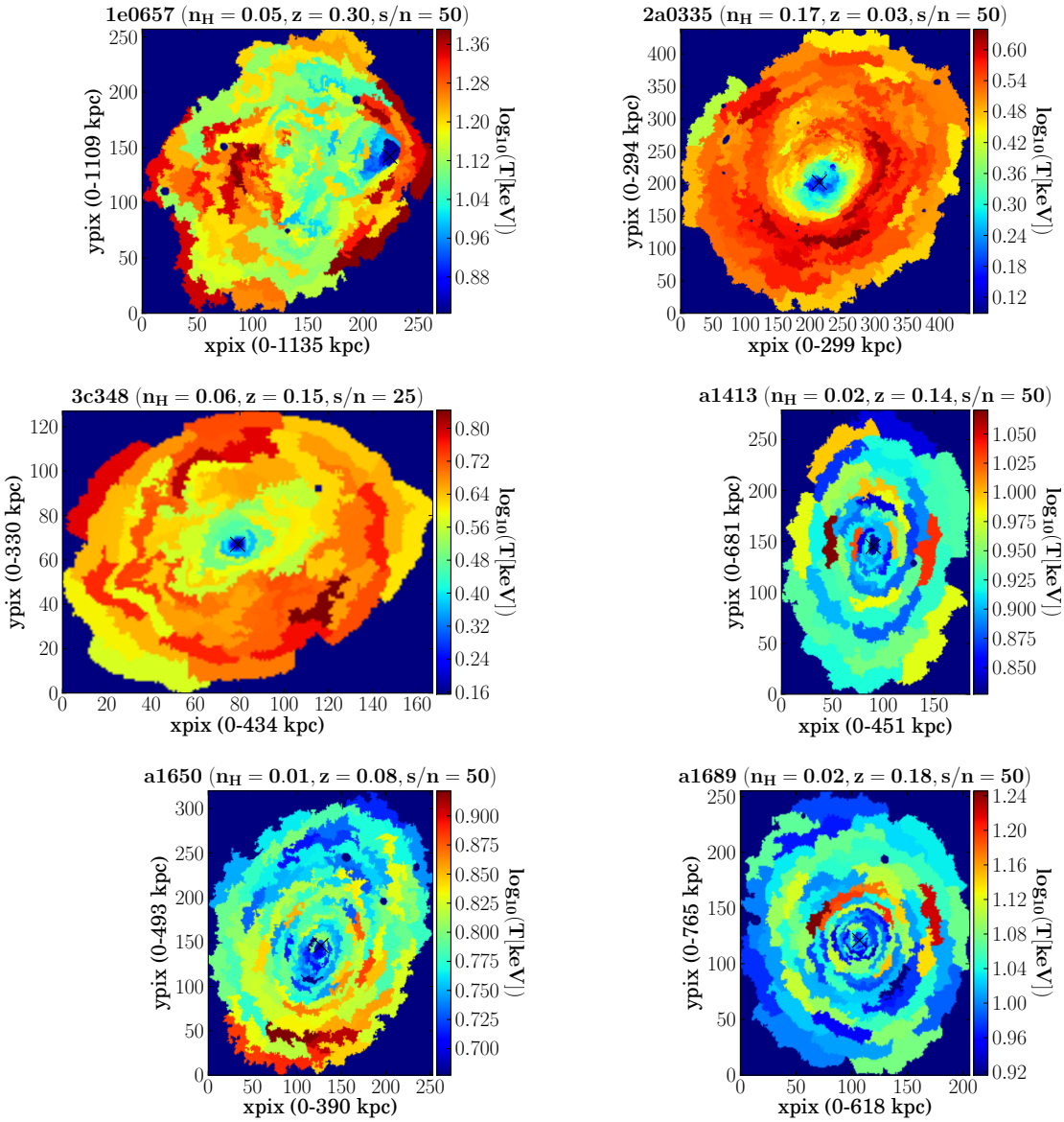

Figure A.1: Temperature maps of all clusters in the sample. Bins have a S/N of 50 or 25 (see Sect. 3.2.1) and temperatures are shown on a logarithmic colour scale. Excluding areas below the surface brightness cut (area-normalised normalisation $> 10^{-7}$ cm^{-5} arcsec^{-2}) and where the errors on temperature are more than twice the best fit temperature value. The plot title gives the abbreviated cluster name, the average foreground column density n_H [cm^{-2}], and the redshift z. Scale: 1pix $\sim$ 1arcsec. Crosses mark the peak of the X-ray emission.

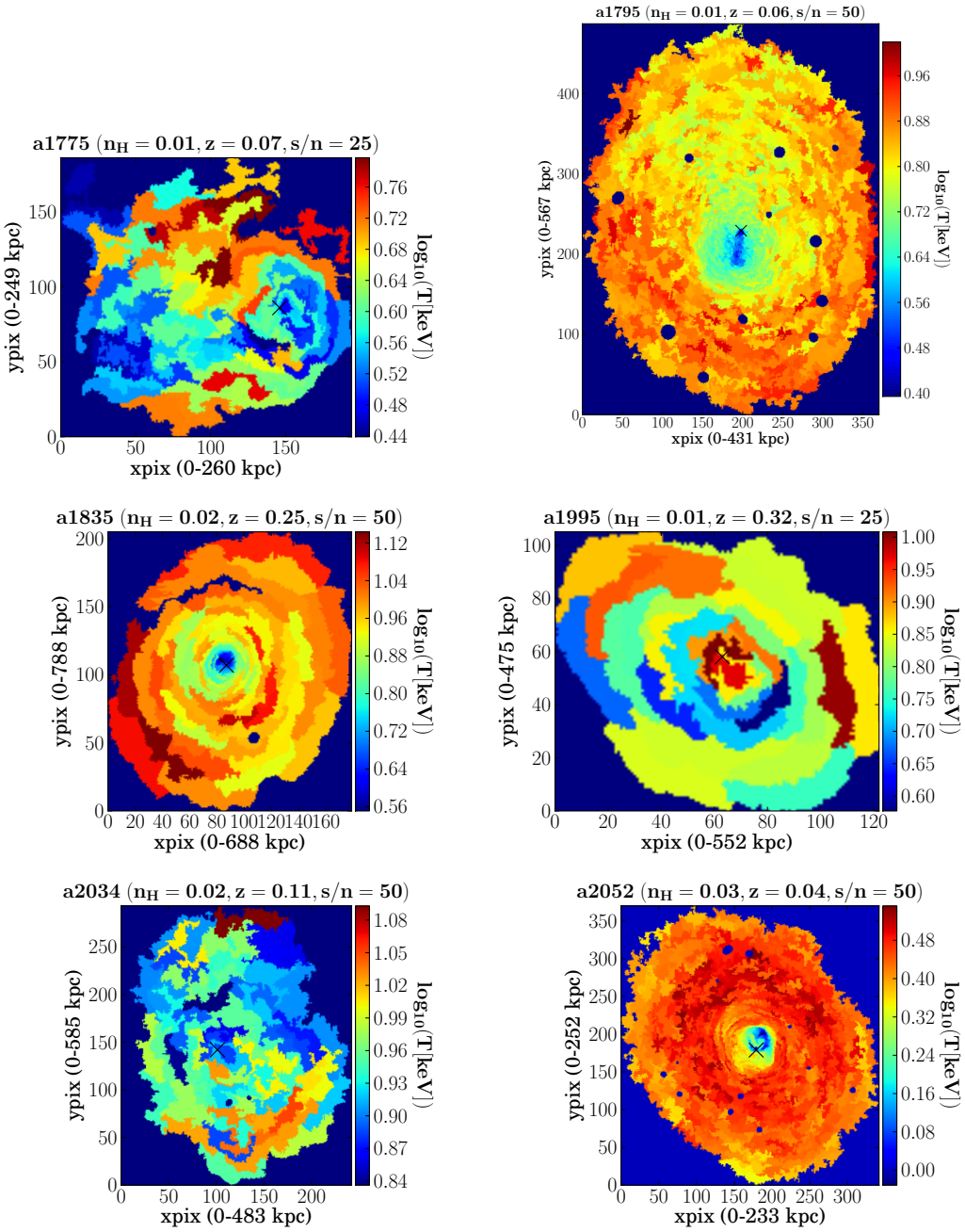

Figure A.1: continued.

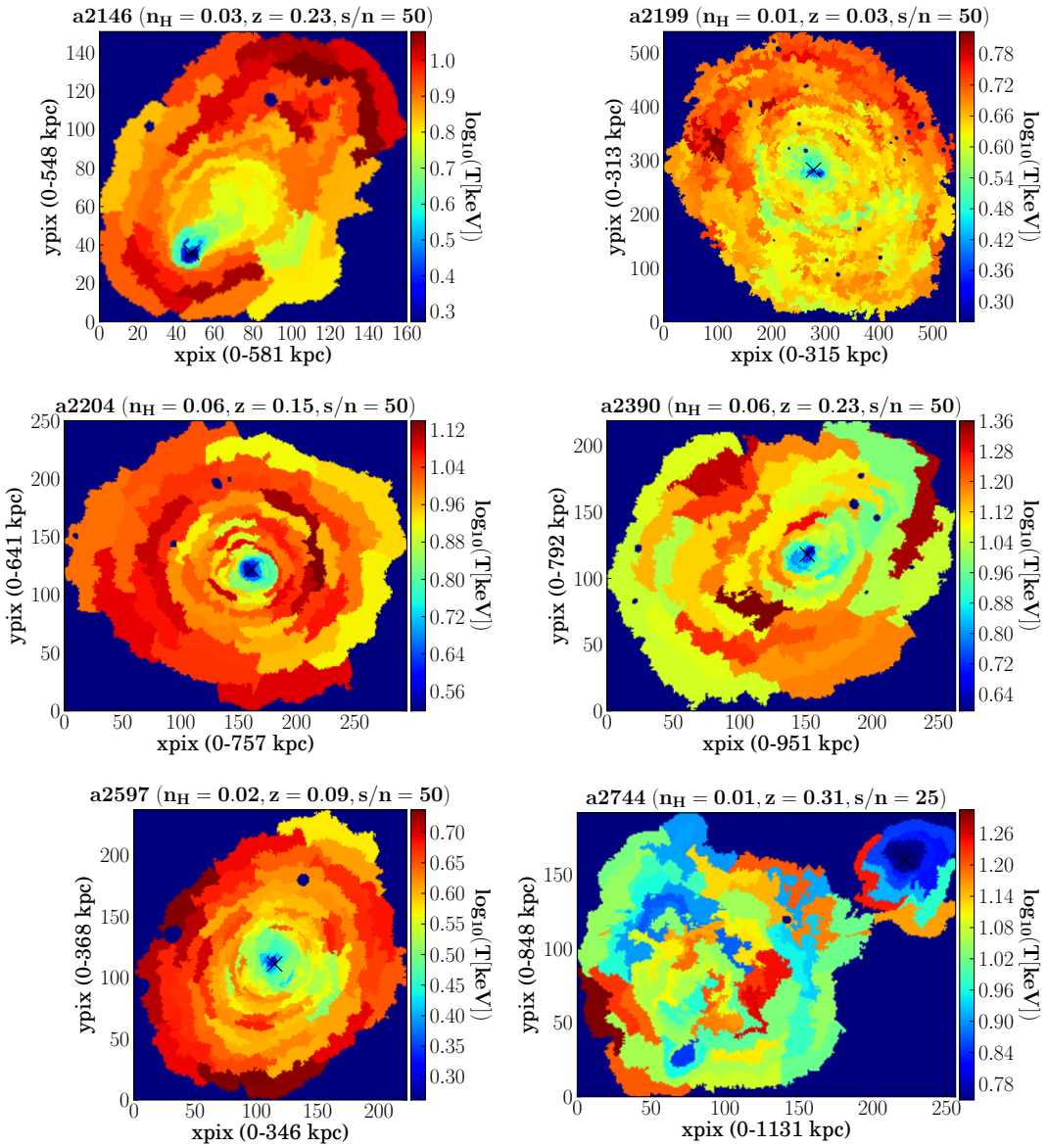

Figure A.1: continued.

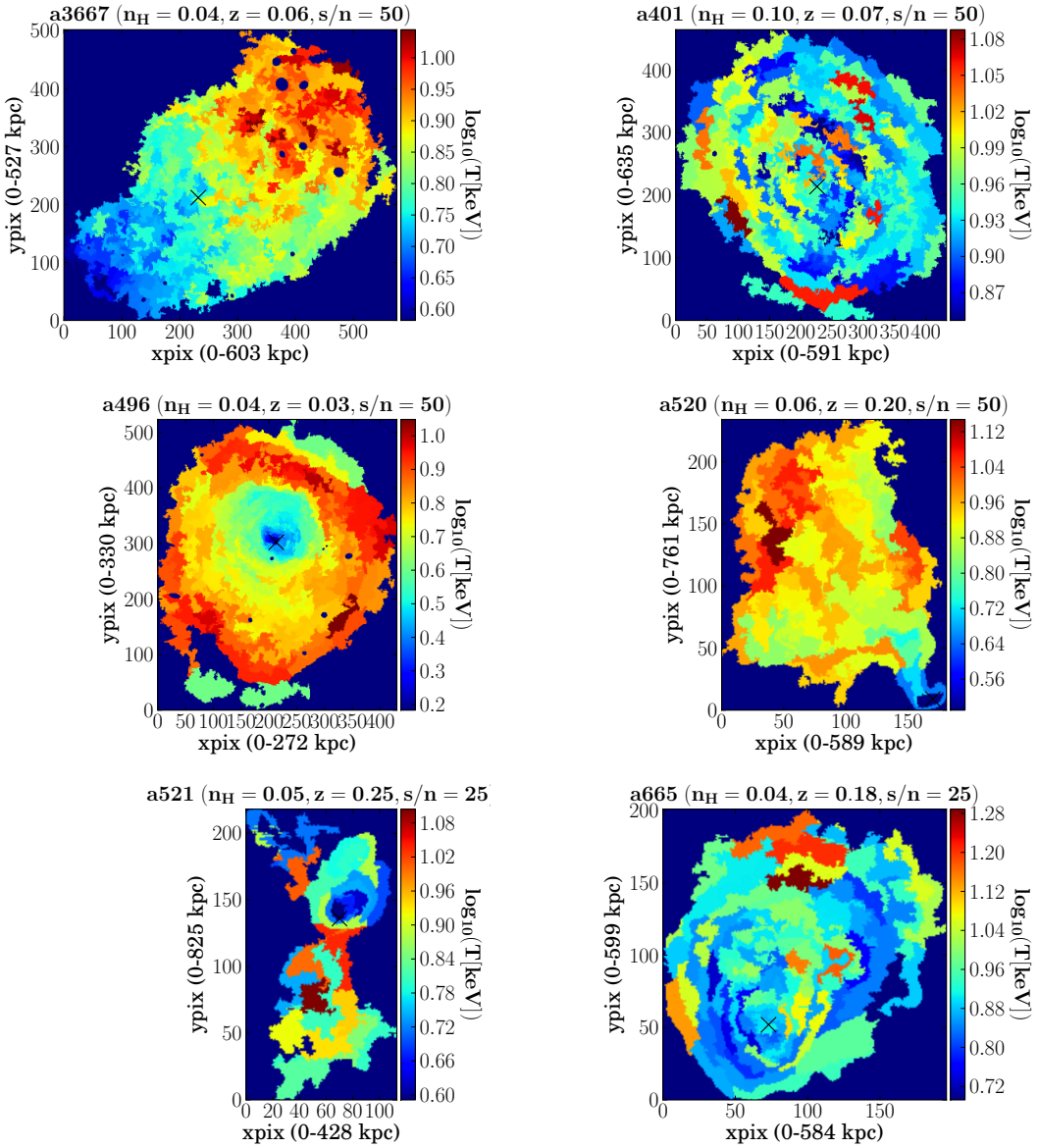

Figure A.1: continued.

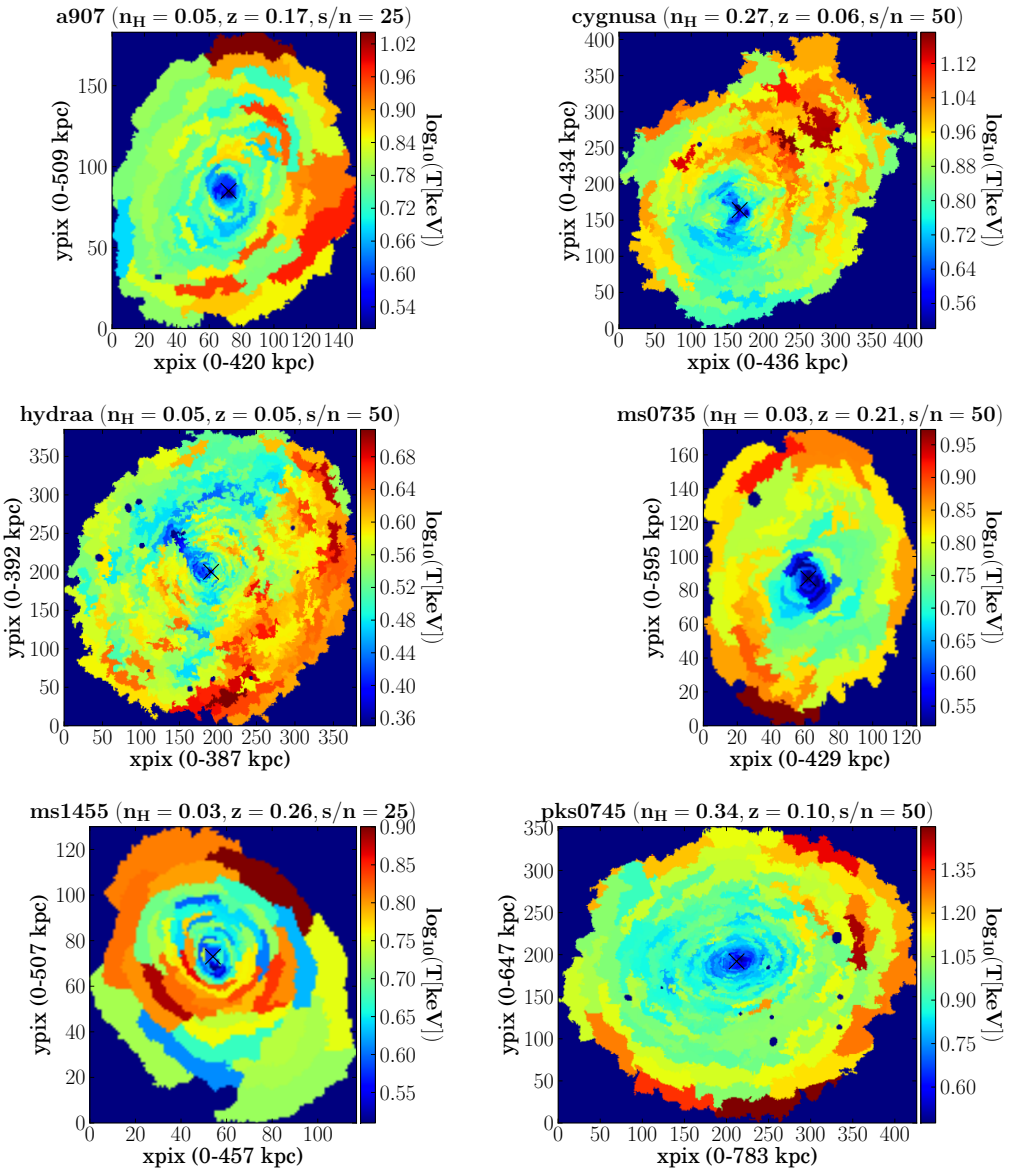

Figure A.1: continued.

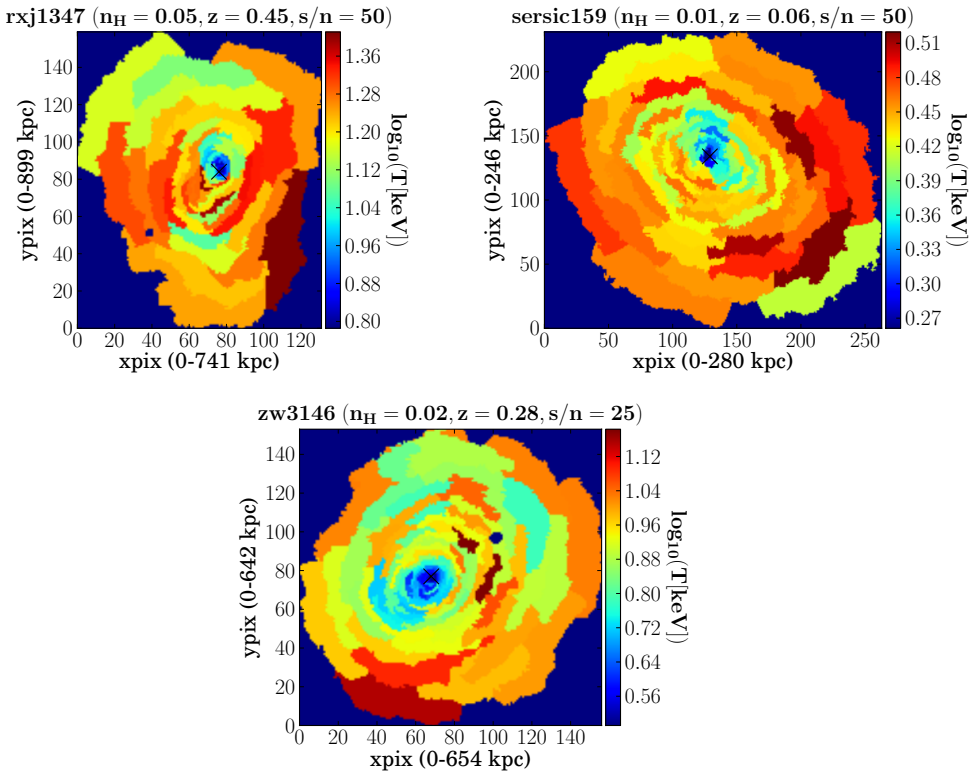

Figure A.1: continued.

A.6 Unsharp-masked count images

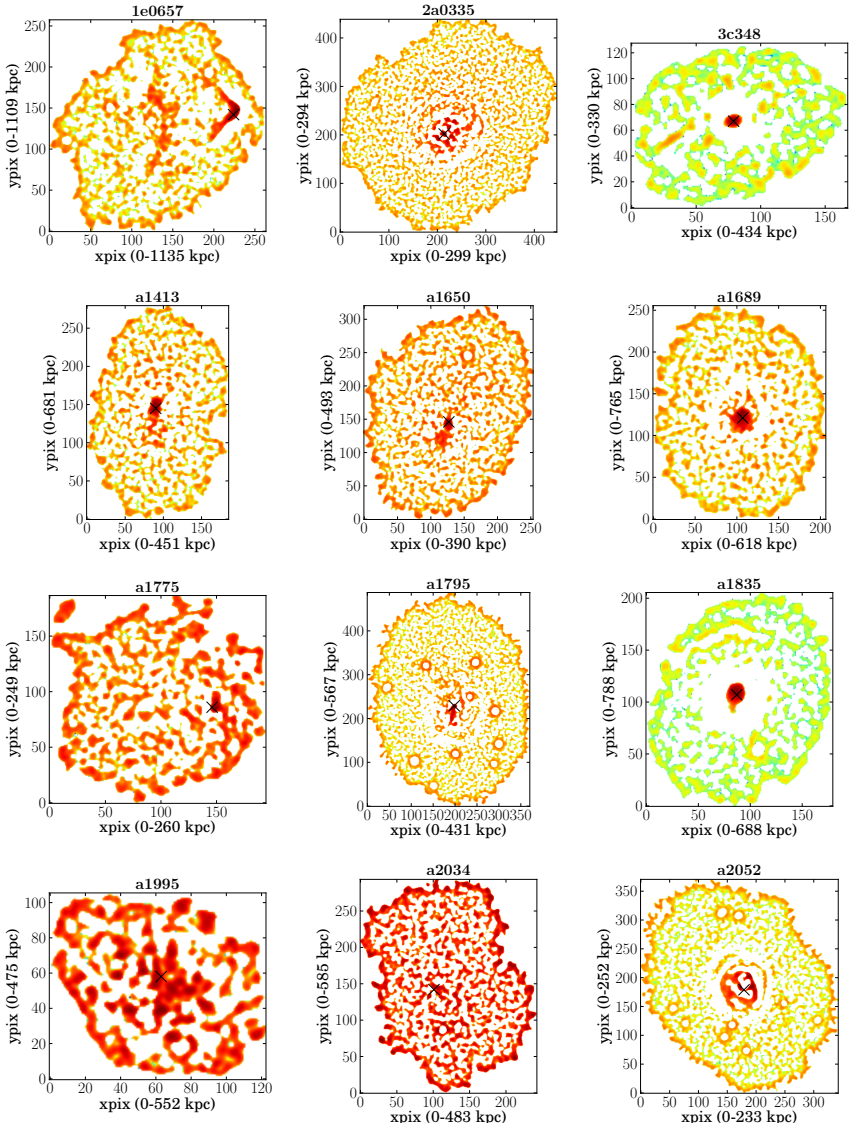

Figure A.2: Unsharp-masked exposure-corrected images (logarithmic colour scale) of all clusters in the sample showing the difference between two count images smoothed with a Gaussian function (2 pixels and 5 pixels sigma). Colours indicate relative surface brightness differences (over-densities dark red, under-dense areas green to white). Scale: 1pix $\sim$ 1arcsec. Crosses mark the peak of the X-ray emission.

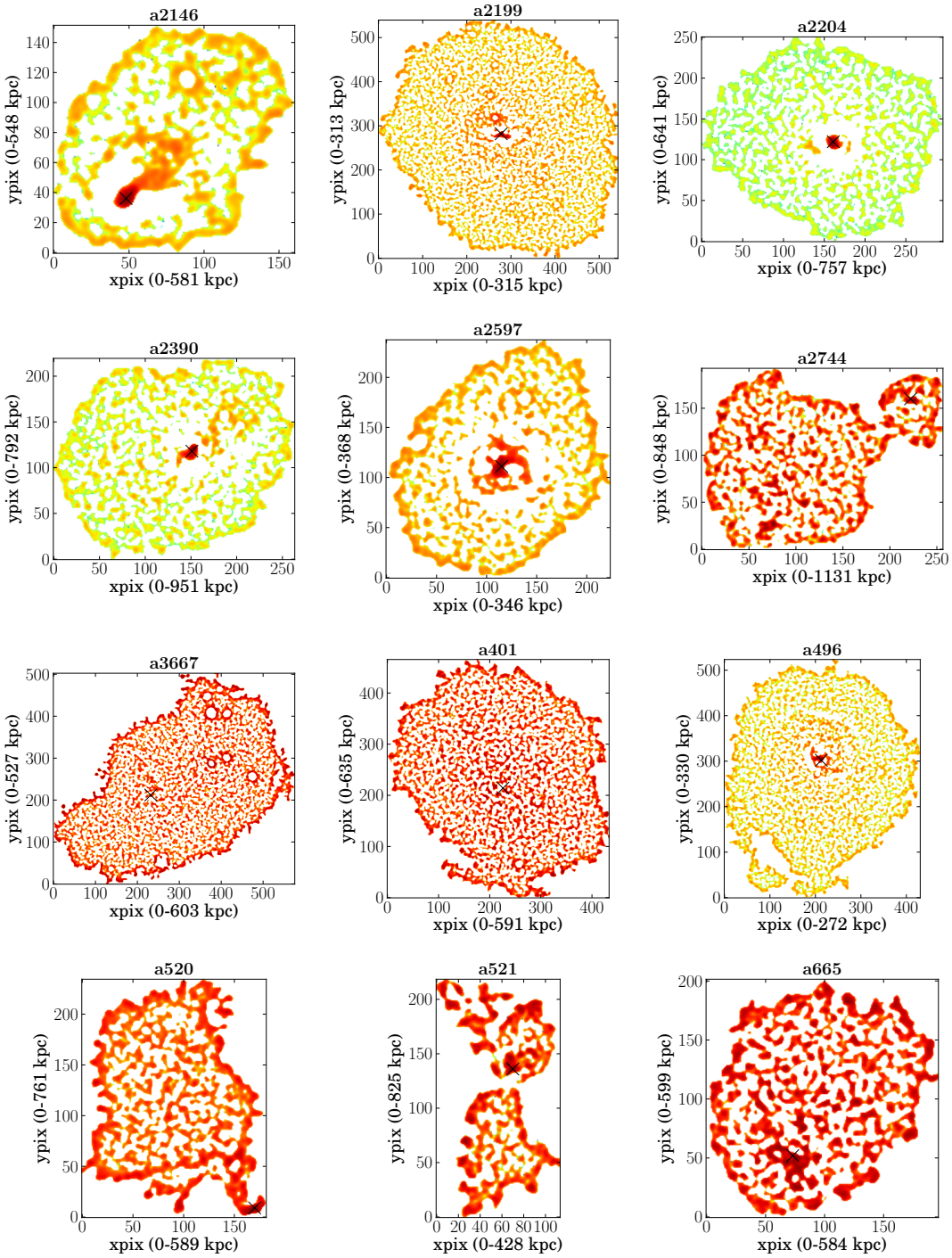

Figure A.2: continued.

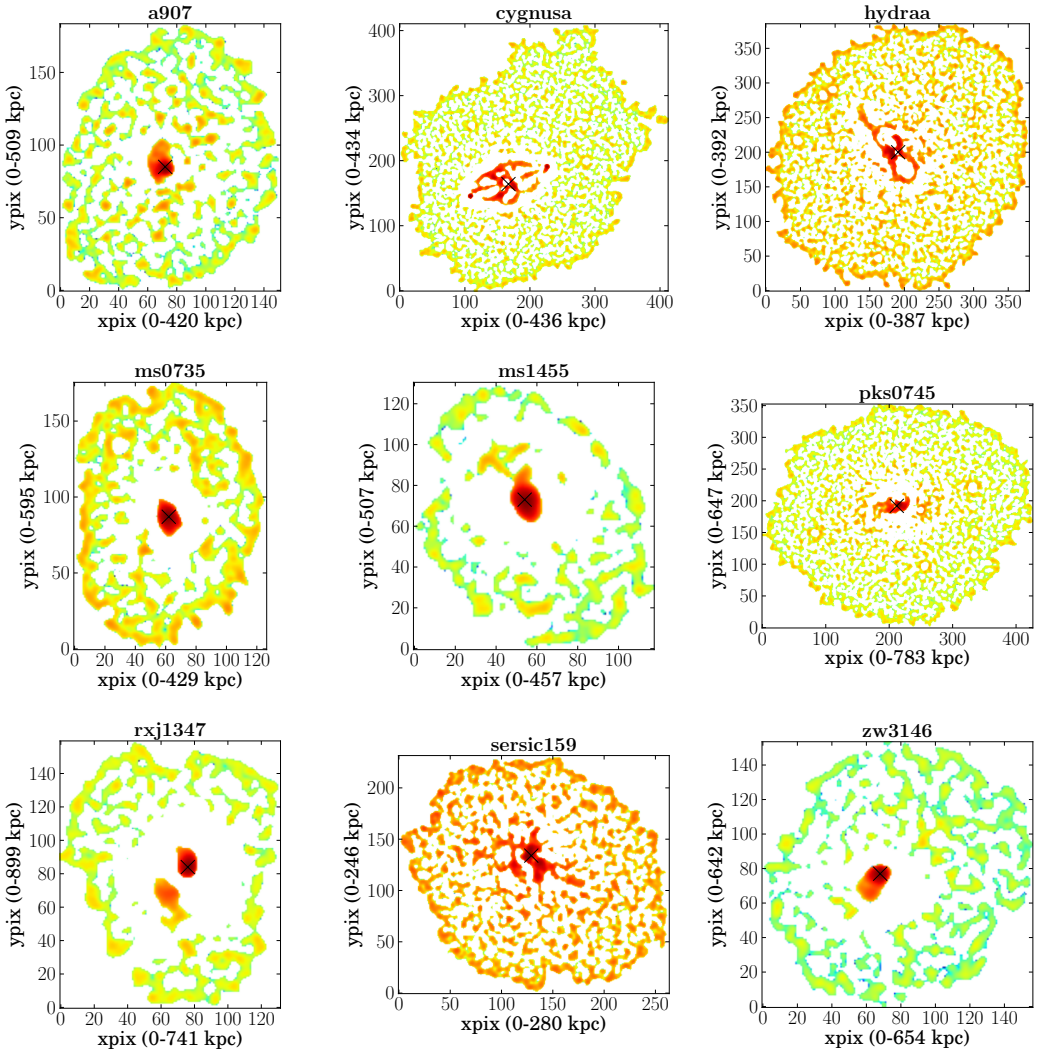

Figure A.2: continued.

A.7 Projected radial profiles

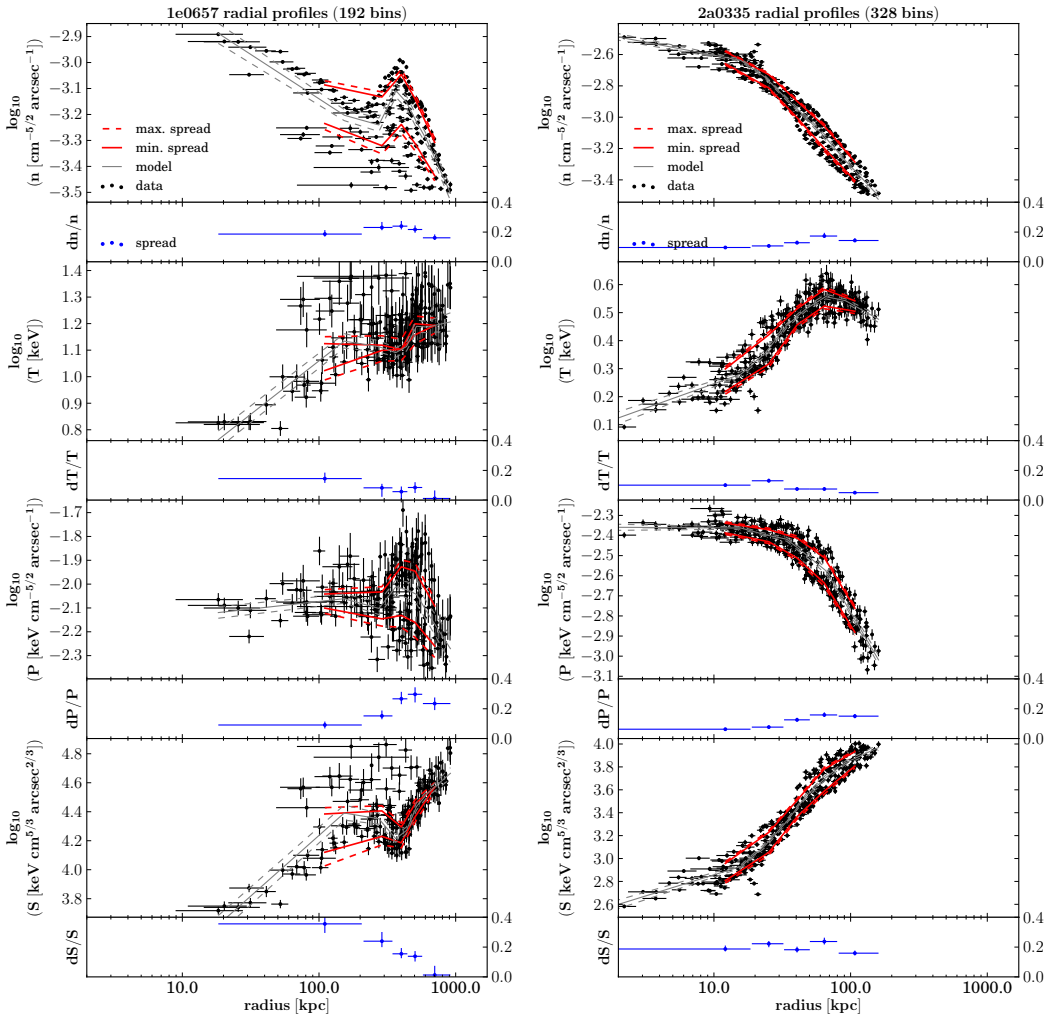

Figure A.3: Radial profiles of projected density, temperature, pressure, and entropy. Cluster names are given in the plot titles. The cluster centres are marked as crosses in Figs. A.1 and A.2. Error bars are the fit-errors and the standard deviation of the radial distribution for all spatial-spectral bins. The Plotted lines show limits on intrinsic scatter around an average seven-node model (grey lines) within the given radial range (see Sect. 3.2.1). The small panels show the measured fractional scatter (M=5) with confidence- and radial-range.

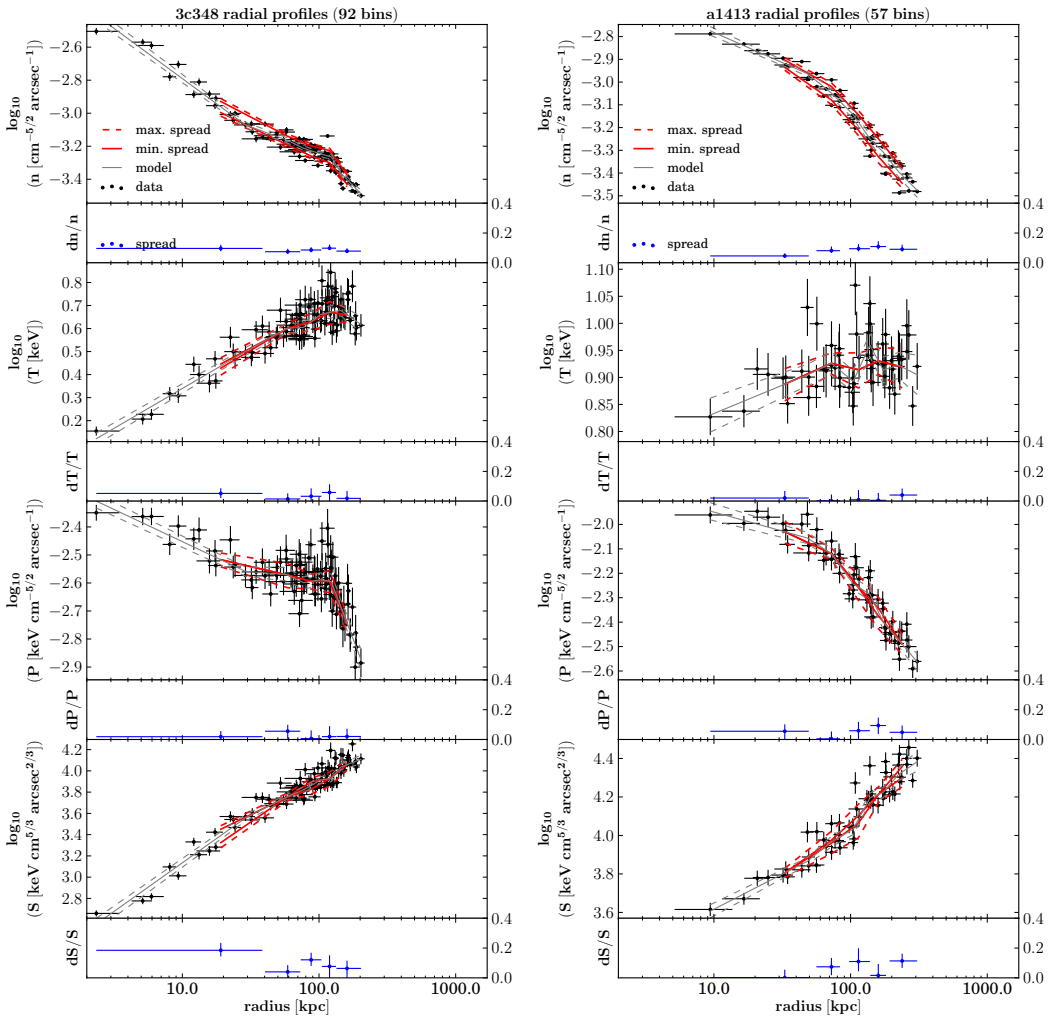

Figure A.3: continued.

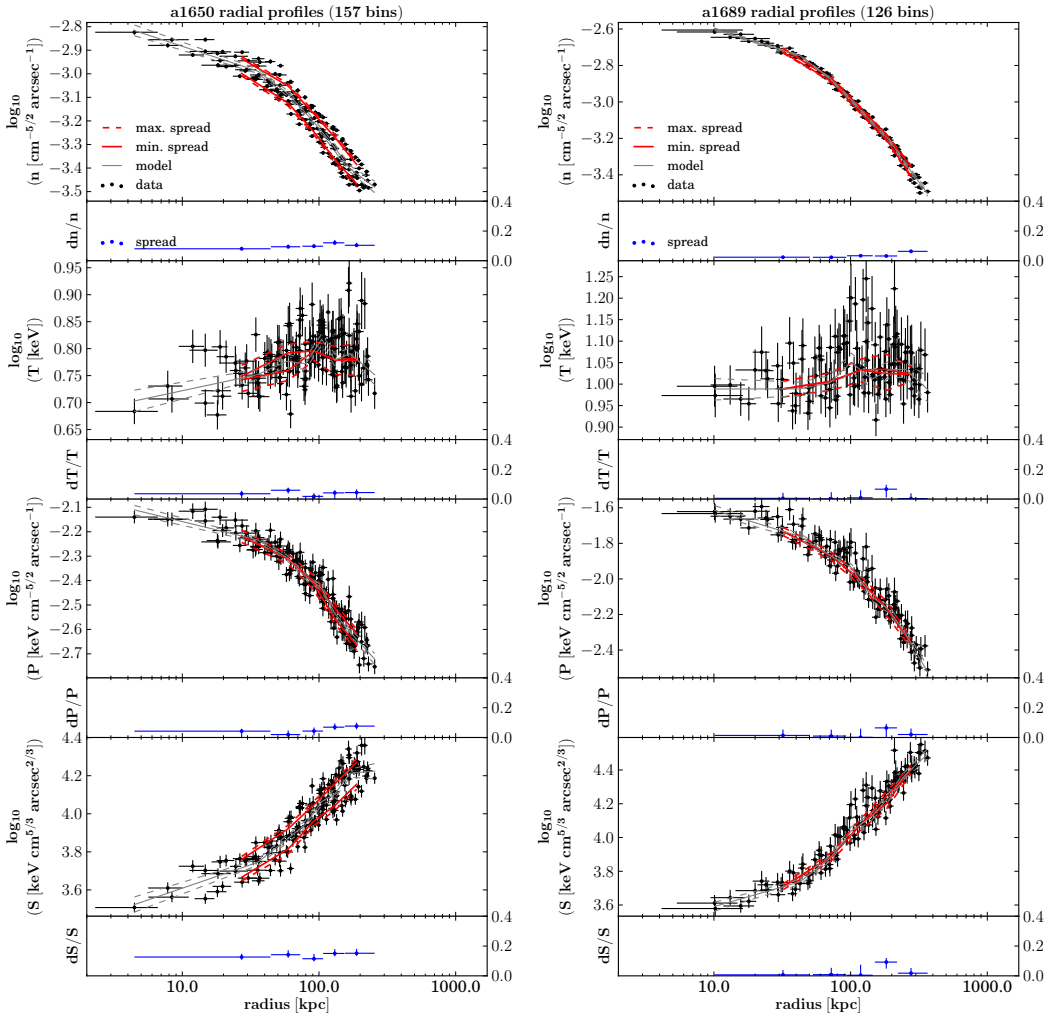

Figure A.3: continued.

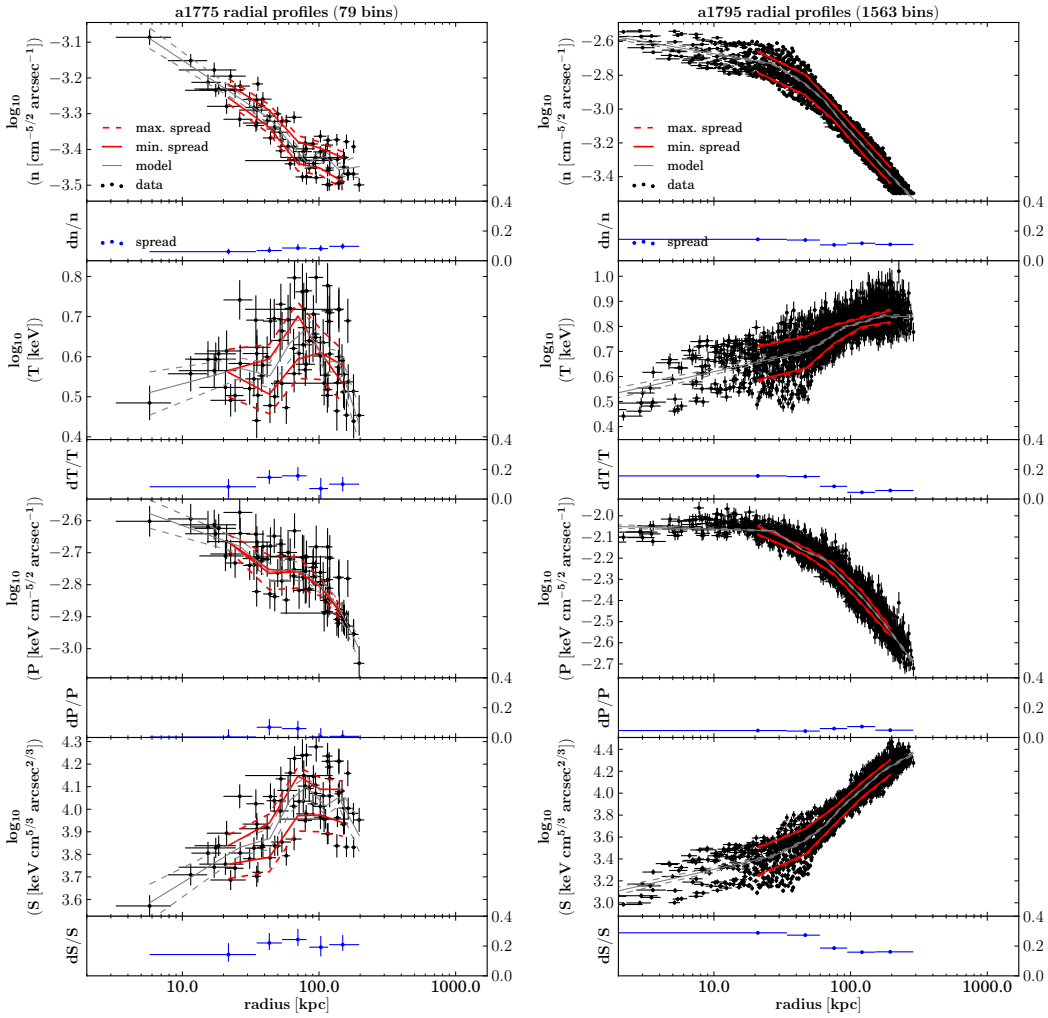

Figure A.3: continued.

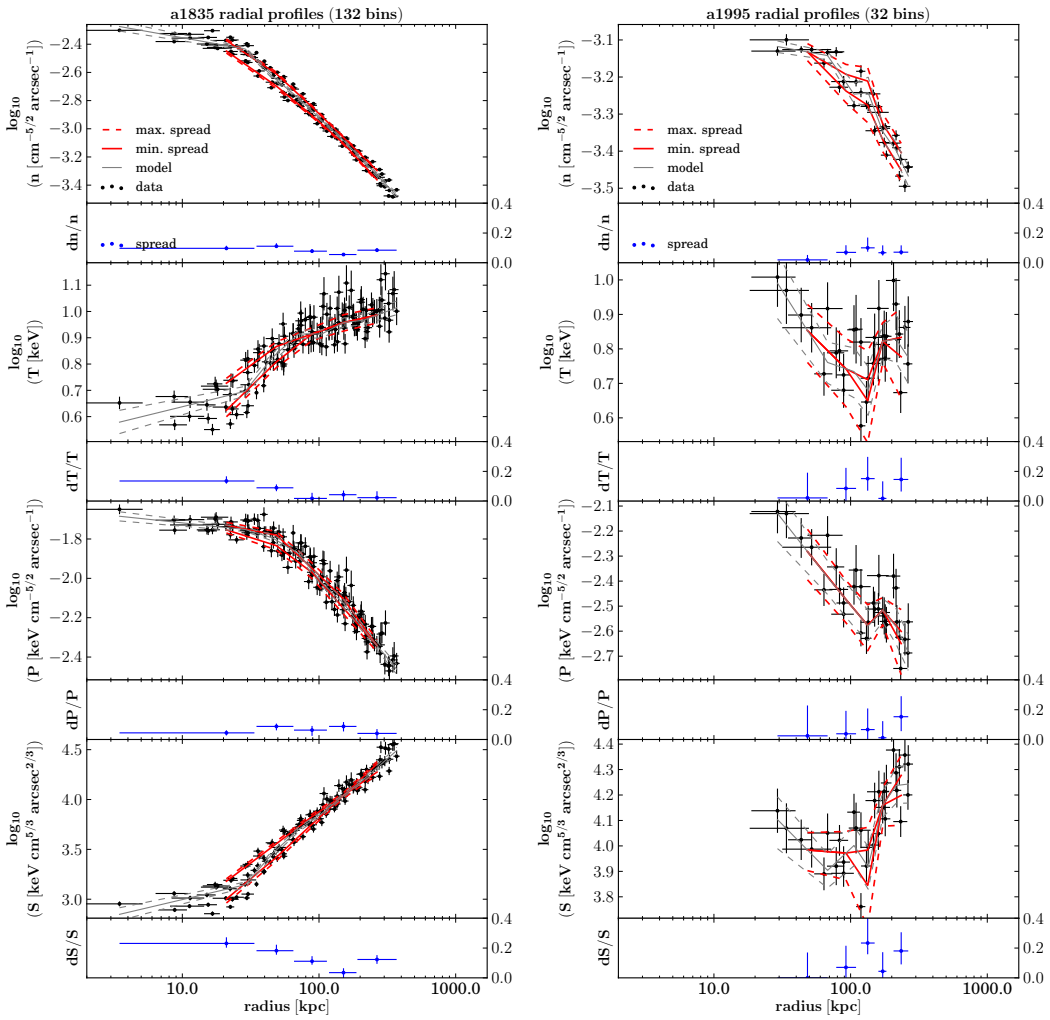

Figure A.3: continued.

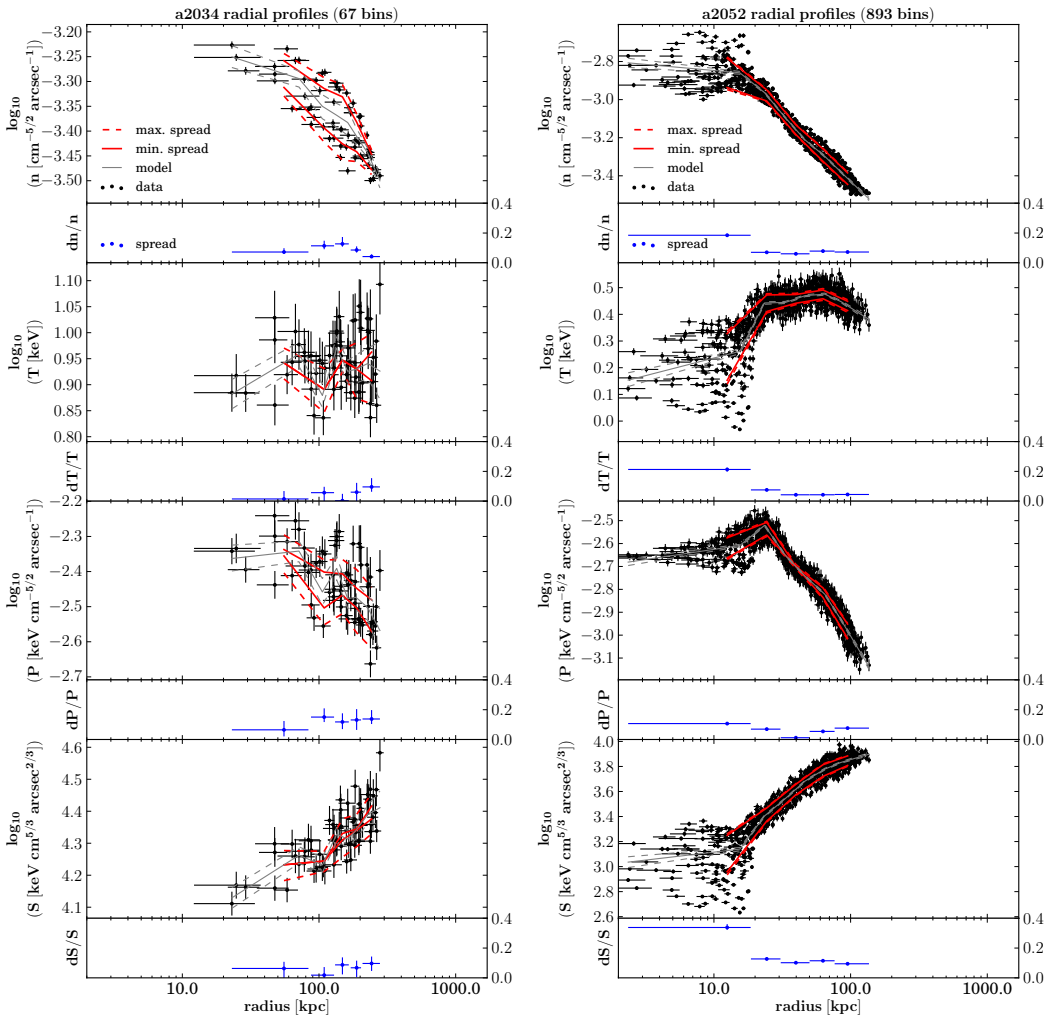

Figure A.3: continued.

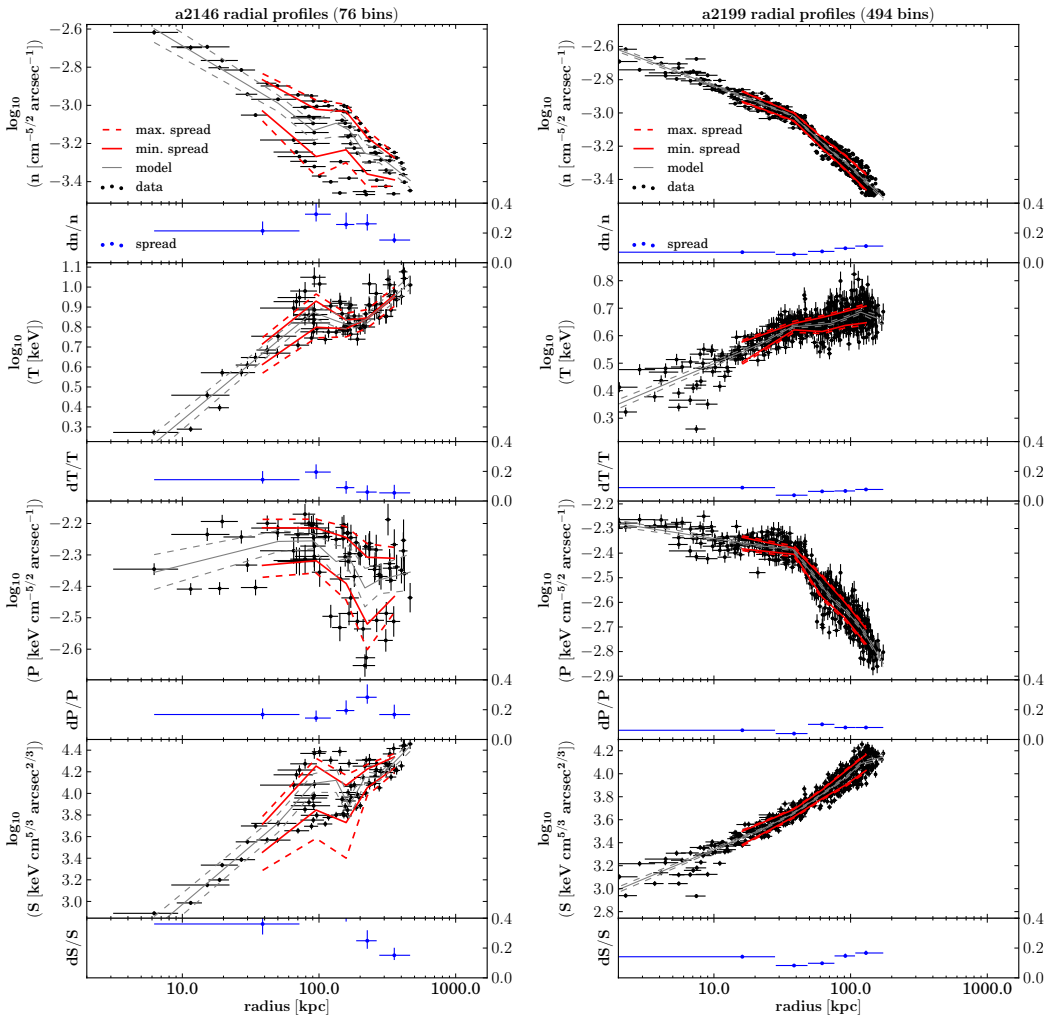

Figure A.3: continued.

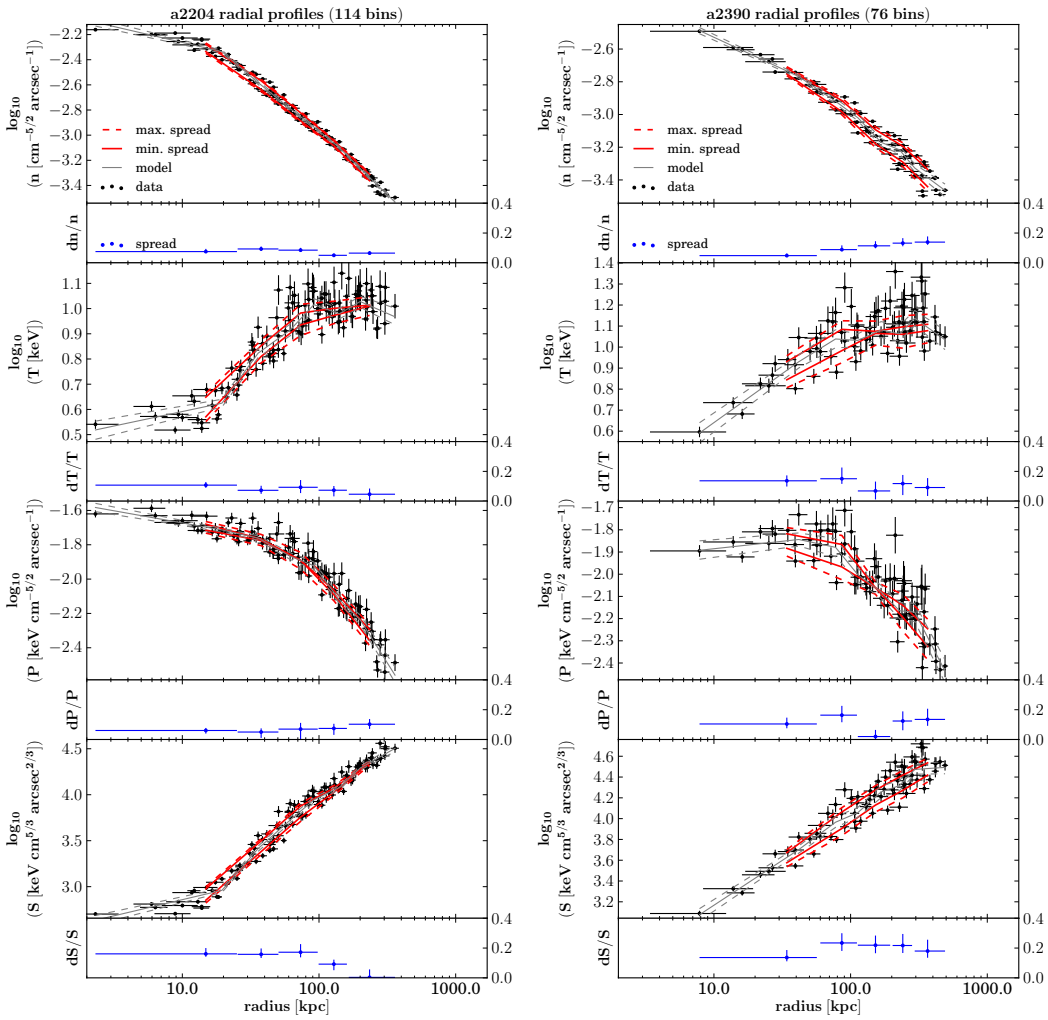

Figure A.3: continued.

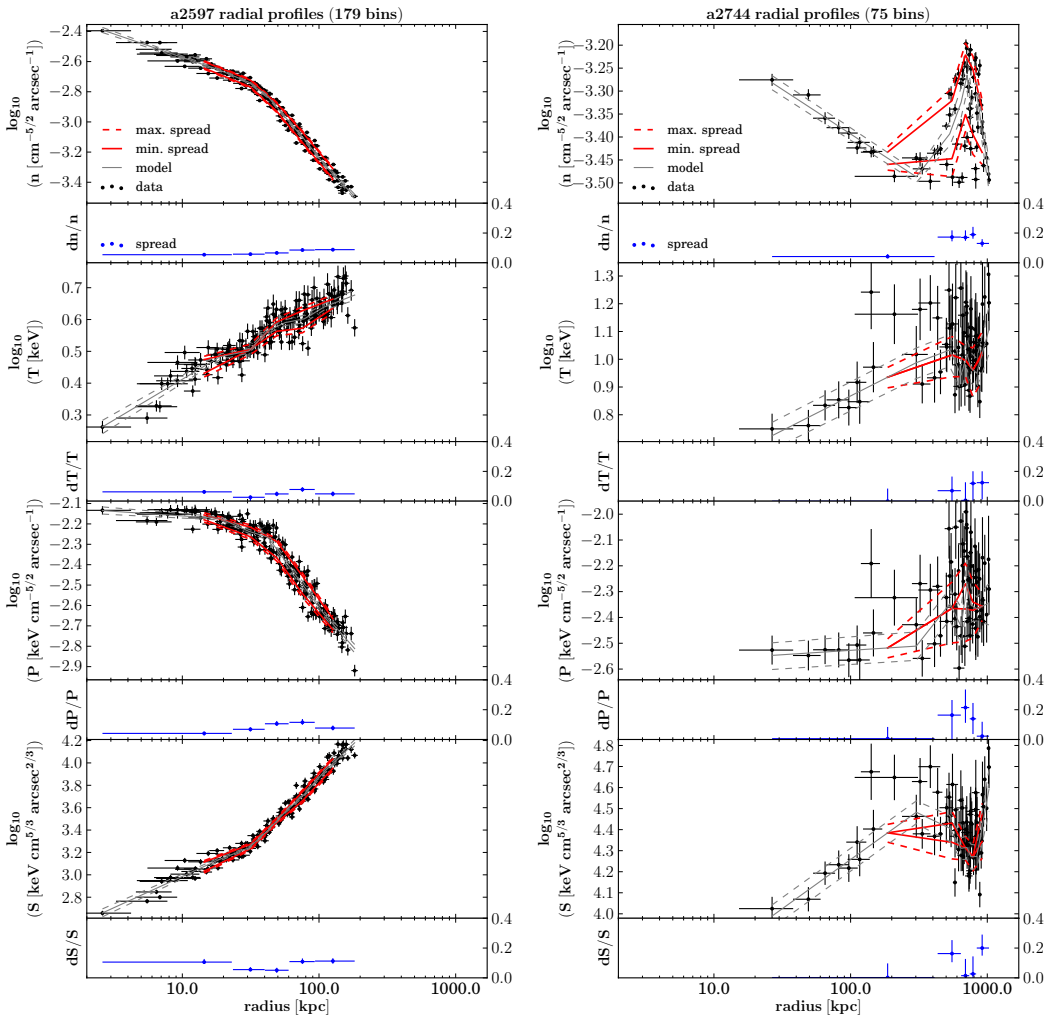

Figure A.3: continued.

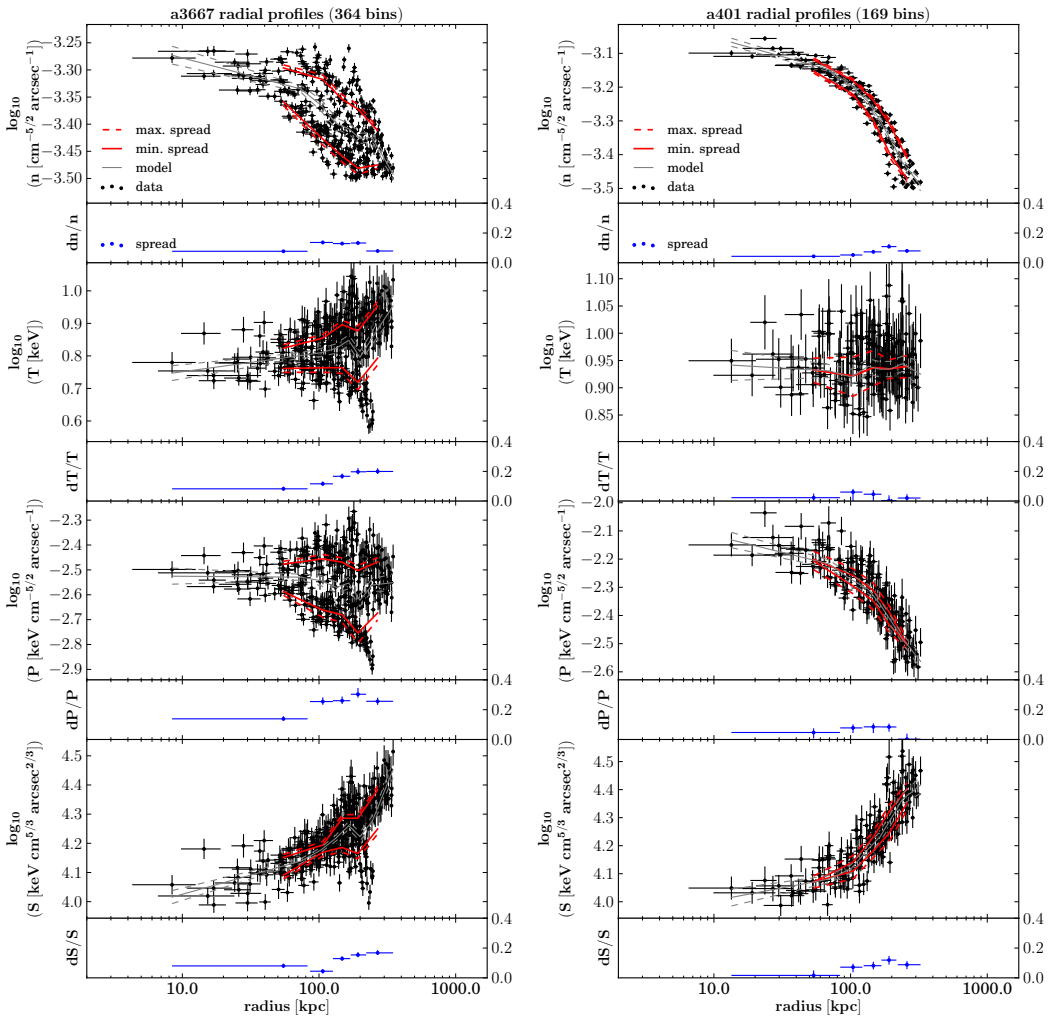

Figure A.3: continued.

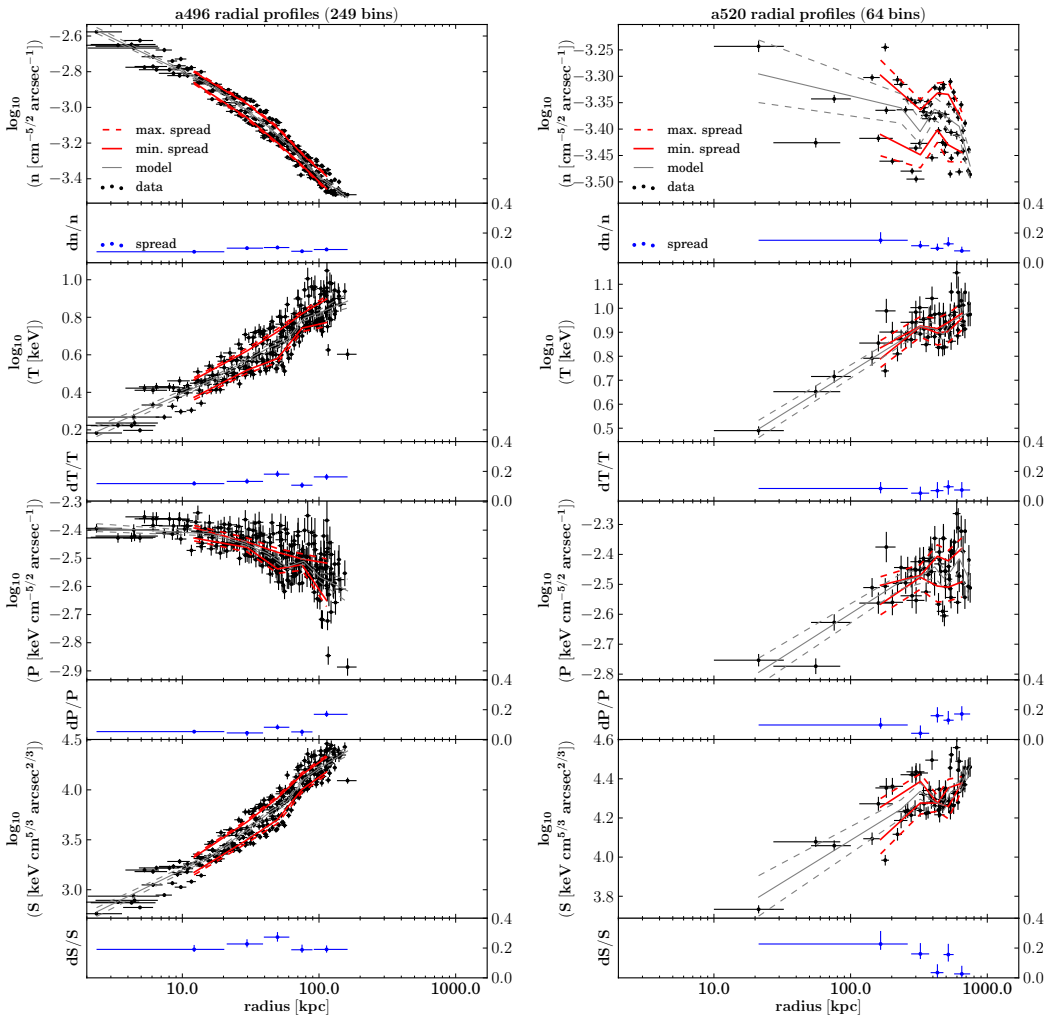

Figure A.3: continued.

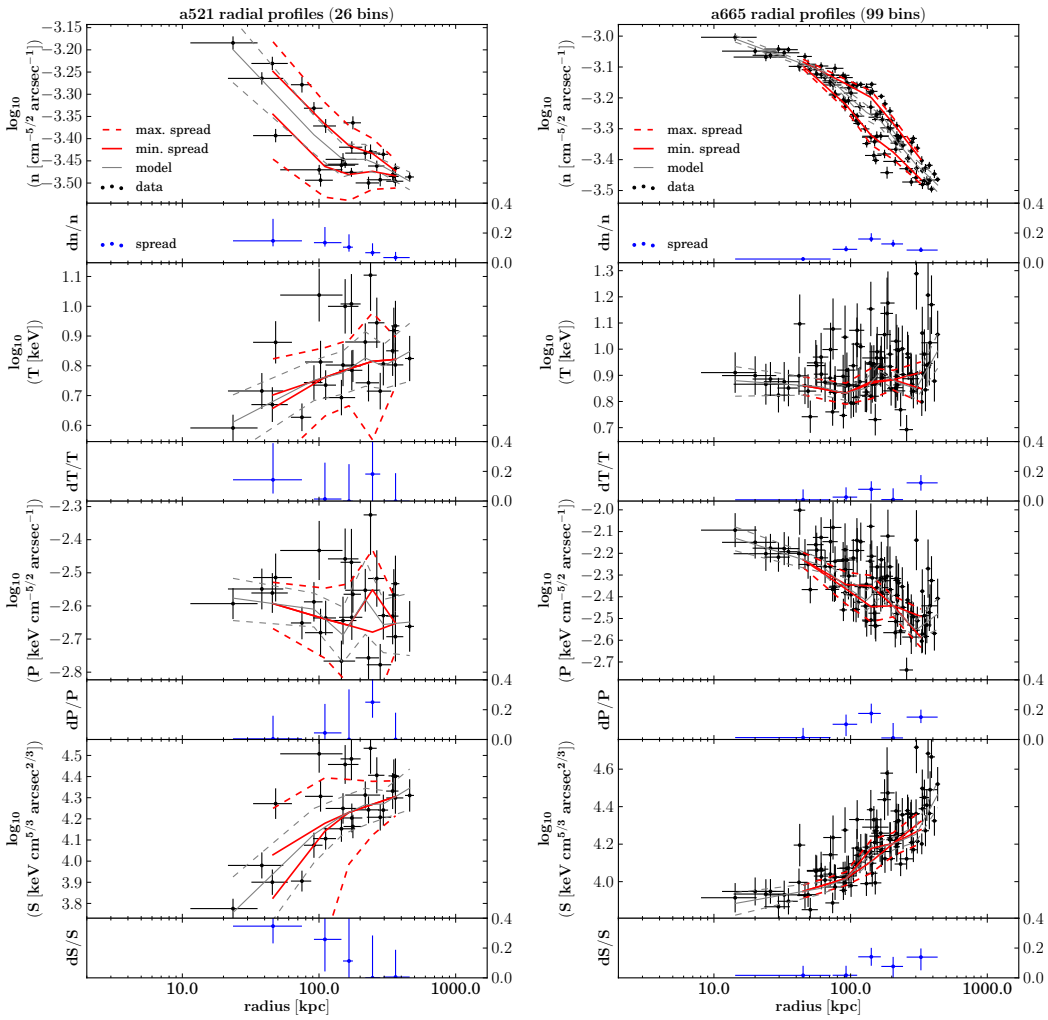

Figure A.3: continued.

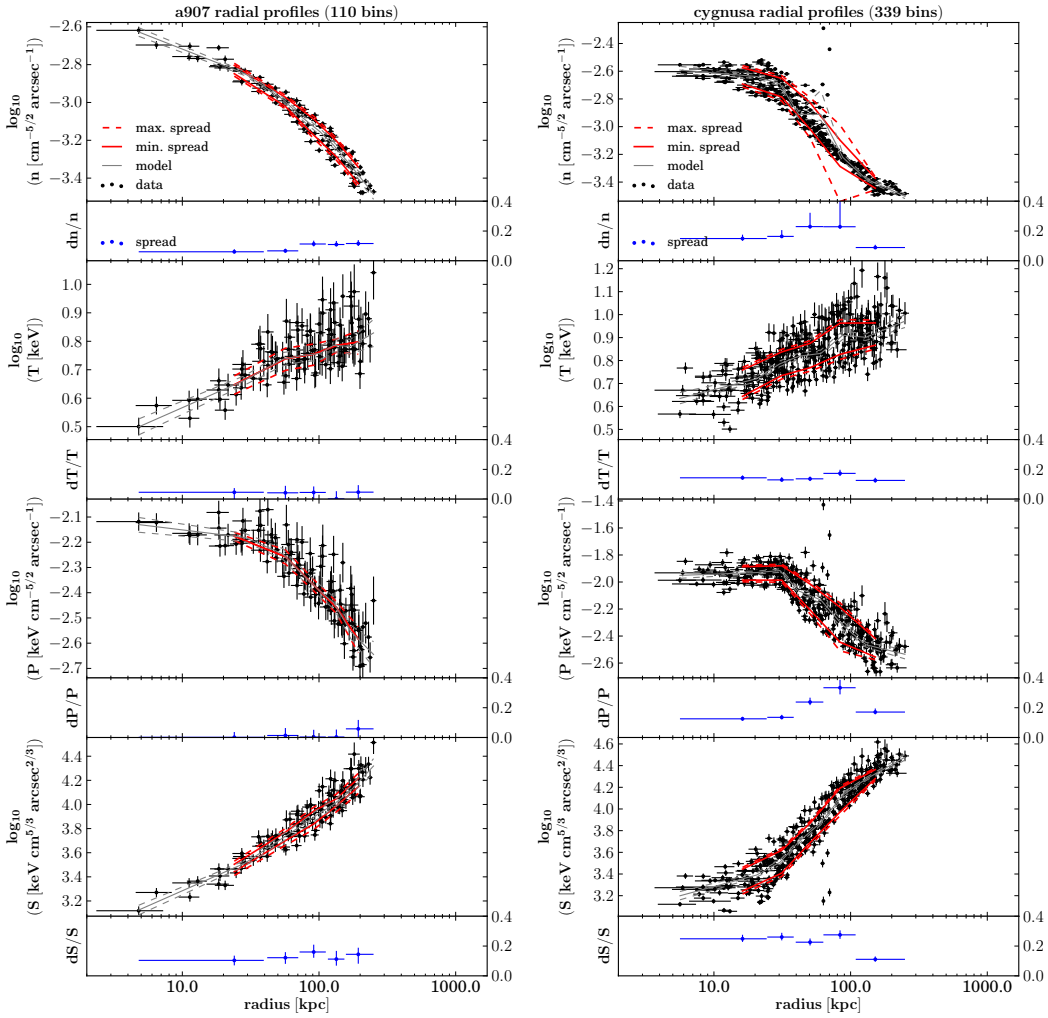

Figure A.3: continued.

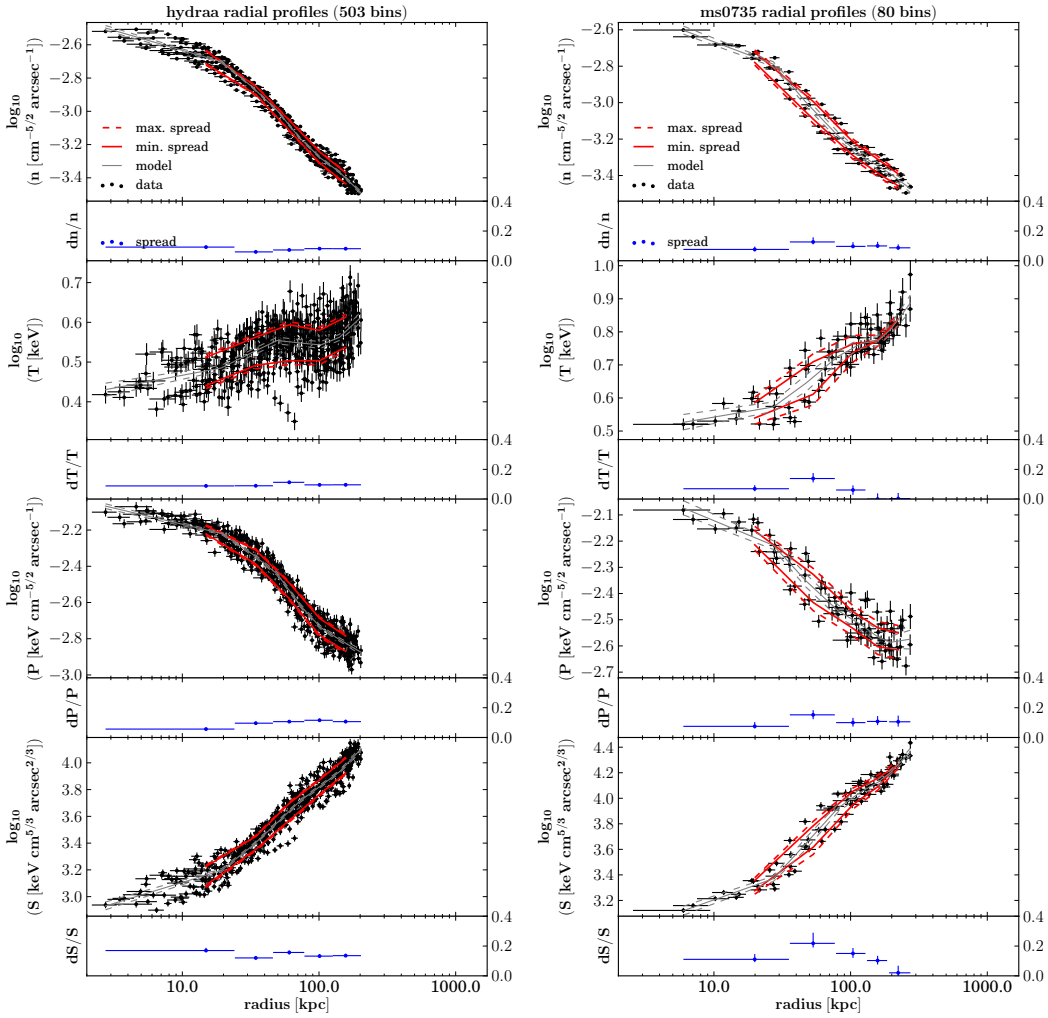

Figure A.3: continued.

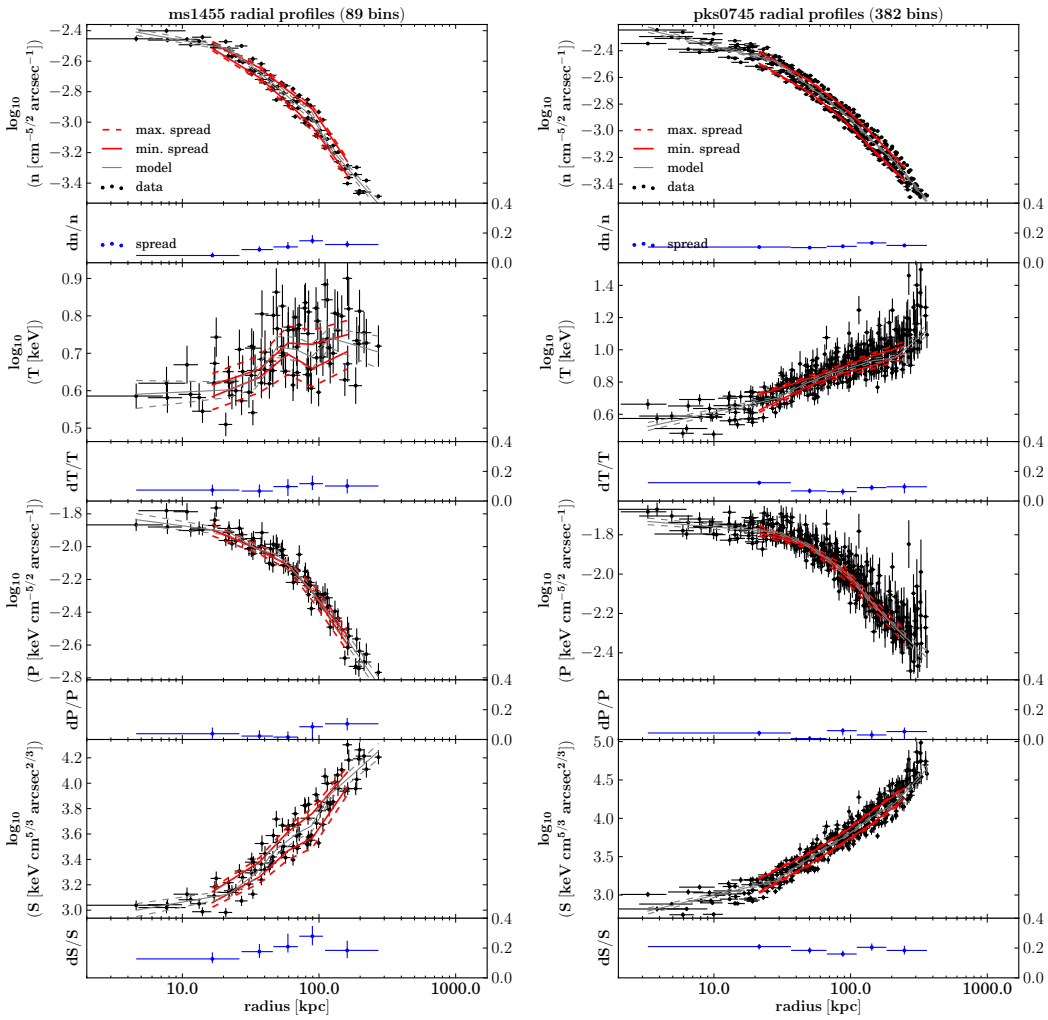

Figure A.3: continued.

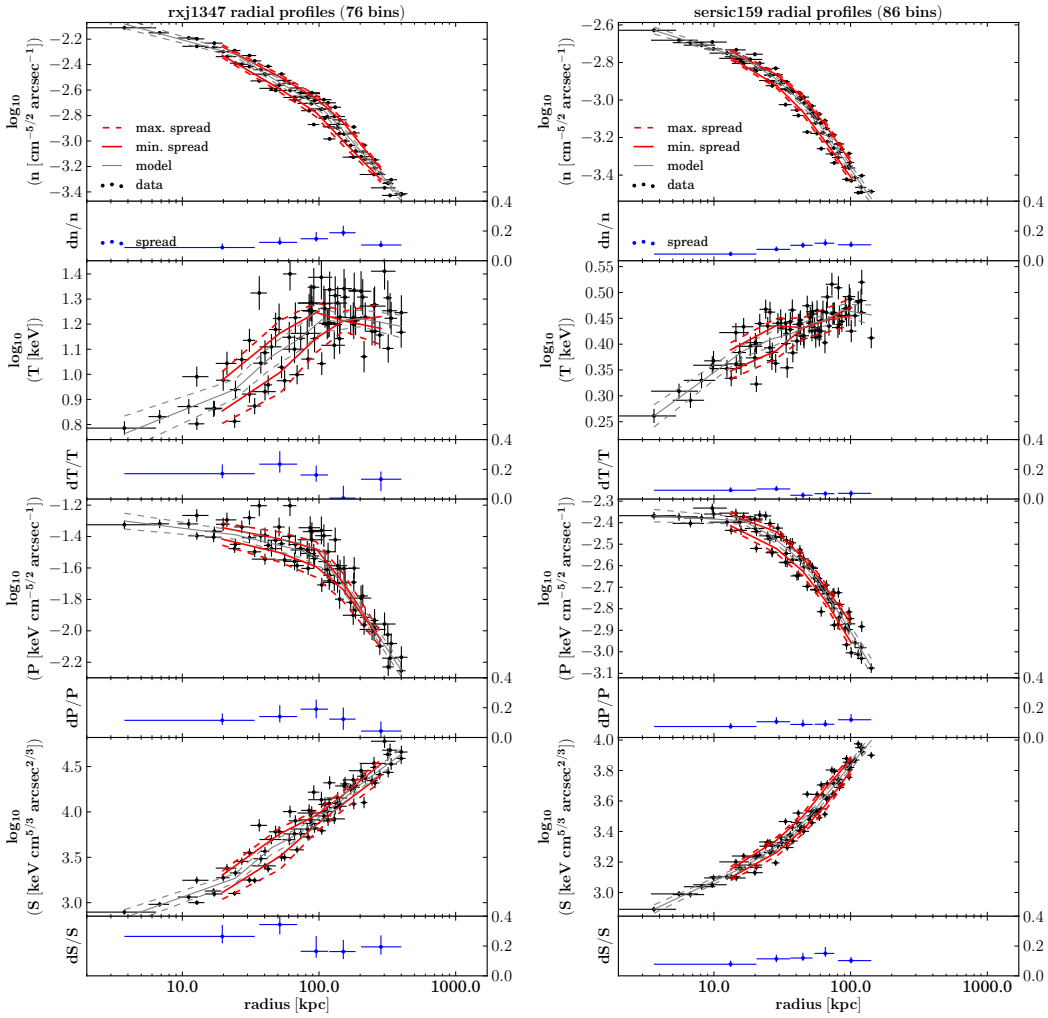

Figure A.3: continued.

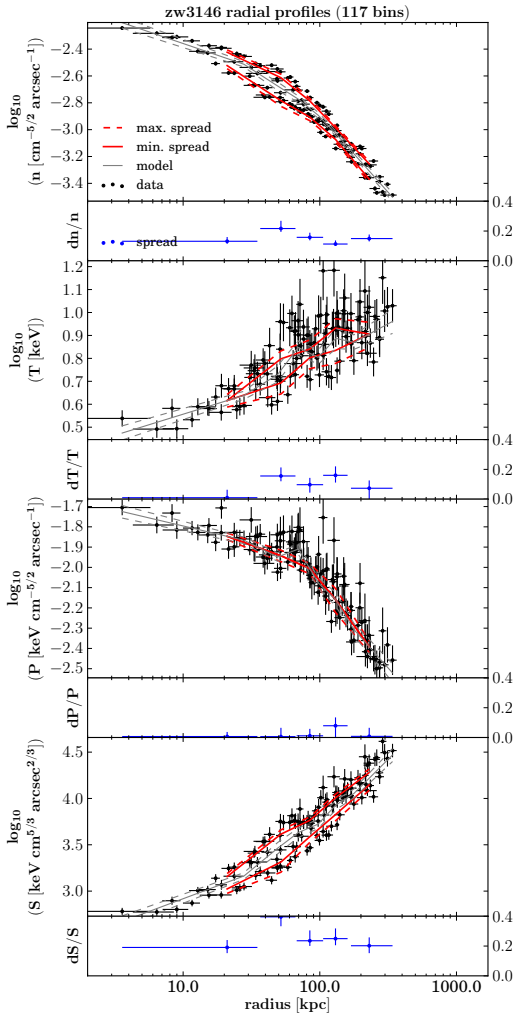

Figure A.3: continued.

Appendix B

7.1 keV sterile neutrino limits

B.1 Dark matter mass profiles

I assumed the cluster density follows an NFW profile (Navarro et al. 1997) depending on the radius r from the centre,

$$\rho(\mathrm{r}) = \frac{\delta_\mathrm{c}\rho_\mathrm{c}}{\mathrm{r}/\mathrm{r_s}\ (1+\mathrm{r}/\mathrm{r_s})^2} \tag{B.1}$$

$$\delta_\mathrm{c} = \frac{500}{3} \times \frac{\mathrm{C}^3}{\ln(1+\mathrm{C}) - \mathrm{C}/(1+\mathrm{C})} \tag{B.2}$$

where concentration C and radius $\mathrm{r_s}$ are empirical cluster specific values. C describes how strongly peaked the density profile is in the centre and $\mathrm{r_s}$ is a specific radius depending on the extent of the cluster (here I define $\mathrm{r_s} = \mathrm{r_{500}}/\mathrm{C}$). ρ_c is the critical density of the universe at the cluster redshift. In the standard ΛCDM cosmology assumed in this study (see Sect. 4.1) the critical density is given as

$$\rho_\mathrm{c} = \frac{3\mathrm{H}^2(\mathrm{z})}{8\pi\mathrm{G}} \tag{B.3}$$

$$\mathrm{H}^2(\mathrm{z}) = \mathrm{H}_0^2\ (0.27\ (1+\mathrm{z})^3 + 0.73) \tag{B.4}$$

with gravitational constant $\mathrm{G} \approx 4.3 \times 10^{-3}$ pc $\mathrm{M}_\odot^{-1}$ $(\mathrm{km/s})^2$.

B.2 Simulated spectra

I used simulated data to test the spectral stacking technique for detecting an additional line at 3.55 keV. For the simulation I created fake spectra using `XSPEC`. Simulated spectra were obtained for the best fit model of every individual cluster with ten times the original exposure to get better statistics. I added a Gaussian line with the expected flux for each cluster assuming a mixing angle of $\sim 7 \times 10^{-11}$ and that all dark matter is made of the

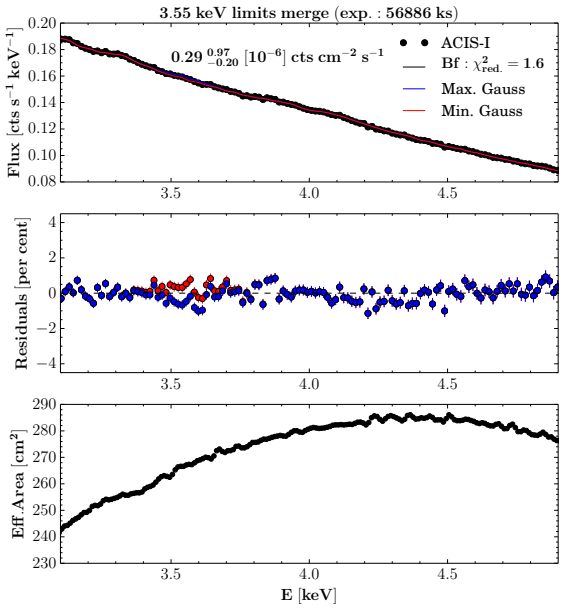

Figure B.1: Merged simulations with 10 times the exposure of original X-ray spectra and an additional Gaussian line at 3.55 keV (ACIS-I) with residuals of different fitted models and the effective area (ARF and RMF combined). Fitted XSPEC models: `apec+apec+zgauss` with best-fit (Bf), upper and lower confidence values (99.7 per cent) of the Gaussian flux in counts cm^{-2} s^{-1}. The annotations show the best-fit value and the confidence interval obtained using MCMC. Residuals are shown for the fit with upper (blue) and lower (red) confidence limit of the Gaussian flux.

7.1 keV sterile neutrinos as in previous detections (see Bulbul et al. 2014; Boyarsky et al. 2014). Exactly the same merging and modelling procedure was performed on the simulations and the real data. Fig. B.2 shows the resulting stacked spectra of the simulation (compare to Fig. 4.1 for the real data). The additional line is recovered between 95 and 99.7 per cent confidence for both ACIS-I and ACIS-S detectors after the stacking. The measured flux can be converted into a mixing angle using the average sample properties of Tab. 4.1. The resulting mixing angles in the simulations are $4.1^{+3.2}_{-2.3}$ (ACIS-I, CI:68) and $14.8^{+3.9}_{-5.2}$ (ACIS-S, CI:68). These simulations show the detection efficiency of the stacking method. There is some hint that the limits of ACIS-S are biased high which is in agreement with the limits obtained from real data (see Fig. 4.4 the best constraints).

There are small fluctuations in the residuals of less than 2 per cent. To asses the uncertainties introduced by the de-redshifting technique of the RMF response files I tested many different combinations of smoothing and number of iterations. The best results were obtained calculating the average of 100 iterations and smoothing them using a Gaussian filter ($\sigma = 1$ pixel). This procedure proved most effective in recovering the simulated flux (see Fig. B.2). The residual structures seen in the merged spectra are partially caused by the averaging over many cluster spectra of different temperatures which are not perfectly

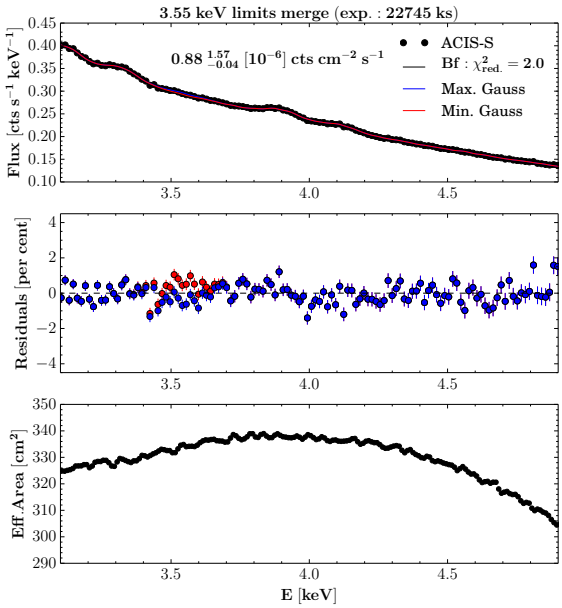

Figure B.2: Merged simulations with 10 times the exposure of original X-ray spectra and an additional Gaussian line at 3.55 keV (ACIS-S) with residuals of different fitted models and the effective area (ARF and RMF combined). Fitted XSPEC models: `apec+apec+zgauss` with best-fit (Bf), upper and lower confidence values (99.7 per cent) of the Gaussian flux in counts cm^{-2} s^{-1}. The annotations show the best-fit value and the confidence interval obtained using MCMC. Residuals are shown for the fit with upper (blue) and lower (red) confidence limit of the Gaussian flux.

modelled by the two temperature component `apec` model. More complex models however made the fit less stable and did not improve the capability to detect the additional line. Another source of residuals can be fluctuations in the average response (see bottom panels Fig. B.2 for combined ARF and RMF). These minor fluctuations did not affect the detection efficiency since they averaged out over the width of a spectral line. I extensively tested the detection efficiency using different stacking methods. Additional smoothing of the response files resulted in lower sensitivity for detecting the simulated line (e.g. using mean, median, and Gaussian filters) because it introduced residuals around spectral features due to broadening of the response. Using linear interpolation to remap the response resulted in smoother response but the simulated line was not recovered. The method I used for the final analysis was the most efficient at recovering the simulated line.

B.3 Detailed parameters of fitting procedure

Table B.1: Best fit XSPEC models.

Cluster[a]	T1 [keV][b]	T2 [keV][b]	Z [$Z_\odot$][b]	n1 [10^{-2} cm^{-5}][b]	n2 [10^{-2} cm^{-5}][b]	Chi^2_{red} [b]
1e0657i	12.5±0.48	-	0.49±0.189	1.11±0.031	-	1.20
a1795i	2.5±0.35	6.4±0.39	0.42±0.026	1.02±0.348	3.57±0.343	1.08
a1795s	3.1±0.45	7.4±0.59	0.46±0.034	1.75±0.454	3.01±0.460	1.04
a1995i	6.8±0.97	-	0.25±0.194	0.18±0.120	-	1.00
a1995s	6.6±0.88	-	0.78±0.665	0.19±0.129	-	1.10
rxj1347i	4.2±1.93	16.2±2.76	0.27±0.050	0.23±0.143	1.08±0.061	0.90
rxj1347s	11.2±1.33	-	0.31±0.055	1.25±0.182	-	0.90
zw3146i	0.5±0.70	6.9±1.02	0.30±0.295	0.90±4.692	1.01±0.105	1.05
a1835i	4.1±2.50	8.8±1.71	0.38±0.207	0.36±0.602	1.21±0.401	1.12
a1835s	2.1±1.21	11.9±4.67	0.08±0.151	0.75±0.394	1.29±0.232	0.92
a665i	4.6±3.04	15.4±10.09	0.39±0.397	0.24±0.276	0.24±0.306	1.03
a520i	8.1±0.30	-	0.73±0.276	0.37±0.027	-	1.07
a1689i	10.7±0.80	-	0.44±0.254	1.66±0.075	-	1.15
ms1455i	3.4±1.87	6.1±3.24	0.10±0.203	0.34±0.757	0.40±0.767	1.07
a401i	8.9±0.42	-	0.44±0.152	2.95±0.089	-	1.23
a1413i	1.4±0.77	8.9±1.37	0.83±0.336	0.09±0.137	0.96±0.049	1.09
a2146i	2.5±2.73	7.1±1.21	0.54±0.198	0.05±0.184	0.48±0.132	0.98
a2146s	1.4±1.03	8.6±2.88	0.32±0.381	0.21±0.296	0.47±0.155	0.94
a521i	6.4±1.12	-	1.78±1.961	0.08±0.105	-	0.88
a521s	8.2±1.65	-	0.01±1.534	0.13±0.116	-	1.15
ms0735i	4.9±0.66	-	0.77±0.239	0.34±0.053	-	1.05
ms0735s	2.5±3.72	5.5±2.75	0.43±0.385	0.08±0.524	0.31±0.434	1.02
pks0745i	2.7±0.64	11.9±5.97	0.68±0.271	1.83±1.055	4.10±0.616	1.03
pks0745s	2.7±0.68	9.4±0.78	0.53±0.074	1.27±0.410	5.10±0.367	1.04
a2204i	2.0±0.27	13.7±3.27	0.47±0.157	1.03±0.213	2.02±0.149	1.06
a2204s	1.7±0.89	8.8±3.26	0.70±0.511	0.56±0.822	2.43±0.326	1.05
a2034i	1.4±0.39	12.9±2.63	0.25±0.122	0.21±0.125	0.63±0.038	0.94
cygnusai	1.5±0.42	7.4±0.36	0.86±0.111	0.31±0.158	3.64±0.094	0.90
cygnusas	2.5±0.40	11.6±3.47	0.68±0.145	1.32±0.450	2.98±0.265	0.99
a907i	3.7±2.94	7.2±2.90	0.40±0.218	0.33±0.756	0.41±0.710	0.88
a3667i	3.2±0.50	10.6±1.37	0.22±0.065	0.92±0.226	1.54±0.207	0.90
2a0335s	1.4±0.39	3.4±0.24	0.67±0.042	1.69±0.831	5.23±0.841	1.41
a2597s	0.8±1.28	3.7±0.10	0.43±0.058	0.14±0.668	1.91±0.063	0.98
a1650i	2.8±2.31	7.3±1.10	0.45±0.102	0.32±0.560	1.25±0.377	0.85
a1650s	4.3±1.63	6.9±2.96	0.63±0.205	0.81±1.128	0.78±1.141	1.09
a2199i	3.0±0.49	5.9±1.02	0.41±0.048	3.35±1.251	2.91±1.271	0.89
a2199s	2.0±0.36	6.1±1.01	0.38±0.058	2.23±1.003	4.74±0.895	0.96
hydraai	3.7±0.14	-	0.83±0.599	2.54±0.428	-	1.55
hydraas	1.4±1.00	4.0±0.22	0.38±0.036	0.36±0.467	3.42±0.333	1.06
a496s	2.1±0.14	7.1±0.59	0.87±0.082	1.10±0.223	3.32±0.172	1.06
sersic159i	2.2±0.27	3.9±1.94	0.38±0.058	1.28±0.752	0.58±0.916	1.14
sersic159s	2.0±0.81	4.3±5.23	0.46±0.154	1.17±1.722	0.66±1.958	1.12
3c348s	2.6±1.11	4.7±1.62	0.75±0.221	0.12±0.385	0.27±0.322	0.98
a1775s	2.3±1.12	5.7±3.89	0.57±0.149	0.20±0.346	0.19±0.339	1.08
a2052s	1.5±0.23	3.4±0.12	0.67±0.029	0.48±0.171	1.96±0.126	1.02
a2744i	10.2±1.65	-	0.31±0.359	0.46±0.093	-	1.02
a2744s	10.9±2.52	-	0.93±1.381	0.43±0.268	-	0.87
a2390s	5.4±5.40	10.3±2.40	0.95±0.305	0.26±0.998	1.02±0.612	0.92
mergei	2.8±0.85	7.3±0.34	0.56±0.099	0.30±0.165	1.54±0.130	1.11
merges	2.2±0.21	5.8±0.32	0.70±0.063	0.97±0.182	2.17±0.155	1.41

[a] Abbreviated cluster name and detector identifier (i: ACIS-I, s: ACIS-s). "merge" indicates the best fit to the merged spectra of the complete sample.

[b] Best fit parameters of the XSPEC `apec` models to the individual cluster emission. Second temperature model was set to zero if temperatures T differed by less than 30 per cent or second normalisation n was less than one per cent of the first model. Metallicity Z was linked between the two models. The goodness of fit is give as Chi^2_{red}.

Table B.2: Fixed cluster parameters and weights.

Cluster[a]	z	n_H [10^{22} cm^{-2}]	Expw.i [per cent][b]	Expw.s [per cent]	ω.i	ω.s	M_{DM}^{FOV} [10^{14} $M_\odot$][c]	M_{DM}^{FOV}/D^2 [10^{10} $M_\odot$ Mpc^{-2}]
1e0657	0.30	0.049	10.0	-	3.5	-	5.92	0.026
a1795	0.06	0.012	10.8	10.6	25.5	19.3	1.59	0.210
a1995	0.32	0.012	1.0	2.0	0.1	0.1	1.66	0.006
rxj1347	0.45	0.046	3.8	0.8	0.6	0.1	6.50	0.010
zw3146	0.28	0.025	1.5	-	0.2	-	2.49	0.012
a1835	0.25	0.020	3.4	1.3	1.0	0.3	3.38	0.021
a665	0.18	0.043	2.4	-	0.8	-	2.03	0.027
a520	0.20	0.057	9.4	-	1.3	-	1.07	0.011
a1689	0.18	0.018	3.5	-	2.2	-	3.99	0.051
ms1455	0.26	0.032	1.9	-	0.2	-	1.26	0.008
a401	0.07	0.099	2.9	-	8.0	-	2.69	0.247
a1413	0.14	0.018	2.4	-	1.6	-	2.39	0.054
a2146	0.23	0.030	6.7	1.9	1.0	0.2	1.51	0.011
a521	0.25	0.049	2.3	1.7	0.2	0.1	1.15	0.008
ms0735	0.21	0.033	8.5	2.0	1.5	0.3	1.51	0.014
pks0745	0.10	0.373	0.3	7.0	0.4	8.7	3.03	0.138
a2204	0.15	0.057	1.5	0.4	1.1	0.3	3.10	0.061
a2034	0.11	0.015	4.6	-	4.3	-	2.14	0.080
cygnusa	0.06	0.272	3.5	1.5	8.5	2.9	1.33	0.218
a907	0.17	0.054	1.8	-	0.5	-	1.44	0.023
a3667	0.06	0.044	8.3	-	22.3	-	1.44	0.240
2a0335	0.03	0.175	-	4.5	-	7.1	0.42	0.187
a2597	0.09	0.025	-	6.2	-	2.6	0.70	0.047
a1650	0.08	0.013	3.6	1.2	3.8	1.0	1.35	0.093
a2199	0.03	0.009	2.1	1.6	9.3	5.4	0.68	0.406
hydraa	0.05	0.047	0.4	8.8	0.6	9.8	0.73	0.130
a496	0.03	0.038	-	3.9	-	9.8	0.60	0.299
sersic159	0.06	0.011	1.7	0.4	1.1	0.2	0.35	0.057
3c348	0.15	0.062	-	5.0	-	0.7	0.77	0.015
a1775	0.07	0.010	-	4.4	-	1.4	0.38	0.037
a2052	0.04	0.027	-	28.7	-	27.9	0.27	0.115
a2744	0.31	0.014	1.8	1.1	0.3	0.1	2.57	0.010
a2390	0.23	0.062	-	4.9	-	1.9	5.14	0.039

[a] Abbreviated cluster name, redshift z, and Galactic foreground absorption from previous catalogs (for convention see Hofmann et al. 2016b).
[b] Expw: fraction of total exposure in per cent; ω: weighting factor for expected contribution to the DM line flux (i: ACIS-I, s: ACIS-S) see equation (4.2).
[c] Averaged DM mass in the FOV, and the same mass divided by the luminosity distance of the cluster (main indicator of expected DM line flux).

Table B.3: Flux and mixing angle constraints.

Cluster[a]	F_X $[10^{-6}$ cts cm^{-2} s$^{-1}]$[b]	F_X^{up}	F_X^{lo}	$\sin^2(2\Theta)$ $[10^{-9}]$[c]	$\sin^2(2\Theta)^{up}$	$\sin^2(2\Theta)^{lo}$
1e0657i	0.13	3.75	-4.08	0.12	3.48	-3.79
a1795i	-1.03	3.22	-5.66	-0.14	0.44	-0.78
a1795s	-1.04	4.73	-6.46	-0.14	0.65	-0.89
a1995i	0.39	5.43	-4.48	1.51	20.77	-17.15
a1995s	0.42	5.27	-4.66	1.59	20.14	-17.84
rxj1347i	1.67	7.27	-4.35	3.41	14.83	-8.87
rxj1347s	-7.79	9.05	-24.55	-15.88	18.45	-50.07
zw3146i	2.12	10.11	-8.25	4.31	20.59	-16.79
a1835i	-2.23	6.42	-8.17	-2.60	7.48	-9.52
a1835s	4.05	13.66	-11.45	4.71	15.92	-13.34
a665i	2.40	6.93	-0.71	2.35	6.78	-0.70
a520i	0.01	2.23	-2.05	0.02	5.23	-4.81
a1689i	5.56	12.59	-0.22	2.81	6.37	-0.11
ms1455i	-1.54	2.58	-6.92	-5.04	8.42	-22.61
a401i	-2.09	7.71	-12.51	-0.24	0.90	-1.46
a1413i	1.51	7.88	-4.42	0.76	3.97	-2.23
a2146i	-0.38	2.24	-3.11	-0.85	4.95	-6.89
a2146s	-2.91	3.20	-10.82	-6.44	7.10	-23.97
a521i	-0.22	1.88	-2.48	-0.73	6.19	-8.15
a521s	-1.51	2.22	-4.16	-4.98	7.30	-13.68
ms0735i	0.98	1.12	-0.45	1.82	2.09	-0.84
ms0735s	-3.44	-0.05	-6.04	-6.41	-0.09	-11.23
pks0745i	1.15	34.50	-34.77	0.23	6.99	-7.05
pks0745s	-2.68	7.50	-13.27	-0.54	1.52	-2.69
a2204i	3.49	14.83	-9.40	1.53	6.51	-4.13
a2204s	3.45	29.91	-22.58	1.51	13.13	-9.91
a2034i	-0.13	2.76	-3.29	-0.05	0.96	-1.14
cygnusai	-8.00	-0.21	-16.11	-1.07	-0.03	-2.16
cygnusas	-2.69	12.85	-19.01	-0.36	1.72	-2.55
a907i	1.74	4.55	-4.02	2.01	5.26	-4.64
a3667i	-0.80	2.54	-6.72	-0.10	0.31	-0.82
2a0335s	3.11	12.07	-7.77	0.50	1.92	-1.24
a2597s	-0.32	4.53	-5.99	-0.19	2.72	-3.60
a1650i	-0.05	5.82	-5.45	-0.02	1.77	-1.66
a1650s	-5.96	3.08	-15.21	-1.81	0.94	-4.63
a2199i	-0.85	9.69	-17.98	-0.06	0.72	-1.33
a2199s	-0.46	12.89	-18.15	-0.03	0.95	-1.34
hydraai	28.58	64.89	-10.65	6.45	14.64	-2.40
hydraas	-0.02	4.96	-4.74	-0.00	1.12	-1.07
a496s	-3.11	7.55	-13.04	-0.31	0.76	-1.30
sersic159i	-0.37	4.77	-6.64	-0.19	2.43	-3.39
sersic159s	9.45	24.14	-6.22	4.82	12.31	-3.17
3c348s	1.08	3.29	-1.90	1.99	6.04	-3.49
a1775s	0.98	3.60	-1.26	0.77	2.83	-0.99
a2052s	-1.03	1.36	-3.57	-0.27	0.35	-0.92
a2744i	-1.70	2.46	-6.98	-3.90	5.65	-16.04
a2744s	0.16	9.70	-10.34	0.36	22.28	-23.74
a2390s	2.00	8.71	-4.40	1.29	5.62	-2.84

[a] Abbreviated cluster name and detector identifier (i: ACIS-I, s: ACIS-s).
[b] Best fit and 3σ upper and lower boundaries of a possible additional flux added by a Gaussian line at 3.55 keV.
[c] Mixing-angle limits (3σ confidence) for the 7.1 keV sterile neutrino decay scenario (negative mixing-angle unphysical, results from allowing negative flux).

B.4 3.55 keV spectra

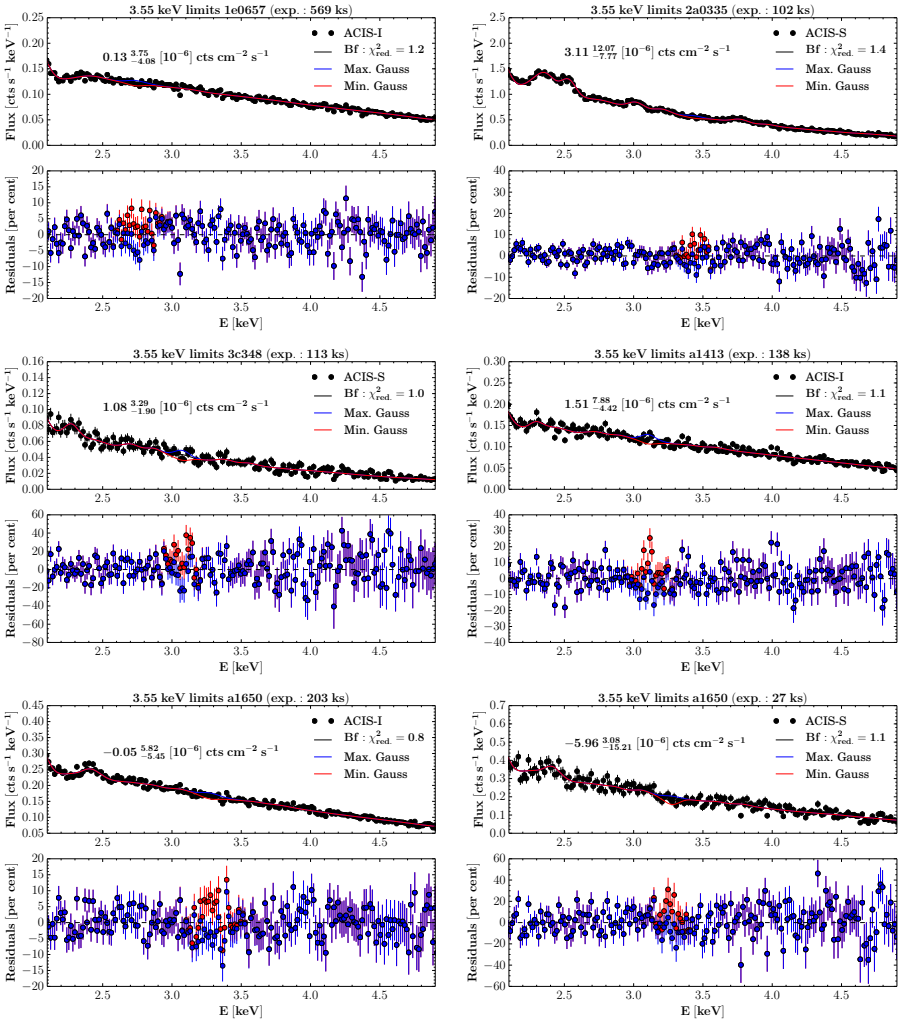

Figure B.3: X-ray spectra (ACIS-I and ACIS-S) with residuals of different fitted models. Fitted models: XSPEC `phabs*(apec+apec+zgauss)` with best-fit, upper and lower confidence values (99.7 per cent) of the Gaussian flux in cm^{-2} s^{-1}. The annotations show the best-fit (Bf) value and the confidence interval obtained using Monte Carlo Markov Chains (MCMC). Residuals are shown for the fit with upper (blue) and lower (red) confidence limit of the Gaussian flux. The plot title indicates the abbreviated cluster name and the exposure time of the observation.

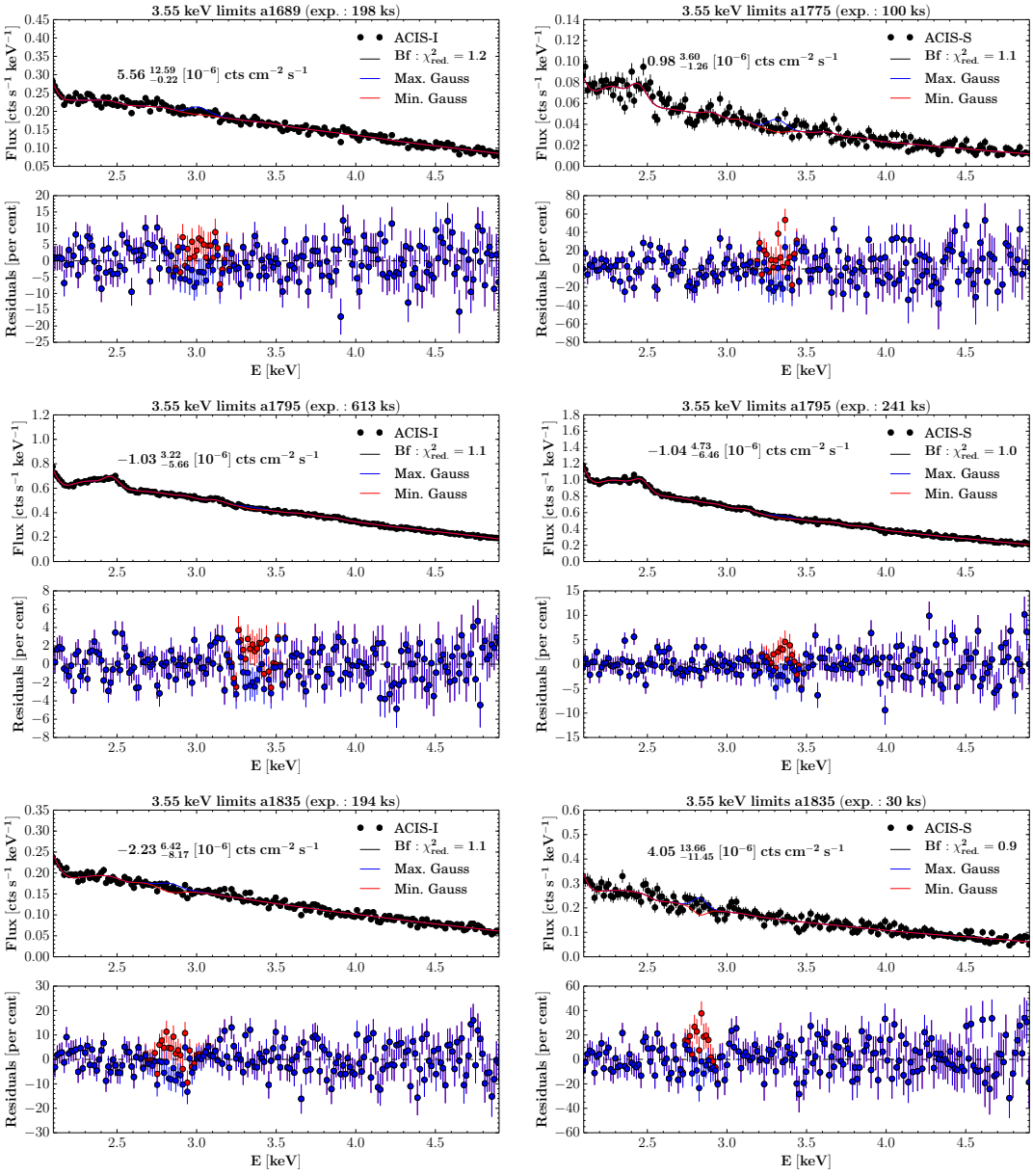

Figure B.3: continued.

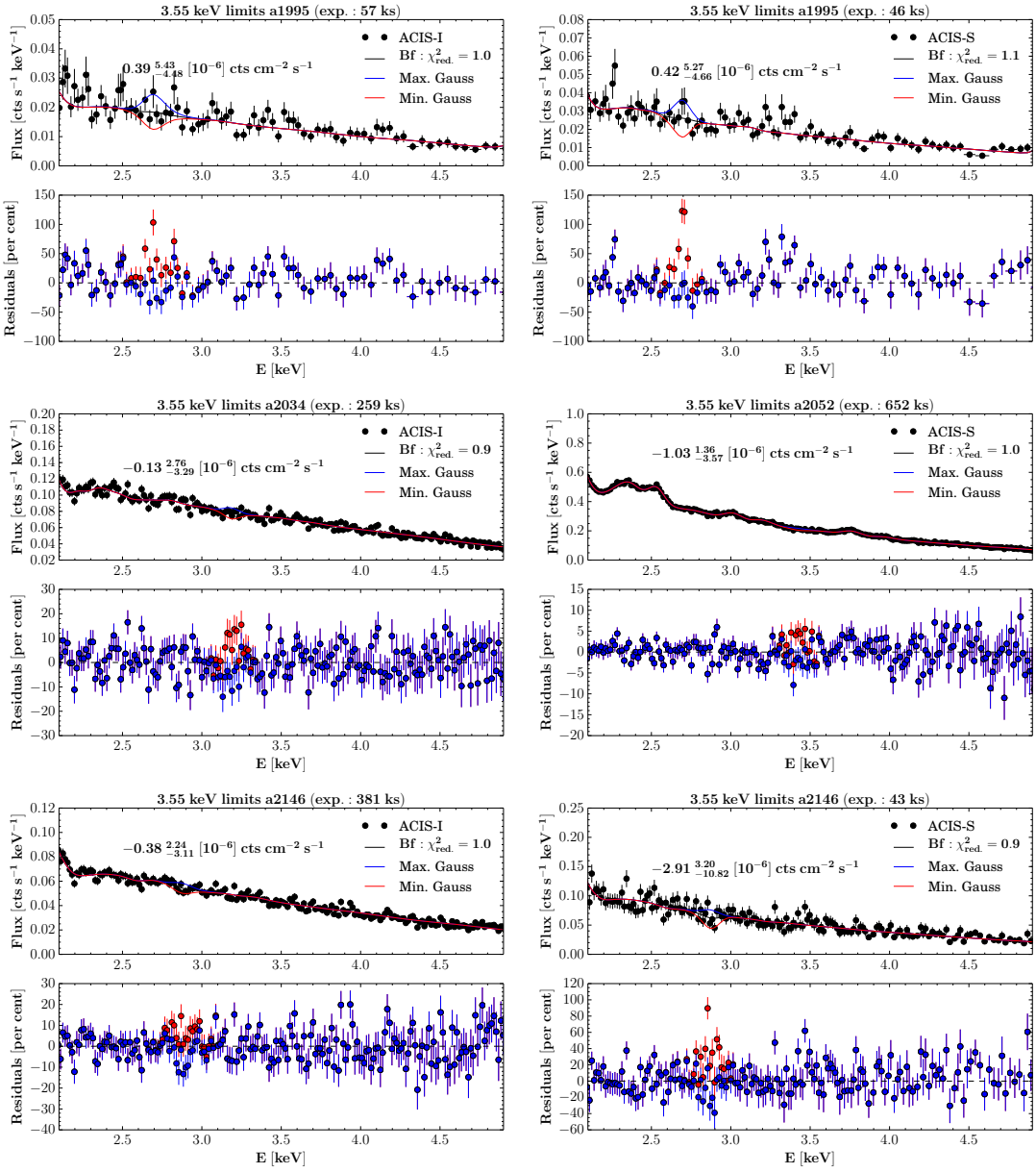

Figure B.3: continued.

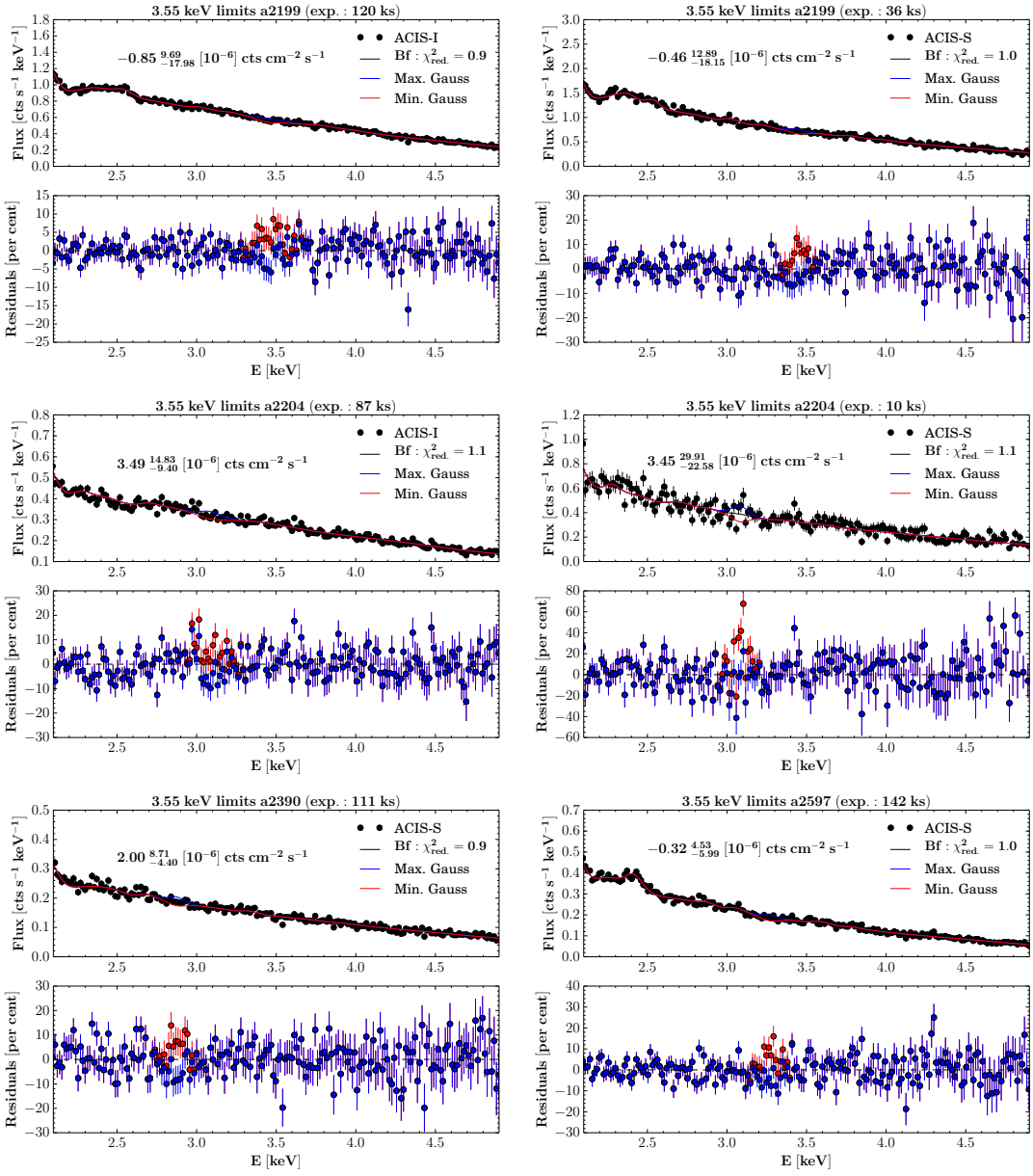

Figure B.3: continued.

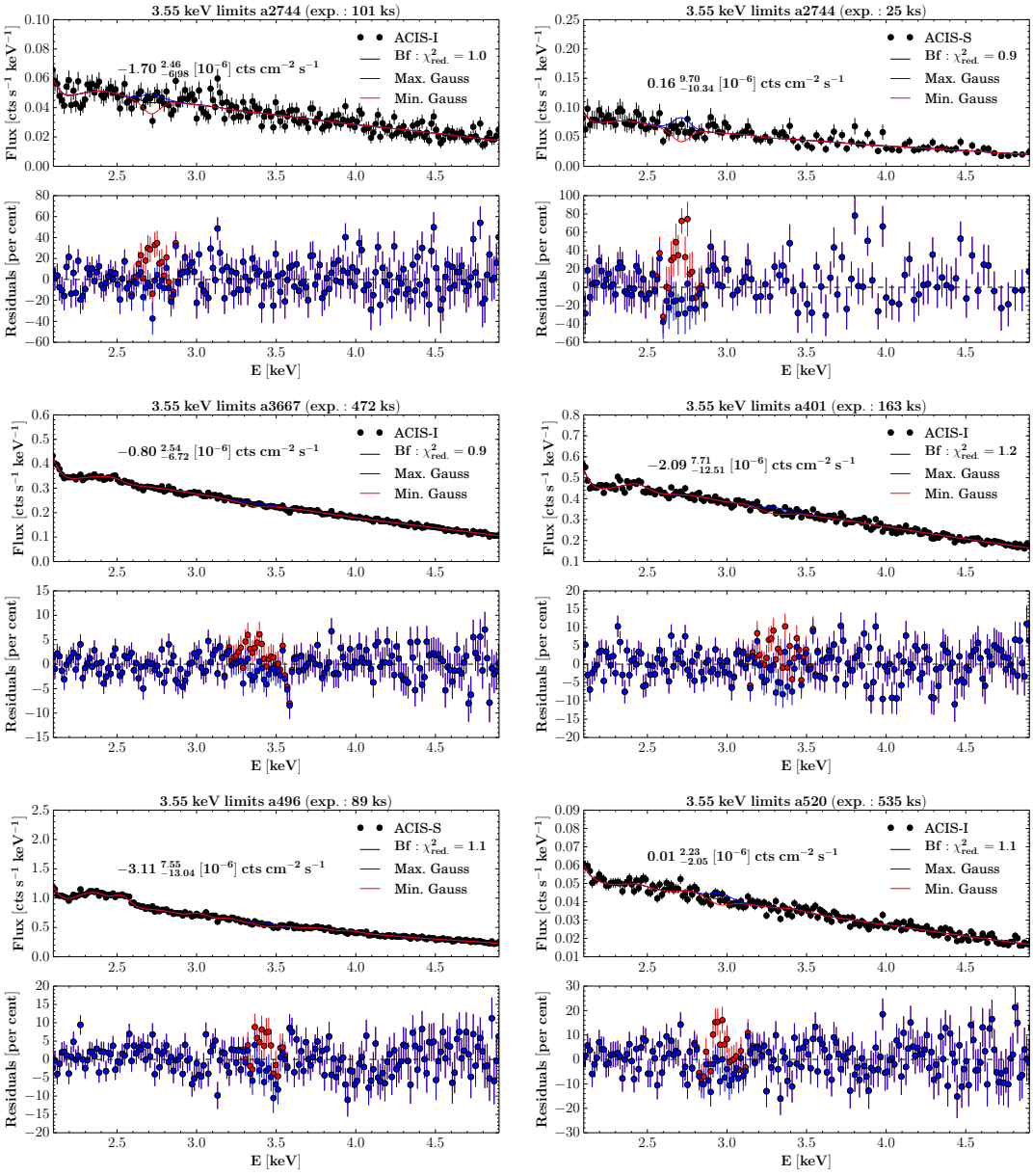

Figure B.3: continued.

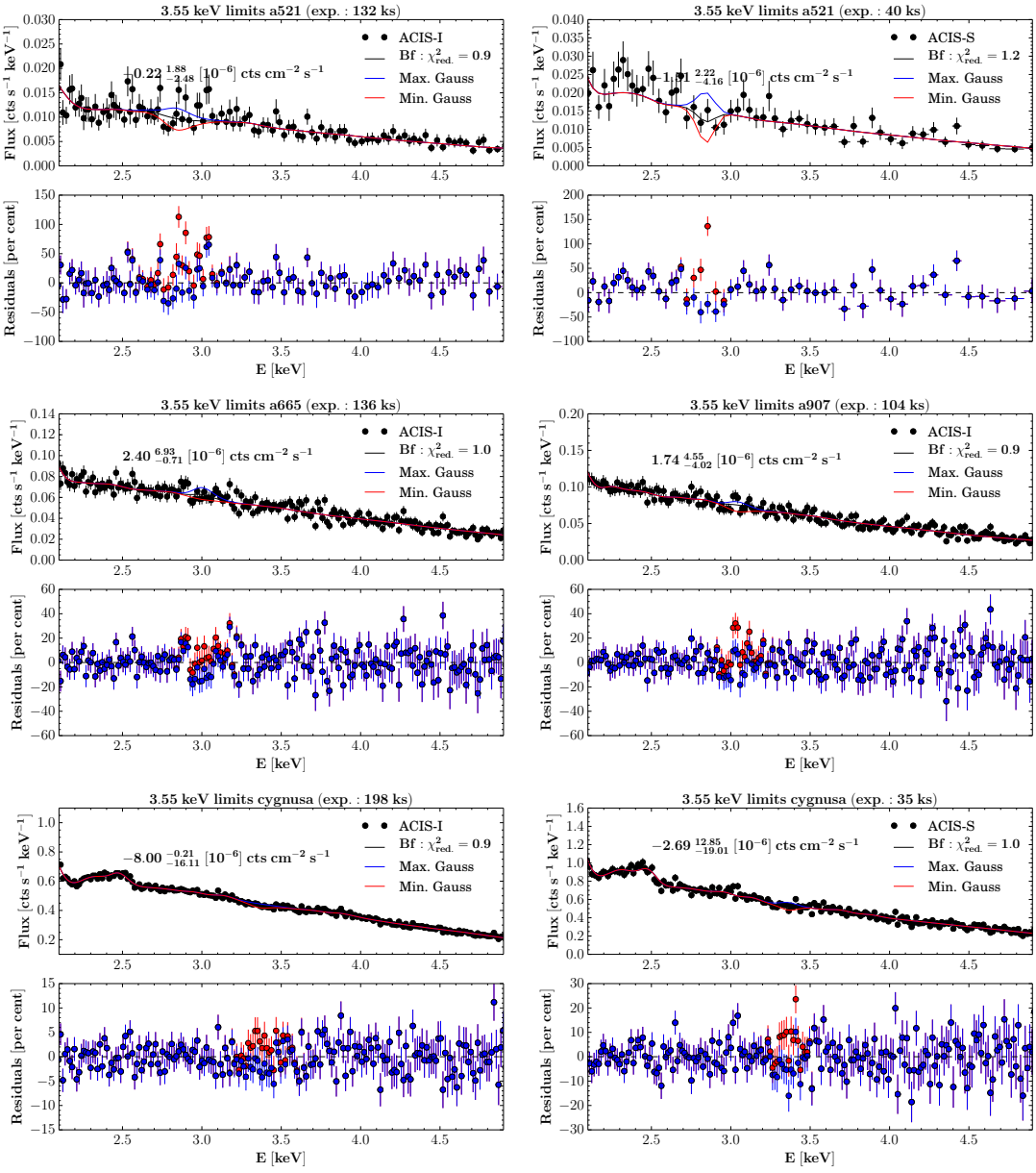

Figure B.3: continued.

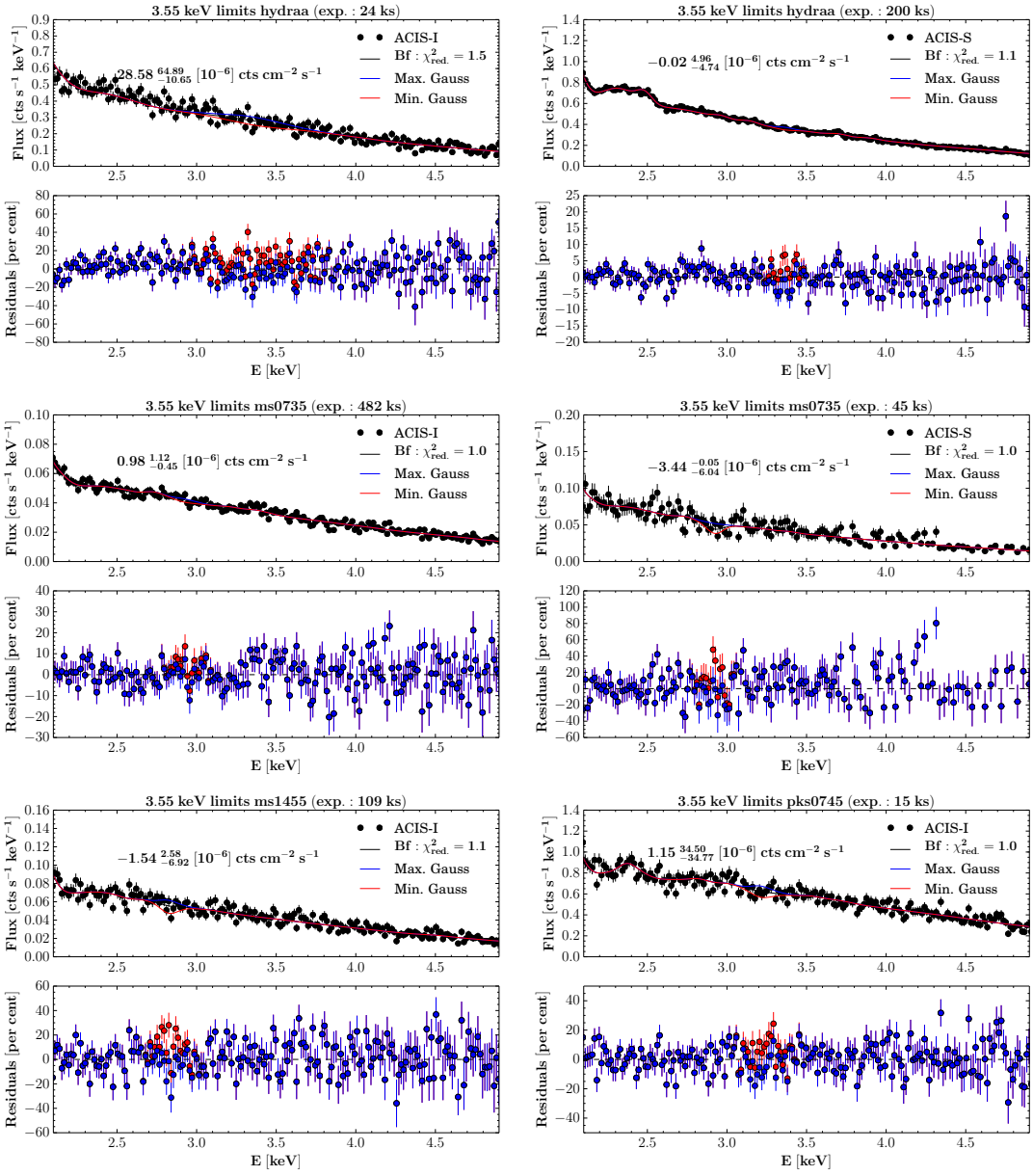

Figure B.3: continued.

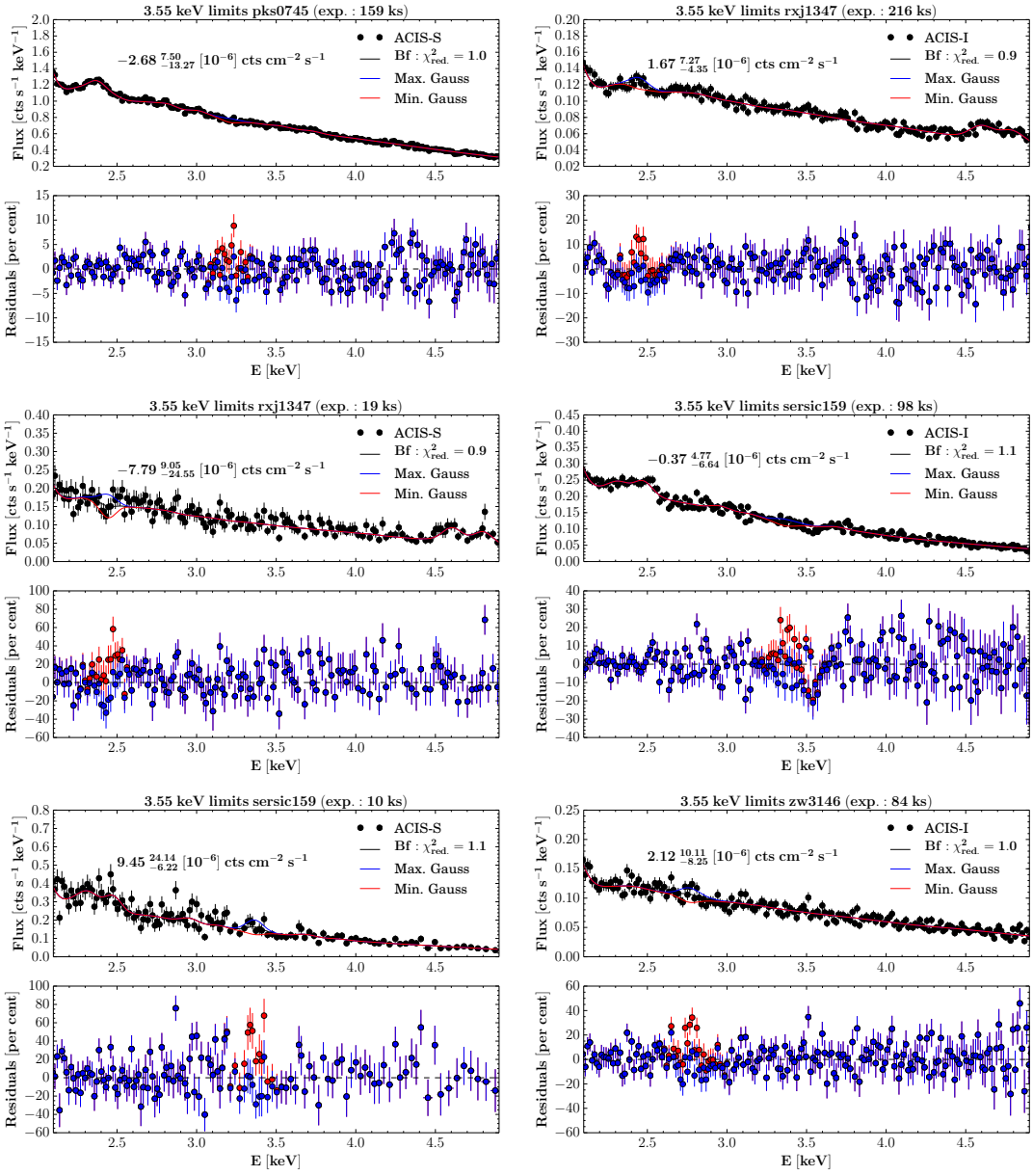

Figure B.3: continued.

Appendix C

eROSITA parameter bias

C.1 Bias in temperature T

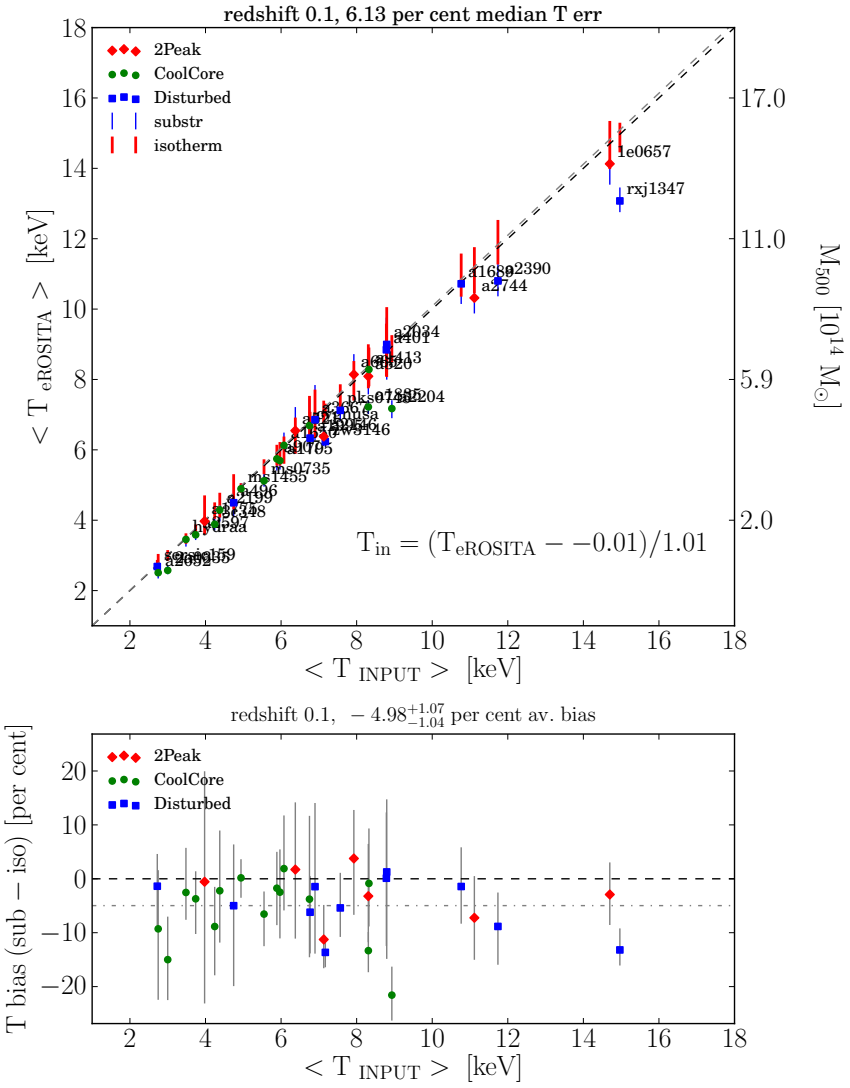

Figure C.1: Temperature substructure bias measurements in simulated eROSITA cluster observations. Top: input and fit temperature comparison. Errorbars are percentiles of medians of 100 best fit values. substructure and isothermal simulation values are plotted separately. The best-fit values in the substructure case is marked by substructure dependent symbols. the dotted black line is the one-to-one correlation. The dotted gray line and annotated formula give the best fit linear bias correction function applied to all datapoints. The second y-axis (right) shows typical masses according to the Vikhlinin et al. (2009a) T-M scaling relation. The plot title shows the average 1σ scatter of median values in per cent and the simulation redshift. Bottom: The offset between substructure and isothermal cluster temperature in per cent with uncertainties. The plot title indicates the average offset for all clusters (blue dotted line).

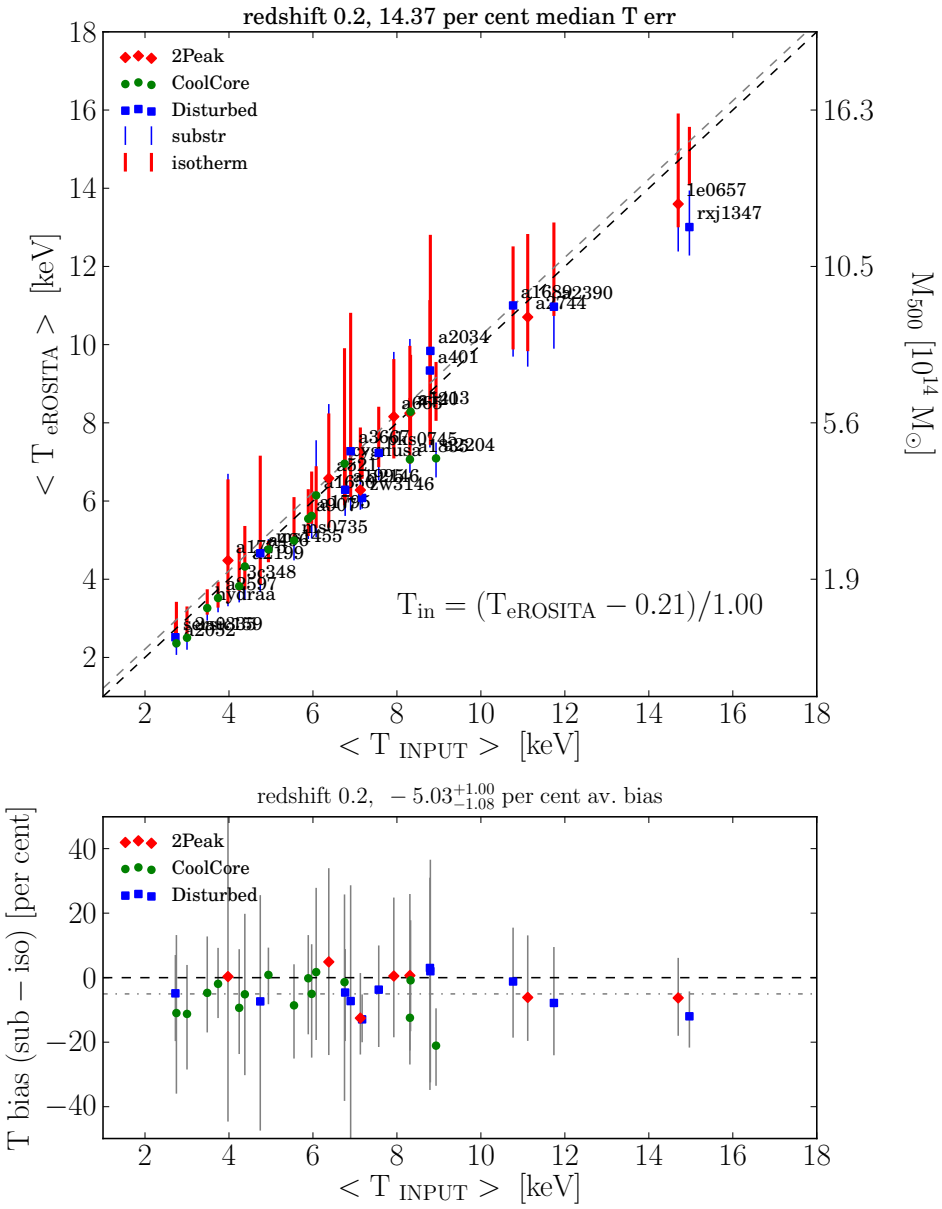

Figure C.1: continued.

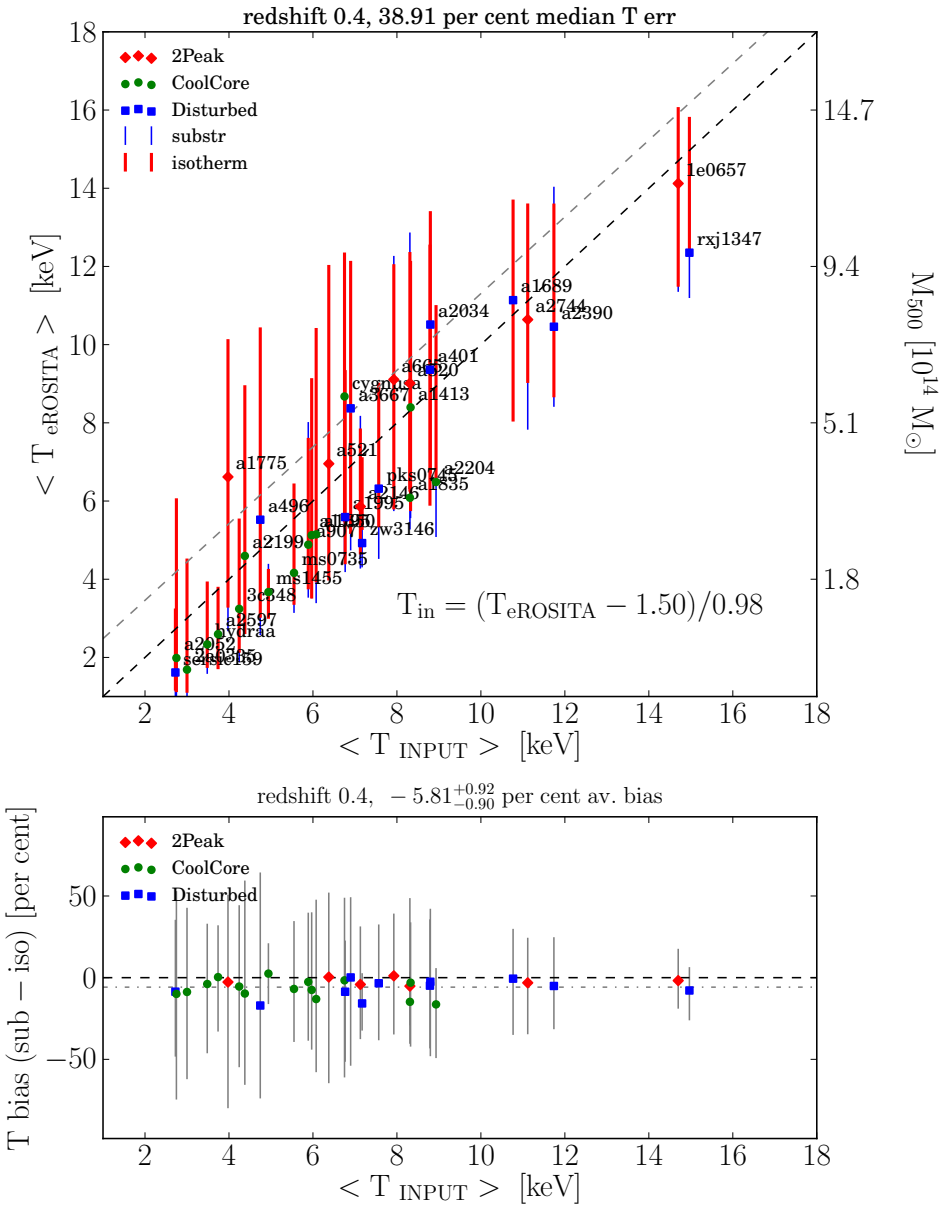

Figure C.1: continued.

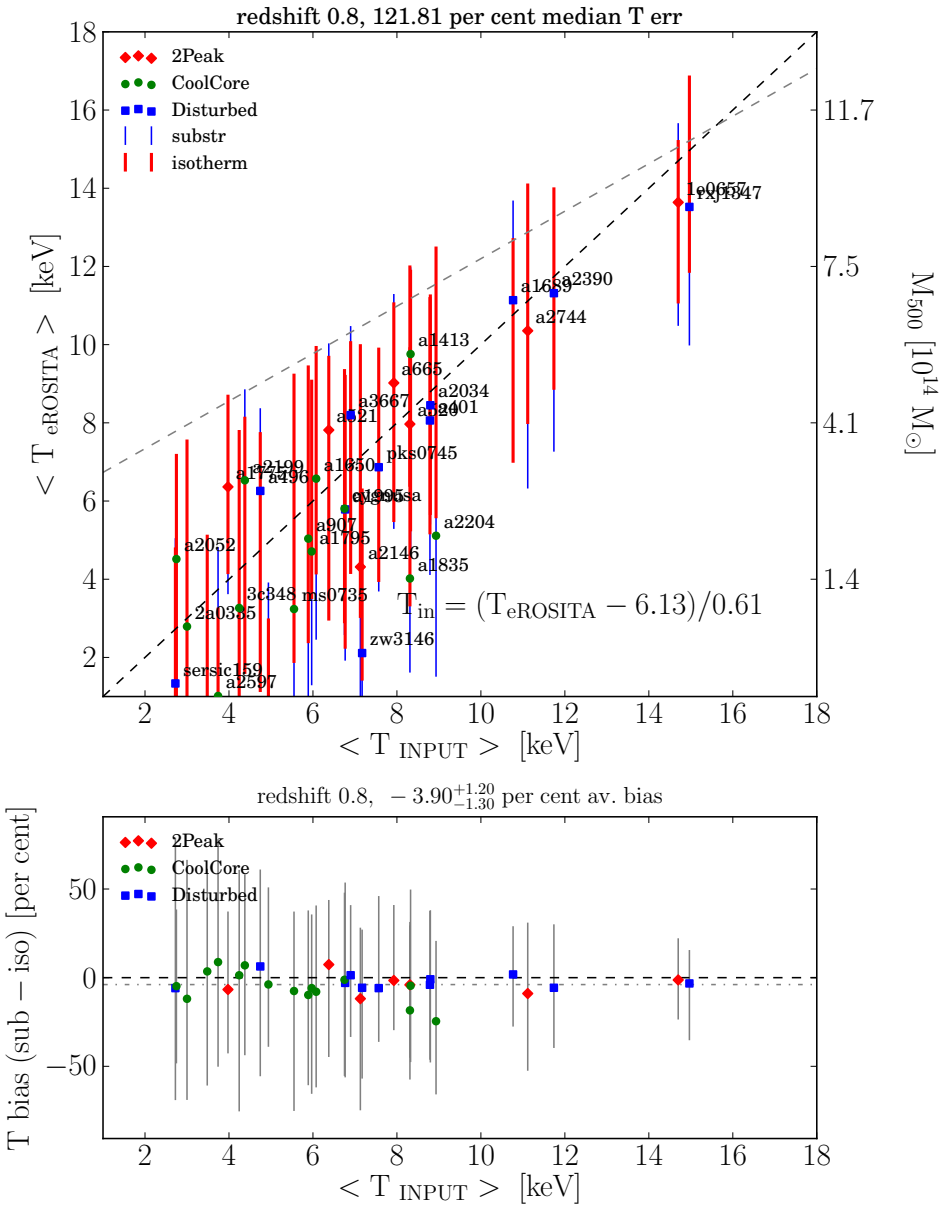

Figure C.1: continued.

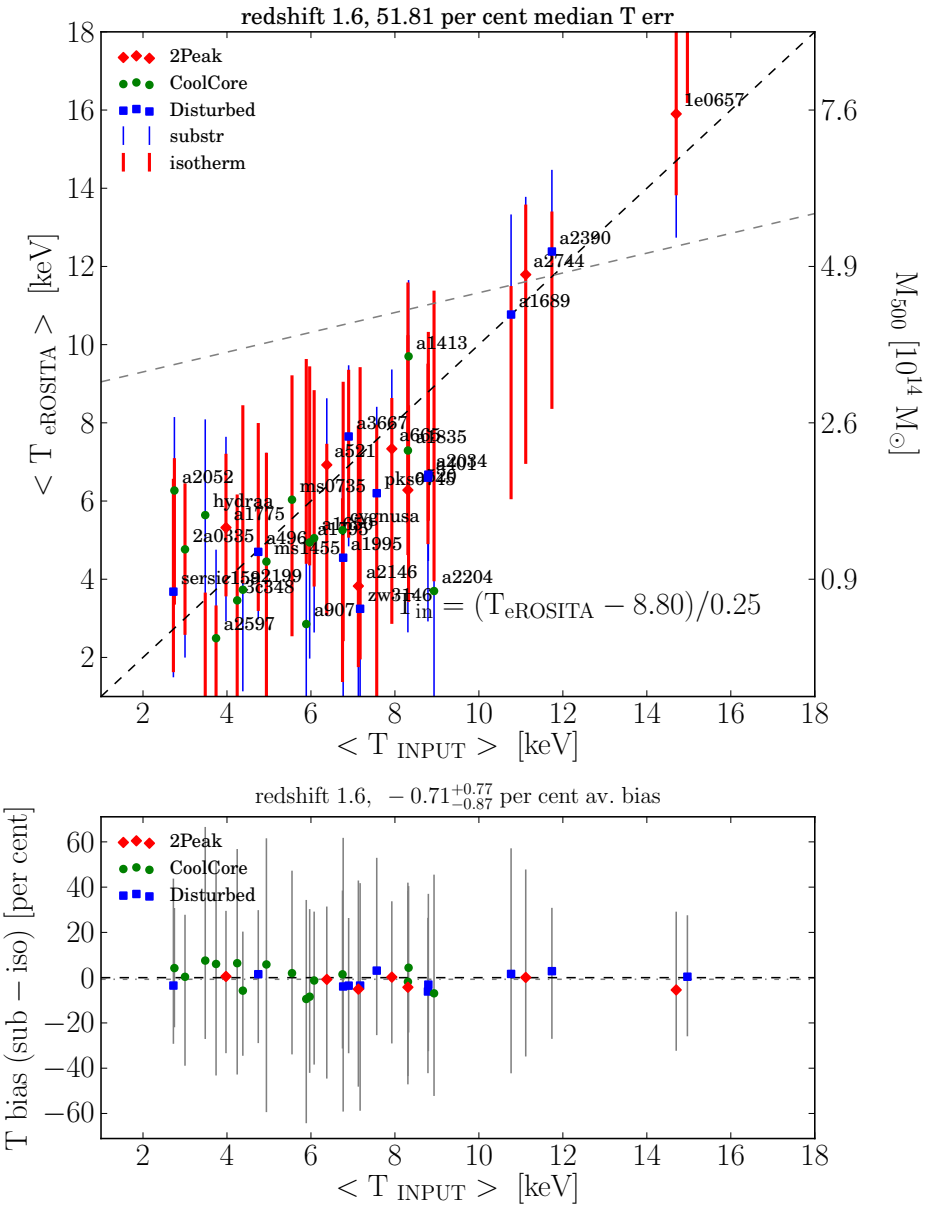

Figure C.1: continued.

C.2 Bias in flux F

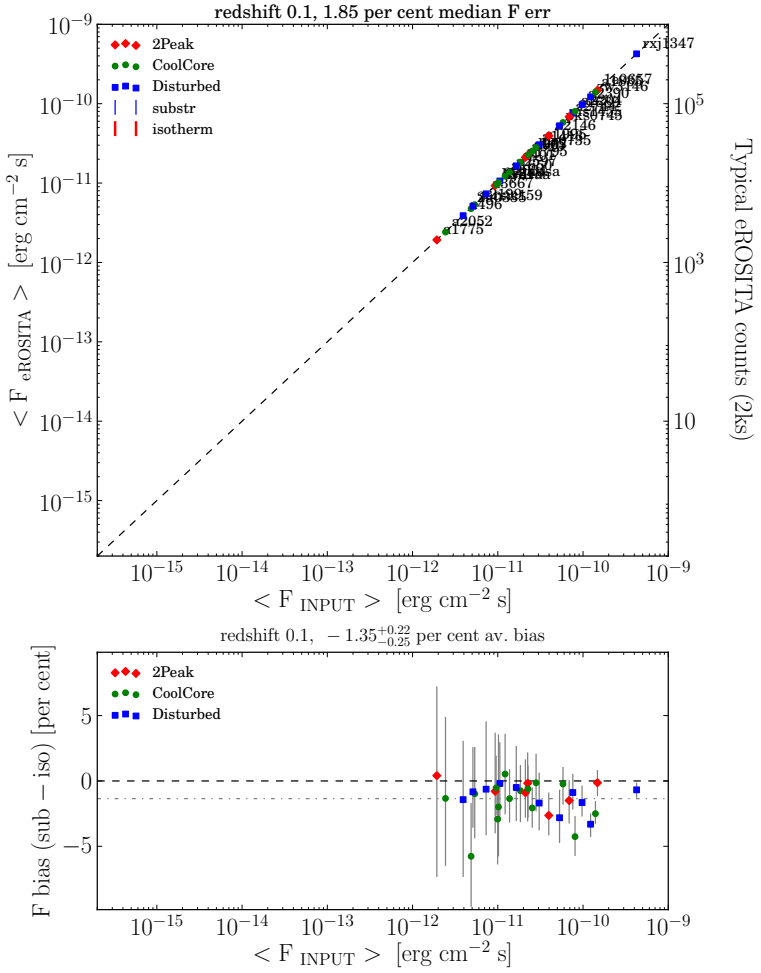

Figure C.2: Flux substructure bias measurements in simulated eROSITA cluster observations. Top: input and fit flux comparison. Errorbars are percentiles of medians of 100 best fit values. substructure and isothermal simulation values are plotted separately. The best-fit values in the substructure case is marked by substructure dependent symbols. the dotted black line is the one-to-one correlation. The second y-axis (right) shows typical counts in a 2 ks eROSITA observation. The plot title shows the average 1σ scatter of median values in per cent and the simulation redshift. Bottom: The offset between substructure and isothermal cluster flux in per cent with uncertainties. The plot title indicates the average offset for all clusters (blue dotted line).

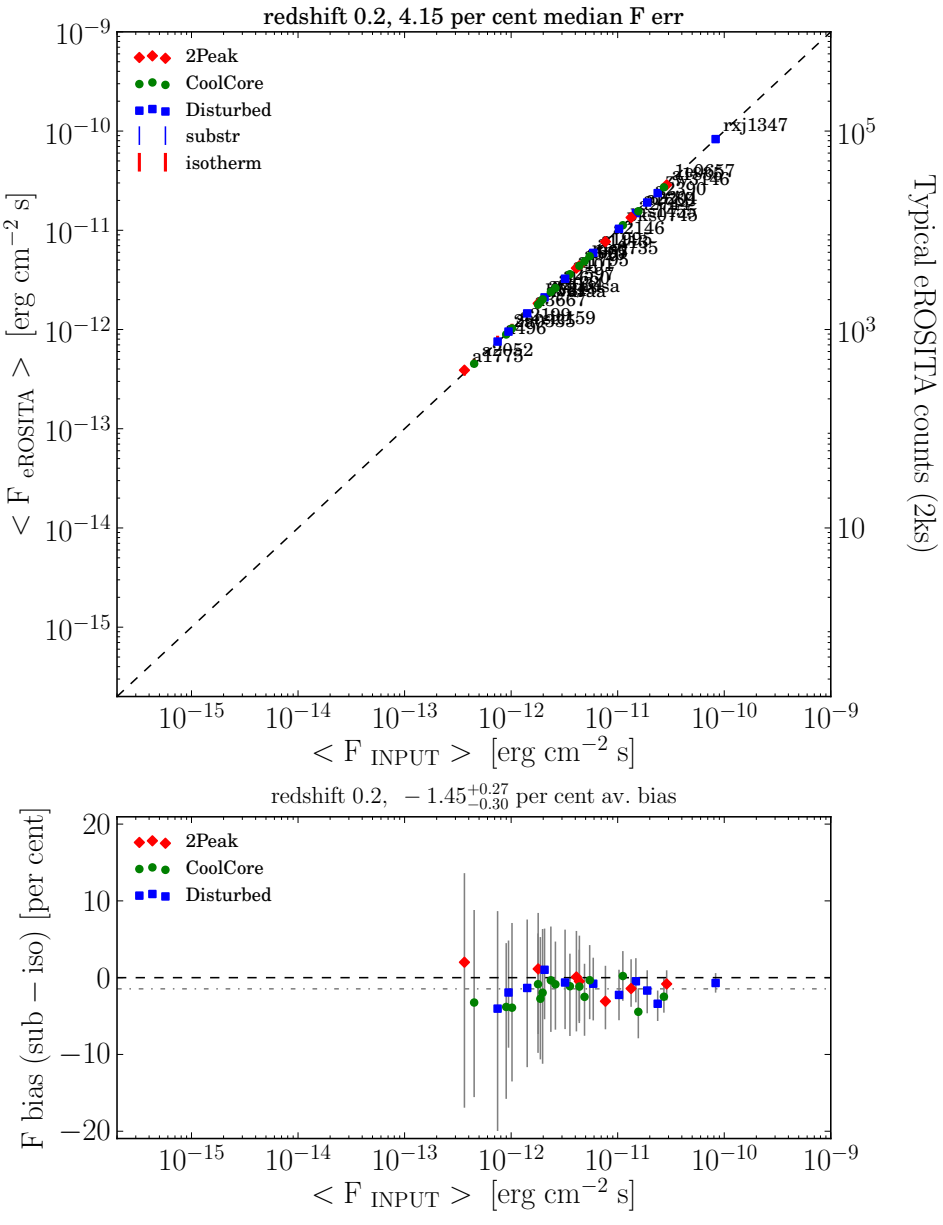

Figure C.2: continued.

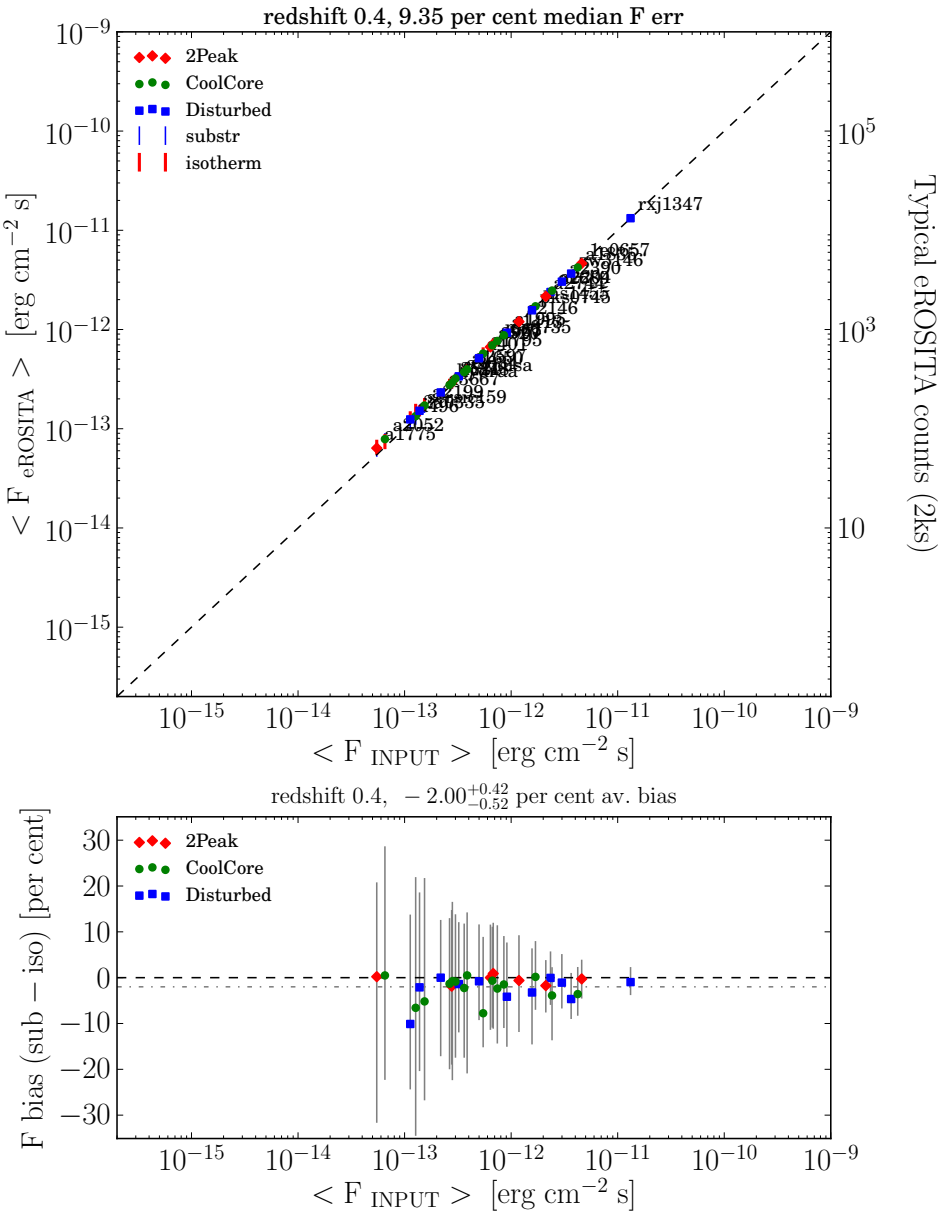

Figure C.2: continued.

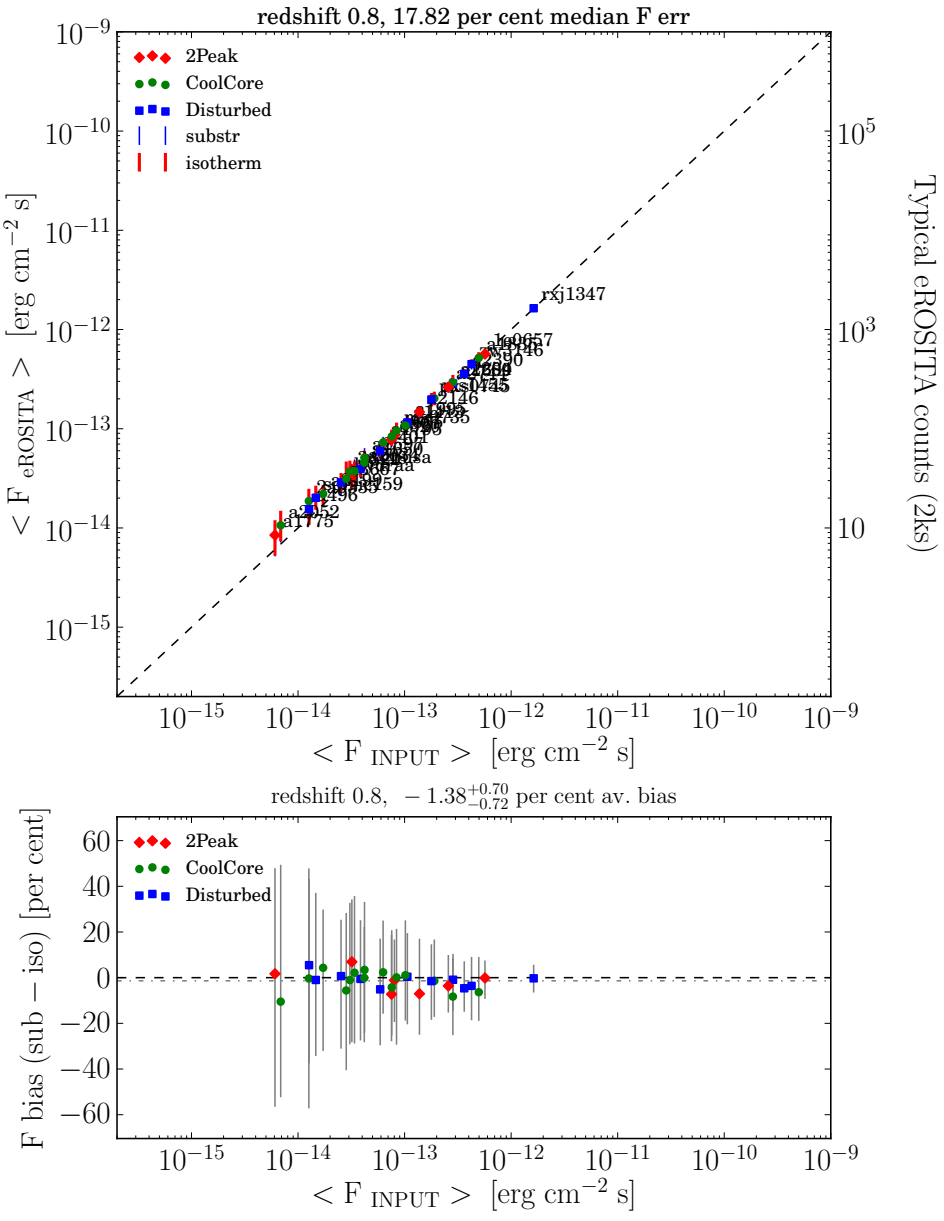

Figure C.2: continued.

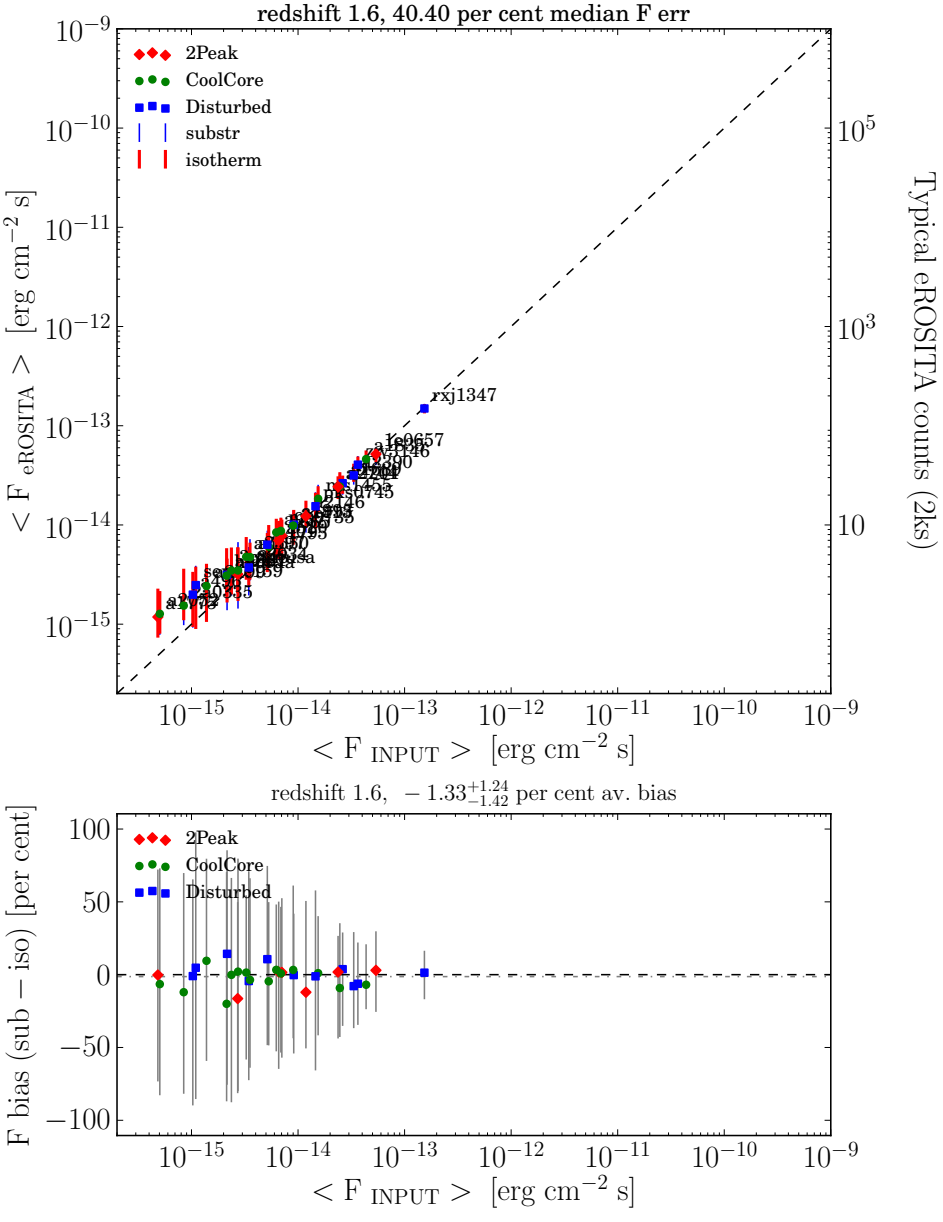

Figure C.2: continued.

Bibliography

Abazajian, K. 2009, in ArXiv Astrophysics e-prints, Vol. 2010, astro2010: The Astronomy and Astrophysics Decadal Survey

Abazajian, K., Fuller, G. M., & Tucker, W. H. 2001, ApJ, 562, 593

Abazajian, K. N., Markevitch, M., & Koushiappas, S. M. an d Hickox, R. C. 2007, Physical Review D, 75, 063511

Adhikari, R., Agostini, M., Ky, N. A., et al. 2016, ArXiv e-prints [arXiv:1602.04816]

Albrecht, A., Bernstein, G., Cahn, R., et al. 2006, ArXiv Astrophysics e-prints [astro-ph/0609591]

Allen, S. W., Evrard, A. E., & Mantz, A. B. 2011, ARA&A, 49, 409

Allen, S. W., Rapetti, D. A., Schmidt, R. W., et al. 2008, MNRAS, 383, 879

Allen, S. W., Schmidt, R. W., Ebeling, H., Fabian, A. C., & van Speybroeck, L. 2004, MNRAS, 353, 457

Allen, S. W., Schmidt, R. W., & Fabian, A. C. 2002, MNRAS, 334, L11

Anders, E. & Grevesse, N. 1989, Geochim. Cosmochim. Acta, 53, 197

Anderson, M. E., Churazov, E., & Bregman, J. N. 2015, MNRAS, 452, 3905

Andreon, S. 2008, MNRAS, 386, 1045

Andreon, S. 2010, MNRAS, 407, 263

Andreon, S. 2012, A&A, 546, A6

Applegate, D. E., Mantz, A., Allen, S. W., et al. 2016, MNRAS, 457, 1522

Arnaud, K. A. 1996a, in Astronomical Society of the Pacific Conference Series, Vol. 99, Cosmic Abundances, ed. S. S. Holt & G. Sonneborn, 409

Arnaud, K. A. 1996b, in Astronomical Society of the Pacific Conference Series, Vol. 101, Astronomical Data Analysis Software and Systems V, ed. G. H. Jacoby & J. Barnes, 17

Aschenbach, B. 1985, Reports on Progress in Physics, 48, 579

Baldi, A., Ettori, S., Molendi, S., Balestra, I. a nd Gastaldello, F., & Tozzi, P. 2012, A&A, 537, A142

Balestra, I., Tozzi, P., Ettori, S., et al. 2007, A&A, 462, 429

Battaglia, N., Bond, J. R., Pfrommer, C., & Sievers, J. L. 2012, ApJ, 758, 74

Berg, M., Conlon, J. P., Day, F., et al. 2016, ArXiv e-prints [arXiv:1605.01043]

Biviano, A. & Poggianti, B. 2010, in American Institute of Physics Conference Series, Vol. 1241, American Institute of Physics Conference Series, ed. J.-M. Alimi & A. Fuözfa, 192–199

Blanton, E. L., Clarke, T. E., Sarazin, C. L., Randall, S. W., & McNamara, B. R. 2010, Proceedings of the National Academy of Science, 107, 7174

Blanton, E. L., Randall, S. W., Clarke, T. E., et al. 2011, ApJ, 737, 99

Blanton, E. L., Sarazin, C. L., & McNamara, B. R. 2003, ApJ, 585, 227

Blanton, E. L., Sarazin, C. L., McNamara, B. R., & Wise, M. W. 2001, ApJ, 558, L15

Bleem, L. E., Stalder, B., de Haan, T., et al. 2015, ApJS, 216, 27

Bocquet, S., Saro, A., Dolag, K., & Mohr, J. J. 2016, MNRAS, 456, 2361

Bocquet, S., Saro, A., Mohr, J. J., et al. 2015, ApJ, 799, 214

Bode, P., Ostriker, J. P., & Turok, N. 2001, ApJ, 556, 93

Böhringer, H., Schuecker, P., Guzzo, L., et al. 2004, A&A, 425, 367

Böhringer, H., Voges, W., Huchra, J. P., et al. 2000, ApJS, 129, 435

Böhringer, H. & Werner, N. 2010, A&A Review, 18, 127

Bond, J. R., Cole, S., Efstathiou, G., & Kaiser, N. 1991, ApJ, 379, 440

Borgani, S. 2008, in Lecture Notes in Physics, Berlin Springer Verlag, Vol. 740, A Pan-Chromatic View of Clusters of Galaxies and the Large-Scale St ructure, ed. M. Plionis, O. López-Cruz, & D. Hughes, 24

Borm, K., Reiprich, T. H., Mohammed, I., & Lovisari, L. 2014, A&A, 567, A65

Boyarsky, A., Franse, J., Iakubovskyi, D., & Ruchaysk iy, O. 2015, Physical Review Letters, 115, 161301

Boyarsky, A., Iakubovskyi, D., Ruchayskiy, O., & Savchenko, V. 2008a, MNRAS, 387, 1361

Boyarsky, A., Neronov, A., Ruchayskiy, O., & Shaposhn ikov, M. 2006, MNRAS, 370, 213

Boyarsky, A., Ruchayskiy, O., Iakubovskyi, D., & Franse, J. 2014, Physical Review Letters, 113, 251301

Boyarsky, A., Ruchayskiy, O., & Markevitch, M. 2008b, ApJ, 673, 752

Boyarsky, A., Ruchayskiy, O., & Shaposhnikov, M. 2009, Annual Review of Nuclear and Particle Science, 59, 191

Bradač, M., Allen, S. W., Treu, T., et al. 2008, ApJ, 687, 959

Bradač, M., Clowe, D., Gonzalez, A. H., et al. 2006, ApJ, 652, 937

Brissenden, R. J. 2001, in Astronomical Society of the Pacific Conference Series, Vol. 238, Astronomical Data Analysis Software and Systems X, ed. F. R. Harnden, Jr., F. A. Primini, & H. E. Payne, 22

Broadhurst, T. J., Taylor, A. N., & Peacock, J. A. 1995, ApJ, 438, 49

Buchner, J., Georgakakis, A., Nandra, K., et al. 2014, A&A, 564, A125

Bulbul, E., Markevitch, M., Foster, A., et al. 2014, ApJ, 789, 13

Canning, R. E. A., Russell, H. R., Hatch, N. A., et al. 2012, MNRAS, 420, 2956

Cash, W. 1979, ApJ, 228, 939

Cassano, R. & Brunetti, G. 2005, MNRAS, 357, 1313

Chon, G., Böhringer, H., & Smith, G. P. 2012, A&A, 548, A59

Churazov, E., Zhuravleva, I., Sazonov, S., & Sunyaev, R. 2010, Space Sci. Rev., 157, 193

Ciotti, L. & Ostriker, J. P. 2007, ApJ, 665, 1038

Clausius, R. 1870, Annalen der Physik, 217, 124

Clerc, N., Adami, C., Lieu, M., et al. 2014, MNRAS, 444, 2723

Clerc, N., Sadibekova, T., Pierre, M., et al. 2012, MNRAS, 423, 3561

Clowe, D., Bradač, M., Gonzalez, A. H., et al. 2006, ApJ, 648, L109

Clowe, D., Gonzalez, A., & Markevitch, M. 2004, ApJ, 604, 596

Colless, M., Dalton, G., Maddox, S., et al. 2001, MNRAS, 328, 1039

Copeland, E. J., Sami, M., & Tsujikawa, S. 2006, International Journal of Modern Physics D, 15, 1753

Cruddace, R. G., Hasinger, G., Truemper, J., Schmitt, J. H. M. M., & Hartner, G. D. 1991, Experimental Astronomy, 1, 365

Dai, X., Bregman, J. N., Kochanek, C. S., & Rasia, E. . 2010, ApJ, 719, 119

De Grandi, S. & Molendi, S. 2001, ApJ, 551, 153

de Jong, R. S., Bellido-Tirado, O., Chiappini, C., et al. 2012, in SPIE conference proceedings, Vol. 8446, Ground-based and Airborne Instrumentation for Astronomy IV, 84460T

De Lucia, G. & Blaizot, J. 2007, MNRAS, 375, 2

De Lucia, G., Kauffmann, G., & White, S. D. M. 2004, MNRAS, 349, 1101

De Lucia, G., Springel, V., White, S. D. M., Croton, D., & Kauffmann, G. 2006, MNRAS, 366, 499

de Plaa, J., Werner, N., Bleeker, J. A. M., et al. 2007, A&A, 465, 345

Dennis, T. J. & Chandran, B. D. G. 2005, ApJ, 622, 205

Dodelson, S. & Widrow, L. M. 1994, Physical Review Letters, 72, 17

Dolag, K. 2015, IAU General Assembly, 22, 2250156

Dolag, K., Schindler, S., Govoni, F., & Feretti, L. 2001, A&A, 378, 777

Dolag, K., Vazza, F., Brunetti, G., & Tormen, G. 2005, MNRAS, 364, 753

Donahue, M., Connor, T., Fogarty, K., et al. 2015, ApJ, 805, 177

Dunkley, J., Komatsu, E., Nolta, M. R., et al. 2009, ApJS, 180, 306

Dunn, R. J. H., Fabian, A. C., & Taylor, G. B. 2005, MNRAS, 364, 1343

Ebeling, H., Mullis, C. R., & Tully, R. B. 2002, ApJ, 580, 774

Ehlert, S., McDonald, M., David, L. P., Miller, E. D., & Bautz, M. W. 2015, ApJ, 799, 174

Einstein, A. 1936, Science, 84, 506

Ettori, S. 2013, MNRAS, 435, 1265

Ettori, S. & Fabian, A. C. 1999, MNRAS, 305, 834

Ettori, S., Fabian, A. C., Allen, S. W., & Johnstone, R. M. 2002, MNRAS, 331, 635

Ettori, S., Morandi, A., Tozzi, P., et al. 2009, A&A, 501, 61

Ettori, S., Pratt, G. W., de Plaa, J., et al. 2013, ArXiv e-prints [arXiv:1306.2322]

Evrard, A. E., Metzler, C. A., & Navarro, J. F. 1996, ApJ, 469, 494

Fabian, A. C. 1994, ARA&A, 32, 277

Fabian, A. C., Nulsen, P. E. J., & Canizares, C. R. 1984, Nature, 310, 733

Fabian, A. C., Sanders, J. S., Allen, S. W., et al. 2003a, MNRAS, 344, L43

Fabian, A. C., Sanders, J. S., Crawford, C. S., et al. 2003b, MNRAS, 344, L48

Fabian, A. C., Sanders, J. S., Ettori, S., et al. 2001, MNRAS, 321, L33

Fabian, A. C., Sanders, J. S., Ettori, S., et al. 2000, MNRAS, 318, L65

Fabian, A. C., Sanders, J. S., Taylor, G. B., et al. 2006, MNRAS, 366, 417

Feroz, F., Hobson, M. P., & Bridges, M. 2009, MNRAS, 398, 1601

Finoguenov, A., Ponman, T. J., Osmond, J. P. F., & Zimer, M. 2007, MNRAS, 374, 737

Finoguenov, A., Reiprich, T. H., & Böhringer, H. 2001, A&A, 368, 749

Fixsen, D. J. 2009, ApJ, 707, 916

Foreman-Mackey, D., Hogg, D. W., Lang, D., & Goodman, J. 2013, PASP, 125, 306

Forman, W., Jones, C., Churazov, E., et al. 2007, ApJ, 665, 1057

Foster, A. R., Ji, L., Smith, R. K., & Brickhouse, N. . S. 2012, ApJ, 756, 128

Franse, J., Bulbul, E., Foster, A., et al. 2016, ArXiv e-prints [arXiv:1604.01759]

Freedman, W. L., Madore, B. F., Gibson, B. K., et al. 2001, ApJ, 553, 47

Fruscione, A., McDowell, J. C., Allen, G. E., et al. 2006, in SPIE conference proceedings, Vol. 6270, Society of Photo-Optical Instrumentation Engineers (SPIE) Conferenc e Series, 62701V

Fryxell, B., Olson, K., Ricker, P., et al. 2000, ApJS, 131, 273

Garmire, G. P., Bautz, M. W., Ford, P. G., Nousek, J. A., & Ricker, Jr., G. R. 2003, in SPIE conference proceedings, Vol. 4851, X-Ray and Gamma-Ray Telescopes and Instruments for Astronomy., ed. J. E. Truemper & H. D. Tananbaum, 28–44

Gaspari, M., Brighenti, F., & Temi, P. 2012a, MNRAS, 424, 190

Gaspari, M. & Churazov, E. 2013, A&A, 559, A78

Gaspari, M., Churazov, E., Nagai, D., & Lau, E. T. a nd Zhuravleva, I. 2014, A&A, 569, A67

Gaspari, M., Melioli, C., Brighenti, F., & D'Ercole, A. 2011, MNRAS, 411, 349

Gaspari, M., Ruszkowski, M., & Sharma, P. 2012b, ApJ, 746, 94

Gastaldello, F., Ettori, S., Balestra, I., et al. 2010, A&A, 522, A34

George, M. R., Fabian, A. C., Sanders, J. S., Young, A. J., & Russell, H. R. 2009, MNRAS, 395, 657

Ghizzardi, S., De Grandi, S., & Molendi, S. 2014, A&A, 570, A117

Giles, P. A., Maughan, B. J., Pacaud, F., et al. 2016, A&A, 592, A3

Gilli, R., Comastri, A., & Hasinger, G. 2007, A&A, 463, 79

Govoni, F., Markevitch, M., Vikhlinin, A., et al. 2004, ApJ, 605, 695

Graessle, D. E., Evans, I. N., Glotfelty, K., et al. 2007, Chandra News, 14, 33

Greisen, E. W. & Calabretta, M. R. 2002, A&A, 395, 1061

Gu, L., Kaastra, J., Raassen, A. J. J., et al. 2015, A&A, 584, L11

Hanisch, R. J., Farris, A., Greisen, E. W., et al. 2001, A&A, 376, 359

Hasinger, G., Miyaji, T., & Schmidt, M. 2005, A&A, 441, 417

Haslam, C. G. T., Salter, C. J., Stoffel, H., & Wilson, W. E. 1982, A&AS, 47, 1

Hicks, A. K. & Mushotzky, R. 2005, ApJ, 635, L9

Hinshaw, G., Larson, D., Komatsu, E., et al. 2013, ApJS, 208, 19

Hitomi Collaboration, Aharonian, F., Akamatsu, H., et al. 2016a, Nature, 535, 117

Hitomi Collaboration, Aharonian, F. A., Akamatsu, H. an d Akimoto, F., et al. 2016b, ArXiv e-prints [arXiv:1607.07420]

Hoekstra, H., Yee, H. K. C., & Gladders, M. D. 2004, ApJ, 606, 67

Hofmann, F., Sanders, J. S., Nandra, K., Clerc, N., & Gaspari, M. 2016a, A&A, 592, A112

Hofmann, F., Sanders, J. S., Nandra, K., Clerc, N., & Gaspari, M. 2016b, A&A, 585, A130

Hogg, D. W., Bovy, J., & Lang, D. 2010, ArXiv e-prints [arXiv:1008.4686]

Horiuchi, S., Humphrey, P. J., Oñorbe, J., et al. 2014, Physical Review D, 89, 025017

Iakubovskyi, D. 2015, MNRAS, 453, 4097

Iakubovskyi, D., Bulbul, E., Foster, A. R., Savchen ko, D., & Sadova, V. 2015, ArXiv e-prints [arXiv:1508.05186]

Iakubovskyi, D. A. 2014, Advances in Astronomy and Space Physics, 4, 9

Iapichino, L., Schmidt, W., Niemeyer, J. C., & Merklein, J. 2011, MNRAS, 414, 2297

Iocco, F., Mangano, G., Miele, G., Pisanti, O., & Serpico, P. D. 2009, Physics Reports, 472, 1

Jeltema, T. & Profumo, S. 2015, MNRAS, 450, 2143

Jeltema, T. & Profumo, S. 2016, MNRAS, 458, 3592

Jeltema, T. E., Hallman, E. J., Burns, J. O., & Motl, P. M. 2008, ApJ, 681, 167

Johnstone, R. M., Allen, S. W., Fabian, A. C., & Sanders, J. S. 2002, MNRAS, 336, 299

Kaastra, J. S., Bykov, A. M., Schindler, S., et al. 2008, Space Sci. Rev., 134, 1

Kaiser, N., Squires, G., & Broadhurst, T. 1995, ApJ, 449, 460

Kajita, T. & Totsuka, Y. 2001, Reviews of Modern Physics, 73, 85

Kalberla, P. M. W., Burton, W. B., Hartmann, D., et al. 2005, A&A, 440, 775

Kettula, K., Giodini, S., van Uitert, E., et al. 2015, MNRAS, 451, 1460

Kitayama, T., Bautz, M., Markevitch, M., et al. 2014, ArXiv e-prints [arXiv:1412.1176]

Kolmogorov, A. 1941, Akademiia Nauk SSSR Doklady, 30, 301

Kolmogorov, A. N. 1962, Journal of Fluid Mechanics, 13, 82

Kolodzig, A., Gilfanov, M., Sunyaev, R., Sazonov, S., & Brusa, M. 2013, A&A, 558, A89

Komatsu, E., Dunkley, J., Nolta, M. R., et al. 2009, ApJS, 180, 330

Komatsu, E., Smith, K. M., Dunkley, J., et al. 2011, ApJS, 192, 18

Kormendy, J., Fisher, D. B., Cornell, M. E., & Bender, R. 2009, ApJS, 182, 216

Kravtsov, A. V. & Borgani, S. 2012, ARA&A, 50, 353

Kravtsov, A. V., Vikhlinin, A., & Nagai, D. 2006, ApJ, 650, 128

Lahav, O. & Liddle, A. R. 2014, ArXiv e-prints [arXiv:1401.1389]

Lau, E. T., Kravtsov, A. V., & Nagai, D. 2009, ApJ, 705, 1129

Leccardi, A. & Molendi, S. 2007, A&A, 472, 21

Leccardi, A. & Molendi, S. 2008, A&A, 487, 461

Lieu, M., Smith, G. P., Giles, P. A., et al. 2016, A&A, 592, A4

Lin, Y.-T., Brodwin, M., Gonzalez, A. H., et al. 2013, ApJ, 771, 61

Lin, Y.-T., Mohr, J. J., & Stanford, S. A. 2003, ApJ, 591, 749

Loewenstein, M., Kusenko, A., & Biermann, P. L. 2009, ApJ, 700, 426

Lovisari, L., Schindler, S., & Kapferer, W. 2011, A&A, 528, A60

Lumb, D. H., Warwick, R. S., Page, M., & De Luca, A. 2002, A&A, 389, 93

Machado, R. E. G. & Lima Neto, G. B. 2015, MNRAS, 447, 2915

Mahdavi, A., Hoekstra, H., Babul, A., et al. 2013, ApJ, 767, 116

Malyshev, D., Neronov, A., & Eckert, D. 2014, Physical Review D, 90, 103506

Mantz, A., Allen, S. W., Rapetti, D., & Ebeling, H. 2010, MNRAS, 406, 1759

Markevitch, M., Bautz, M. W., Biller, B., et al. 2003, ApJ, 583, 70

Markevitch, M., Gonzalez, A. H., Clowe, D., et al. 2004, ApJ, 606, 819

Markevitch, M., Gonzalez, A. H., David, L., et al. 2002, ApJ, 567, L27

Markevitch, M., Ponman, T. J., Nulsen, P. E. J., et al. 2000, ApJ, 541, 542

Markevitch, M. & Vikhlinin, A. 2007, Physics Reports, 443, 1

Markevitch, M., Vikhlinin, A., Forman, W. R., & Sarazin, C. L. 1999, ApJ, 527, 545

Markevitch, M., Vikhlinin, A., & Mazzotta, P. 2001, ApJ, 562, L153

Mathiesen, B. F. & Evrard, A. E. 2001, ApJ, 546, 100

Maughan, B. J., Jones, C., Forman, W., & Van Speybroe ck, L. 2008, ApJS, 174, 117

Mazzotta, P., Rasia, E., Moscardini, L., & Tormen, G. . 2004, MNRAS, 354, 10

McDonald, M., Benson, B. A., Vikhlinin, A., et al. 2013, ApJ, 774, 23

McDonald, M., Stalder, B., Bayliss, M., et al. 2016, ApJ, 817, 86

McDonald, M., Veilleux, S., Rupke, D. S. N., Mushotzky, R., & Reynolds, C. 2011, ApJ, 734, 95

McNamara, B. R., Nulsen, P. E. J., Wise, M. W., et al. 2005, Nature, 433, 45

McNamara, B. R., Wise, M., Nulsen, P. E. J., et al. 2000, ApJ, 534, L135

Menanteau, F., Hughes, J. P., Sifón, C., et al. 2012, ApJ, 748, 7

Merloni, A., Predehl, P., Becker, W., et al. 2012, ArXiv e-prints [arXiv:1209.3114]

Million, E. T. & Allen, S. W. 2009, MNRAS, 399, 1307

Miniati, F. 2014, ApJ, 782, 21

Mohr, J. J., Evrard, A. E., Fabricant, D. G., & Geller, M. J. 1995, ApJ, 447, 8

Mukhanov, V. F., Feldman, H. A., & Brandenberger, R. H. 1992, Physics Reports, 215, 203

Nagai, D., Lau, E. T., Avestruz, C., & Nelson, K. an d Rudd, D. H. 2013, ApJ, 777, 137

Nagai, D., Vikhlinin, A., & Kravtsov, A. V. 2007, ApJ, 655, 98

Nandra, K., Barret, D., Barcons, X., et al. 2013, ArXiv e-prints [arXiv:1306.2307]

Navarro, J. F., Frenk, C. S., & White, S. D. M. 1995, MNRAS, 275, 720

Navarro, J. F., Frenk, C. S., & White, S. D. M. 1996, ApJ, 462, 563

Navarro, J. F., Frenk, C. S., & White, S. D. M. 1997, ApJ, 490, 493

Nelson, K., Lau, E. T., & Nagai, D. 2014, ApJ, 792, 25

Nelson, K., Rudd, D. H., Shaw, L., & Nagai, D. 2012, ApJ, 751, 121

Norman, M. L. & Bryan, G. L. 1999, in Lecture Notes in Physics, Berlin Springer Verlag, Vol. 530, The Radio Galaxy Messier 87, ed. H.-J. Röser & K. Meisenheimer, 106

Nulsen, P. E. J., David, L. P., McNamara, B. R., et al. 2002, ApJ, 568, 163

Nulsen, P. E. J., Li, Z., Forman, W. R., et al. 2013, ApJ, 775, 117

Nulsen, P. E. J., McNamara, B. R., Wise, M. W., & David, L. P. 2005, ApJ, 628, 629

Oegerle, W. R. & Hill, J. M. 1994, AJ, 107, 857

Pacaud, F., Clerc, N., Giles, P. A., et al. 2016, A&A, 592, A2

Panagoulia, E. K., Fabian, A. C., & Sanders, J. S. 2013, MNRAS, 433, 3290

Parekh, V., van der Heyden, K., Ferrari, C., Angus, G., & Holwerda, B. 2015, A&A, 575, A127

Pavlinsky, M., Akimov, V., Levin, V., et al. 2011, in SPIE conference proceedings, Vol. 8147, Society of Photo-Optical Instrumentation Engineers (SPIE) Conferenc e Series, 814706

Peebles, P. J. & Ratra, B. 2003, Reviews of Modern Physics, 75, 559

Peebles, P. J. E. 1993, Principles of Physical Cosmology

Pence, W. D., Chiappetti, L., Page, C. G., Shaw, R. . A., & Stobie, E. 2010, A&A, 524, A42

Perlmutter, S., Aldering, G., Goldhaber, G., et al. 1999, ApJ, 517, 565

Peterson, J. R. & Fabian, A. C. 2006, Physics Reports, 427, 1

Pierpaoli, E., Borgani, S., Scott, D., & White, M. 2003, MNRAS, 342, 163

Piffaretti, R., Arnaud, M., Pratt, G. W., Pointecou teau, E., & Melin, J.-B. 2011, A&A, 534, A109

Pillepich, A., Porciani, C., & Reiprich, T. H. 2012, MNRAS, 422, 44

Pinto, C., Sanders, J. S., Werner, N., et al. 2015, A&A, 575, A38

Plagge, T., Benson, B. A., Ade, P. A. R., et al. 2010, ApJ, 716, 1118

Planck Collaboration, Ade, P. A. R., Aghanim, N., et al. 2014a, A&A, 571, A16

Planck Collaboration, Ade, P. A. R., Aghanim, N., et al. 2014b, A&A, 571, A20

Plionis, M., López-Cruz, O., & Hughes, D., eds. 2008, Lecture Notes in Physics, Berlin Springer Verlag, Vol. 740, A Pan-Chromatic View of Clusters of Galaxies and the Large-Scale S tructure, 24

Pointecouteau, E., Reiprich, T. H., Adami, C., et al. 2013, ArXiv e-prints [arXiv:1306.2319]

Ponman, T. J., Cannon, D. B., & Navarro, J. F. 1999, Nature, 397, 135

Popesso, P., Biviano, A., Böhringer, H., & Romaniello, M. 2007, A&A, 464, 451

Popesso, P., Biviano, A., Finoguenov, A., et al. 2015, A&A, 574, A105

Popesso, P., Biviano, A., Rodighiero, G., et al. 2012, A&A, 537, A58

Popesso, P., Böhringer, H., Brinkmann, J., Voges, W., & York, D. G. 2004, A&A, 423, 449

Popesso, P., Böhringer, H., Romaniello, M., & Voges, W. 2005, A&A, 433, 415

Pratt, G. W., Croston, J. H., Arnaud, M., & Böhri nger, H. 2009, A&A, 498, 361

Predehl, P., Andritschke, R., Böhringer, H., et al. 2010, in SPIE conference proceedings, Vol. 7732, Space Telescopes and Instrumentation 2010: Ultraviolet to Gamma Ray, 77320U

Predehl, P., Andritschke, R., Bornemann, W., et al. 2007, in SPIE conference proceedings, Vol. 6686, UV, X-Ray, and Gamma-Ray Space Instrumentation for Astronomy XV, 668617

Press, W. H. & Schechter, P. 1974, ApJ, 187, 425

Primack, J. R. 2005, New Astronomy Reviews, 49, 25

Puchwein, E., Springel, V., Sijacki, D., & Dolag, K. 2010, MNRAS, 406, 936

Randall, S. W., Markevitch, M., Clowe, D., Gonzalez , A. H., & Bradač, M. 2008, ApJ, 679, 1173

Rasia, E., Ettori, S., Moscardini, L., et al. 2006, MNRAS, 369, 2013

Rasia, E., Mazzotta, P., Borgani, S., et al. 2005, ApJ, 618, L1

Rasia, E., Mazzotta, P., Bourdin, H., et al. 2008, ApJ, 674, 728

Rasia, E., Meneghetti, M., Martino, R., et al. 2012, New Journal of Physics, 14, 055018

Reichert, A., Böhringer, H., Fassbender, R., & Mühlegger, M. 2011, A&A, 535, A4

Reiprich, T. H., Basu, K., Ettori, S., et al. 2013, Space Sci. Rev., 177, 195

Reiprich, T. H. & Böhringer, H. 2002, ApJ, 567, 716

Reiprich, T. H., Sarazin, C. L., Kempner, J. C., & Tittley, E. 2004, ApJ, 608, 179

Richard, J., Patricio, V., Martinez, J., et al. 2015, MNRAS, 446, L16

Riemer-Sørensen, S., Wik, D., Madejski, G., et al. 2015, ApJ, 810, 48

Riess, A. G., Filippenko, A. V., Challis, P., et al. 1998, AJ, 116, 1009

Rines, K., Geller, M. J., Diaferio, A., & Kurtz, M. J. 2013, ApJ, 767, 15

Roediger, E., Brüggen, M., Simionescu, A., et al. 2011, MNRAS, 413, 2057

Roediger, E., Lovisari, L., Dupke, R., et al. 2012, MNRAS, 420, 3632

Ruchayskiy, O., Boyarsky, A., Iakubovskyi, D., et al. 2016, MNRAS, 460, 1390

Russell, H. R., McNamara, B. R., Sanders, J. S., et al. 2012, MNRAS, 423, 236

Russell, H. R., Sanders, J. S., Fabian, A. C., et al. 2010, MNRAS, 406, 1721

Russell, H. R., van Weeren, R. J., Edge, A. C., et al. 2011, MNRAS, 417, L1

Ruszkowski, M. & Oh, S. P. 2010, ApJ, 713, 1332

Salvato, M., Ilbert, O., Hasinger, G., et al. 2011, ApJ, 742, 61

Sanders, J. S. 2006, MNRAS, 371, 829

Sanders, J. S. & Fabian, A. C. 2006a, MNRAS, 371, 1483

Sanders, J. S. & Fabian, A. C. 2006b, MNRAS, 371, L65

Sanders, J. S. & Fabian, A. C. 2007, MNRAS, 381, 1381

Sanders, J. S. & Fabian, A. C. 2008, MNRAS, 390, L93

Sanders, J. S. & Fabian, A. C. 2013, MNRAS, 429, 2727

Sanders, J. S., Fabian, A. C., Allen, S. W., & Schmidt, R. W. 2004, MNRAS, 349, 952

Sanders, J. S., Fabian, A. C., & Dunn, R. J. H. 2005a, MNRAS, 360, 133

Sanders, J. S., Fabian, A. C., Hlavacek-Larrondo, J. an d Russell, H. R., et al. 2014, MNRAS, 444, 1497

Sanders, J. S., Fabian, A. C., & Smith, R. K. 2011, MNRAS, 410, 1797

Sanders, J. S., Fabian, A. C., & Taylor, G. B. 2005b, MNRAS, 356, 1022

Sarazin, C. L. 1986, Reviews of Modern Physics, 58, 1

Schaye, J., Crain, R. A., Bower, R. G., et al. 2015, MNRAS, 446, 521

Schmid, C., Martin, M., Wilms, J., et al. 2010, X-ray Astronomy 2009; Present Status, Multi-Wavelength Approach and Future Perspectives, 1248, 591

Schmidt, W., Almgren, A. S., Braun, H., et al. 2014, MNRAS, 440, 3051

Schuecker, P., Finoguenov, A., Miniati, F., Böh ringer, H., & Briel, U. G. 2004, A&A, 426, 387

Simionescu, A., Werner, N., Böhringer, H., et al. 2009, A&A, 493, 409

Smith, D. A., Wilson, A. S., Arnaud, K. A., Terashi ma, Y., & Young, A. J. 2002, ApJ, 565, 195

Smith, G. P., Mazzotta, P., Okabe, N., et al. 2016, MNRAS, 456, L74

Spergel, D. N., Verde, L., Peiris, H. V., et al. 2003, ApJS, 148, 175

Springel, V., Frenk, C. S., & White, S. D. M. 2006, Nature, 440, 1137

Springel, V., White, S. D. M., Jenkins, A., et al. 2005, Nature, 435, 629

Stanek, R., Evrard, A. E., Böhringer, H., Schuecker, P., & Nord, B. 2006, ApJ, 648, 956

Strigari, L. E., Bullock, J. S., Kaplinghat, M., et al. 2006, ApJ, 652, 306

Sun, M., Voit, G. M., Donahue, M., et al. 2009, ApJ, 693, 1142

Sunyaev, R. A., Norman, M. L., & Bryan, G. L. 2003, Astronomy Letters, 29, 783

Sunyaev, R. A. & Zeldovich, I. B. 1980a, ARA&A, 18, 537

Sunyaev, R. A. & Zeldovich, I. B. 1980b, MNRAS, 190, 413

Tamura, T., Bleeker, J. A. M., Kaastra, J. S., Ferrigno, C., & Molendi, S. 2001, A&A, 379, 107

Tamura, T., Iizuka, R., Maeda, Y., Mitsuda, K., & Yamasaki, N. Y. 2015, PASJ, 67, 23

Tanaka, T., Kunieda, H., Hudaverdi, M., Furuzawa, A., & Tawara, Y. 2006, PASJ, 58, 703

Tenzer, C., Warth, G., Kendziorra, E., & Santangelo, A. 2010, in SPIE conference proceedings, Vol. 7742, High Energy, Optical, and Infrared Detectors for Astronomy IV, 77420Y

Tinker, J., Kravtsov, A. V., Klypin, A., et al. 2008, ApJ, 688, 709

Tremaine, S. & Gunn, J. E. 1979, Physical Review Letters, 42, 407

Truemper, J. 1982, Advances in Space Research, 2, 241

Tylka, A. J., Adams, J. H., Boberg, P. R., et al. 1997, IEEE Transactions on Nuclear Science, 44, 2150

Urban, O., Werner, N., Allen, S. W., et al. 2015, MNRAS, 451, 2447

Vazza, F., Brunetti, G., Gheller, C., Brunino, R., & Brüggen, M. 2011, A&A, 529, A17

Vazza, F., Brunetti, G., Kritsuk, A., Wagner, R. a nd Gheller, C., & Norman, M. 2009, A&A, 504, 33

Vazza, F., Roediger, E., & Brüggen, M. 2012, A&A, 544, A103

Vikhlinin, A. 2006, ApJ, 640, 710

Vikhlinin, A., Burenin, R. A., Ebeling, H., et al. 2009a, ApJ, 692, 1033

Vikhlinin, A., Kravtsov, A., Forman, W., et al. 2006, ApJ, 640, 691

Vikhlinin, A., Kravtsov, A. V., Burenin, R. A., et al. 2009b, ApJ, 692, 1060

Vogelsberger, M., Genel, S., Springel, V., et al. 2014, MNRAS, 444, 1518

Voit, G. M. 2005, Reviews of Modern Physics, 77, 207

von der Linden, A., Allen, M. T., Applegate, D. E., et al. 2014, MNRAS, 439, 2

Walker, S. A., Fabian, A. C., & Kosec, P. 2014, MNRAS, 445, 3444

Watson, C. R., Li, Z., & Polley, N. K. 2012, Journal of Cosmology and Astroparticle Physics, 3, 018

Weinberg, D. H., Mortonson, M. J., Eisenstein, D. J. an d Hirata, C., Riess, A. G., & Rozo, E. 2013, Physics Reports, 530, 87

Weißmann, A., Böhringer, H., & Šuhada, R. an d Ameglio, S. 2013, A&A, 549, A19

Werner, N., Böhringer, H., Kaastra, J. S., et al. 2006a, A&A, 459, 353

Werner, N., de Plaa, J., Kaastra, J. S., et al. 2006b, A&A, 449, 475

Werner, N., Durret, F., Ohashi, T., Schindler, S., & Wiersma, R. P. C. 2008, Space Sci. Rev., 134, 337

Werner, N., Urban, O., Simionescu, A., & Allen, S. W. . 2013, Nature, 502, 656

Werner, N., Zhuravleva, I., Churazov, E., et al. 2009, MNRAS, 398, 23

White, S. D. M., Navarro, J. F., Evrard, A. E., & Frenk, C. S. 1993, Nature, 366, 429

Wright, C. O. & Brainerd, T. G. 2000, ApJ, 534, 34

Wright, E. L. 2006, PASP, 118, 1711

York, D. G., Adelman, J., Anderson, Jr., J. E., et al. 2000, AJ, 120, 1579

Zandanel, F., Weniger, C., & Ando, S. 2015, Journal of Cosmology and Astroparticle Physics, 9, 060

Zhang, C., Xu, H., Zhu, Z., et al. 2016, ApJ, 823, 116

Zhang, Y.-Y., Andernach, H., Caretta, C. A., et al. 2011a, A&A, 526, A105

Zhang, Y.-Y., Finoguenov, A., Böhringer, H., et al. 2008, A&A, 482, 451

Zhang, Y.-Y., Laganá, T. F., Pierini, D., et al. 2011b, A&A, 535, A78

Zhang, Y.-Y., Okabe, N., Finoguenov, A., et al. 2010, ApJ, 711, 1033

Zhuravleva, I., Churazov, E., Arévalo, P., et al. 2015, MNRAS, 450, 4184

Zhuravleva, I., Churazov, E., Schekochihin, A. A., et al. 2014a, Nature, 515, 85

Zhuravleva, I., Churazov, E., Sunyaev, R., et al. 2013, MNRAS, 435, 3111

Zhuravleva, I., Churazov, E. M., Schekochihin, A. A. an d Lau, E. T., et al. 2014b, ApJ, 788, L13

Danksagung

First of all I would like to thank the supervisors of my PhD project Dr. Jeremy Sanders and Prof. Kirpal Nandra for giving me the opportunity to work on this research project and for their great support over the past three years. I would like to thank Dr. Nicolas Clerc for his great support with eROSITA simulations and cosmological analysis. Thank you also to Dr. Massimo Gaspari for helping in comparing my results to hydrodynamical simulations and many discussions about ICM simulations in general. I thank Dr. Johannes Buchner for helpful discussions about his BXA fitting procedure. Thank you also to Jethro Ridl for helped with the analysis of GROND observations. I would like to thank Dr. Vadim Burwitz and the team at the PANTER test facility for insight into the hardware calibration of eROSITA. Thank you to Ondrej Urban who hosted me at his place in Stanford and organized my talk at the KIPAC. I am thankful to many other colleagues who helped me with various problems over the years especially Dr. Frank Haberl, Dr. Hermann Brunner, Dr. Konrad Dennerl, Dr. Tom Dwelly, Dr. Mara Salvato. Thank you also to Harald Baumgartner, Joachim Paul, and Achim Bohnet for always taking care of IT problems quickly. I would also like to thank my office mates Torben Simm and Damien Coffey for carefully proof reading parts of the thesis.

My special thanks goes to my wife Claudia for her support in so many ways and to our new small family. I thank my parents Angelika and Reinhard for their ongoing support as well as my brother Michael and my sister Lisa. Thank you also to my parents in law Alessandra and Maurizio as well as all my big family. Thank you to all our friends for making these years of the PhD more fun. Thank you to many more people involved in making this project a success.

I acknowledge the use of the following data, programs, and fundings:

This research has made use of data obtained from the *Chandra* Data Archive and the *Chandra* Source Catalog, and software provided by the *Chandra* X-ray Center (CXC) in the application packages CIAO, ChIPS, and Sherpa. This research has made use of NASA's Astrophysics Data System. This research has made use of the VizieR catalogue access tool, CDS, Strasbourg, France. This research has made use of SAOImage DS9, developed by Smithsonian Astrophysical Observatory. This research has made use of data and software provided by the High Energy Astrophysics Science Archive Research Center (HEASARC), which is a service of the Astrophysics Science Division at NASA/GSFC

and the High Energy Astrophysics Division of the Smithsonian Astrophysical Observatory. This research has made use of the SIMBAD database, operated at CDS, Strasbourg, France. This research has made use of the tools Veusz, the matplotlib library for Python, and TOPCAT. My collaborator Massimo Gaspari was supported by the National Aeronautics and Space Administration through Einstein Postdoctoral Fellowship Award Number PF-160137 issued by the *Chandra* X-ray Observatory Center, which is operated by the Smithsonian Astrophysical Observatory for and on behalf of the National Aeronautics Space Administration under contract NAS8-03060. I acknowledge funding of this thesis by the Max-Planck-Institute for extraterrestrial Physics in Garching. I received a grant from the DAAD RISE program for hosting the undergraduate student Benjamin Kaiser for a 10 week internship working on the substructure analysis in my simulated eROSITA image.